BUDAPEST UNIVERSITY OF TECHNOLOGY AND ECONOMICS
FACULTY OF ELECTRICAL ENGINEERING AND INFORMATICS
DOCTORAL SCHOOL OF ELECTRICAL ENGINEERING

Innovative methods for the sound design of organ pipes

Ph.D. Thesis

Péter Rucz
M.Sc.E.E.

Supervisor Fülöp Augusztinovicz, D.Sc.
Co-promotor Judit Angster, Dr. rer. nat.

Department of Networked Systems and Services

Budapest, 2015.

Statement of authorship

I (undersigned) **Péter Rucz** declare that I have prepared and written the present doctoral dissertation "Innovative methods for the sound design of organ pipes" by myself, and I have used only the listed sources during the work. These sources are clearly highlighted at any part that has been re-used literally, or with identical content.

Budapest, August 31st, 2015.

. . . .
Péter Rucz

Abstract

Despite the fact that organ building is quite an orthodox art with roots going back more than two thousand years, organ builders are still looking for improvements of the quality of their instruments. Pipe organ research aims at providing answers to the questions of the craftsmen by seeking the physical explanations of the phenomena observed, and thus supplementing the traditional craftsmanship with scientific background.

The objective of this thesis is to contribute to organ research regarding two main aspects. On the one hand, solutions to particular design issues in organ building practice are sought. This task consists of investigating the acoustic behavior of specific pipe families, understanding their physics, predicting the impact of changing the geometry of the pipe, and finally, developing strategies that lead to the desired sound characteristics by optimal design. On the other hand, the dissertation introduces novel modeling and optimization methodology for examining and solving the aforementioned problems. The latter involves the establishment of one- and three-dimensional or hybrid acoustic models and computer simulations of fluid flow relying on state of the art techniques. Both aspects are approached making use of analytical and numerical methods and validating the attained results by comparing them to measured data.

Kivonat

Annak ellenére, hogy az orgonaépítés egy meglehetősen hagyománytisztelő mesterség, mely több mint két évezredes gyökerekkel rendelkezik, az orgonaépítők napjainkban is keresik hangszereik tökéletesítésének módjait. Az orgonakutatás célja az orgonaépítő mesterek kérdéseinek megválaszolása, az általuk megfigyelt jelenségek fizikai magyarázatának feltárása, így támogatva tudományos háttérismeretekkel ezt a tradícionális szakmát.

Ez a disszertáció két területen igyekszik az orgonakutatás eredményeihez hozzájárulni. Egyrészt választ keres az orgonaépítés bizonyos aktuális tervezési kérdéseire. Ez a feladat adott síptípusok akusztikai viselkedésének tanulmányozását, fizikai működésük megértését, egyes változtatások hatásainak előrejelzését, végül pedig olyan optimális méretezési eljárások megalkotását foglalja magában, melyekkel a sípok kívánt hangzása elérhető. Másrészt az értekezés új modellezési és optimalizálási technikákat mutat be az előbbi problémák megoldásához. Utóbbi egy- és háromdimenziós vagy hibrid akusztikai modellek létrehozását, illetve áramlástani szimulációk megalkotását jelenti a legkorszerűbb számítógépes eljárásokra támaszkodva. Mindkét területet analitikus és numerikus módszerek alkalmazásával közelítjük meg, a modellezés eredményeit pedig mérési adatokkal összehasonlítva ellenőrizzük.

Acknowledgments

This thesis presents my work carried out at the Laboratory of Acoustics and Studio Technologies at Budapest University of Technology and Economics, Budapest, Hungary and at the Group of Musical and Photoacoustics of the Fraunhofer Institute for Building Physics in Stuttgart, Germany. The research has been conducted between 2009 and 2013 under the supervision of Fülöp Augusztinovicz and co-supervision of Judit Angster and András Miklós.

I would like to thank my supervisor, Fülöp Augusztinovicz for supervising the research presented herein and welcoming me on board at the Laboratory of Acoustics. I express my gratitude to Judit Angster and András Miklós, not only for guiding the research and for letting me join their research group, but also for inviting me to their home several times. I am thankful for the guidance and helpful remarks of Péter Fiala. I also thank Máté Márton Lohász the lectures on fluid dynamics and large eddy simulation.

I thank my colleagues the years spent together at the Laboratory of Acoustics and Studio Technologies: Bendegúz Bartha, Gergely Firtha, Krisztián Gulyás, István Koller, Ferenc Márki, Tamás Mócsai, Attila Balázs Nagy, and Péter Pfliegel. I appriciate the hospitality and the cooperation of the colleagues at the Group of Musical Acoustics: Hubert Außerlechner, Kai Dolde, Zlatko Dubovski, Andreas Gloos, Nadine Kotzur, Wei Kuang, Natalia Manrique Ortiz, Felipe Merino Reyes, Stephan Pitsch, Tim Preukschat, Miguel José Ruiz González, Sergej Sel, and Thomas Trommer.

I thankfully acknowledge the cooperation of Thomas Barthold organ builder and Konrad Mühleisen and Johannes Kirschmann voicers, for their participation in the laboratory experiments and listening tests presented in Chapters 5–6. I appreciate the kindliness and encouragement of all the organ builder partners participating in the European projects.

I am grateful for the financial support of the European Commission (Grant Agreement Refs. #222104 and #286539) and the Hungarian research grant TÁMOP – 4.2.2.B-10/1-2010-0009. I am also indebted to the National Information Infrastructure Development Institute (NIIF) for providing me access to the computational capacities of their supercomputers.

The support of the Huszty Dénes Grant is greatly appreciated. The Young Professionals Grant provided by the International Institute of Noise Control Engineering (I-INCE) supporting participation at the Inter-Noise 2013 conference is gratefully acknowledged.

I would also like to thank my students, for their quality work and contributions in the improvent of the in-house modeling tools utilized in this thesis.

Last, but certainly not least, I am grateful for my wife, Eszter and my family for their support and care during the years this work was performed.

Contents

Chapter 1

Introduction

1.1 About pipe organ research in a nutshell

Pipe organ research supplements traditional craftsmanship by novel theoretical, measurement and simulation techniques and results. Despite the fact that pipe organs have already been built for several hundreds of years, and that organ building is quite an orthodox art, organ builders are still seeking ways to improve the quality of their instruments.

Traditionally, organ building is a hand manufacturing process, which means that all pipes in a pipe organ are assembled, tuned, and voiced[1] by handwork. Pipe organ research does not aim to replace the work of organ builders and voicers, rather to increase the efficiency of the planning, building, tuning, and voicing processes. This aim is achieved by means of the development of novel—often computer aided—design methods and technologies based on scientific background.

Novel industrial and artistic requirements also force the organ building community to apply new techniques in pipe design. One of the recent industrial challanges is the prohibition of the usage of lead—one of the essential pipe materials—inside the European Union. From the artistic point of view, a new requirement for the organ sound is the need of reproducing the timbre of exotic (African or Asian) musical instruments by means of organ pipes. Both issues procure the need for new materials and pipe constructions.

From the physical point of view, the sound generation mechanism of organ pipes—either *labial* or *lingual*—is a complex process involving acoustical, mechanical and fluid dynamical phenomena inherently and non-linearly coupled. The complexity of the process explains the fact that the sound generation of wind instruments is still an active research field in musical, aero- and numerical acoustics, and even in fluid dynamics. From the 19$^{\text{th}}$ century, a great number of related scientific contributions have been published, including theoretical, measurement, and simulation results.

1.2 Motivation and background

Discussions with a number of organ builders revealed that a lot of design rules in organ building practice lack scientific explanation. Traditional scaling rules are sufficient usually; however, in case of certain design problems no generally accepted methods exist. In special cases, due to practical or aesthetic reasons, the organ builder has to scale the pipes of some ranks giving up on the conventional rules. Then, the craftsmen can only rely on their personal experience and intuitions determining the dimensions of the pipes.

[1] The definitions of the processes *scaling*, *voicing*, and *tuning* are given in Section 2.1.4.

motivation

The motivation of the research reported in this thesis is twofold. On the one hand it seeks solutions for specific issues in organ pipe scaling, proposing novel design methods in order to attain extended control over the sound characteristics and better percieved sound quality. On the other hand the thesis intends to provide a scientific background for the aforementioned issues leading to more detailed physical models and a better understanding of the sound generation mechanism. Both objectives are approached by means of analytical and numerical modeling and validation by comparison to measurement data.

project background

The industrial background of this thesis is covered by the European projects INNOSOUND and REEDDESIGN. Beside the financial support provided by the European Commission, these projects have given an invaluable forum for discussions with the leaders of the European organ building community.[2] The examination of particular design issues that are addressed in this thesis were also initiated by the organ builder partners participating in these projects.

1.3 Workflow and structure

workflow

The workflow of the research presented in this dissertation is followable in Figure 1.1. The first objective, i.e. to solve certain design problems of organ building practice, is approached by utilizing 1D and 3D modeling tools, with validating and comparing the results to measurements, whenever it is possible. The second objective, developing novel modeling methodology, is inherently involved in the approach utilized for the examination of the design problems.

Experimental investigations were carried out at the Group of Musical and Photacoustics of the Fraunhofer Institute of Building Physics, Stuttgart, Germany, while the modeling and software tools were developed mainly at the Laboratory of Acoustics and Studio Technologies of the Budapest University of Technology and Economics, Budapest, Hungary.

software tools

To be able to apply the results in practice, some software tools were also developed. These tools were already used for some examinations and the evaluation of measurement results. The developments making use of the acoustical finite element method were incorporated into an open source toolbox.

overall structure

The thesis is structured as depicted in Figure 1.1. Chapters 2–4 introduce the background and the state of the art in pipe organ research, as well as the basics of the modeling techniques utilized in this thesis. Chapters 5–9 present the achieved results, each focusing on a specific application. The appendices A–D briefly demonstrate the developed software tools.

background chapters

The purpose of the first part of the thesis is to set the stage for the second part. Chapter 2 gives a short introduction to the history and the structure of the classical pipe organ and the sound generation mechanism of organ pipes. A summary of the state of the art in organ research and an overview of the methodology applied throughout the thesis is also given there. Chapter 3 covers the background of the one-dimensional modeling methodology. Starting from the fundamental equations of linear acoustics, an equivalent transmission line model of an open straight cylindrical pipe is derived, including intrinsic, viscothermal, and radiation losses. An introduction to the three-dimensional numerical techniques applied in the thesis is presented in Chapter 4, where the acoustical finite element method (FEM) and two of its extensions for modeling problems with open boundaries are discussed.

result chapters

The second part of the thesis presents the results of the research. This part with its five chapters is a collection of revised and extended material already published by the author.[3] Chapters 5–8 address specific design problems of organ building practice, whereas Chapter 9 presents a modeling approach for the numerical examination of the sound generation of labial pipes. Chapters 6–7 are closely related, while the other chapters of the second part of the thesis are more self-contained.

[2] Organ builder companies participating in the projects are listed in Appendix E.

[3] A list of these publications is presented on pages 159–161.

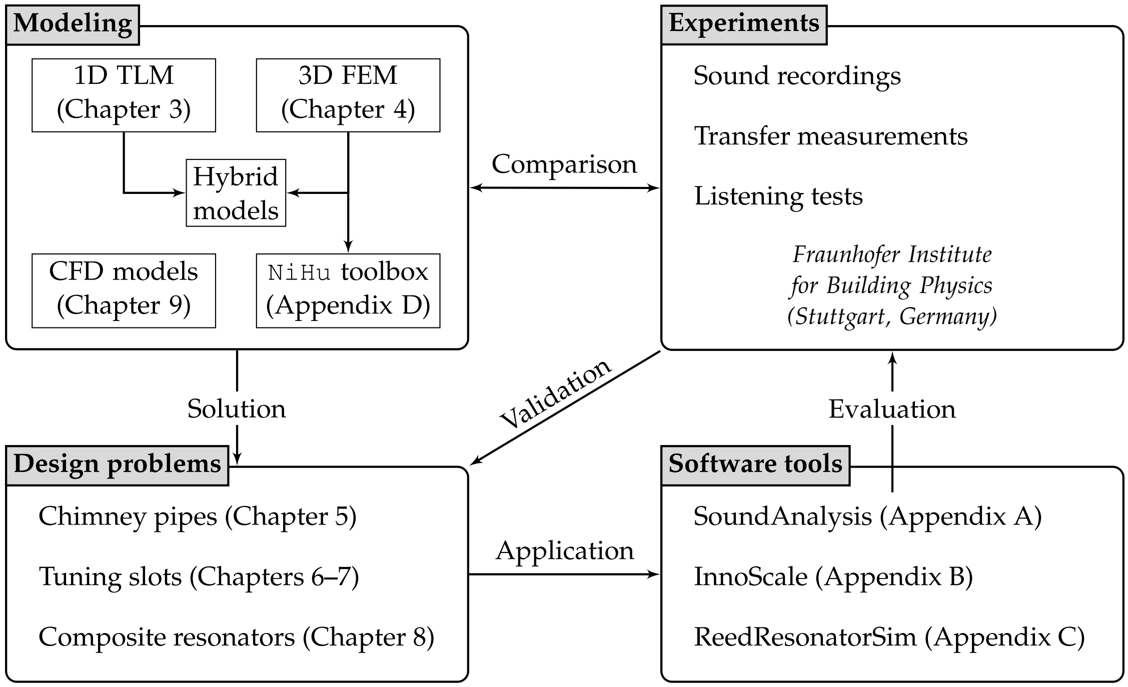

Figure 1.1. Workflow and structure of this thesis

Chapter 5 discusses the development of a novel scaling method for the sound design of *chimney pipes*. An optimization algorithm is elaborated by which the geometry of the resonator is adjusted to enhance the target harmonics in the steady state pipe sound.

Chapter 6 presents the results of a measurement campaign for the examination of the acoustic behavior of labial organ pipes with *tuning slots*. Previously unknown phenomena are documented and the impact of changing the design parameters of the tuning slot is investigated using experimental pipes. In Chapter 7 an accurate acoustic model of labial pipes with a tuning slot is established, by which a scaling method that enables sound design can be attained. The model is elaborated using a hybrid system consisting of one-dimensional transmission line elements supplemented by three-dimensional finite element simulations.

A modeling technique for axisymmetric resonators of *lingual organ pipes* is introduced in Chapter 8. The proposed method incorporates the results of numerical simulations of the radiation impedance and a low frequency *shallot* model, that lead to an accurate prediction of the natural resonance frequencies of the acoustic system consisting of the shallot and the resonator.

For the examination of the flow phenomena in the sound production of flue organ pipes, Chapter 9 presents fluid flow simulations of the air jet and edge tone generation in the foot of a labial pipe. Two- and three-dimensional models are compared for predicting the velocity profiles of the free jet and the hydrodynamic modes of the edge tone.

The results are summarized in Chapter 10 with an outlook on further research possibilities. Novel scientific achievements presented in this dissertation are also given there in the form of thesis statements.

The software tools developed in the framework of the European projects INNOSOUND and REEDDESIGN are presented in Appendices A–C. Finally, Appendix D demonstrates the toolbox `NiHu`, focusing on its parts elaborated in the workflow of this thesis. appendices

Chapter 2

Background

This chapter serves as a background for introducing the classical pipe organ as a musical instrument and discussing the basics of the sound generation mechanism of labial and lingual organ pipes. The characteristic properties of the sound of individual pipes in the steady state and transient phases are also introduced. The state of the art in pipe organ research is presented in this chapter in order to familiarize the reader with the results achieved so far and the questions that are still open.

objective

The objective of this chapter is not to give a complete overview, but to facilitate a better understanding of the methods and results presented in subsequent chapters. Therefore, for more details on specific questions, the reader is referred to the cited literature. Since a large number of papers, books and other publications have been published in the topic, it is almost impossible to give a complete review that addresses all aspects. Hence, the review of the state of the art presented in this chapter summarizes the works related to the topic of this thesis. This review also serves as a guide to the reader to be able to adjudicate the novelty and relevance of the results presented in this thesis.

structure

First, the pipe organ is introduced with a brief discussion about its history and main parts. Then, the sound production mechanism of labial and lingual organ pipes is examined. The most important properties of organ pipe sounds are discussed in Section 2.2. A common approach for modeling the sound generation of wind instruments and its application for organ pipes is reviewed in Section 2.3. Finally, the chapter is concluded with a brief introduction to the methodology applied throughout the thesis in Section 2.4.

2.1 The pipe organ and organ pipes

This section demonstrates the pipe organ as a complete musical instrument. Its history, main parts and principles of operation are reviewed briefly, then labial and lingual pipes and their sound generation mechanism are introduced. Finally, the processes of scaling, tuning, and voicing are discussed briefly. German translations of certain terms are also given in this section for the sake of better understanding for German speaking readers.

2.1.1 The queen of musical instruments

The history of the pipe organ

the hydraulus

The earliest known wind instrument not blown by the human lungs is believed to belong to Ctesibius of Alexandria (*fl.* 285–222 B.C.) [146, pp. 1–2]. This instrument was composed of a water tank and a trumpet attached to it, with the mouthpiece connected to an open hole on the top of the tank. To produce sound, air was conveyed into the trumpet by pumping more water into the tank, which forced the remaining air out of the tank through the hole at the top. This idea was extended by Hero—a student of Ctesibius—who attached a row of pipes to the water tank arranged in a musical scale. This instrument is called the *hydraulus* (hydraulic organ) and it became widespread in antique Greece and the Roman Empire.

organum pneumaticum

While the hydraulus enjoyed great popularity, a similar instrument called *organum pneumaticum* (pneumatic organ) appeared around the second century [150, p. 35]. In this instrument, which presumably originated from the *bagpipe*, unlike the hydraulus, the pressure needed for air to flow into the pipes was not provided by water, but air. At that times, the organum pneumaticum referred to a smaller instrument compared to the hydraulus with less pipes and smaller sound power, used mainly for entertainment in the Roman era. However, by the eighth century, becoming larger and gaining more sound power, the pneumatic organ had assumed its prominent place in the liturgy of the catholic church, as initiated by Pope Vitalian [146, pp. 26–29].

medieval organs

In the medieval era the size of pneumatic organs started to grow rapidly. As an extraordinary example, the organ in the cathedral of Winchester (built around 980 A.D.), had more than 400 pipes, 26 blower machines, which required 70 people to operate them [150, p. 52]. At this time one key on the keyboard could sound more than ten pipes at the same time. The increased size also introduced new problems and required technical improvements to solve them. One of the greatest inventions is the mechanical transmission, the so-called *rollerboard* (Wellenbrett), which was introduced in the 14th century and enabled the reduction of the size of the keyboard.

modern pipe organs

The pipe organ has undergone a lot of innovations and technical improvements while preserving its main principle of functioning from the 15th century. Along with the clock, the pipe organ was considered one of the most complex human-made mechanical creations before the Industrial Revolution. Due to its wide tonal range, its ability of imitating the sound of various instruments, and its grandiose size, the pipe organ is often called the "*queen of musical instruments*", after W. A. Mozart.

Parts of the pipe organ

The schematic of a modern pipe organ is depicted in Figure 2.1. The picture only illustrates the most important parts of the instrument and their connections while omitting several details.

ventilation system

In modern pipe organs the *ventilation system*—or wind system (Windwerk)—consists of four essential parts. The *blower* (Gebläse), which is often an electrical fan nowadays, is the air supply of the instrument. It pumps air into the ventilation system, according to the "wind consumption" of the instrument. The *roller valve* (Rollenventil) regulates the air flow from the blower into the bellows. The *bellows* (Balg) ensure that the pressure in the windchest remains constant. By placing different weights on the top of the bellows the pressure can be controlled. Finally, the *wind duct* (Windkanal) connects the ventilation system with the *windchest*, providing the air supply for the pipes. In large organs, more ventilation systems can be present and operate at the same time.

voices, ranks, stops

The *windchest* (Windlade) is one of the most important parts of the pipe organ that connects the wind system, the keyboards and the pipes. The pipes are connected to the windchest, arranged into *ranks* (Pfeifenreihe) and *stops* (Register). Each stop covers a certain range of musical tones. Special stops, such as *mixtures* (Mixtur) can consist of multiple ranks, activated by the same keys and hence multiple *voices* (Stimme) can sound at the same time.

the windchest

There are various kinds of windchest constuctions, such as the slider chest, the spring chest, the cone valve chest, and the Pitman chest, see [57, ch. 7] for further details. In the traditional windchest—the so-called *slider chest* (Schleiflade), which is also shown in Figure 2.1—the pipes corresponding to the same musical note from all stops are connected to one *key channel* (Tonkanzelle). The key channels are separated by valves from the *pallet box* (Windkasten), which is the lowest part of the windchest. The pipes are separated from the key channels by the *slides* (Schleife), which are controlled by the *drawstops* (Registerzug). The slider is a wooden plate that has a

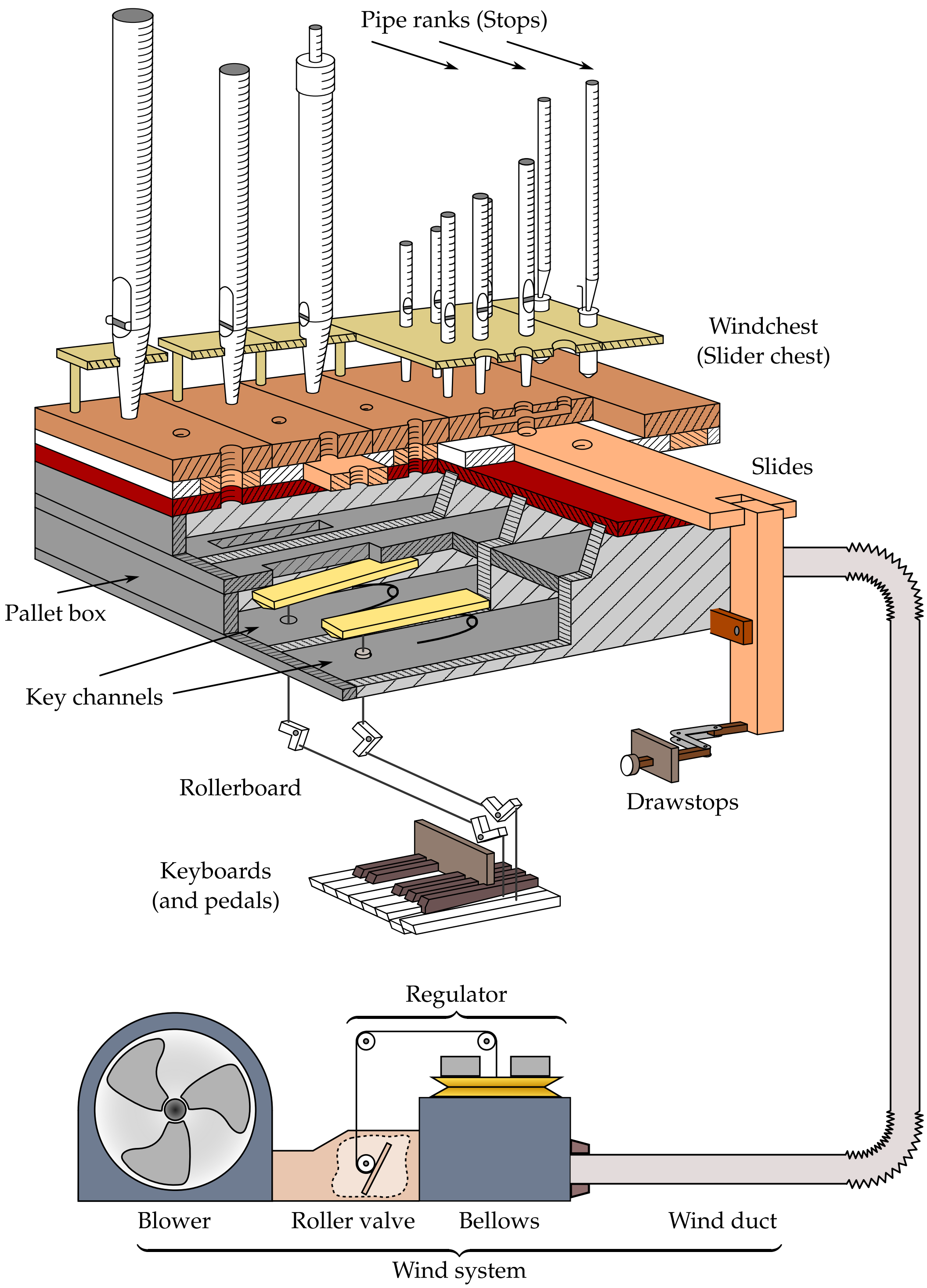

Figure 2.1. The schematic of a modern pipe organ and its most important parts

number of holes in it, corresponding to the position of the pipes. By activating a stop, the holes of the slider plate let the air flow from the key channel into the pipes. Thus, by means of the keys (or pedals) and the drawstops the pipes to be sounded are selected like selecting certain rows and columns of a matrix.

keyboards and pedals

The keyboards and pedals control the valves inside the pallet box and hence the flow of air into the key channels. In organ building, it is usual to express the pitch of the note in *feet* (Fußlage). Usually, the keyboards cover five octaves with 61 keys from the 8′ C to 1/4′ C, while the pedals cover the range of 2 1/2 octaves from 8′ C to 1 1/2′ F. By drawing different stops, the pitch corresponding to one key or pedal can be changed (e.g. by choosing a 16′ stop, the first key will sound a 16′ C note), and thus the musical range of the keyboard can be extended. The keyboards and pedals are traditionally connected to the windchest by a mechanical transmission, called the *rollerboard* (Wellenbrett); however, remote electronical controllers also exist.

All organ pipes produce sound by means of air flowing into the pipe. When a key on the keyboard is pressed the corresponding valve in the pallet opens, which lets air flow into the key channels and the pipes selected by the drawstops. When the key is released a spring closes the valve and the way of the airflow is blocked. Unlike the keys of the piano, for example, the sound power is not controlled directly by the strength of the strike on the keyboard.[1] Thus, the loudness of a tone or chord can be controlled by special devices, such as the *swell* (Schwellwerk); however, the resulting sound power mainly depends on the configuration of the individual pipes. In a usual setup, about the 85–90% of the pipes are *labial* (Labialpfeife), while the rest are *lingual* pipes (Zungenpfeife). In some modern pipe organs, a third type of pipes, the so called *diaphone* pipes are also present. These pipes have some characteristics in common both with labial and lingual organ pipes and are mainly used in bass (16′ or 32′) stops. In the next sections, labial and lingual pipes are discussed separately. Diaphone pipes are not addressed in the following parts of the thesis.

2.1.2 Labial organ pipes

Labial pipes, also referred to as *flue pipes* produce sound by means of an oscillating air jet exciting the air column in the resonator of the pipe. Labial pipes can be made of metal (cylindrical and conical pipes) or wood (rectangular pipes). The upper end of labial pipes can be *open* (offen), *stopped* (gedackt), or partially open, like in case of *chimney pipes* (Rohrflöte), see later in Chapter 5.

parts of labial pipes

The structure of a labial organ pipe is displayed in Figure 2.2. The pipe consists of two main parts: (1) the *pipe foot* (Pfeifenfuß), and (2) the *pipe body* (Pfeifenkörper), also known as the *resonator*.

In case of labial pipes air can enter the pipe through the *foot hole* (Fußloch), which is often referred to as *bore* in case of wooden pipes. As air flows into the pipe from the windchest, the pressure grows inside the pipe foot. Air can leave the pipe foot through the thin gap between the *lower lip* (Unterlabium) and the *languid* (Kern). This thin gap is called the *windway* or *flue*. The area between the lower lip and the *upper lip* (Oberlabium) is referred to as the *mouth* (Mund) of the pipe. In some cases the pipe body is mounted with *ears* (Seitenbart), which are located on both sides of the mouth, or different types of *beards* (Bart), that can be found under or around the mouth of the pipe. The latter accessories are not shown in Figure 2.2.

jet–lip interaction

Due to the overpressure in the pipe foot a thin jet of air develops in the windway. This jet is directed towards the upper lip, and when the air jet hits the lip, it becomes destabilized. In the interaction of the jet with the lip vortices are detaching from the upper lip in a quasi-periodic manner. The pressure oscillations due to the movement of the jet are known as the *edge tone* (Schneidenton) phenomenon, see later in Chapter 9. The oscillating air jet provides the excitation of the air column encompassed by the pipe body.

[1] Different kinds of tracker actions and valve constructions can provide different types of "touch sensitivity" of the keyboard, which can be exploited while playing the instrument. However, these effects are related more to the attack and decay transients of the sound rather than the loudness.

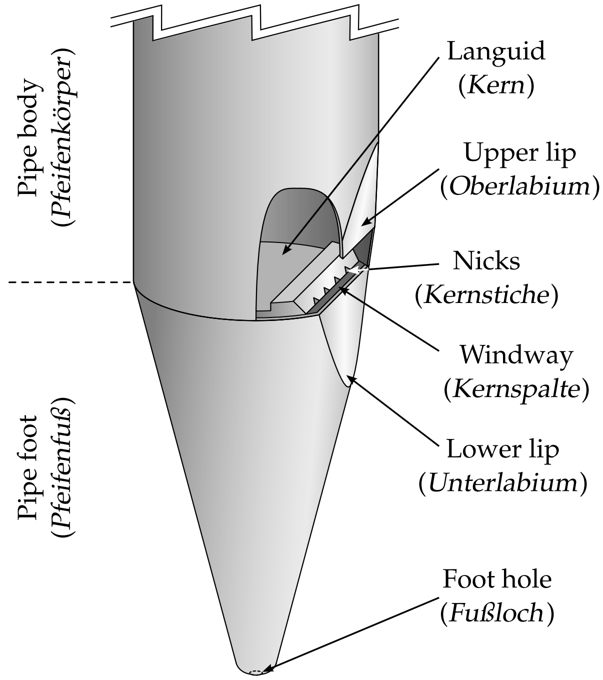

Figure 2.2. The parts of a labial organ pipe

With a proper configuration of the pipe geometry and the pressure in the windchest, the air column can be driven into resonance. If strong pressure oscillations develop inside the resonator, these oscillations have a strong feedback on the jet, and the jet–resonator system acts as a strongly coupled oscillator. In normal conditions the acoustic (resonator) and hydrodynamic (jet) oscillators become synchronized and oscillate at the same frequency determined by the coupled system. The frequency in most cases is very close to the first natural resonance frequency of the acoustic resonator, however, this is not unconditionally true (see Section 2.2.3). When the pressure driving the air jet or the geometry of the resonator are chosen poorly, the system can not synchronize and a strong and stable steady state sound is not produced.

steady state

When the steady state is reached, the oscillations stabilize and the sound becomes periodic, disregarding minor perturbations, e.g. small disturbances of the pressure in the windchest. The amplitude is also stabilized in this phase of the sound generation, which means that a balance of the entrained energy, the radiated sound energy and losses is attained. This steady state is referred to as the *self-sustained oscillation* of wind instruments.

2.1.3 Lingual organ pipes

Contrary to flue pipes, lingual pipes do not produce sound by an air jet, but by means of a vibrating metal tongue, which is often referred to as *reed*. Hence, lingual pipes are often called *reed pipes*. The parts of a lingual organ pipe are depicted in Figure 2.3.

parts of reed pipes

The pipe is composed of three main parts: (1) The *boot* (*Stiefel*) is the foot of the pipe, on which the pipe can stand. The boot is open at its bottom end, the hole through which air can flow into the pipe is called the *bore* (*Fußloch*). (2) The *nut* (*Kopf, Nuss*) is the middle section of the pipe, that connects the boot and the resonator. The boot end of the nut holds the *shallot* (*Kehle*), which is the most important part of the whole pipe. The shallot is a metal "boat", on which the *tongue* (*Zunge*) is fixed. The *tuning wire* (*Stimmkrücke*) goes through the nut and provides

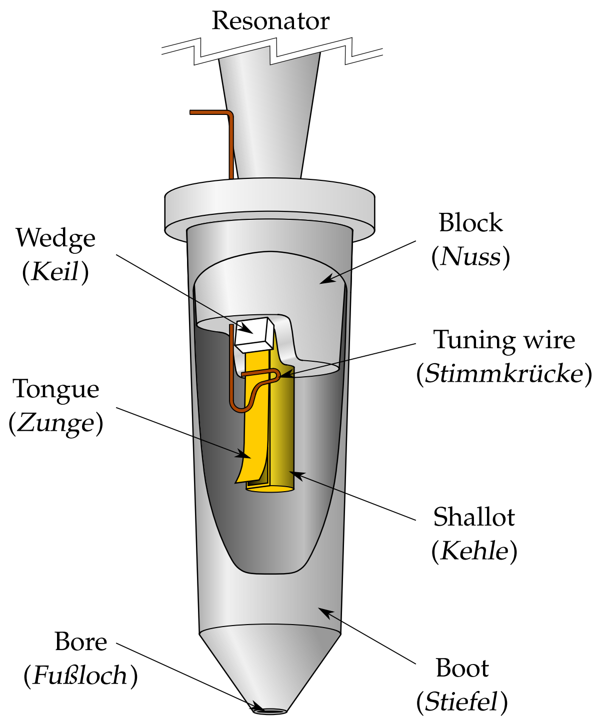

Figure 2.3. The parts of a lingual organ pipe

the possibility of tuning the pipe by changing the free length of the vibrating tongue, without disassembling the pipe. (3) The *resonator* is the upper part of the pipe, which can have various forms in case of lingual organ pipes.

When the pipe is sounded air flows into the pipe through the bore. The pressure in the boot rises, and air flows through the small gap between the tongue and the shallot. The increased pressure also pushes the tongue towards the shallot, whereas *Bernoulli's force* due to the air flow "pulls" the tongue in the same direction. The restoring force due to the elasticity of the tongue acts in the opposite direction.

beating and free reeds

There are two main types of reed pipes, characterized by the type of the shallot. These two types of pipes are used in different types of stops. In case of *beating reeds* (*aufschlagende Zunge*), the tongue hits the shallot in every period of its movement, and it can not go inside the shallot. Beating reeds are used in stops such as the *Crumhorn*, the *Trumpet*, or the *Vox Humana*. In case of *free reeds* (*durchschlagende Zunge*) the tongue moves into the shallot in every period of its movement instead of hitting it. Free reads are used in *Clarinet* and *Oboe* stops, for example.

acoustic feedback

In order to start and maintain the oscillation of the tongue, acoustic feedback from the shallot–resonator system is required. The pressure pertubations accompanying the movement of the reed travel along the shallot and the resonator and are reflected at the open end. When the reflected pressure wave reaches the tongue again, it exerts pressure force on it. With a proper setup of the geometry, these pressure forces can amplify the movement of the reed, and periodic oscillations can be achieved in the steady state. With a poor configuration, however, the acoustic feedback represses the motion of the tongue and the pipe can not produce sound.

Depending on the geometry of the pipe, the coupling between the vibration of the tongue and the pressure oscillations of the air column inside the resonator can either be weak or strong. In most cases, however, the pipe is scaled and tuned such that strong coupling is avoided. Therefore, the pitch of the pipe is mostly determined by the tongue and affected by the resonator only to a smaller extent. In the steady state phase of the sound generation, similar to labial pipes, the frequency of the tongue vibration and the pressure oscillations inside the resonator synchronizes and their amplitudes stabilize.

2.1.4 Scaling, voicing, and tuning

This section briefly introduces three procedures associated with the adjustment of different parameters of the pipes, affecting their sound characteristics. These processes are referred to as *scaling* (*Mensurierung*), *voicing* (*Intonierung*) and *tuning* (*Stimmung*), respectively.

Scaling refers to the phase in which the geometrical parameters of the pipes are decided. In traditional organ building the first parameter determined is the diameter (or the equivalent diameter in case of rectangular pipes). This is usually done by using a *reference scale* (such as the Töpfer scale [138]), that defines a reference diameter for an 8′ C pipe, say, and a ratio by which the diameter is decreased per octave. Then, the diameter of each pipe in each stop is defined individually by means of *scaling lines* that describe positive (wider pipes) or negative (narrower pipes) deviations from this reference scale for all pipe ranks. The deviations are chosen based on the registration and the acoustic environment of the organ. The length of the pipe is calculated such that the pipe produces the desired pitch. Further parameters, such as the height and the width of the mouth in case of labial pipes are determined by ratios compared to the diameter.

Voicing is performed after the pipes are built and the complete organ is assembled. In this process the organ builder or *voicer* (*Intonateur*) adjusts the speech of each pipe individually. Voicing adjustments alter the air flow parametrs (e.g. changing the foot hole diameter) or jet–lip interaction (e.g. nicking of the languid) in the pipe. Such manipulations can have a remarkable effect on the timbre and the attack transient of the pipe sound.

Tuning refers to the adjustment of the pitch of the pipe. Since even small changes in temperature or humidity affect the pitch, all pipes must be tunable. This is often achieved by mounting *tuning devices*, such as tuning slides, tuning rolls, or tuning slots in case of labial organ pipes. Pipes with clear cut end are usually retuned by means of broadening or narrowing the pipe at the open end to a small extent. Lingual pipes are tunable by means of the tuning wire.

2.2 Properties of organ pipe sounds

This section summarizes the most important properties of organ pipe sounds. First, the steady state pipe sound is examined by looking at the characteristics of the steady state spectrum and its envelope. Then, properties of the attack transient are discussed. Finally, special effects such as overblowing are explained briefly.

2.2.1 The steady state sound spectrum and the envelope

In the steady state phase of the sound generation the sound of both labial and lingual pipes can be considered periodic with small perturbations, thus, the steady state sound spectra of organ pipes are dominated by harmonic components. The frequency corresponding to the period of the oscillations is referred to as the *fundamental frequency* (*Grundton*). Harmonics of the fundamental frequency are known as *overtones* (*Obertöne*). Beside the harmonics, other non-harmonic components can be present, see later in Section 2.2.3. The harmonic and non-harmonic components are called collectively as *partials* (*Teiltöne*).

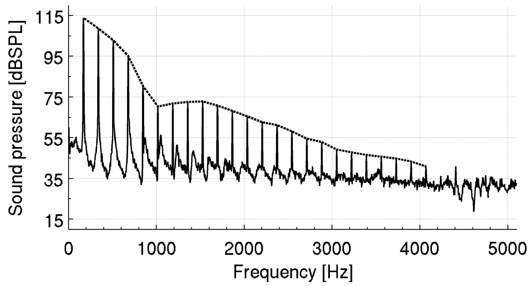

(a) Measurement at the mouth

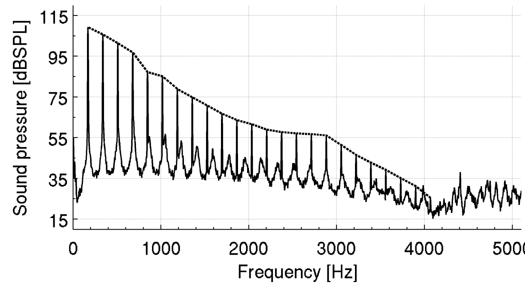

(b) Measurement at the open end

Figure 2.4. Steady state sound spectrum of a narrow open labial organ pipe. Solid lines: spectrum measurements. Dashed lines: spectral envelopes.

Figure 2.4 demonstrates the typical steady state sound spectrum of a narrow open labial pipe. As it can be seen, the spectra measured[2] at the mouth (Figure 2.4(a)) and at the open end (Figure 2.4(b)) are similar in some aspects, but also show remarkable differences. The sound is dominated by strong harmonic components, with the fundamental frequency of $f_1 = 169.5\,\mathrm{Hz}$. The equivalent loudness of the two recordings are also slightly different, they are 116.9 and $114.4\,\mathrm{dB}$ for the mouth and open end spectra, respectively. As in this case, it is common for labial organ pipes to have stronger radiated sound from the mouth than from the open end.

Both in the mouth and open end spectra more than twenty harmonics can be distinguished clearly. The amplitude of the partials decays with the frequency; however, the spectral envelopes (shown by the dashed lines in Figure 2.4) are remarkably different. This difference is explained by the inequality of the surface of the mouth and the open end, as discussed in detail by Miklós & Angster [101].

spectral baseline

Examination of the baseline of the steady state sound spectrum can also reveal a lot of important information concerning the sound. Since the harmonic content of the sound is dominant, capturing the baseline requires high quality measurement equipment and well-fitted signal processing tools. From the spectral baseline the natural resonance frequencies of the pipe can be identified as less sharp peaks of the baseline. The frequencies of natural resonances are non-harmonic, they show a "stretching" behavior compared to the harmonic partials. This effect is explained later in Sections 3.4 and 3.5. Around $4\,\mathrm{kHz}$ the spectra and their baselines become quite irregular. This phenomenon is due to the appearance of transversal acoustic modes, and is referred to as *cutoff*, see later in Section 3.2.1.

normalized frequency

For the comparison of spectra and spectral envelopes with different pitches it is usually useful to introduce *normalized frequencies*, by dividing the frequency scale by the corresponding fundamental frequency.

2.2.2 Attack and decay transients

The attack transient is a very important property regarding the subjective assessment of the sound quality of a pipe. With cutting out the transient part of the sound, even an experienced organ builder can hardly identify what type of pipe the sound belongs to.

normalized time

Figure 2.5 displays the attack and decay transients of the same narrow labial organ pipe. For analyzing transients it is useful to introduce *normalized time* by dividing the time scale by the period corresponding to the fundamental frequency. In the attack transient (Figure 2.5(a)) it is

[2]These measurements were performed by the author on the "reference pipe", introduced in Chapter 6. The microphones were located at a distance of $50 \pm 5\,\mathrm{mm}$ from the corresponding openings.

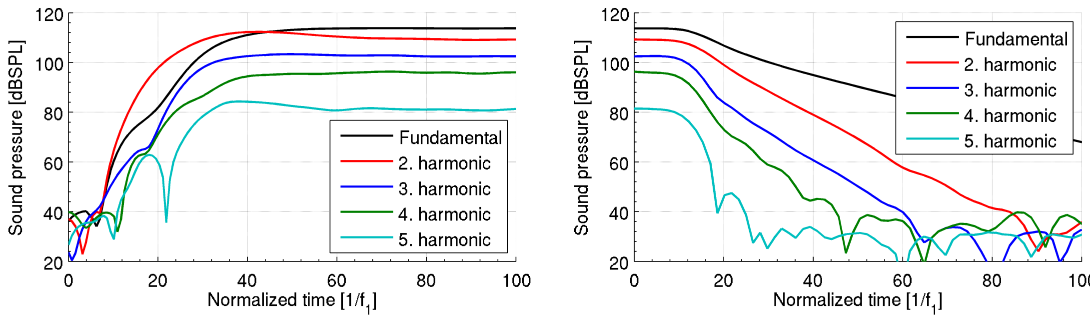

(a) Attack transient

(b) Decay transient

Figure 2.5. The attack and decay transients of a narrow labial organ pipe

seen that the relative strength of the harmonics are quite different in the first 50 periods of the attack than that in the steady state. Apparently, the second harmonic (octave) dominates over the fundamental in the initial transient. This phenomenon can clearly be heard in the pipe sound. The length (speed) of the attack is also an important property that depends on the scaling and voicing configuration of the pipe. The detailed examination of other effects in the attack transient achieved by different voicing steps is out of the scope of this thesis; for further discussion the reader is referred to the references [12, 102, 119].

In the decay phase the order of the strength of the partials is usually the same as that in the steady state sound, as also observable in Figure 2.5(b). The decay time of harmonics decreases with the frequency, thus, the fundamental has the slowest decay usually.

2.2.3 Overblowing and other effects

Overblowing (*Überblasen*) is an interesting phenomenon that can appear when a labial pipe is sounded. The pipe is said to be overblown when it sounds on an upper frequency of natural resonance. The effect can be explained by the relation of the air jet excitation and the frequencies of natural resononce of the resonator. The dynamic behavior of the air jet greatly depends on the blowing pressure. When the blowing pressure is configured such that the jet perturbations are in phase with the acoustic feedback determined by the natural resonance frequencies of the air column inside the pipe body, the perturbations of the jet are amplified and stable oscillations develop at the corresponding frequency. Since the conditions of self-sustained oscillation can be satisfied at different blowing pressures by different natural resonances (see e.g. [67, chapter 16]), overblowing can occur either by increasing or decreasing the blowing pressure from its nominal value. While overblowing is an unwanted phenomenon in most cases, there are special stops that are intentionally designed for overblowing, such as the *Harmonic flute* (*Flûte Harmonique*).

overblowing

Aside from overblowing , higher modes of the resonator can also be excited during the steady state sound generation. These resonances are not strong enough to be dominant in the sound, but such pipe sounds are identified as “rough” as documented recently by Trommer *et al.* [139].

roughness of sound

Further interesting phenomena can appear and affect the sound of individual pipes when more pipes are played together. One among these is the synchronization of the fundamental frequencies of two pipes having nearly the same pitch and located at a small physical distance from each other. This phenomenon was examined in detail by Abel *et al.* [4]. Since in organ music more pipes sound at the same time most of the time, the interactions between the pipes can have a remarkable influence on the sound quality of the instrument, see e.g. [17, chapters 10–11]. Nevertheless, this thesis deals with the physics and sound of single pipes, thus, such effects are not discussed here in detail.

The above paragraphs focused on the properties of the sound of labial pipes. A detailed review on the same topic is found in the paper by Miklós & Angster [102]. As far as lingual pipes are concerned, far less is known about the details of their sound generation mechanism, as discussed in the next section. The measurement and signal processing tools used for analyzing pipe sounds are reviewed in more details in Chapter 6 and Appendix A.

2.3 State of the art in pipe organ research

This section briefly discusses the results and open questions of organ research up to now. First, a general modeling approach of wind instruments and its applications are introduced. Then, the results of the research on the sound generation of labial and lingual pipes are summarized.

2.3.1 A general approach for modeling wind instruments

All wind instruments produce sound by means of pressure oscillations of an air column inside the pipe body, also called as the acoustic resonator. In order to achieve steady state sound generation (self-sustained oscillations), the pressure oscillations must be maintained by means of an excitation mechanism. The excitation mechanism is realized in various manners in different families of wind instruments as summarized by Adachi [6]. The excitation and the vibrating air column can also interact in different manners, as it was seen in case of labial and lingual organ pipes. Hence, a complete model of the sound production of wind instruments requires the incorporation of the excitation mechanism, the acoustic resonator, their interaction, and finally the sound radiation to the listener.

basics of the general approach

A general approach for modeling wind instruments is the separation of the model into two parts. The excitation is usually treated as a nonlinear system, incorporating the underlying physical model of the aeroacoustical, mechanical, or coupled excitation system. The acoustic resonator is most often treated as a linear, often one-dimensional system. This simplification is justified by the fact that the resonator usually operates at moderate amplitudes, that are in the linear acoustic regime. The feedback from the acoustic system on the excitation must inherently be incorporated into the differential equations describing the physics of the excitation. A brief summary of the papers published about the application of this simple model is given in the sequel.

The McIntyre – Schumacher – Woodhouse model is one of the first applications of this simplified structure [99]. For the nonlinear modeling of the excitation time domain simulation of the sound generation is preferred in this model. The model is very general, it was applied for modeling bowed strings, woodwind reeds, and flute-like instruments. The authors have performed simulations on the simplified model of a flue organ pipe and found good agreement with the waveforms of Coltman's experiments [42].

Fletcher & Douglas [66] presented a simplified model of harmonic generation in flute-like instruments. By means of expressing the harmonic components of the flow entering the pipe, the strength of the harmonics in the steady state sound were predicted for different positions of the upper lip. Measurements performed by the same authors on an experimental organ pipe with adjustable upper lip matched the expectations from the model.

Verge *et al.* [141] have introduced nondimensional quantities for the analysis of the sound production in recorder-like instruments. It was shown that the amplitude of the fundamental is limited by a nonlinear interaction of the jet and the acoustic resonator. Furthermore, the effect of the size of the mouth opening and the mouth width to height ratio was also examined and found to affect the produced tone to a great extent. Verge *et al.* [143] presented a one-dimensional simulation model of the same system. This simple model enabled the correct prediction of the amplitude of the fundamental in the steady state. The authors concluded that even such a simple model can reproduce a large number of observations on the functioning of flue instruments.

Dequand *et al.* [49] have examined the role of the mouth geometry and the sharpness of the upper lip on the harmonic content of the sound. Two different models of the sound generation mechanism were presented for different mouth width to height ratios. The two models explain the variations of the amplitudes experienced with changing the mouth geometry; however, the two models were not combined in a global model that would allow sound synthesis.

A similar model was also applied for the time domain simulation of the trumpet by Adachi & Sato [7, 8]. The latter authors introduced one- and two-dimensional lip models for the representation of the excitation mechanism. By adjusting the lip resonance frequency, trumpet sounds were reproduced operating different acoustic modes of the resonator.

A detailed review of this general modeling approach for wind instruments is found in the paper by Fabre & Hirschberg [60].

2.3.2 Research on labial pipes

Labial organ pipes and the physics of their sound generation have already been studied for long. The first scientific papers on the topic known to the author were published in the 1930s [32, 90]. These papers do not focus on a particular phenomenon or quality of the sound, but summarize some observations regarding different pipe types.

Later on, specific aspects of the sound generation were investigated in more detail. Nolle & Boner [112] investigated the steady state sound generation in organ pipes and a vibrating string. They found that the partials in organ pipe sound are always exactly harmonic, while a string exhibits inharmonic behavior. The same authors examined the transient phenomena of flue and reed organ pipes [113]. They found that the time to reach the steady state sound requires the same number of cycles of the fundamental (i.e. normalized time, see p. 12) for pipes of the same stop. The presence of non-harmonic components at the transient state of the sound was also documented.

sound generation mechanism

Cremer & Ising [43] gave a description of the sound generation in a labial organ pipe. It was supposed that the jet and the resonator form a coupled system, whose combined transfer function must give unity, due to the balance of energy. In their model, the driving pressure of the pipe is directly proportional to the jet velocity, which contradicts the observations that suggest a square dependence. Coltman [41] expressed the acoustic driving force of the pipe by the momentum of the jet, which explained the square dependence of the driving pressure on the jet velocity. Elder [56] proposed a model of the sound generation based on the conservation of linear momentum that comprehends the models of Cremer & Ising and Coltman. Coltman further examined the jet drive mechanism in edge tones and organ pipes [42]. He found that the presence of the resonator introduces an additional phase shift between the volume displacement of the jet and the sound pressure compared to the edge tone case.

jet–resonator interaction

Based on the idea of Coltman [41], a nonlinear model of jet and resonator interaction was developed by Fletcher [63]. This model was limited to a pipe with a few natural resonances, but the model gave results quantitatively comparable to experimental data. Fletcher [64] extended his model to incorporate the theory of Elder [56]. He concluded that although the model gives good agreement with experiments in certain regimes of the blowing pressure, it fails to predict the effects for low blowing pressures. Thwaites & Fletcher [137] further investigated the interaction of the jet and the acoustic resonator by determining the admittance of the jet in an experimental manner. They concluded that the current theory of jet–resonator interaction is still not capable of comprehending all effects occuring in measurements. Later, Verge *et al.* [142] examined the interaction of the jet and the resonator in the onset of the pipe sound. It was found that the steepness of the pressure rise in the pipe foot has a great effect on the transient behavior of the jet.

voicing

Voicing steps affecting the air jet generation have also been studied in a number of papers. The first review known to the author that summarizes different voicing techniques is by Mercer [100].

Since voicing is a delicate procedure that requires expertise, it was already found that the interoperation of researchers and organ builders is essential for examining the effect of voicing steps. Nolle [110] examined voicing steps using an organ pipe constructed with certain parameters of its geometry adjustable. It was found that the pipe can only function properly in a very limited range of geometrical parameters. Angster *et al.* [12] performed measurements on a *diapason* (*Prinzipal*) pipe carrying out subsequent voicing steps, starting from the "raw" (unvoiced) pipe. The expected effects of voicing steps were in good qualitative agreement with the measurement results.

flow visualization

Paál *et al.* [119, 120] utilized the *laser doppler anemometry* (LDA) and *Schlieren* imaging techniques for the visualization of the air jet of open and stopped labial pipes. They observed that the measurements show large differences of real instruments and simplified models. By means of flow visualization techniques and high speed camera recordings the jet-wave amplification and the vortex formation in the transients of flue organ pipes was studied by Yoshikawa [147, 148]. He found that an envelope-based estimation method for the jet-wave amplification and the mouth field strength provides good agreement with measurements. Later, Yoshikawa *et al.* [149] proposed a jet–vortex-layer formation model for the vortex-sound generation in an organ pipe. This model provided more information on the generation of acoustic velocity at the pipe mouth than previous models.

wall vibrations

The effects of wall vibrations in the sound generation of labial pipes was also a subject of numerous publications. Backus & Hundley [20] performed experiments to find that the magnitude of wall vibrations is negligibly small in most organ pipes, so as their effect on the sound character of the pipe. They concluded that stronger vibration of the walls is undesired. Kob [85] analyzed the effect of wall vibrations on the attack of organ pipes. It was observed that the thin walls of a baroque flue pipe are likely to exhibit strong vibrations. These vibrations were found to have remarkable effect on the transient spectrum of the pipe; however, the influence on the steady state spectrum was found negligible. Nederveen & Dalmont [107] showed that the wall vibrations of a thin-walled, slightly elliptical pipe can have a significant effect on the pitch and the level of the produced sound. They found instabilities similar to wolf tones of bowed string instruments, which were explained by a proposed phenomenological model.

pipe foot model

A high precision model of the foot of a labial organ pipe was assembled by Außerlechner *et al.* [19]. In this model various parameters of the geometry were adjustable by means of micrometer screws. In reproducible measurements using a hot wire anemometer and a microphone, velocity profiles of the free air jet and the frequencies of the tonal components of the edge tone were determined in various configurations. The evaluation of the measurements have revealed that different hydrodynamical modes of the air jet coexist in a realistic edge tone configuration. Außerlechner [18] also presented visualizations of the transient and steady state movement of the air jet by means of *particle image velocimetry* (PIV) measurements.

numerical simulation

With the increased computational capacity at hand, computer simulation of the edge tone by means of numerically solving the Navier – Stokes differential equations has become feasible in the last decade. Adachi [5] performed the *computational fluid dynamics* (CFD) analysis of an air jet deflected by acoustic waves and found good agreement with Nolle's measurements [111]. Kühnelt [87] performed simulation of the sound generation mechanism of a stopped rectangular labial pipe by means of the *lattice Boltzmann method* (LBM). Nevertheless, due to limitations of computational capacity, the viscosity had to be increased in the simulations which rendered the results incomparable to measurements.

recent contributions

Further contributions have appeared recently on the numerical simulation of wind instruments. Vaik & Paál [140] published the results of two-dimensional numerical simulations of the edge tone using various turbulence models. Agreement with the measured data of Außerlechner *et al.* [19] was found regarding the velocity profiles of the free air jet and the mode frequencies of the edge tone. The latter were determined from the spectra of the pressure forces acting in the upper lip. Fischer & Abel [62] have utilized two-dimensional Large Eddy Simulation (LES) of the compressible Navier – Stokes equations to model the synchronization effect of two organ pipes. Akamura *et al.* [10] proposed a numerical approach for calculatng Howe's integral formula (see [75]) for the vortex sound sources of a wind instrument. The current challenges of numerical simulation of flue influenced were reviewed recently by Takahashi *et al.* [136].

As it is seen, a good amount of knowledge is already available on the sound production of flue instruments such as labial organ pipes. Nevertheless, there are phenomena—such as the role of the edge tone after the attack—in the sound generation mechanism that are still not completely understood, neither explained by theoretical models or numerical simulations.

2.3.3 Research on lingual pipes

While the sound generation mechanism of labial organ pipes has already been studied by a great number of researchers, and a remarkable amount of knowledge on the physics of the sound generation process has been obtained, much less is known about the physics of lingual pipes. The reason for this might be that the process of sound generation is even more complicated than in case of labial pipes: the vibrating tongue is coupled to the acoustical system consisting of the shallot and the resonator, while its motion is driven mostly by flow effects. Therefore, a complete and reliable model of a lingual pipe needs to handle all three subsystems and their interaction. The preliminary steps towards such a model are summarized in the following.

Fletcher [65] classified pressure-controlled valves that are responsible of sound generation in woodwind and brass intruments and the vocalization of a lot of animals. In a model with a single degree of freedom, four configurations are possible, among which lingual organ pipes belong to the group labeled as "striking inwards". It was shown that depending on the valve configuration, there exist particular ranges of acoustical input impedance where self-sustained valve oscillations are possible. pressure-controlled valves

A simple analytical model of the stationary flow through the mouthpiece of a single reed instrument was developed by van Zon *et al.* [152]. The flow was determined and measured in the high and low Reynolds number limit and a good agreement for a clarinet reed has been found. A similar model for a reed organ pipe was given by Hirschberg *et al.* [72] and a nonlinear relation of the hydrodynamic forces acting on the tongue and the gap size between the tongue and the shallot has been obtained. analytical stationary flow model

Miklós *et al.* [103] compared the vibration frequency of plucked and blown reeds of lingual organ pipes without the resonators, which lead to interesting observations. It was found—among other phenomena—that the frequency of the blown reed is significantly greater than that of the plucked reed, which is explained by the shortening of the free length of the tongue due to the blowing pressure in the boot. Later, the same authors have examined the interaction of the reed with the shallot–resonator system [104]. It was observed that when a strong coupling of the two system occurs—i.e. the vibrating frequency of the reed is close to a natural resonance frequeny of the acoustical system—the fundamental frequency of the pipe jumps abruptly and the pipe can not be tuned to a pitch that is in one of these "forbidden" domains of frequencies. The investigations of the aforementioned papers [103, 104] resulted in a better understanding of the physics of reed pipes; however, the physical model used for the explanation of the observed phenomena was not verified quantitatively due to the large number of parameters involved. plucked and blown reeds coupling of reed and resonator

Reed vibration of lingual pipes was also studied by Huber *et al.* [76]. They developed a methodology by which non-contact modal analysis of the reed can be performed, providing useful information on the modal behavior of the tongue. Vibration characteristics of different types of reed curvatures and their effects on the tone were studied by Plitnik [125] and Plitnik & Angster [126]. By means of comparing different shallots with different reed curvatures, it was found that both the shallot and the reed curvature have a remarkable effect on the sound quality of the pipe. Nevertheless, a simple relation between reed curvature and the speech and stationary sound characteristics was not found. reed curvature recent work

The most recent work in the topic known to the author is by Preukschat *et al.* [127, 128]. They examined the behavior of lingual pipes by decomposing the complete system and performing measurements on the different parts separately. Preukschat also set up a pressure pulse reflection model of the sound generation in lingual pipes, which gave good match with the measured waveforms.

Although the last two decades provided a lot of new information on the physics and sound generation mechanism of lingual organ pipes, all details of the process are still not completely understood. A complete model of a lingual pipe—that can be utilized for sound reproduction, for example—has to able to handle the coupled fluid dynamical–mechanical–acoustical system, which seems to be a very challenging task due to its complexity.

2.4 Methodology

This section briefly presents the methodology applied throughout this thesis. As it was mentioned in Chapter 1, the thesis focuses on two main aspects. On the one hand, specific design problems of labial and lingual organ pipes are addressed and novel procedures are introduced to overcome the limitations of current scaling methods. On the other hand, the methodology for modeling organ pipes is developed by extending some of the techniques summarized in Section 2.3. An approach that combines theory, numerical modeling, and validation by means of measurements is chosen in both aspects.

resonator design

Following the general methodology presented in Section 2.3.1, the techniques discussed in the thesis also rely on the separation of the sound generation mechanism into a nonlinear excitation and a linear acoustic resonator part. Although most of the cited literature concentrate more on the nonlinear excitation part and give less focus to the resonator, Chapters 5–8 of this thesis are dedicated entirely to the design issues of resonators of specific pipe families.

optimization

Most of the resonator forms investigated in this thesis are axisymmetric. In these cases, one-dimensional acoustic models (see Chapter 3) are applied in order to determine the characteristic properties of the resonators. The one-dimensional model is also applied for the optimization of the resonator geometry, e.g. in case of chimney pipes (see Chapter 5). Development of scaling methods allowing sound design requires the usage of heuristic and unconstrained global optimization methods, such as the Nelder – Mead technique [109].

numerical techniques

hybrid models

Modeling irregularities, like tuning slots (see Chapter 7) or the radiation impedance from the open conical pipe end (see Chapter 8), involves the usage of numerical techniques, such as finite or boundary element methods (see Chapter 4). In order to reduce the size of the computational model and increase the flexibility of the simulations, postprocessing techniques for deriving equivalent parameters from the calculated acoustic fields are applied. Hence, the resulting equivalent acoustic elements could be inserted into various one-dimensional models. These so-called *hybrid models* combine the accuracy attainable by three-dimensional models and the efficiency of one-dimensional techniques.

edge tone simulation

In Chapter 9 the simulation of the free air jet and edge tone in a pipe foot model is discussed. The simulation is carried out by solving the Navier – Stokes set of equations numerically, by means of the *finite volume method*. Three-dimensional flow models with over a million degrees of freedom involve the usage of highly parallelized simulation runs performed on a supercomputer grid.

validation techniques

The validation of the results obtained using theoretical models or simulations is an important step of the methodology applied throughout the thesis. Results attained either by analytical or numerical techniques are validated by means of measurements, whenever it is possible. When the sound quality of certain pipe designs have to be assessed, comparative listening tests are performed with the help of experienced organ builders and voicers.

Chapter 3

One-dimensional modeling techniques in linear acoustics

This chapter presents the background of unidimensional modeling techniques for the simulation of acoustic wave propagation in ducts and pipes. Despite the limitations of one-dimensional models, they are often applied in physics-based simulations of the sound generation of various musical instruments thanks to their simplicity and efficiency required by a computationally effective (real-time or near real-time) simulation model. Furthermore, unidimensional models can be extended by results from three-dimensional simulations (see Chapter 4), resulting in hybrid models and overcoming some of the limitations of the unidimensional framework. introduction

The objective of this chapter is to derive the relations of one-dimensional models applied in the subsequent chapters starting from the basic relations and clarifying the assumptions and neglects. Since the physical background and the derivation of the wave equation is covered in a large number of textbooks, this chapter does not intend to give a complete and detailed review, instead the reader is referred to the cited literature for further discussion. Nevertheless, the chapter aims to provide the reader with the background on which the following chapters are built. The chapter focuses on the modeling of the propagation of pressure waves in cylindrical tubes, which is the simplest and the most important one-dimensional acoustical system for simulating the resonators of organ pipes. the aim of this chapter

This chapter is structured as follows. Section 3.1 presents the governing equations of linear acoustics and derives the wave equation from the fundamental relations of continuum mechanics and thermodynamical laws. The properties of the propagation of pressure waves in cylindrical ducts are discussed in Section 3.2. The theory of acoustic transmission lines and lumped parameter elements is presented in Section 3.3. Section 3.4 discusses the phenomenon of sound radiation from openings of different shapes. Finally, in Section 3.5, a simple model of a straight cylindrical labial pipe is assembled and examined. structure

3.1 The governing equations

This section derives the wave equation for ideal gases such as air. The discussion starts from the fundamental laws of continuum mechanics. Then, the wave equation is obtained by means of linearization and using the equation of state for adiabatic processes. Finally, the Helmholtz equation is attained by transforming the wave equation into the frequency domain. Our discussion follows the references [67], [84], [96], and [106].

3.1.1 Laws of continuum mechanics

The governing equations of linear acoustics are based on the basic laws of continuum mechanics. For the derivation of the fundamental equations the Eulerian approach [21] is used. In our discussion a domain Ω in the d-dimensional space is considered $\Omega \subseteq \mathbb{R}^d$. It is assumed that the domain Ω is limited by the boundary Γ. It is also assumed that the normal vector $\boldsymbol{n}$ points *outward* of Ω in all points of Γ.

Conservation of mass means that no mass is generated or destroyed during the motion. Thus, the change of mass in the domain Ω must be equal to the amount of mass flowing into the region through the boundary Γ. The total amount of mass is expressed as $M = \int_\Omega \rho(\boldsymbol{x}, t)\,\mathrm{d}\boldsymbol{x}$, with ρ denoting density, $\boldsymbol{x}$ and t representing spatial and time coordinates, respectively. The rate of mass flow into the region is given as $-\int_\Gamma \rho(\boldsymbol{x}, t)\boldsymbol{v}(\boldsymbol{x}, t)\cdot\boldsymbol{n}(\boldsymbol{x})\,\mathrm{d}\boldsymbol{x}$, with $\boldsymbol{v}$ denoting the flow velocity vector. Hence, the law of mass conservation is expressed as

$$\frac{\partial M}{\partial t} = \frac{\partial}{\partial t}\int_\Omega \rho(\boldsymbol{x}, t)\,\mathrm{d}\boldsymbol{x} = -\int_\Gamma \rho(\boldsymbol{x}, t)\boldsymbol{v}(\boldsymbol{x}, t)\cdot\boldsymbol{n}(\boldsymbol{x})\,\mathrm{d}\boldsymbol{x}. \tag{3.1}$$

Changing the order of integration and differentiation, converting the right hand side into a volume integral making of the divergence theorem and rearranging the equation yields

$$\int_\Omega \left(\frac{\partial \rho}{\partial t} + \nabla\cdot(\rho\boldsymbol{v})\right)\mathrm{d}\boldsymbol{x} = 0. \tag{3.2}$$

In addition to the global validity of the conservation of mass we require that equation (3.2) is also valid for any arbitrarily small neighborhood of each material point (often referred to as *control volume*), which implies the differential form of equation (3.2) as

conservation of mass

$$\frac{\partial \rho}{\partial t} + \nabla\cdot(\rho\boldsymbol{v}) = 0. \tag{3.3}$$

The principle of *balance of momentum* means that the time rate of change of momentum equals the resultant force $\boldsymbol{f}_\mathrm{R}$ acting on the body. Denoting the momentum vector by $\boldsymbol{P}$ the conservation law for the momentum is expressed as

$$\frac{\partial \boldsymbol{P}}{\partial t} = \frac{\partial}{\partial t}\int_\Omega \rho(\boldsymbol{x}, t)\boldsymbol{v}(\boldsymbol{x}, t)\,\mathrm{d}\boldsymbol{x} = -\int_\Gamma \Big(\rho(\boldsymbol{x}, t)\boldsymbol{v}(\boldsymbol{x}, t)\Big)\,\boldsymbol{v}(\boldsymbol{x}, t)\cdot\boldsymbol{n}(\boldsymbol{x})\,\mathrm{d}\boldsymbol{x} + \boldsymbol{f}_\mathrm{R}, \tag{3.4}$$

where the first term on the right hand side is the momentum flux through the boundary Γ. Applying the divergence theorem on the momentum flux, then expanding the resulting terms and substituting from equation (3.3) gives

$$\int_\Omega \left(\rho\frac{\partial \boldsymbol{v}}{\partial t} + \rho\,(\boldsymbol{v}\cdot\nabla)\,\boldsymbol{v}\right)\mathrm{d}\boldsymbol{x} = \boldsymbol{f}_\mathrm{R}. \tag{3.5}$$

The vector of the resultant force contains volume forces $\boldsymbol{b}$ and external forces $\boldsymbol{\sigma}$. By neglecting friction (assuming zero viscosity) external forces incorporate only pressure forces $p\boldsymbol{n}$ acting in the normal direction, and hence $\boldsymbol{f}_\mathrm{R}$ is expressed as

$$\boldsymbol{f}_\mathrm{R} = \int_\Omega \boldsymbol{b}\rho\,\mathrm{d}\boldsymbol{x} - \int_\Gamma p\boldsymbol{n}\,\mathrm{d}\boldsymbol{x}. \tag{3.6}$$

In acoustics, body forces $\boldsymbol{b}$—that incorporate the effect of gravity for example—are usually negligible compared to the pressure forces and thus the resultant force is expressed by the pressure forces only, which can be transformed into a volume integral by means of the divergence theorem

$$\boldsymbol{f}_\mathrm{R} = -\int_\Gamma p\boldsymbol{n}\,\mathrm{d}\boldsymbol{x} = -\int_\Omega \nabla p\,\mathrm{d}\boldsymbol{x}. \tag{3.7}$$

Substituting equation (3.7) into (3.5) leads to the integral form

$$\int_{\Omega} \left(\rho \frac{\partial \boldsymbol{v}}{\partial t} + \rho \left(\boldsymbol{v} \cdot \nabla \right) \boldsymbol{v} + \nabla p \right) \, \mathrm{d}\boldsymbol{x} = 0. \tag{3.8}$$

Similar to the conversation of mass (3.2), momentum is also required to be balanced in any arbitrarily small control volume. This leads to the local form of conservation of momentum, also known as the *Euler equation*, which reads as

$$\rho \frac{\partial \boldsymbol{v}}{\partial t} + \rho \left(\boldsymbol{v} \cdot \nabla \right) \boldsymbol{v} + \nabla p = 0. \tag{3.9}$$

Euler equation

3.1.2 Linearization

Commonly, problems of linear acoustics refer to small perturbations of the ambient quantities. The latter are denoted here by the subscript 0. The time dependent total quantities are the superposition of the time independent ambient quantities and the small perturbations, with the latter denoted by $\tilde{\cdot}$.

$$\begin{aligned} p(\boldsymbol{x}, t) &= p_0 + \tilde{p}(\boldsymbol{x}, t) \\ \rho(\boldsymbol{x}, t) &= \rho_0 + \tilde{\rho}(\boldsymbol{x}, t) \\ \boldsymbol{v}(\boldsymbol{x}, t) &= \boldsymbol{v}_0 + \tilde{\boldsymbol{v}}(\boldsymbol{x}, t). \end{aligned} \tag{3.10}$$

It is also assumed that the ambient velocity of the fluid is zero, i.e. $\boldsymbol{v}_0 = \boldsymbol{0}$. After substituting and neglecting second order terms, the law of conservation of mass (3.3) reads as

$$\frac{\partial \tilde{\rho}}{\partial t} + \rho_0 \nabla \cdot \tilde{\boldsymbol{v}} = 0. \tag{3.11}$$

linearized mass conservation

Similarly, the Euler equation (3.9) is linearized and simplified as

$$\rho_0 \frac{\partial \tilde{\boldsymbol{v}}}{\partial t} + \nabla \tilde{p} = 0. \tag{3.12}$$

linearized Euler equation

In the linearized equations (3.11) and (3.12) there are three unknowns depending on the spatial and time coordinates: $\tilde{p}$, $\tilde{\rho}$ and $\tilde{\boldsymbol{v}}$. Therefore, in order to obtain a unified wave equation, a third relation is needed, which is discussed in the sequel.

3.1.3 The constitutive equation

In fluids sound propagates through *pressure waves* only. Other fluctuations of the quantities p, ρ and $\boldsymbol{v}$, caused by effects such as eddies—although detectable by acoustic sensors such as microphones or the human ear—are not regarded as sound, but perturbations out of the scope of the linear acoustic framework. In linear acoustics the fluctuations are considered to cause negligibly small heat flow and appear quickly, so that the temperature cannot equalize. Therefore the propagation of pressure waves can be characterized as an *adiabatic process*.

The propagation speed of pressure waves, also known as the *speed of sound* depends on the material properties of the fluid. Hence, the speed of sound is one of the characteristic properties of the fluid, which can be deduced from other characteristics of the material, depending on its state of matter. The speed of sound c is introduced as a constant relating the pressure and density fluctuations as

$$\tilde{p} = c^2 \tilde{\rho} \qquad \Longleftrightarrow \qquad c \triangleq \sqrt{\frac{\partial p}{\partial \rho}}. \tag{3.13}$$

speed of sound

In this thesis only sound propagation in air is considered, thus, the speed of sound is only derived here for *ideal gases*. To obtain the relation (3.13) our constitutive equation is the equation of state, which reads for ideal gases in case of an adiabatic process as $p\rho^{-\gamma} = \mathrm{const}$, with γ denoting the ratio of specific heats. Substituting from (3.10) and linearizing gives

$$c = \sqrt{\frac{\gamma p_0}{\rho_0}}. \tag{3.14}$$

γ can be regarded as independent of the temperature in a relatively wide range, whereas the constants p_0 and ρ_0 are interrelated with the ambient temperature T_0. The relation between the temperature, pressure and density is given by the *ideal gas law*, that is $p = \rho RT$. The individual gas constant for dry air is $R = 287.058\,\mathrm{J/kg\,K}$. The atmospheric pressure is $p_0 = 101\,325\,\mathrm{Pa}$. Thus, the density of air and the speed of sound at the standard temperature $T_0 = 0°\mathrm{C}$ ($273.15\,\mathrm{K}$) are obtained as

$$\rho_0\Big|_{T_0=0°\mathrm{C}} = \frac{101\,325\,\mathrm{Pa}}{287.058\,\mathrm{J/kg\,K}\cdot 273.15\,\mathrm{K}} = 1.2922\,\mathrm{kg/m^3}, \tag{3.15a}$$

$$c\Big|_{T_0=0°\mathrm{C}} = \sqrt{\frac{1.401\cdot 101\,325\ \mathrm{Pa}}{1.2922\ \mathrm{kg/m^3}}} = 331.45\ \mathrm{m/s}. \tag{3.15b}$$

The dependence of the ambient density and the speed of sound on the temperature is also derived from the ideal gas law. If the temperature scale is relatively narrow, it is generally sufficient in engineering applications to assume linear dependence of the aforementioned quantities. Using the results of (3.15) we get

$$\rho_0 = 1.2922\cdot(1-0.0047\cdot T_0^{[°\mathrm{C}]})\quad [\mathrm{kg/m^3}]\qquad \text{and} \tag{3.16a}$$

$$c = 331.45\cdot(1+0.0018\cdot T_0^{[°\mathrm{C}]})\quad [\mathrm{m/s}], \tag{3.16b}$$

with $T_0^{[°\mathrm{C}]}$ denoting the ambient temperature expressed in Celsius degrees.

3.1.4 The wave equation

In order to relate the equations (3.11) and (3.12), the constitutive equation (3.14) is used. The wave equation for linear acoustic problems is found by subtracting the time derivative of the linearized version of the conservation of mass (3.11) from the divergence of the linearized Euler equation (3.12). Thus, the *homogeneous wave equation* for linear acoustic problems is attained in the form

acoustic wave equation

$$\nabla^2\tilde{p}(\boldsymbol{x},t) - \frac{1}{c^2}\frac{\partial^2\tilde{p}(\boldsymbol{x},t)}{\partial t^2} = 0. \tag{3.17}$$

The operator ∇^2 is usually referred to as the *Laplace operator* and is often denoted by Δ. The wave equation (3.17) was derived using the pressure perturbations as the variable. Since equation (3.14) relates pressure and density perturbations, the same equation is also valid for the density perturbations $\tilde{\rho}$.

The wave equation (3.17) is a *partial differential equation* (PDE), thus, in order to obtain its solution for a specific problem, boundary and initial conditions have to be specified. In the following sections special cases of acoustic wave propagation problems are examined, or—in other words—the solutions of the acoustic wave equation are sought in specific configurations. Based on the three-dimensional wave equation (3.17) further, problem-specific relations are derived.

For the sake of convenience, the $\tilde{\ }$ notation of the time dependent perturbations is omitted in the following and the symbols p, ρ and $\boldsymbol{v}$ refer to the perturbations unless otherwise noted.

3.1.5 The Helmholtz equation

In a significant number of cases we are interested in steady-state processes, where a frequency domain analysis is preferred for simplicity. In these cases time-harmonic perturbations with an angular frequency ω can be assumed, i.e.

$$p(\boldsymbol{x},t) = |p(\boldsymbol{x})| \cos(\omega t + \phi(\boldsymbol{x})) = \mathfrak{Re}\left\{|p(\boldsymbol{x})| \, \mathrm{e}^{\mathrm{j}(\omega t + \phi(\boldsymbol{x}))}\right\}. \tag{3.18}$$

It is useful to introduce the *complex amplitude* $\hat{p}(\boldsymbol{x}) = |p(\boldsymbol{x})| \, \mathrm{e}^{\mathrm{j}\phi(\boldsymbol{x})}$ that inherently contains the amplitude and the phase of the time-harmonic perturbations.

For a non time-harmonic signal, frequency dependent complex amplitudes $\hat{p}(\boldsymbol{x},\omega)$ can be introduced by using the Fourier transformed variables $\hat{\cdot}$ that satisfy the relation

$$y(\boldsymbol{x},t) = \frac{1}{2\pi}\int_{-\infty}^{+\infty} \hat{y}(\boldsymbol{x},\omega)\mathrm{e}^{-\mathrm{j}\omega t}\,\mathrm{d}\omega. \tag{3.19}$$

inverse Fourier transform

The Fourier transformed variables can then be attained as

$$\hat{y}(\boldsymbol{x},\omega) = \int_{-\infty}^{+\infty} y(\boldsymbol{x},t)\mathrm{e}^{\mathrm{j}\omega t}\,\mathrm{d}t \tag{3.20}$$

Fourier transform

if the corresponding integral exsists.[1]

Making use of the interchangeability of the second derivative with respect to time $\partial^2/\partial t^2$ and the factor $(\mathrm{j}\omega)^2$ for the Fourier transformed variables in equation (3.17) and introducing the acoustic wave number $k = \omega/c$, the *homogeneous Helmholtz equation* is obtained as

$$\nabla^2\hat{p}(\boldsymbol{x},\omega) + k^2\hat{p}(\boldsymbol{x},\omega) = 0. \tag{3.21}$$

Helmholtz equation

The operator $\mathcal{H} = \nabla^2 + k^2$ is often referred to as the *Helmholtz operator*.

3.2 Wave propagation in cylindrical ducts

In this section the Helmholtz equation (3.21) is applied for solving acoustic wave propagation problems in cylindrical ducts. Since a cylindrical duct with perfectly rigid walls is the simplest model of a straight cylindrical organ pipe, cylindrical ducts are the essential elements of the acoustic model of the resonator of an organ pipe. First, an infinite cylindrical duct is examined, then the properties of finite pipes are discussed.

3.2.1 The infinite cylindrical duct

Let us assume an infinite cylindrical duct of inner radius a with its axis of symmetry located at the z-axis of the cartesian coordinate system. It is useful to describe the problem in cylindrical coordinates $\boldsymbol{r} = (r,\theta,z)$, with $r = \sqrt{x^2+y^2}$ and $\theta = \tan^{-1}(y/x)$. The problem domain is defined as $\Omega = \{\boldsymbol{r} \mid r \le a, \theta \in [0,2\pi), z \in \mathbb{R}\}$, whereas the boundary is given as $\Gamma = \{\boldsymbol{r} \mid r = a\}$. The Helmholtz equation in cylindrical coordinates—omitting the notation of the dependence of the pressure variable on space and angular frequency for simplicity—reads as

$$\frac{\partial^2}{\partial r^2}\hat{p} + \frac{1}{r}\frac{\partial}{\partial r}\hat{p} + \frac{1}{r^2}\frac{\partial^2}{\partial\theta^2}\hat{p} + \frac{\partial^2}{\partial z^2}\hat{p} + k^2\hat{p} = 0 \qquad \boldsymbol{r} \in \Omega. \tag{3.22}$$

It is assumed for the time being that the walls of the duct are perfectly rigid, which means that the normal component of the particle velocity v_n vanishes at $r = a$. Making use of the linearized Euler equation (3.12) this boundary condition is stated as

$$v_n(a,\theta,z) = -\frac{1}{\mathrm{j}\omega\rho_0}\left.\frac{\partial p}{\partial r}\right|_{r=a} = 0 \qquad \text{if} \qquad \boldsymbol{r} \in \Gamma. \tag{3.23}$$

[1]The existence of the integral in (3.20) is not required for the existence of $\hat{y}(\boldsymbol{x},\omega)$, see [34].

The general solution of the boundary value problem posed by the PDE (3.22) and the Neumann type boundary condition (3.23) reads as

$$\hat{p}_{mn}(r,\theta,z) = P\cos(m\theta+\phi_{mn})J_m\left(\frac{\pi q_{mn} r}{a}\right)\mathrm{e}^{-\mathrm{j}k_{mn}z}, \tag{3.24}$$

with P standing for an arbitrary pressure amplitude, J_m denoting the mth order Bessel function of the first kind, ϕ_{mn} being an arbitrary angle and q_{mn} defined to satisfy the boundary condition (3.23), such that the derivative $J'_m(\pi q_{mn})$ is zero. The propagation wave number k_{mn} for mode (m,n) is obtained by substituting equation (3.24) into (3.22) as

$$k_{mn}^2 = \left(\frac{\omega}{c}\right)^2 - \left(\frac{\pi q_{mn}}{a}\right)^2. \tag{3.25}$$

The plane wave mode with $m = n = 0$ can always propagate with the wave number $k_{00} = \omega/c$, whereas higher modes can only propagate above a certain angular frequency, often referred to as a cutoff angular frequency

$$\omega_{\text{cut},mn} = \frac{\pi q_{mn} c}{a}. \tag{3.26}$$

Under its cutoff frequency the wave number k_{mn} is imaginary, and from equation (3.24) it is seen that the solution decays exponentially with z. The cutoff frequency of the first transversal mode $(1,0)$ is of special interest both theoretically and practically. The corresponding coefficient is found as the first positive root of the Bessel function $J'_1(\pi q_{10})$ giving $\pi q_{10} \approx 1.8412$. This first cutoff frequency is often simply referred to as the *cutoff frequency*, and is given as

cutoff frequency

$$\omega_{\text{cut}} = \frac{1.8412\cdot c}{a} \qquad \Longleftrightarrow \qquad (ka)_{\text{cut}} = 1.8412, \tag{3.27}$$

with $(ka)_{\text{cut}}$ denoting the *nondimensional cutoff frequency*.

Under the cutoff frequency of the first transversal mode ω_{cut} only the plane wave mode can propagate inside the duct, and if the evanescent components can be neglected—which is the case in most applications—the problem can be considered one-dimensional. Then the model is significantly simplified and the one-dimensional Helmholtz equation can be utilized for its description, that is

1D Helmholtz eq.

$$\frac{\partial^2 \hat{p}(z,\omega)}{\partial z^2} + k^2\hat{p}(z,\omega) = 0 \qquad\qquad \boldsymbol{r}\in\Omega. \tag{3.28}$$

The solution of (3.28) is given in the so-called d'Alembert form as

$$\hat{p}(z,\omega) = p^+\mathrm{e}^{-\mathrm{j}kz} + p^-\mathrm{e}^{\mathrm{j}kz}, \tag{3.29}$$

with p^+ and p^- denoting arbitrarily chosen complex amplitudes. Similarly, utilizing the one-dimensional linearized Euler equation, i.e. $\mathrm{j}\omega\rho_0 v = -\partial p/\partial z$, the particle velocity is given as

$$\hat{v}(z,\omega) = v^+\mathrm{e}^{-\mathrm{j}kz} - v^-\mathrm{e}^{\mathrm{j}kz} = \left(\frac{1}{\rho_0 c}\right)\left[p^+\mathrm{e}^{-\mathrm{j}kz} - p^-\mathrm{e}^{\mathrm{j}kz}\right]. \tag{3.30}$$

plane wave impedances

The quantity relating the pressure and velocity plane wave amplitudes ($p^+/v^+ = p^-/v^-$) is denoted by $Z_0^{(\text{spec})} = \rho_0 c$ is known as the *specific plane wave impedance* and is measured in units $\mathrm{kg/m^2s}$. By using the *volume velocity* $U = vS$ (S denoting the cross sectional area of the duct), the *acoustic plane wave impedance* relates the pressure and volume velocity amplitudes in a similar manner as $Z_0^{(\text{acou})} = \rho_0 c/S$ and is measured in units $\mathrm{kg/m^4s}$, also known as *acoustic ohms*.

3.2.2 Lossy wave propagation

The wave equation (3.17) and the Helmholtz equation (3.21) were derived above assuming ideal materials without any sources of internal losses. In reality, however, no material can be considered ideal, thus, the propagation of acoustic waves in all types of material is inherently lossy. The losses are conveniently quantified by the *absorption coefficient*, denoted by α, which affects the propagation wave number k by introducing the lossy wave number k' as

$$k' = k - \mathrm{j}\alpha. \tag{3.31}$$

lossy wave number

Assuming that α is positive it can be seen that the solution to the one-dimensional Helmholtz equation (3.28) becomes the superposition of waves with exponentially decaying amplitude along the direction of propagation. The sources of losses can be classified as follows.

Intrinsic losses are characteristic to the medium in which sound propagates. These losses may be subdivided into three basic types. (1) *Friction losses* occur whenever there is relative motion between adjacent control volumes of the fluid, i.e. during shear deformations or compressions and expansions that accompany the transmission of a sound wave. (2) *Heat conduction losses* are present whenever thermal energy is conducted between regions of different temperatures. (3) *Molecular losses* refer to processes in which the kinetic energy of the molecules is converted into potential, rotational, or vibrational energy.

Boundary losses occur at the interface of the fluid and its solid boundaries have two basic types. (4) *Viscous losses* are due to the friction between the boundary and the fluid. (5) *Thermal losses* arise from heat transfer between the wall and the fluid.

The intrinsic losses due to viscosity (1) and thermal conduction (2) are incorporated by the *classical absorption coefficient* α_c, given as

$$\alpha_\mathrm{c} = \frac{\omega^2\eta}{2\rho_0 c^3}\left(\frac{4}{3} + \frac{\gamma - 1}{\mathrm{Pr}}\right), \tag{3.32}$$

classical absorption coefficient

with η representing the dynamic viscosity of the fluid, Pr denoting the Prandtl number, defined as $\mathrm{Pr} = \eta c_\mathcal{P}/\kappa$, where $c_\mathcal{P}$ is the specific heat at constant pressure and κ stands for the thermal conductivity of the fluid. In dry air at atmospheric pressure and the temperature of $T_0 = 20°\mathrm{C}$ the classical absorption coefficient is $\alpha_\mathrm{c}/f^2 \approx 1.4 \cdot 10^{-11}\,\mathrm{m}^{-1}\mathrm{s}^2$.

The deduction of equation (3.32) is found in [84, chapter 8]. In the applications presented in this thesis boundary losses are dominant over intrinsic losses, therefore they are examined in more detail in Section 3.2.3.

3.2.3 Viscous and thermal losses at rigid walls

In the previous section we have assumed that the wall is completely rigid and hence the normal derivative of the pressure in the radial direction is zero at $r = a$. In real life conditions this can never be achieved, however, in lot of practical cases the vibration of the walls can be neglected.

There are no real walls immune to viscous and thermal effects, which makes the latter important in practical applications, such as modeling the walls of wind instruments. In the following paragraphs the viscous and thermal losses at rigid walls are briefly introduced in order to finally attain the wall absorption coefficient that characterizes wall losses in a unified manner.

Viscous boundary layer

If friction is present between the fluid and the walls, a so-called *no-slip boundary condition* should be prescribed at the walls, meaning that the difference of the velocity of the wall and the particle velocity of the fluid at the wall vanishes. For a non-moving wall this means that the particle velocity is zero at the walls, i.e. $\boldsymbol{v} = \mathbf{0}$ if $r = a$. To fulfill the no-slip condition the total velocity field $\boldsymbol{v}$ is written as a superposition of a *primary plane wave* $\boldsymbol{v}_z$ and a *secondary wave* $\boldsymbol{v}'$, so that

$$\boldsymbol{v}(r, z, t) = \boldsymbol{v}_z(z, t) + \boldsymbol{v}'(r, z, t). \tag{3.33}$$

By solving the Navier – Stokes equation with the no-slip condition after some simplifications (see [84, chapter 8]) the secondary wave is obtained as

viscous skin depth

$$\boldsymbol{v}' = -\boldsymbol{v}_z \mathrm{e}^{-(1+\mathrm{j})(a-r)/\delta_{\mathrm{v}}} \qquad \text{with} \qquad \delta_{\mathrm{v}} = \sqrt{\frac{2\eta}{\rho_0 \omega}}. \tag{3.34}$$

δ_{v} denotes the *viscous boundary layer thickness*, also known as the viscous skin depth.

Thermal conduction

The temperature field corresponding to a planar wave given by the particle velocity $v_z(z,t) = v^+ \mathrm{e}^{-\mathrm{j}(kz-\omega t)}$ is given as

$$T(z, t) = T_0 + T_0(\gamma - 1)\frac{v^+}{c}\mathrm{e}^{-\mathrm{j}(kz-\omega t)}. \tag{3.35}$$

With the assumption of an isothermal wall, analogous to the viscous boundary layer, the temperature field is also found as the superposition of a primary and a secondary wave. After solving the diffusion equation, the skin depth of the thermal boundary layer δ_{t} is found as

thermal skin depth

$$\delta_{\mathrm{t}} = \sqrt{\frac{2\kappa}{c_{\mathcal{P}} \rho_0 \omega}}. \tag{3.36}$$

The wall absorption coefficient

For the deduction of the wall absorption coefficient α_{w} the nondimensional ratios r_{v} and r_{t} are introduced as

$$r_{\mathrm{v}} = \frac{\sqrt{2}a}{\delta_{\mathrm{v}}} = \left(\frac{\omega\rho_0}{\eta}\right)^{1/2} a \qquad \text{and} \qquad r_{\mathrm{t}} = \frac{\sqrt{2}a}{\delta_{\mathrm{t}}} = \left(\frac{\omega\rho_0 c_{\mathcal{P}}}{\kappa}\right)^{1/2} a. \tag{3.37}$$

By means of the boundary layer thicknesses the series impedance Z_{v} and shunt admittance Y_{t} of a tube section of unit length can be given (see e.g. [25]) as

$$Z_{\mathrm{v}} = \mathrm{j}\frac{\omega\rho_0}{S}\frac{1}{1-F_{\mathrm{v}}} \qquad \text{and} \qquad Y_{\mathrm{t}} = \mathrm{j}\frac{\omega S}{\rho_0 c^2}\left[1 + (\gamma - 1)F_{\mathrm{t}}\right]. \tag{3.38}$$

The complex valued parameters F_{v} and F_{t} are defined as

$$F_* = \frac{2}{r_* \mathrm{j}^{3/2}} \frac{J_1\left(r_* \mathrm{j}^{3/2}\right)}{J_0\left(r_* \mathrm{j}^{3/2}\right)}, \tag{3.39}$$

with using r_{v} and r_{t} as r_* for calculating F_{v} and F_{t}, respectively.

The viscous and thermal skin depths in air at atmospheric pressure and $T_0 = 20°\mathrm{C}$ at the frequency of $f = 20\,\mathrm{Hz}$ are obtained as $\delta_{\mathrm{v}} \approx 4.9 \times 10^{-4}\,\mathrm{m}$ and $\delta_{\mathrm{t}} \approx 5.8 \times 10^{-4}\,\mathrm{m}$. Therefore, in the case of cylindrical ducts of real musical instruments, such as organ pipes, it is generally valid to assume $a \gg \delta_{\mathrm{v}}$ and $a \gg \delta_{\mathrm{t}}$. With this assumption the *wall absorption coefficient* α_{w} can be expressed using the asymptotic approximation of Benade [25] (see also [67, chapter 8])

wall absorption coefficient

$$\alpha_{\mathrm{w}} \approx \frac{\omega}{c}\left[\frac{1}{r_{\mathrm{v}}\sqrt{2}} + \frac{\gamma - 1}{r_{\mathrm{t}}\sqrt{2}}\right] \approx \frac{3 \cdot 10^{-5} f^{1/2}}{a}. \tag{3.40}$$

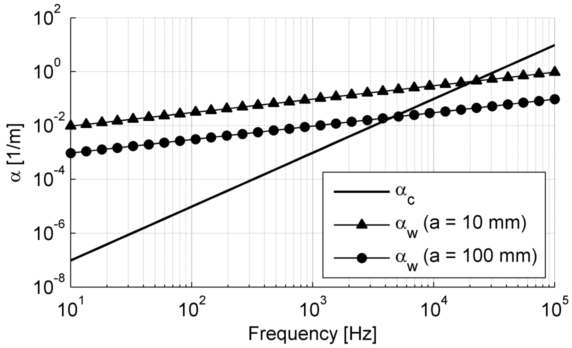

Figure 3.1. Frequency dependence of coefficients of intrinsic (α_c) and wall (α_w) losses in cylindrical ducts at temperature $T_0 = 20°\mathrm{C}$

Finally, the *total absorption coefficient* α is obtained as the sum of the classical and the wall absorption coefficients as

total absorption coefficient

$$\alpha = \alpha_\mathrm{c} + \alpha_\mathrm{w}. \tag{3.41}$$

For the example of a typical cylindrical organ pipe in an 8′, 4′, or 2′ stop, having a fundamental frequency of roughly 65 to $260\,\mathrm{Hz}$, a is in the range of centimeters. In this case, it can be seen by evaluating the expressions given in equations (3.32) and (3.40) that the wall losses are dominant over the intrinsic losses in the whole frequency range of musical relevance (i.e. where the strong harmonic components are present), as illustrated by Figure 3.1. Therefore, it is reasonable to neglect intrinsic losses in the applications of this thesis.

A more detailed elaboration of intrinsic and wall propagation losses can be found in the books by Zwikker & Kosten [154] or Kinsler *et al.* [84].

3.2.4 Finite cylindrical pipes

Obviously, the pipes that appear in real musical instruments are of finite length. This means that pressure waves are reflected at the (open or closed) ends of the duct. A property of key importance for the characterization of such ducts is the *input impedance*, introduced in the sequel.

Let us consider a finite cylindrical tube that extends from $z = 0$ to $z = L$ terminated by the acoustic impedance $Z_L(\omega)$ at $z = L$. Since the unidimensional Helmholtz equation (3.28) is valid inside the pipe under the cutoff frequency, the resulting pressure field of the pipe is the superposition of two counterpropagating planar waves, as obtained by the d'Alembert form solution (3.29).

The reflection coefficient at the far end ($z = L$) of the tube $R_L(\omega)$ is expressed as the ratio of the complex amplitudes of the counterpropagating plane waves at the location $z = L$. Making use of the fact that $\hat{p}(L,\omega)/\hat{U}(L,\omega) = Z_L(\omega)$, it is found that

reflection coefficient

$$R_L(\omega) = \frac{p^-\mathrm{e}^{+\mathrm{j}kL}}{p^+\mathrm{e}^{-\mathrm{j}kL}} = \frac{Z_L(\omega) - Z_0}{Z_L(\omega) + Z_0} \tag{3.42}$$

with $Z_0 = \rho_0 c/S$ denoting the acoustic plane wave impedance of the tube. Consequently, the ratio of the complex amplitudes p^- and p^+ is attained as

$$\frac{p^-}{p^+} = R_L(\omega)\mathrm{e}^{-2\mathrm{j}kL}. \tag{3.43}$$

The input impedance of the pipe Z_in is defined as the ratio of the complex amplitude of the pressure and volume velocity at $z = 0$. This can be expressed by rewriting the complex exponentials using trigonometric functions to get

input impedance

$$Z_{\text{in}}(\omega) = \frac{\hat{p}(0,\omega)}{\hat{U}(0,\omega)} = Z_0 \frac{Z_{\text{L}}(\omega) + \text{j}Z_0 \tan kL}{Z_0 + \text{j}Z_{\text{L}}(\omega)\tan kL}. \tag{3.44}$$

For the characterization of an acoustic system the input impedance is of key importance. Its reciprocal, the *input admittance* $Y_{\text{in}} = 1/Z_{\text{in}}$ is also often used for the same purpose. Since the system responds with maximal pressure to unit input volume velocity when $Z_{\text{in}}(\omega)$ has a local maximum, the natural resonance and anti-resonance frequencies of the system can also be found as the local extrema of the input impedance or input admittance functions.

Two extremal cases regarding the termination impedance Z_L are of special interest. The first case is when the pipe is terminated by zero impedance. This corresponds to zero pressure at the pipe end, $p(L,\omega) = 0$. In this case the system can be considered *ideally open* and from equation (3.44) the input impedance is attained as

$$Z_{\text{in}}^{(\text{open})} = \text{j}Z_0 \tan kL. \tag{3.45}$$

The second case corresponds to the pipe being terminated by a rigid wall, meaning that $Z_L \to \infty$ and implying zero volume velocity at $z = L$. In this case the system is considered *ideally closed* (often referred to as *stopped*) and its input impedance can be expressed by taking the limit $Z_L \to \infty$ of equation (3.44) to get

$$Z_{\text{in}}^{(\text{closed})} = -\text{j}Z_0 \cot kL. \tag{3.46}$$

Let us assume a simple model of a labial organ pipe. It was discussed in Chapter 2 that the air jet drives the pipe at the pipe mouth. The driving jet produces a pressure fluctuation on the air inside the tube. The frequencies of natural resonance of the pipe are found where the pressure oscillations induce maximal response inside the tube (see [105, chapter 23]), i.e. when the acoustic input impedance of the pipe Z_{in} is minimal. Hence the *frequencies of natural resonance* $f_n = c/\lambda_n$ of the system are found by the corresponding wavelengths λ_n as

$$\lambda_n = \begin{cases} \dfrac{4L}{2n} & \text{if} \quad Z_L = 0 \\[2ex] \dfrac{4L}{2n-1} & \text{if} \quad Z_L \to \infty \end{cases} \qquad n = 1, 2, \ldots \tag{3.47}$$

Therefore, the cylindrical pipe open at both ends acts as a half-wave resonator, whereas the pipe with one end open and the other end closed is a quarter-wave resonator.

3.3 Acoustic circuits and transmission lines

In the previous sections, only simple systems consisting of one or two elements were examined. For such simple systems it was straightforward to infer the proper boundary conditions and the relations describing the interactions of the elements of the system. However, when having more complex systems at hand, it is useful to describe and visualize the systems by means of acoustic circuits, in which the connections relating the elements of the system can easily be followed.

This section introduces the concentrated and distibuted parameter elements of acoustic circuits. The *electrical–mechanical–acoustical analogies* are useful for finding the correspondence between circuits of the three types. The transfer matrix description of acoustic transmission lines is of great potential when systems consisting of multiple waveguide elements are considered. The theory of acoustic circuits is an essential tool for the analysis of acoustic transmission lines, such as the air columns of wind instruments of various kinds.

3.3.1 Lumped two-pole elements

Lumped or concentrated parameter two-pole elements of a circuit can be described by a single parameter, the impedance $Z(\omega)$ that is the ratio of pressure difference between the poles and the acoustic volume velocity flowing through the element. The three basic types of the lumped two-pole elements are introduced in the sequel.

The simplest lumped acoustic element is a short tube of length L with both ends open. The impedance of the tube is found under the assumption that the air inside it moves without compression, as a rigid piston. This gives

$$Z_{\text{tube}} = \text{j}\omega \left(\frac{\rho_0 L}{S} \right) = \text{j} Z_0 kL. \tag{3.48}$$

impedance of a short tube

The same result is also obtained as a first order approximation of (3.45) as $\tan kL \approx kL$ with $kL \ll \pi/2$. The acoustic impedance of such small tube is analogous to the mechanical impedance of a mass $M = \rho_0 SL$, and is similar to an inductance in an electrical circuit. Based on this analogy a small tube can be referred to as an *acoustical inductance*.

The second element that can be described by a lumped parameter is a small cavity of volume V. The change of the volume $-\delta V$ occupied by the air inside the cavity as a response to a pressure perturbation p is found as

$$p = -B \frac{\delta V}{V} \qquad \text{with} \qquad B = \gamma p_0 = \rho_0 c^2. \tag{3.49}$$

B is known as the *bulk modulus* of air. Due to the principle of continuity, the change of volume δV is expressed as the time integral of volume flow into the cavity, and the acoustic impedance of the cavity is obtained as (see e.g. [67, pp. 152–153])

$$Z_{\text{cavity}} = \frac{1}{\text{j}\omega} \left(\frac{\rho_0 c^2}{V} \right) = -\text{j} Z_0 \frac{1}{kL}, \tag{3.50}$$

impedance of a small cavity

with substituting $V = SL$. It is seen that (3.50) is the first order approximation of (3.46) as $\cot kL \approx (kL)^{-1}$ with $kL \ll \pi/2$. The acoustic impedance of such a cavity is analogous to the mechanical impedance of a spring with compliance $C = V/\rho_0 c^2$. The corresponding element of an electrical circuit is a capacitance, thus, a small cavity is an *acoustical capacitance*.

The third element, the *acoustical resistance* is modeled as acoustic flow throgh a plate with small perforations. It is assumed this time that the radius of the perforations a_p are smaller than the boundary layer thicknesses, that is $a_\text{p} < \delta_\text{v}$ and $a_\text{p} < \delta_\text{t}$. Then, the motion is dominated by viscothermal losses and the volume velocity perturbations are in phase with that of the pressure. The acoustic impedance of this element is given as

$$Z_{\text{resist}} = R, \tag{3.51}$$

acoustical resistance

with R denoting the value of the acoustical resistance depending on the number and size of the aperture channels.

Using a combination of these three elements, a lumped element with arbitrary impedance can be constructed. When an acoustic circuit is constructed from a physical system care must be taken at the range of applicability of concentrated parameter elements. It was discussed above that the impedances of acoustical inductances and capacitances are the first order approximations of an open and a closed tube, respectively. Therefore, the error of the approximation depends on the ratio of the (characteristic) length of the element and the wavelength, L/λ. As a rule of thumb, $L/\lambda < 1/8$ is taken usually (see e.g. [27, part XIII]) as the upper frequency limit of regarding tubes or cavities as lumped elements.

limits of applicability

3.3.2 Acoustic transmission lines

Contrary to lumped elements, transmission lines can not be characterized by a sole parameter, therefore they are often referred to as *distributed parameter* or *waveguide* elements. Such an element, for example, is a duct with a length comparable to the wavelength. Transmission lines will be the essential building blocks of the acoustic circuits utilized for modeling organ pipes. Transfer quantities of acoustic circuits are often of special interest in musical acoustic applications. In these cases the so-called *transfer matrix description* is a useful tool for characterizing the system.

The transfer matrix approach

Generally, the acoustic transfer matrix of a two-port (four-pole) circuit is defined as the matrix relating the input and output sound pressures and volume velocities of the system, that is

transfer matrix

$$\begin{bmatrix} \hat{p}_{\text{in}} \\ \hat{U}_{\text{in}} \end{bmatrix} = \begin{bmatrix} T_{11} & T_{12} \\ T_{21} & T_{22} \end{bmatrix} \begin{bmatrix} \hat{p}_{\text{out}} \\ \hat{U}_{\text{out}} \end{bmatrix}. \tag{3.52}$$

Note that the matrix elements have different dimensions in the above description. The quantities T_{11} and T_{22} are nondimensional, whereas T_{12} has impedance dimension and T_{21} has admittance dimension. In general, the transmission matrix $\mathbf{T}(\omega)$ is dependent on the frequency.

The greatest advantage of the transfer matrix approach is that systems with different transfer matrices can easily be joined connecting the input port of one system to the output system of the other. Assuming N systems connected in a serial manner and denoting the transfer matrix of the ith system by $\mathbf{T}_i$, the complete system is characterized as

$$\begin{bmatrix} \hat{p}_{\text{in}} \\ \hat{U}_{\text{in}} \end{bmatrix} = \left(\prod_{i=1}^{N} \mathbf{T}_i \right) \begin{bmatrix} \hat{p}_{\text{out}} \\ \hat{U}_{\text{out}} \end{bmatrix}. \tag{3.53}$$

The total transfer matrix is then expressed as $\mathbf{T}_{\text{tot}} = \prod \mathbf{T}_i$.

Another quantity of our interest is usually the transfer impedance or admittance of the system, relating one of the input quantities with the other output quantity. If the termination impedance Z_L is known, the transfer quantities or the input impedance can readily be expressed from the transfer matrix description (3.52).

The transfer matrix of a cylindrical duct[2]

The transfer matrix of a cylindrical duct can be calculated based on the fundamental laws of mass and momentum conservation. Taking the one-dimensional versions of equations (3.11) and (3.12), making use of the constitutive equation (3.13) we get

$$\frac{1}{c^2}\mathrm{j}\omega\hat{p}(z) + \rho_0 \frac{\partial \hat{v}(z)}{\partial z} = 0 \tag{3.54a}$$

$$\mathrm{j}\omega\rho_0\hat{v}(z) + \frac{\partial \hat{p}(z)}{\partial z} = 0. \tag{3.54b}$$

Introducing the quantities Z and Y as

$$Z = \frac{\mathrm{j}\omega\rho_0}{S} \qquad \text{and} \qquad Y = \frac{\mathrm{j}\omega S}{\rho_0 c^2}, \tag{3.55}$$

multiplying by S, and using $\hat{U} = S\hat{v}$ we get the system of linear differential equations

$$\frac{\partial}{\partial z} \begin{bmatrix} \hat{p}(z) \\ \hat{U}(z) \end{bmatrix} = \begin{bmatrix} 0 & -Z \\ -Y & 0 \end{bmatrix} \begin{bmatrix} \hat{p}(z) \\ \hat{U}(z) \end{bmatrix}. \tag{3.56}$$

[2] This section is written based on S. Adachi: *Personal letter to the author* (2010).

The solution for a section of length L is obtained by integrating from $z = z_1$ to $z = z_2 = z_1 + L$ as

$$\begin{bmatrix} \hat{p}(z_1) \\ \hat{U}(z_1) \end{bmatrix} = \begin{bmatrix} \cos k'L & \mathrm{j}Z_0' \sin k'L \\ \mathrm{j}\frac{1}{Z_0'} \sin k'L & \cos k'L \end{bmatrix} \begin{bmatrix} \hat{p}(z_2) \\ \hat{U}(z_2) \end{bmatrix}, \tag{3.57}$$

transfer matrix of a cylindrical duct

with $k' = -\mathrm{j}\sqrt{ZY}$ and $Z_0' = \sqrt{Z/Y}$. Using the definitions (3.55) we obtain $k' = k = \omega/c$ and $Z_0' = Z_0 = \rho_0 c/S$. In order to take viscous and thermal losses into account $Z = Z_\mathrm{v}$ and $Y = Y_\mathrm{t}$ can be applied, with the definitions given in equations (3.38) and (3.39). If a termination impedance $Z_L(\omega)$ is assumed at $z = z_2$, the input impedance of the tube is found as

$$Z_\mathrm{in}(\omega) = \frac{\hat{p}(z_1)}{\hat{U}(z_1)} = \frac{Z_L(\omega)T_{11} + T_{12}}{Z_L(\omega)T_{21} + T_{22}} = Z_0' \frac{Z_L(\omega)\cos k'L + \mathrm{j}Z_0' \sin k'L}{\mathrm{j}Z_L(\omega)\sin k'L + Z_0' \cos k'L}, \tag{3.58}$$

with T_{ij} denoting the elements of the transfer matrix in equation (3.57). As expected, the result is identical to the relation found in (3.44).

3.4 Sound radiation from open tubes

While infinite termination impedance is a reasonable approximation of a closed pipe, assuming zero termination impedance is a quite rough and inaccurate approximation for an open pipe end. In this section radiation impedances of different openings of a cylindrical organ pipe are examined. The radiation impedance from the open end, the mouth, and other irregular openings are discussed.

3.4.1 Flanged and unflanged pipe ends

Radiation by a rigid piston in an infinite baffle can be calculated analytically by means of the *Rayleigh integral* (see e.g. [61, pp. 122–124]). The latter gives the pressure field over an infinite plane as

$$\hat{p}(\boldsymbol{x}) = \int_\Gamma G(\boldsymbol{x}, \boldsymbol{y}) \frac{\partial p(\boldsymbol{y})}{\partial n} \,\mathrm{d}\boldsymbol{y} \qquad \boldsymbol{x} \in \Omega, \tag{3.59}$$

Rayleigh integral

where $G(\boldsymbol{x}, \boldsymbol{y})$ denotes the *Green's function* for the Helmholtz equation with a Dirac-delta source $\delta(\boldsymbol{x})$ located at the point $\boldsymbol{y}$:

$$\nabla^2 G(\boldsymbol{x}, \boldsymbol{y}) + k^2 G(\boldsymbol{x}, \boldsymbol{y}) = -\delta(\boldsymbol{x} - \boldsymbol{y}). \tag{3.60}$$

The Green's function in three dimensions is given as

$$G(\boldsymbol{x}, \boldsymbol{y}) = \frac{\mathrm{e}^{-\mathrm{j}k|\boldsymbol{x}-\boldsymbol{y}|}}{4\pi\,|\boldsymbol{x} - \boldsymbol{y}|}. \tag{3.61}$$

The acoustical *radiation impedance* of the piston is found by evaluating the Rayleigh integral for the piston of radius a moving with unit velocity (see [116, p. 92])

$$Z_\mathrm{R}^{(\mathrm{pi})}(ka) = \frac{\rho_0 c}{\pi a^2} \left[1 - \frac{J_1(2ka)}{ka}\right] + \mathrm{j}\frac{\rho_0 c}{\pi a^2} \frac{H_1(2ka)}{ka}, \tag{3.62}$$

radiation impedance of a rigid piston

with H_1 denoting the first order Struve function of the first kind (see [122, pp. 288–289]) and the superscript (pi) referring to the piston case. When radiation from a pipe is examined, it is often useful to regard the imaginary part of the radiation impedance as a *length correction*, i.e. an extra length increasing the effective length of the given tube compared to an ideally open ($Z_R = 0$)

tube. The relation between the reflection coefficient $R(ka)$, the length correction $\Delta L(ka)$ and the radiation impedance $Z_\mathrm{R}(ka)$ is expressed as

radiation impedance and length correction

$$R(ka) = -\left|R(ka)\right| \mathrm{e}^{\mathrm{j}2k\Delta L(ka)} \qquad \Longleftrightarrow \qquad Z_\mathrm{R}(ka) = Z_0 \frac{1 - R(ka)}{1 + R(ka)}. \tag{3.63}$$

This approach is effective for the approximation of the natural resonance frequencies of the pipe, by using $L_\text{eff} = L + \Delta L(0)$ instead of L in equation (3.47), with $\Delta L(0)$ denoting the low frequency approximation of the length correction. The latter for the piston case is found as $\Delta L^{(\mathrm{pi})}(0) = 8a/3\pi \approx 0.8488a$.

A rigid piston is only an approximation for an open pipe, since assuming constant particle velocity for the radiating pipe end neglects the contribution of non-planar-wave modes to the pressure and velocity fields, which can be significant at higher frequencies [114, 115]. Nomura *et al.* [114] solved the radiation problem of a flanged pipe end and obtained the radiation impedance and the corresponding length corrections in the frequency range $ka < 3.8317$.[3] Later, Norris & Scheng [115] provided a simpler solution for the same problem and also gave approximative formulas for the radiation impedance and length correction as

radiation impedance of a flanged pipe end

$$\left|R^{(\mathrm{fl})}(ka)\right| = \frac{1 + 0.323ka - 0.077(ka)^2}{1 + 0.323ka + (1 - 0.077)(ka)^2}, \tag{3.64a}$$

$$\frac{\Delta L^{(\mathrm{fl})}}{a} = 0.8216 \cdot \left(1 + \frac{(0.77ka)^2}{1 + 0.77ka}\right)^{-1}. \tag{3.64b}$$

The superscript (fl) refers to the flanged case. At low frequencies $\Delta L^{(\mathrm{fl})}(0) \approx 0.8216a$.

The radiation impedance of an unflanged pipe was derived by Levine & Schwinger [93] by means of the Wiener – Hopf technique. The result of the tedious calculation is

radiation impedance of an unflanged pipe end

$$\left|R^{(\mathrm{uf})}(ka)\right| = \exp\left(-\frac{2ka}{\pi}\int_0^{ka} \frac{\tan^{-1}\left\{-J_1(x)/N_1(x)\right\}}{x\sqrt{(ka)^2 - x^2}}\,\mathrm{d}x\right), \tag{3.65a}$$

$$\frac{\Delta L^{(\mathrm{uf})}(ka)}{a} = \frac{1}{\pi}\int_0^{ka} \frac{\log\left\{\pi J_1(x)\sqrt{J_1^2(x) + N_1^2(x)}\right\}}{x\sqrt{(ka)^2 - x^2}}\,\mathrm{d}x - \frac{1}{\pi}\int_0^{\infty} \frac{\log\left\{2I_1(x)K_1(x)\right\}}{x\sqrt{(ka)^2 + x^2}}\,\mathrm{d}x. \tag{3.65b}$$

N_1 denotes the first order Bessel function of the second kind and the superscript (uf) refers to the unflanged configuration. The low frequency approximation is found as $\Delta L^{(\mathrm{uf})}(0) \approx 0.6133a$. Despite that Levine & Schwinger [93] assume infinitely thin rigid walls, their formula provides a good approximation for an open pipe end and is often applied in various applications. Figure 3.2 displays the results of equations (3.62), (3.64), and (3.65).[4]

Radiation from pipes with different flanges is further discussed in a number of papers. The ones most closely related to the topic of this thesis are breifly summarized in the following. Zorumski [153] generalized the formulation for the radiation impedance of the moving piston for circular and annular ducts with arbitrary wall admittance. Karal [81] evaluated the radiation impedance of a flanged pipe radiating into an other pipe of arbitrary diameter. Ando [11] examined the radiation impedance of an open tube with diffent wall thicknesses as the transition between the unflanged and flanged cases. Nonlinear losses contributing to the radiation loss from an open pipe end was examined recently by Buick *et al.* [35] by means of numerical flow simulations. It was found that the nonlinear losses are signifcant only at very high amplitudes. Thus, the effect of nonlinear radiation losses are neglected in this thesis.

[3]This nondimensional cutoff frequency corresponds to the first positive root of the function $J_0'(ka)$. Since a symmetrical excitation cannot excite nonsymmetrical modes, the limit of the calculation is the cutoff frequency of the first symmetrical mode, i.e. $(m, n) = (0, 1)$ in equation (3.24).

[4]The integrals in (3.65) were evaluated numerically, using Gauss – Legendre and Gauss – Chebyshev quadratures.

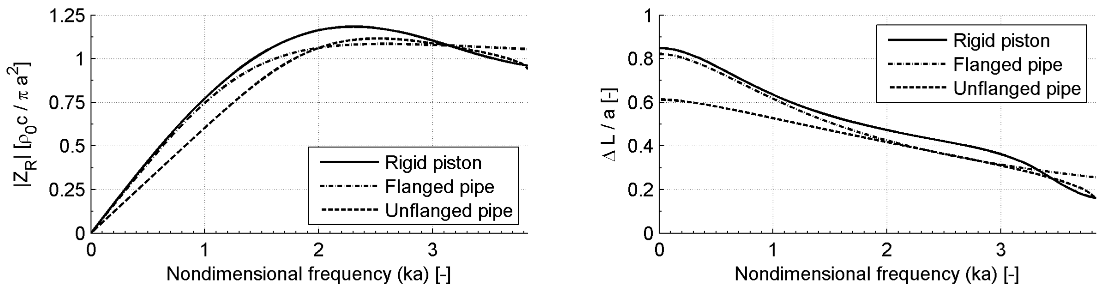

(a) Frequency dependence of $|Z_{\mathrm{R}}(ka)|$

(b) Frequency dependence of $\Delta L(ka)/a$

Figure 3.2. Radiation impedance and length correction factor of different pipe end configurations

3.4.2 The pipe mouth

For a labial organ pipe, the radiaton characteristics from the pipe mouth are also of crucial importance. This topic has already been examined by a number of researchers [47, 78, 79, 101].

Ingerslev & Frobenius [78] have formulated the length correction of a rectangular opening by using an ellipse of equivalent area and width to height ratio. Their expression for the modified length correction $\Delta L'(ka)$ is

$$\Delta L'(ka) = K(\varepsilon)\Delta L(ka) = \frac{2}{\pi}F(\varepsilon)\sqrt[4]{1-\varepsilon^2}\cdot\Delta L(ka), \tag{3.66}$$

with ε representing the eccentricity of the ellipse and $F(\varepsilon)$ denoting the complete elliptic integral of the first order (see [37, p. 486]), defined as

$$F(\varepsilon) = \int_0^{\pi/2} \frac{\mathrm{d}\theta}{\sqrt{1-\varepsilon^2\sin^2\theta}}. \tag{3.67}$$

first order elliptic integral

The length correction for the mouth ΔL_M is found by assuming unbaffled radiation outward the pipe and baffled radiation inward, i.e. letting $\Delta L(0) \approx (0.61 + 0.82)a$. With a usual scaling $W_{\mathrm{M}}/H_{\mathrm{M}} \approx 4$ for a labial organ pipe, with W_{M} and H_{M} denoting the width and the height of the mouth opening, respectively, $K(\varepsilon) \approx 0.89$ is found using (3.66). Scaling the length correction using the ratio of the mouth area and cross sectional area of the pipe the formula of Fletcher & Rossing [67, eq. (17.5) on p. 475] is obtained:

$$\Delta L_{\mathrm{M}}(0) \approx \frac{2.3\,a^2}{\sqrt{W_{\mathrm{M}}H_{\mathrm{M}}}}. \tag{3.68}$$

mouth correction

In case of labial organ pipes the mouth correction is usually much greater than the open end correction, i.e. $\Delta L_{\mathrm{M}} \gg \Delta L^{(\mathrm{uf})}$. For calculating the radiation impedance at the mouth, the resistive part is often neglected and the impedance Z_{M} is expressed as

$$Z_{\mathrm{M}} \approx \frac{\mathrm{j}\omega\Delta L_{\mathrm{M}}(0)}{\pi a^2}. \tag{3.69}$$

mouth impedance

3.4.3 Other openings of the resonator

Besides the open end and the pipe mouth, other openings of various shapes can also be present on the resonators of organ pipes. Among these types of openings, tuning slots are of particular interest in this thesis. These are to be discussed in detail in Chapters 6–7. The radiation impedance of such openings is generally too cumbersome to evaluate analytically, therefore their calculation is performed based on numerical techniques, see e.g. [46, 91, 92]

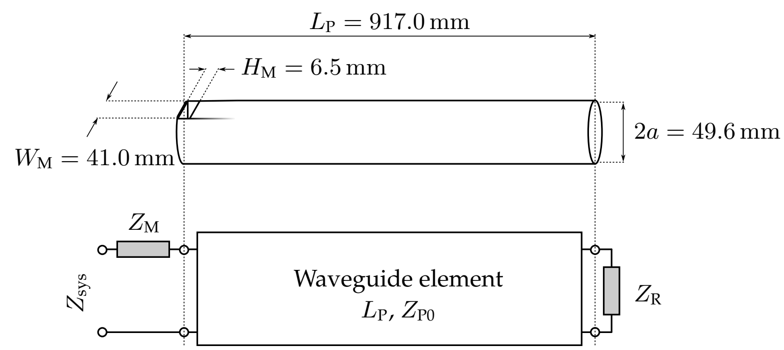

Figure 3.3. Simple one-dimensional model of the resonator of a cylindrical labial pipe

3.5 A simple model of a labial organ pipe

Based on the results discussed in this chapter so far, a simple one-dimensional acoustic model of the resonator of a straight cylindrical open flue organ pipe can be assembled. The model consists of a distributed parameter element, representing the wave propagation inside the pipe body, and two lumped elements corresponding to the radiation impedances at the open end and the mouth. The geometry and the equivalent acoustic circuit of the model is depicted in Figure 3.3. This model is naturally only valid under the cutoff frequency, i.e. $ka < 1.8412$.

All calculations in this example are performed assuming atmospheric pressure and $T_0 = 23°\mathrm{C}$ ambient temperature, that corresponds to the temperature at which the reference measurement on the same pipe was performed. Viscous and thermal wall losses are incorporated into the model using equations (3.37), (3.38), and (3.39), while the much smaller intrinsic losses of air are neglected. The impedances Z_R and Z_M are calculated making use of (3.63), (3.65), (3.68), and (3.69). The impedance of the pipe, Z_P is calculated using the transfer matrix approach as given in equation (3.58). Finally, the input impedance of the complete system Z_{sys} is obtained as

$$Z_{sys} = Z_M + Z_P = Z_M + Z_{P0}\frac{Z_R + \mathrm{j}Z_{P0}\tan k'L}{Z_{P0} + \mathrm{j}Z_R \tan k'L}, \tag{3.70}$$

with $Z_{P0} = \rho_0 c/\pi a^2$ denoting the acoustic plane wave impedance of the pipe.

Figure 3.4 displays the input admittance $Y_{sys} = 1/Z_{sys}$ of the pipe. In order to demonstrate the validity of the model, the input admittance calculation is readily compared to the steady state spectrum of the pipe.[5] It can clearly be seen that the calculated input admittance is in very good correspondence with the baseline of the measured spectrum. From the input admittance function displayed in Figure 3.4 the following information can readily be attained.

Natural resonance frequencies (or acoustic eigenfrequencies) are the frequencies where the system has maximal input admittance (minimal input impedance), as explained in Section 3.2.4. The *fundamental frequency*, denoted by f_1, corresponds to the pitch of the pipe (see Section 2.2.1). The fundamental is very near to the first calculated eigenfrequency, the former measured as $169.5\,\mathrm{Hz}$, and the latter calculated as $169.0\,\mathrm{Hz}$. The eigenfrequency of the first transversal mode—i.e. the *cutoff frequency*—is found as $f_{cut} = 4\,078\,\mathrm{Hz}$. The cutoff frequency is in good agreement with the frequency above which the measured spectrum becomes quite irregular. This phenomenon is due to the unevitable excitation of transversal and hybrid modes caused by the assymetry of the air jet–pipe mouth configuration.

[5]This example pipe is identical with the "Reference pipe" introduced later in Chapter 6, see Section 6.2.1.

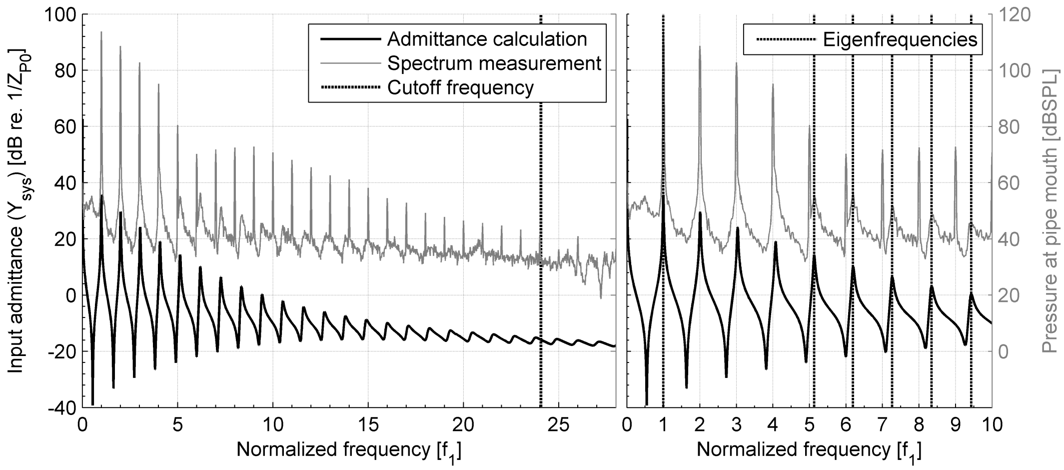

(a) Comparison of input admittance and sound spectrum

(b) Illustration of the stretching behavior

Figure 3.4. Input admittance calculation and steady state spectrum measurement of the example pipe

Stretching behavior of the eigenfrequencies can clearly be observed. *Stretching* refers to the slowly increasing *inharmonicity* of the eigenfrequencies—i.e. the eigenfrequencies become more and more shifted upwards from the harmonics—that is typical of open labial pipes [101, 102]. The stretching behavior is explained by the frequency dependence of the length corrections (see Figure 3.2). In Figure 3.4(b) the usage of normalized frequencies enhances the visibility of the stretching effect. As it can be seen the fifth to ninth eigenfrequencies are shifted more and more upwards from the corresponding harmonic partials.

The *stretching factor* Str_n and its normalized version NStr_n related to the nth eigenfrequency f_n can be defined as (see [135])

$$\mathrm{Str}_n = \frac{f_n}{f_1} \qquad \text{and} \qquad \mathrm{NStr}_n = \frac{f_n}{n f_1} \qquad\qquad n = 2, 3, \ldots \tag{3.71}$$

stretching factors

For the example pipe, the first five stretching factors (Str_2 to Str_6) are: 2.013, 3.041, 4.086, 5.143, and 6.213, respectively.

Quality factors of natural resonances are decreasing with the frequency, as can be identified by the width of the input admittance peaks. Since the real part of the radiation impedance grows with the frequency and converges to the plane wave impedance (as seen in Figure 3.2), the radiation losses increase with the frequency, which explains the decreasing Q-factors. The Q-factors can be evaluated from the input admittance function as:

$$\frac{1}{Q_n} = \frac{\Delta f_n^{[-3\,\mathrm{dB}]}}{f_n}, \tag{3.72}$$

Q-factors

with $\Delta f_n^{[-3\,\mathrm{dB}]}$ denoting the bandwidth in which the input admittance is no less than the maxima measured at f_n minus $3\,\mathrm{dB}$. For our example pipe, the resulting Q-factors are: $Q_1 \approx 90$, $Q_{10} \approx 60$, and $Q_{20} \approx 20$. These results are in good correspondence with that given in [102] for a narrow scaled labial pipe.

3.6 Concluding remarks

This chapter introduced basic one-dimensional modeling techniques for applications in linear acoustics. From the governing equations based on the principles of continuum mechanics, a unidimensional modeling framework was deduced. Intrinsic and wall losses as well as radiation effects from different openings were incorporated into the model. As an example application, the equivalent acoustic circuit of the resonator of an open cylindrical flue pipe was constructed. It was demonstrated that the one-dimensional description can provide a lot of useful information on the acoustical system at hand by means of a few straightforward calculation steps.

The limitations of the one-dimensional model are that (1) it is only capable of handling *simple geometries*, and (2) it is only applicable *under the cutoff* frequency of the system. In order to overcome the limitations of one-dimensional models, numerical techniques can be applied for the simulation of two- or three-dimensional systems. Some of these techniques are discussed in the next chapter.

Chapter 4

An introduction to finite element methods in acoustics

This chapter introduces the numerical techniques used in the thesis for three-dimensional acoustic simulations. Using numerical models have various advantages, some of them are listed below.

1. By means of numerical simulations approximative solutions of problems whose analytical solution is not known—or too cumbersome to evaluate—can be attained. The error of these approximations only depend on the accuracy of the underlying physical model and the computational capacity available at hand.

2. By decomposing a problem into sub-problems of different complexity, results of numerical simulations can also be incorporated into analytical models. The resulting hybrid models lead to an advantageous combination of accuracy and computational performance. hybrid models

3. Numerical techniques can also be used in order to assess the validity of analytical approximations of the solutions of certain problems.

The aim of this chapter is to summarize the most important features of the techniques and their implementation in order to facilitate a better understanding of their applications. The discussion, however, is presented as a general framework and is not limited by the specific field of application utilized later on in the thesis. Explaining the background of numerical analysis methods and discussing each technique in detail are certainly not the objective of this chapter. For more explanation and in-depth analyses the reader is referred to the cited sources. objective

As far as three-dimensional acoustic simulation is concerned, there are quite a few options to choose from, the most common being the *boundary element method* (BEM), the *finite element method* (FEM), and the *finite difference time domain method* (FDTD). Among these the FEM seems to provide the most flexibility for the applications discussed in the dissertation because of the following reasons. (1) It can easily handle elements of arbitrary shape and arbitrarily varying material properties, unlike the BEM or FDTD. (2) The same formulation can be used both in the time and the frequency domain, which is not the case neither for the BEM, nor for FDTD. (3) By means of the extensions introduced in Sections 4.3 and 4.4 the FEM can be applied for unbounded and semi-infinite problems. Since this versatility is exploited in the studies presented in Chapters 7 and 8, the FEM seems a reasonable choice for solving the corresponding problems. choice of the FEM

This chapter first presents the finite element formulation of the Helmholtz equation and the corresponding boundary value problem in Section 4.1. The problem of open boundaries is addressed in Section 4.2. The following two sections discuss two different approaches for finite element simulations with open boundaries. The infinite element method is introduced in Section 4.3, whereas the perfectly matched layer technique is presented in Section 4.4. structure

4.1 Finite element formulation for acoustic problems

This section presents the general formulation of the acoustic *finite element method* (FEM) using the *Galerkin variational procedure*. The finite element method is a general technique for obtaining the approximative solution of boundary value problems of partial differential equations. Although the techniques presented in the sequel can be applied for various problems, the methodology is discussed using the acoustic Helmholtz equation.

4.1.1 The boundary value problem for the Helmholtz equation

Our discussion starts with the homogeneous Helmholtz equation (3.21) for the sound pressure $p(\boldsymbol{x}, \omega)$ in d-dimensional space, that is

Helmholtz equation

$$\nabla^2 p(\boldsymbol{x}, \omega) + k^2 p(\boldsymbol{x}, \omega) = 0 \qquad \boldsymbol{x} \in \Omega \subseteq \mathbb{R}^d. \tag{4.1}$$

It is assumed that the domain Ω is bounded by the boundary Γ. In order to get a well-posed problem the boundary conditions for the partial differential equation must be known in all points of Γ. For the Helmholtz equation (4.1) three types of boundary conditions can be defined.

Dirichlet boundary conditions also known as first-type boundary conditions for the Helmholtz equation define the pressure on one part of the boundary $\Gamma_p \subseteq \Gamma$ as

Dirichlet condition

$$p(\boldsymbol{x}, \omega) = \bar{p}(\boldsymbol{x}, \omega) \qquad \boldsymbol{x} \in \Gamma_p. \tag{4.2}$$

Neumann boundary conditions also called second-type boundary conditions for the Helmholtz equation define the normal derivative of the pressure, or equivalently the normal particle velocity v_n on a part of the boundary $\Gamma_v \subseteq \Gamma$ as

Neumann condition

$$\frac{\partial p(\boldsymbol{x}, \omega)}{\partial n} = \mathrm{j}\omega\rho_0 \bar{v}_n(\boldsymbol{x}, \omega) \qquad \boldsymbol{x} \in \Gamma_v. \tag{4.3}$$

Robin boundary conditions are obtained as the linear combination of Dirichlet and Neumann boundary conditions. The Robin boundary condition prescribes the specific impedance Z relating the pressure and its normal derivative on a subdomain of the boundary $\Gamma_z \subseteq \Gamma$.

boundary value problem

Boundary conditions must be specified on the whole boundary, such that $\Gamma_p \cup \Gamma_v \cup \Gamma_z = \Gamma$. With the boundary conditions defined, the uniqueness of the solution to the Helmholtz equation (4.1) is ensured. The differential equation together with its boundary conditions form a *boundary value problem*.

4.1.2 The weak form of the boundary value problem

The *weak form* of a differential equation is its transformation into an integral equation. The weak form is obtained by multiplying the PDE by an arbitrary test function $\phi(\boldsymbol{x})$ and integrating the result over the whole domain Ω. The integral form is called "weak" since—after integration by parts—it defines less strict criteria for the solution than the original PDE, see e.g. [151, chapter 3]. For the homogeneous Helmholtz equation (4.1) this gives

$$\int_\Omega \phi(\boldsymbol{x}) \nabla^2 p(\boldsymbol{x}) \,\mathrm{d}\boldsymbol{x} + \int_\Omega \phi(\boldsymbol{x}) k^2 p(\boldsymbol{x}) \,\mathrm{d}\boldsymbol{x} = 0. \tag{4.4}$$

For the sake of convenience the notation of the dependence on ω is omitted hereafter.

Making use of the identity that $\nabla \cdot [\phi(\boldsymbol{x})\nabla p(\boldsymbol{x})] = \nabla\phi(\boldsymbol{x}) \cdot \nabla p(\boldsymbol{x}) + \phi(\boldsymbol{x})\nabla^2 p(\boldsymbol{x})$, the first integral can be extracted into two parts, which gives

$$\int_\Omega \nabla\phi(\boldsymbol{x}) \cdot \nabla p(\boldsymbol{x})\,\mathrm{d}\boldsymbol{x} - \int_\Omega \phi(\boldsymbol{x})k^2 p(\boldsymbol{x})\,\mathrm{d}\boldsymbol{x} = \int_\Omega \nabla \cdot [\phi(\boldsymbol{x})\nabla p(\boldsymbol{x})]\,\mathrm{d}\boldsymbol{x}. \tag{4.5}$$

The right hand side can be transformed into a surface integral using the divergence theorem:

$$\int_\Omega \nabla\phi(\boldsymbol{x}) \cdot \nabla p(\boldsymbol{x})\,\mathrm{d}\boldsymbol{x} - \int_\Omega \phi(\boldsymbol{x})k^2 p(\boldsymbol{x})\,\mathrm{d}\boldsymbol{x} = \int_\Gamma \phi(\boldsymbol{x})\frac{\partial p(\boldsymbol{x})}{\partial n}\,\mathrm{d}\boldsymbol{x}. \tag{4.6}$$

Expressing the normal derivative of the pressure from the Neumann boundary condition (4.3) in the right hand side, and multiplying by $\rho_0 c^2$ gives the final equation of the weak form:

$$\rho_0 c^2 \int_\Omega \nabla\phi(\boldsymbol{x}) \cdot \nabla p(\boldsymbol{x})\,\mathrm{d}\boldsymbol{x} - \rho_0\omega^2 \int_\Omega \phi(\boldsymbol{x})p(\boldsymbol{x})\,\mathrm{d}\boldsymbol{x} = \mathrm{j}\omega\rho_0^2 c^2 \int_\Gamma \phi(\boldsymbol{x})\bar{v}_n(\boldsymbol{x})\,\mathrm{d}\boldsymbol{x}. \tag{4.7}$$

Helmholtz weak form

4.1.3 The Galerkin variational method

To arrive at a system of equations with a finite number of unknowns, the weak form must be *discretized*. The discretization is done by representing the solution and test functions—$p(\boldsymbol{x})$ and $\phi(\boldsymbol{x})$ for the Helmholtz equation—by a finite space of *shape functions*. When the approximation is substituted into the original integral statement—(4.4) in our case—the result is a weighted integral of the residual error over the test function space. Thus, this approximation can also be called the *method of weighted residuals*. There are different approaches for choosing the shape function spaces, see e.g. [151, chapter 3] for details. Here only the most commonly used Galerkin procedure is introduced.

weighted residual

In the Galerkin variational method both the solution function and the test function are approximated by the linear combination of a finite set of *elementary shape functions* of the same function space. The approximation using the shape functions $N_j(\boldsymbol{x})$ is given as

$$\begin{aligned} p(\boldsymbol{x}) &\approx \sum_{j=1}^{n} N_j(\boldsymbol{x})p_j = \mathbf{N}(\boldsymbol{x})\mathbf{p}, \\ \phi(\boldsymbol{x}) &\approx \sum_{j=1}^{n} N_j(\boldsymbol{x})\phi_j = \mathbf{N}(\boldsymbol{x})\boldsymbol{\Phi} = \boldsymbol{\Phi}^{\mathrm{T}}\mathbf{N}(\boldsymbol{x})^{\mathrm{T}}. \end{aligned} \tag{4.8}$$

In the above notation the vector of shape functions $\mathbf{N}(\boldsymbol{x})$ is defined as a row vector, whereas the vector of test and solution weights $\boldsymbol{\Phi}$ and $\mathbf{p}$, respectively, are column vectors. The number of shape functions (and corresponding weights) n is the number of *degrees of freedom* (DOF) of the system. Similarly, the gradient of the above variables is attained as

degrees of freedom

$$\begin{aligned} \nabla p(\boldsymbol{x}) &\approx \sum_{j=1}^{n} \nabla N_j(\boldsymbol{x})p_j = \nabla\mathbf{N}\mathbf{p} \\ \nabla\phi(\boldsymbol{x}) &\approx \sum_{j=1}^{n} \nabla N_j(\boldsymbol{x})\phi_j = \nabla\mathbf{N}\boldsymbol{\Phi} = \boldsymbol{\Phi}^{\mathrm{T}}\nabla\mathbf{N}^{\mathrm{T}}, \end{aligned} \tag{4.9}$$

with $\nabla\mathbf{N}$ denoting a $d \times n$ matrix, $(\nabla N)_{ij}$ representing the derivative of the jth shape function with respect to the ith coordinate $\partial N_j/\partial x_i$.

In the following the Galerkin formulation of the weak form of the Helmholtz equation is discussed. Substituting equations (4.8) and (4.9) into the weak form of the Helmholtz equation (4.7) and approximating $\bar{v}_n(\boldsymbol{x})$ also by the same shape functions $N_j(\boldsymbol{x})$ as $p(\boldsymbol{x})$ and $\phi(\boldsymbol{x})$ we get

$$\rho_0 c^2 \int_\Omega \boldsymbol{\Phi}^{\mathrm{T}}\nabla\mathbf{N}(\boldsymbol{x})^{\mathrm{T}}\nabla\mathbf{N}(\boldsymbol{x})\mathbf{p}\,\mathrm{d}\boldsymbol{x} - \rho_0\omega^2 \int_\Omega \boldsymbol{\Phi}^{\mathrm{T}}\mathbf{N}(\boldsymbol{x})^{\mathrm{T}}\mathbf{N}(\boldsymbol{x})\mathbf{p}\,\mathrm{d}\boldsymbol{x} = \mathrm{j}\omega\rho_0^2 c^2 \int_\Gamma \boldsymbol{\Phi}^{\mathrm{T}}\mathbf{N}(\boldsymbol{x})^{\mathrm{T}}\mathbf{N}(\boldsymbol{x})\mathbf{v}\,\mathrm{d}\boldsymbol{x}. \tag{4.10}$$

Finally, taking the spatially independent terms out of the integrals, and noticing that the common multiplier $\mathbf{\Phi}^{\mathrm{T}}$ can be omitted, the Galerkin weak form reads as

Galerkin weak form

$$\rho_0 c^2 \int_\Omega \nabla\mathbf{N}(\boldsymbol{x})^{\mathrm{T}}\nabla\mathbf{N}(\boldsymbol{x})\,\mathrm{d}\boldsymbol{x}\,\mathbf{p} - \rho_0\omega^2 \int_\Omega \mathbf{N}(\boldsymbol{x})^{\mathrm{T}}\mathbf{N}(\boldsymbol{x})\,\mathrm{d}\boldsymbol{x}\,\mathbf{p} = \mathrm{j}\omega\rho_0^2 c^2 \int_\Gamma \mathbf{N}(\boldsymbol{x})^{\mathrm{T}}\mathbf{N}(\boldsymbol{x})\,\mathrm{d}\boldsymbol{x}\,\mathbf{v}. \tag{4.11}$$

Equation (4.11) is usually given in its matrix form as

matrix form

$$\mathbf{K}\mathbf{p} - \omega^2\mathbf{M}\mathbf{p} = \mathrm{j}\omega\mathbf{A}\mathbf{v}. \tag{4.12}$$

In the above equation the matrices are defined as

system matrices

$$\mathbf{K} = \rho_0 c^2 \int_\Omega \nabla\mathbf{N}(\boldsymbol{x})^{\mathrm{T}}\nabla\mathbf{N}(\boldsymbol{x})\,\mathrm{d}\boldsymbol{x}, \tag{4.13a}$$

$$\mathbf{M} = \rho_0 \int_\Omega \mathbf{N}(\boldsymbol{x})^{\mathrm{T}}\mathbf{N}(\boldsymbol{x})\,\mathrm{d}\boldsymbol{x}, \tag{4.13b}$$

$$\mathbf{A} = \rho_0^2 c^2 \int_\Gamma \mathbf{N}(\boldsymbol{x})^{\mathrm{T}}\mathbf{N}(\boldsymbol{x})\,\mathrm{d}\boldsymbol{x}. \tag{4.13c}$$

The $n \times n$ type matrices $\mathbf{K}$ and $\mathbf{M}$ are referred to as the acoustic *stiffness* and *mass system matrices*, respectively. From equation (4.13) it can be seen that the resulting matrices are hermitian, which is an advantageous property of the Galerkin method, since such matrices require less storage area in memory and enable the usage of faster matrix solver routines [129, p. 153].

4.1.4 Spatial discretization

Spatial discretization refers to the process in which the solution domain is decomposed into a finite number of non-overlapping subdomains Ω_k as

domain decomposition

$$\Omega \approx \bigcup_{k=1}^{m} \Omega_k \qquad \text{and} \qquad \Omega_i \cap \Omega_j = \emptyset \quad \text{if} \quad i \neq j. \tag{4.14}$$

It should be noted that the approximation in the above equation means that the numerical solution domain is not necessarily congruent with the original domain; however, the error of the approximation is usually negligibly small.

The subdomains Ω_k are called *elements* in the finite element framework, and they are defined by *mapping transformations* from finite parent domains $\mathcal{O}_e$. The coordinate transformation from local $\boldsymbol{\xi} \in \mathcal{O}_e$ to global $\boldsymbol{x} \in \Omega$ coordinates is given as

element mapping

$$\boldsymbol{x}(\boldsymbol{\xi}) = \sum_{i=1}^{n_e} L_i(\boldsymbol{\xi})\boldsymbol{x}_i = \mathbf{L}(\boldsymbol{\xi})\mathbf{X} \qquad \boldsymbol{\xi} \in \mathcal{O}_e, \tag{4.15}$$

with $L_i(\boldsymbol{\xi})$ denoting the mapping functions, also referred to as geometry shape functions, and $\boldsymbol{x}_i$ being the ith *node* of the element, which is defined by a total number of n_e nodes and the corresponding mapping functions. As a shorter notation the row vector $\mathbf{L}(\boldsymbol{\xi})$ contains the geometry shape functions and the $n_e \times d$ matrix $\mathbf{X}$ is composed of the spatial coordinates of the nodes.

matrix assembly

It is usually useful to define the shape functions N_j in the local coordinate system $\boldsymbol{\xi}$. Then, by applying the domain decomposition defined in equation (4.14) and using the element mapping (4.15) the system matrices in equation 4.13 can be assembled in an element-by-element manner with evaluating integrals only over the parent domains $\mathcal{O}_e$. As for one element type the parent domains are the same, the integration can be performed using simple numerical quadrature rules. In some special cases even analytical integration is possible. Furthermore, with the proper—and usual—choice of $N_j(\boldsymbol{\xi})$, the system matrices become sparse, which significantly reduces the computational effort required for the solution.

4.1.5 Sources

When a source $q(\boldsymbol{x})$ is located inside the solution domain Ω, the inhomogeneous Helmholtz equation needs to be solved inside the domain

Inhomo-geneous Helmholtz equation

$$\nabla^2 p(\boldsymbol{x}) + k^2 p(\boldsymbol{x}) = q(\boldsymbol{x}) \qquad\qquad \boldsymbol{x} \in \Omega \subseteq \mathbb{R}^d. \tag{4.16}$$

Since equation (4.16) is an inhomogeneous linear partial differential equation, its solution is obtained as a superposition of the solution of the homogeneous equation (4.1) (also referred to as the complementary solution), and a particular solution of (4.16).

In acoustics the complementary solution is usually called the scattered pressure field, denoted by $p^{(\text{scat})}$, whereas the particular solution is referred to as the incident pressure field $p^{(\text{inc})}$. From a physical viewpoint the incident and the scattered fields can be interpreted as the excitation and the response of the linear acoustic system, respectively. The total field is obtained as:

$$p(\boldsymbol{x}) = p^{(\text{inc})}(\boldsymbol{x}) + p^{(\text{scat})}(\boldsymbol{x}), \tag{4.17a}$$

$$\boldsymbol{v}(\boldsymbol{x}) = \boldsymbol{v}^{(\text{inc})}(\boldsymbol{x}) + \boldsymbol{v}^{(\text{scat})}(\boldsymbol{x}). \tag{4.17b}$$

The sources can be incorporated into the discretized boundary value problem, and the resulting matrix equation is attained after a few algebraic steps, see e.g. [96, pp. 16–18]. The special case of scattering from acoustically rigid bodies is worth mentioning here as an example often used in practice. In this case the homogeneous Neumann boundary condition, i.e. $\bar{v}_n(\boldsymbol{x}) = 0$ holds on Γ. Thus, the complementary solution $p^{(\text{scat})}$ is obtained by imposing $\bar{v}_n(\boldsymbol{x}) = -v_n^{(\text{inc})}(\boldsymbol{x})$ on Γ.

4.1.6 Solution methods

The matrix equation (4.12) can readily be transformed back into the time domain, by substituting $\partial/\partial t$ instead of the factor $\mathrm{j}\omega$ as

$$\mathbf{K}\mathbf{p} + \mathbf{M}\ddot{\mathbf{p}} = \rho\mathbf{A}\dot{\mathbf{v}}. \tag{4.18}$$

Both in the time and the frequency domain the matrix equation can be solved by means of direct or iterative solvers, see e.g. [48]. In the frequency domain it is also common to perform a *modal solution*, i.e. expressing the solution as the linear combination of the eigenmodes of the system. The latter is done by solving the *generalized eigenvalue problem* by setting $\mathbf{v} = \mathbf{0}$ in equation (4.12).

4.2 Open boundaries

Real-life applications in acoustics naturally involve radiation and scattering problems with open boundaries. Since the finite element method presented in Section 4.1 relies on the decomposition of the computational domain into a finite number of elements of finite size, simulation of infinite spaces using the FEM is not straightforward. This section introduces the general background of free field problems and the challange they mean in the finite element framework.

An unbounded problem can be treated as a bounded problem by having its domain truncated and limited by an outer, *artificial boundary* Γ_∞ located at an infinite distance. The requirement that only components propagating in the outward direction are present at large distances from the radiating surface must be imposed on unbounded time harmonic solutions to satisfy causality. This is assured provided that the *Sommerfeld radiation condition* [133] is satisfied:

Sommerfeld radiation condition

$$\lim_{r\to\infty} r^{(d-1)/2} \left(\frac{\partial p}{\partial r} + \mathrm{j}kp \right) = 0, \tag{4.19}$$

where $r = |\boldsymbol{x}|$ is the distance from the origin. In case of a one-dimensional problem with $d = 1$ equation (4.19) holds not only at $r \to \infty$ but also at any finite r. In two or three dimensions, the equation only holds at infinity.

The fundamental difficulty that arises is that in the finite element context the artificial boundary Γ_∞ can not be located at an infinite distance, naturally. Nevertheless, in order to get a well-posed problem, a boundary condition must be defined over Γ_∞, which has to be transmissive of impinging waves coming from the domain Ω according to the Sommerfeld condition. Hence, a non-reflecting boundary condition is sought on the artificial boundary. These transparent conditions are usually referred to as *absorbing boundary conditions*. It is also clear that with the truncation of domain Ω the boundary Γ_∞ becomes solely responsible for the correct representation of the original domain lying outside of it. It is usually appropriate to suppose that the outer domain is isotropic and homogeneous. Imposing such a condition might seem to be simple; however, this simplicity is deceptive.

absorbing boundary conditions

To overcome the inherent difficulty of unbounded problems various *local* and *global* absorbing boundary approaches were elaborated in the last four decades. A global condition means that a full impedance matrix relates the pressure and velocity weights corresponding the DOFs on Γ_∞ to each other. With such an impedance matrix the sparsity of the resulting system matrices is severely damaged; furthermore, the coupling impedance matrix is generally frequency dependent. Such conditions are implemented by the *coupled FE/BE method*, or *Dirichlet-to-Neumann maps*. Local non-reflecting conditions, on the other hand, preserve the adjacency relations of the elements and also the sparsity of the system matrices. Local absorbing boundary conditions can lead to frequency dependent or independent matrices, depending on the specific technique. Two of these methods, which are applied in the subsequent chapters of this thesis, are discussed in the next sections. A detailed review on absorbing boundary techniques is found in [68].

local and global absorbing conditions

4.3 Infinite elements

This section presents the formulation of the *infinite element method* (IEM), a technique for handling unbounded computational acoustic problems in the finite element framework. In the first part of this section the multipole expansion and the Atkinson – Wilcox theorem are discussed. Then, the infinite element formulation utilizing the Astley – Leis mapped approach is explained.

4.3.1 Multipole expansion

The solution of the Helmholtz equation in three dimensions in closed and open domains can be expanded in terms of separable solutions in spherical coordinates $\boldsymbol{x}(r,\theta,\varphi)$ as

$$\begin{aligned} p(\boldsymbol{x},\omega) = &\sum_{n=0}^{\infty}\sum_{m=0}^{n} h_n^{(2)}(kr)P_n^m(cos\theta)\left\{A_{nm}\sin(m\varphi)+B_{nm}\cos(m\varphi)\right\} \\ &+\sum_{n=0}^{\infty}\sum_{m=0}^{n} h_n^{(1)}(kr)P_n^m(cos\theta)\left\{C_{nm}\sin(m\varphi)+D_{nm}\cos(m\varphi)\right\}, \end{aligned} \tag{4.20}$$

with P_n^m representing Legendre polynomials, $h_n^{(1)}$ and $h_n^{(2)}$ denoting Hankel functions of the first and second kind, respectively, and A_{nm}, B_{nm}, C_{nm}, D_{nm} being constants. The Hankel functions can be expaneded as

$$\begin{aligned} h_n^{(1)}(kr) &= \frac{1}{kr}\left[\alpha_0+\frac{\alpha_1}{r}+\frac{\alpha_2}{r^2}+\cdots+\frac{\alpha_n}{r^n}\right]\mathrm{e}^{+\mathrm{j}kr} \qquad (\alpha_j,\ j=0\ldots n \quad \text{constants}) \\ h_n^{(2)}(kr) &= \frac{1}{kr}\left[\beta_0+\frac{\beta_1}{r}+\frac{\beta_2}{r^2}+\cdots+\frac{\beta_n}{r^n}\right]\mathrm{e}^{-\mathrm{j}kr} \qquad (\beta_j,\ j=0\ldots n \quad \text{constants}) \end{aligned} \tag{4.21}$$

When only outwardly propagating waves are assumed, which means that the Sommerfeld radiation conditon (4.19) is fulfilled, the second summation in equation (4.20) can be omitted and

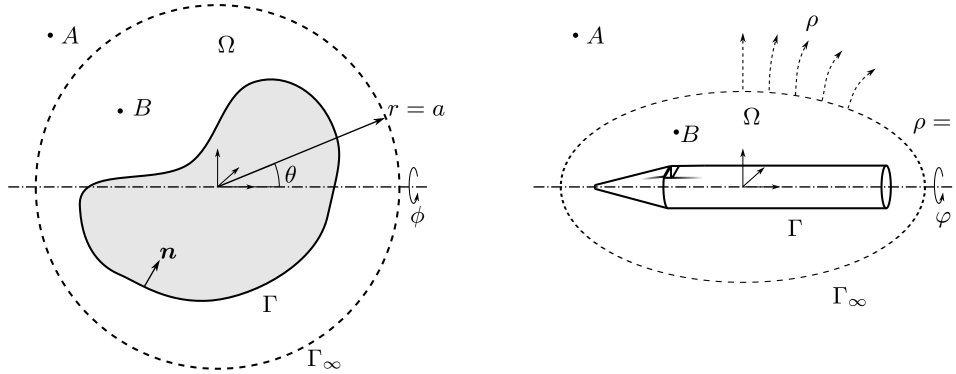

(a) Spherical coordinates (b) Spheroidal coordinates

Figure 4.1. Illustration of the Atkinson – Wilcox criterion. Point A satisfies the criterion, while point B does not. After Fig. 7.4 of [13].

the expansions of the Hankel functions can be rearranged to give

multipole expansion

$$p(\boldsymbol{x}, \omega) = \mathrm{e}^{-\mathrm{j}kr} \sum_{n=0}^{\infty} \frac{G_n(\theta, \varphi, \omega)}{r^n}, \tag{4.22}$$

with $G_n(\theta, \varphi, \omega)$ denoting a directivity function associated with the nth inverse power of r. This form is called a *multipole expansion*. The expansion can also be interpreted in terms of near and far field contributions. The leading term, associated with r^{-1}, determines the far field directivity, while the remaining terms contribute to the near and intermediate field. If expression (4.22) is truncated—as it will be the case when trial solutions are defined for infinite elements—the number of terms retained determines the extent to which the truncated expansion is able to resolve near field effects.

Atkinson – Wilcox theorem

The multipole expansion (4.22) is expected to hold in the far field, but the extent of its validity in the near field is not obvious. This question is answered by the Atkinson – Wilcox theorem [145]. It states that the sound field at any point that lies entirely outside a circumscribing sphere, which itself encloses all radiating and scattering sources, can be written as a multipole expansion of type (4.22), and that this expansion is absolutely and uniformly convergent.

The principle is illustrated in Figure 4.1, with the point A lying outside a circumscribing sphere of radius a and therefore satisfies the criterion, whereas point B does not. The Atkinson – Wilcox criterion was first derived for a spherical coordinate system [145] (Figure 4.1(a)), and a similar result was found later [36] for spheroidal or ellipsoidal coordinate systems (Figure 4.1(b)). The inner region, in which the multipole expansion cannot be used, can be greatly reduced by using a spheroidal rather than a spherical surface when modeling oblong objects.

4.3.2 Mesh, mapping, shape and test functions

infinite element mesh

When a mesh is created using infinite elements, the infinite elements are attached to the artificial boundary Γ_∞, as depicted in Figure 4.2. The whole unbounded domain is subdivided into a finite number of elements of infinite size, so that (4.14) holds. The infinite elements must be defined so that their inner faces overlap with the outer faces of the finite elements located at Γ_∞. The region occupied by the infinite elements is denoted by Ω_∞ in the following.

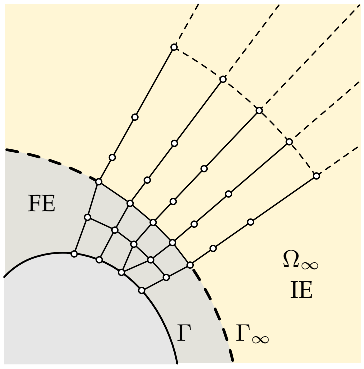

Figure 4.2. Infinite element mesh

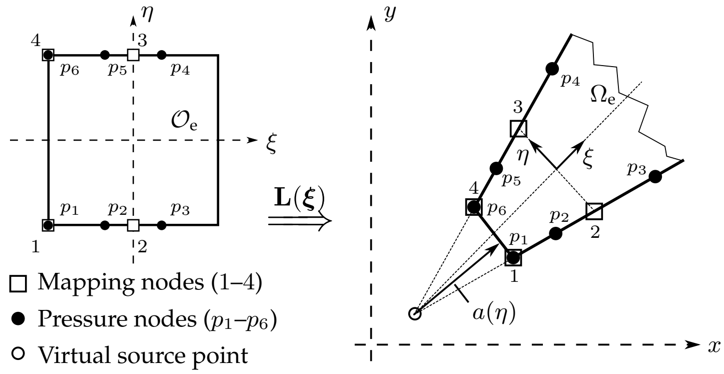

Figure 4.3. Coordinate mapping for infinite elements

There are a large number of formulations of infinite elements, as summarized in [13]. The infinite elements can be defined over the global coordinate system (*unmapped* or *separable formulation*, see e.g. [36, 131]), or can be defined over common finite parent domains in the local coordinate system (*mapped formulation*). In the following our discussion is restricted to the Astley – Leis conjugated formulation with mapped elements.

The basis of mapping infinite element formulations is the coordinate transform, which maps the element from a standard, finite domain into an infinite region of the physical domain. The mapping is carried out similar to equation (4.15), and is depicted in Figure 4.3. This finite to infinite transformation is performed by the proper definition of geometry shape functions $\mathbf{L}(\boldsymbol{\xi})$ in the standard parent domain $\mathcal{O}_\text{e}$. It can be seen that the simple one-dimensional mapping function

finite to infinite mapping

$$x = \frac{2\xi}{\xi - 1}x_1 + \frac{1+\xi}{1-\xi}x_2 \tag{4.23}$$

maps the section $-1 \leq \xi \leq 1$ to the infinite section $x \in [x_1, +\infty)$, with $x_2 > x_1$ being the point mapped from $\xi = 0$. The multiplicators of x_1 and x_2 in equation (4.23) are the geometrical shape functions of a simple line infinite element.

The mapping can directly be extended into two or three dimensions, as illustrated in Figure 4.3 for a quadrilateral element. The element geometry is defined by the *mapping nodes*, while the *pressure nodes*, corresponding to the DOFs of the solution, can be defined independently from the mapping nodes. The interpolating shape functions for the pressure field are defined in a different manner compared to standard finite elements: they are chosen so that they inherently follow the oscillating behavior of the solution [13, 15, 31]. This is achieved by inserting a phase term into the standard shape functions, represented by the *phase function* $\mu(\boldsymbol{x})$, thus the approximation of the pressure, in analogy with equation (4.8) becomes

pressure interpolation

$$p(\boldsymbol{x}) \approx \sum_{i=1}^{n} N_i(\boldsymbol{x})p_i = \sum_{i=1}^{n} P_i(\boldsymbol{x})\mathrm{e}^{-\mathrm{j}k\mu(\boldsymbol{x})}p_i \qquad \boldsymbol{x} \in \Omega_\infty. \tag{4.24}$$

The phase function $\mu(\boldsymbol{x})$ is defined over $\mathcal{O}_\text{e}$ in the $\boldsymbol{\xi} = (\xi, \eta, \zeta)$ coordinate system as:

phase function

$$\mu(\boldsymbol{\xi}) = \sum_{i=1}^{n_f} S_i(\eta,\zeta)a_i\frac{1+\xi}{1-\xi} \tag{4.25}$$

with S_i denoting the standard shape function on the inner face of the element, n_f the number of mapping nodes on this face, and a_i representing the distance of these mapping nodes from an imaginary source point located inside Ω (see Figure 4.3). The function $a(\eta,\zeta) = \sum_i S_i(\eta,\zeta)a_i$ that results of the interpolating summation in equation (4.25) is continuous inside the element and in the whole domain Ω_∞.

The other part of the pressure interpolation functions P_i can also be expressed in the local coordinate system. Astley *et al.* [15] define these shape functions by using the standard finite element shape functions in the η and ζ directions and the Lagrange polynomials L_j^m in the ξ direction as

$$P_i(\boldsymbol{\xi}) = S_i(\eta, \zeta)\frac{1-\xi}{2}L_j^m(\xi). \tag{4.26}$$

The Lagrange polynomials are defined as

Lagrange polynomials

$$L_j^m(\xi) = \prod_{\substack{1\leq k\leq m\\ k\neq j}} \frac{\xi - \xi_k}{\xi_j - \xi_k}, \tag{4.27}$$

with ξ_k denoting the ξ coordinate of the kth pressure node of the infinite element. The number of different ξ locations for the pressure nodes of the element is denoted here by m and is also called as the *radial order* of the element. One of the pressure nodes is located on the Γ_∞ surface, at $\xi = -1$, to ensure the direct coupling of the FE and IE parts of the mesh. The other pressure nodes are distributed in an equidistant manner over the $-1 \leq \xi < 1$ region.

Such a choice of shape functions provides the following properties

1. $N_i(\boldsymbol{\xi}) = 0$ in all nodes of the element, except for node i.
2. $N_i(\boldsymbol{\xi}) \equiv S_i(\eta, \zeta)$ on the face of the element.
3. $N_i(\boldsymbol{\xi})$ is a polynomial of order m multiplied by the phase term $\mathrm{e}^{-\mathrm{j}k(r-a)}$.

The first two properties ensure a compatible matching with the inner finite element mesh. From the third property the radial behavior of N_i can be assessed. With keeping η and ζ constant, the local behavior along the ξ-axis gives the global behavior

$$N_i(\boldsymbol{x}) \sim \left[\frac{\alpha_1}{r} + \frac{\alpha_2}{r^2} + \cdots + \frac{\alpha_m}{r^m}\right]\mathrm{e}^{-\mathrm{j}k(r-a)} \qquad (\alpha_1, \alpha_2, \ldots, \alpha_m \quad \text{constants}). \tag{4.28}$$

The absence of the constant (order r^0) term in equation (4.28) is due to the multiplicator $(1-\xi)/2$ in the definition of the pressure shape functions, see eq. (4.26). It can be seen that the above behavior follows the expansion for outgoing waves defined in equations (4.20) and (4.22) truncated to the mth order. Thus, by defining an infinite element of radial order m, an mth order approximation of the multipole expansion can be achieved.

4.3.3 The discretized form

In the Astley – Leis conjugated formulation the test functions (also called weighting functions) are defined as the complex conjugate of the pressure interpolation functions N_i, multiplied by the Astley – Leis weight $D(\boldsymbol{x})$. The test functions $\phi_i(\boldsymbol{x})$ therefore become

Astley – Leis weighting

$$\phi_i(\boldsymbol{x}) = D(\boldsymbol{x})P_i(\boldsymbol{x})\mathrm{e}^{\mathrm{j}k\mu(\boldsymbol{x})}, \qquad \text{with} \qquad D(\boldsymbol{\xi}) = \left(\frac{1-\xi}{2}\right)^2. \tag{4.29}$$

The weight $D(\boldsymbol{\xi})$ cancels out the $\propto (1-\xi)^{-2}$ term arising in the Jacobian from the derivatives $\partial/\partial\xi L_i$, see equation (4.23). The gradients of the shape and weighting functions defined by equations (4.26) and (4.29) are obtained as

$$\nabla N_i = \nabla P_i \mathrm{e}^{-\mathrm{j}k\mu} - \mathrm{j}k\nabla\mu P_i \mathrm{e}^{-\mathrm{j}k\mu} \tag{4.30}$$

$$\nabla \phi_i = \nabla D P_i \mathrm{e}^{\mathrm{j}k\mu} + D\nabla P_i \mathrm{e}^{\mathrm{j}k\mu} + \mathrm{j}k\nabla\mu P_i \mathrm{e}^{\mathrm{j}k\mu}. \tag{4.31}$$

It can be seen that the complex multiplicators of the weight and shape functions, $\mathrm{e}^{\mathrm{j}k\mu}$ and $\mathrm{e}^{-\mathrm{j}k\mu}$, respectively, cancel out in all terms of the products $\phi_i N_j$ and $\nabla\phi_i \cdot \nabla N_j$.

Substituting the definitions from the previous section into the discrtized weak form, the following form of infinite element matrices is obtained

infinite element system matrices

$$M_{ij}^{\mathrm{IE}} = \rho_0 \int_{\Omega_\infty} DP_iP_j\left(1 - \nabla\mu_i \cdot \nabla\mu_j\right)\,\mathrm{d}\boldsymbol{x}, \tag{4.32a}$$

$$C_{ij}^{\mathrm{IE}} = \rho_0 c \int_{\Omega_\infty} DP_i\nabla\mu_i \cdot \nabla P_j - \nabla DP_i \cdot P_j\nabla\mu_j - D\nabla P_i \cdot P_j\nabla\mu_j\,\mathrm{d}\boldsymbol{x}, \tag{4.32b}$$

$$K_{ij}^{\mathrm{IE}} = \rho_0 c^2 \int_{\Omega_\infty} \left(\nabla DP_i + D\nabla P_i\right) \cdot \nabla P_j\,\mathrm{d}\boldsymbol{x}. \tag{4.32c}$$

The final matrix equation of the discretized finite–infinite element problem becomes

$$\mathbf{K}\mathbf{p}' + \mathrm{j}\omega\mathbf{C}\mathbf{p}' - \omega^2\mathbf{M}\mathbf{p}' = \mathrm{j}\omega\mathbf{A}\mathbf{v}. \tag{4.33}$$

Here the matrices $\mathbf{K}$, $\mathbf{C}$, and $\mathbf{M}$ already incorporate the finite element contributions defined in equation (4.13). The damping matrix $\mathbf{C}$ has only infinite element contributions. All three matrices are real valued and sparse; however, the Astley – Leis weighting introduces asymmetry. In equation (4.33) the notation $\mathbf{p}'$ is applied since the nodal values of the solution do not exactly correspond to the complex pressure amplitudes at the given nodes in case of infinite elements.

matrix conditioning

An issue that needs to be taken into account in the numerical solution of the matrix equation (4.33) is the condition number of the system matrices; as using infinite elements of high radial orders can result in *ill-conditioned matrices*. This issue is addressed in a number of publications, and is usually solved by choosing special orthogonal polynomials for the pressure interpolation functions $P_i(\boldsymbol{x})$, see references [31, 51, 52, 74]. It is also worth mentioning that under special conditions (see [14]), similar to (4.12), equation (4.33) can be transformed and solved in the time domain in case of transient problems.

4.4 Perfectly matched layers

An alternative approach for the solution of unbounded problems by means of the finite element method and the implementation of absorbing boundary conditions is the usage of *absorbing layers*. This family of techniques relies on the truncation of the computational domain and attaching a layer of elements on the truncated boundary that absorbs waves traveling outwards the domain. The thickness of such layers is usually a few elements. In case of *perfectly matched layers* (PML) the "perfect match" means satisfying the following criteria:

1. There is no reflection of outwardly propagating waves hitting the interface of the truncated domain and the absorbing layer.

2. Waves reflected from the outer boundary of the absorbing layer are attenuated sufficiently when they reach the interface again, so that they can not cause any damage to the solution in the inner, truncated domain.

In this section the implementation of such a layer is discussed. First, the basic idea of the formulation and the incorporation of absorption into the governing equation is discussed. Then, the choice of the absorbing function is examined by means of a simple two-dimensional example. Finally, the discretized PML and the resulting system matrices are presented.

4.4.1 Basic formulation

The first formulation of the PML was introduced by Berenger [28]. In the original formulation the PML was deduced by splitting variables, and other PML formulation following a similar pattern are often referred to as *split formulations*. An alternative deduction of the PML equations can also performed without splitting, referred to as *unsplit formulation*. A review on different PML formulations can be found in [29]. In the following, for the sake of brevity, only the unsplit formulation applied in the subsequent chapters is discussed.

split and unsplit formulations

The basic idea of the PML is to modify the differential operator of the Helmholtz equation inside the absorbing layer, by introducing absorbing terms as

$$\frac{\partial}{\partial \breve{x}_j} = \frac{1}{\gamma_j}\frac{\partial}{\partial x_j} \qquad \boldsymbol{x} \in \Omega_{\mathrm{L}}, \tag{4.34}$$

with Ω_{L} denoting the domain occupied by the layer and

$$\gamma_j(x_j) = \begin{cases} 1 & \text{if} \quad x \notin \Omega_{\mathrm{L}} \\ 1 - \dfrac{\mathrm{j}}{\omega}\sigma_j(x_j) & \text{if} \quad x \in \Omega_{\mathrm{L}}, \end{cases} \tag{4.35}$$

where σ_j is the absorbing function along the jth direction. In the following it is assumed for the sake of simplicity that the layer occupies the region $a_j \leq x_j \leq a_j^*$. This assumption does not mean any restrictions to the formulation. Modifying the differential operator inside the layer as written in equation (4.34) is equivalent to introducing the change of variables

$$\breve{x}_j(x_j) = \int_0^{x_j} \gamma_j(s)\,\mathrm{d}s = x_j - \int_{a_j}^{x_j} \frac{\mathrm{j}}{\omega}\sigma_j(s)\,\mathrm{d}s, \tag{4.36}$$

since

$$\frac{\partial \breve{x}_j}{\partial x_j} = \gamma_j, \qquad \text{and} \qquad \frac{\partial}{\partial \breve{x}_j} = \frac{1}{\gamma_j}\frac{\partial}{\partial x_j}. \tag{4.37}$$

Therefore, introducing absorption in the PML layer can also be interpreted as a complex stretching of coordinates. The result is the *anisotropic Helmholtz equation*, written as

anisotropic Helmholtz equation

$$\breve{\nabla}^2 p(\boldsymbol{x}) + k^2 p(\boldsymbol{x}) = 0 \qquad \boldsymbol{x} \in \Omega_{\mathrm{L}}, \tag{4.38}$$

with $\breve{\nabla}$ denoting the ∇ operator acting on the $\breve{x}_j$ coordinates.

In one dimension, introducing the notation $\breve{p}(x) = p(\breve{x})$, the relation between the isotropic and anisotropic versions of the Helmholtz equation can be identified as

$$\frac{1}{\gamma}\frac{\partial}{\partial x}\left(\frac{1}{\gamma}\frac{\partial p}{\partial x}\right) + k^2 p = 0 \quad \Longleftrightarrow \quad \frac{\partial^2 \breve{p}}{\partial \breve{x}^2} + k^2 \breve{p} = 0. \tag{4.39}$$

By expressing the one-dimensional d'Alembert solution (3.29) and substituting the complex coordinate $\breve{x}$ from equation (4.36) we get for $x \in \Omega_{\mathrm{L}}$ that

$$\breve{p}(x) = p^+ \mathrm{e}^{-\mathrm{j}k\breve{x}} + p^- \mathrm{e}^{+\mathrm{j}k\breve{x}} = p^+ \mathrm{e}^{-\mathrm{j}kx} \mathrm{e}^{-\frac{k}{\omega}\int_a^x \sigma(s)\,\mathrm{d}s} + p^- \mathrm{e}^{+\mathrm{j}kx} \mathrm{e}^{-\frac{k}{\omega}\int_a^x \sigma(s)\,\mathrm{d}s}. \tag{4.40}$$

The latter means that the exponential decay of the pressure amplitude inside the layer is ensured provided that the absorption function σ is positive. Nevertheless, finding an absorbing function that satisfies both criteria defined above is not a straightforward task.

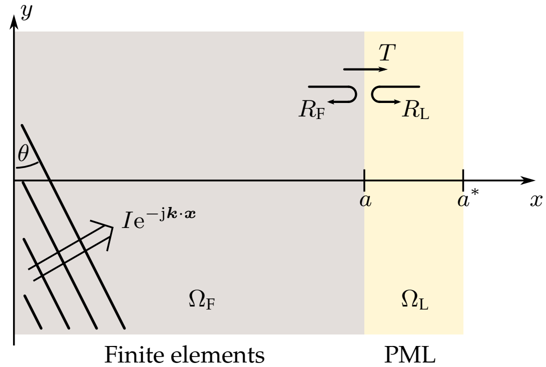

Figure 4.4. Simple example problem for 2D PML

4.4.2 Choice of the absorbing function

A crucial point for an effective PML formulation is the choice of the absorbing functions $\sigma_j(x_j)$. The absorbing functions must be smooth at the interface to prevent reflections and at the same time they have to be rapidly increasing to provide the sufficient amount of absorption.

The effect of choosing the absorbing function in the continuous level is examined in the sequel using a two-dimensional example illustrated in Figure 4.4. The solution domain Ω is semi-infinite in $\boldsymbol{x} = (x, y)$ with $x \in [0, a^*]$ and $y \in \mathbb{R}$. An absorbing layer is defined in the subdomain $\Omega_\text{L} : x \in [a, a^*]$. It is assumed that a plane wave enters the domain from the left hand side with an amplitude I, wave vector $\boldsymbol{k} = (k_x, k_y)$ and incident angle $-\pi/2 < \theta < \pi/2$ between its traveling direction and the x-axis. The analytical solution of the problem is expressed as

$$p(x, y) = I\text{e}^{-\text{j}k_x x}\text{e}^{-\text{j}k_y y} \qquad (x, y) \in \Omega, \tag{4.41}$$

with $k_x = k\cos\theta$, $k_y = k\sin\theta$, and $k = \sqrt{k_x^2 + k_y^2}$.

By denoting the solution in the truncated domain $\Omega_\text{F} = \Omega \setminus \Omega_\text{L}$ by p_F and that in Ω_L by p_L , the solution of the two-dimensional problem can be expressed as

$$p_\text{F}(x, y) = (I\text{e}^{-\text{j}k_x x} + R_\text{F}\text{e}^{\text{j}k_x x})\text{e}^{-\text{j}k_y y} \tag{4.42a}$$

$$\hat{p}_\text{L}(x, y) = (T\text{e}^{-\text{j}k_x \hat{x}} + R_\text{L}\text{e}^{\text{j}k_x \hat{x}})\text{e}^{-\text{j}k_y y}. \tag{4.42b}$$

The constants R_F, R_L and T denote the reflection coefficient of the free field to layer transition, the same of the layer to free field transition and the transmission coefficient from the free field to the layer, respectively.

Substituting the transformed coordinates into equation (4.42b), the pressure field inside the layer is expressed as

$$p_\text{L}(x, y) = (T\text{e}^{-\text{j}k_x x} + R_\text{L}\text{e}^{\text{j}k_x x}\text{e}^{-\frac{\cos\theta}{c}\int_a^x \sigma(s)\,\text{d}s})\text{e}^{-\text{j}k_y y}. \tag{4.43}$$

From the boundary condition at $x = 0$ it is seen that $I = 1 - R_\text{F}$, and since the perfect match condition of the absorbing layer prescribes no reflection at the interface, $T = I$ and $R_\text{F} = R_\text{L}$ are also implied. Finally, the homogeneos Dirichlet boundary condition at the outer edge of the layer, i.e. $p_\text{L}(x = a^*, y) = 0$ gives the following expression for R_L

$$R_\text{L} = \frac{\text{e}^{-2\text{j}k_x a^*}}{\text{e}^{-2\text{j}k_x a^*} - \text{e}^{-2\frac{\cos\theta}{c}\int_a^{a^*}\sigma(s)\text{d}s}}. \tag{4.44}$$

The $\mathbb{L}_2$ error of the solution can be expressed from the difference of the analytical (4.41) and the free field (4.42a) solutions. The error is attained after some algebraic manipulations as

$$\int_0^a |p_{\mathrm{a}}(x,y) - p_{\mathrm{F}}|^2 = |R_{\mathrm{L}}|^2 \frac{2ak_x + \sin k_x a}{k_x}. \tag{4.45}$$

In order to minimalize the error by achieving $R_{\mathrm{L}} \approx 0$ different authors use various formulations in order to make the integral of σ very large. Bermúdez *et al.* [30] proposed the usage of non-integrable absorbing functions which have the property

$$\int_a^{a^*} \sigma(s)\,\mathrm{d}s \to +\infty. \tag{4.46}$$

non-integrable absorbing function

From equation (4.44) it can be seen that zero reflection is achieved if the above condition is fulfilled, thus, the error of the solution vanishes.

4.4.3 The PML in the discretized system

The discretized form of the PML is discussed in the sequel. For the sake of simplicity a two-dimensional formulation is given, which can readily be extended into three dimensions. The weak form of the anisotropic Helmholtz equation (4.38) using the transformation functions γ_x and γ_y is obtained as

$$\begin{aligned}\rho_0 c^2 \int_{\Omega_{\mathrm{F}}} \nabla\phi \cdot \nabla p \,\mathrm{d}\boldsymbol{x} + \rho_0 c^2 \int_{\Omega_{\mathrm{L}}} \frac{\gamma_y}{\gamma_x} \frac{\partial \phi}{\partial x} \frac{\partial p}{\partial x} \,\mathrm{d}\boldsymbol{x} + \rho_0 c^2 \int_{\Omega_{\mathrm{L}}} \frac{\gamma_x}{\gamma_y} \frac{\partial \phi}{\partial y} \frac{\partial p}{\partial y} \,\mathrm{d}\boldsymbol{x} \\ - \rho_0 \omega^2 \int_{\Omega_{\mathrm{F}}} \phi p \,\mathrm{d}\boldsymbol{x} - \rho_0 \omega^2 \int_{\Omega_{\mathrm{L}}} \gamma_x \gamma_y \phi p \,\mathrm{d}\boldsymbol{x} = \mathrm{j}\omega \rho_0^2 c^2 \int_{\Gamma} \phi \bar{v}_n \,\mathrm{d}\boldsymbol{x}.\end{aligned} \tag{4.47}$$

PML weak form

The PML contributions to the mass and stiffness system matrices are attained in the Galerkin formulation of the weak form with using the shape function approximation (4.8) and (4.9) as

$$\mathbf{M}^{\mathrm{PML}} = \rho_0 \int_{\Omega_{\mathrm{L}}} \gamma_x \gamma_y \mathbf{N}^{\mathrm{T}} \mathbf{N} \,\mathrm{d}\boldsymbol{x} \tag{4.48a}$$

$$\mathbf{K}^{\mathrm{PML}} = \rho_0 c^2 \int_{\Omega_{\mathrm{L}}} \left[\frac{\gamma_y}{\gamma_x} \frac{\partial \mathbf{N}^{\mathrm{T}}}{\partial x} \frac{\partial \mathbf{N}}{\partial x} + \frac{\gamma_x}{\gamma_y} \frac{\partial \mathbf{N}^{\mathrm{T}}}{\partial y} \frac{\partial \mathbf{N}}{\partial y} \right] \mathrm{d}\boldsymbol{x}. \tag{4.48b}$$

PML system matrices

Since the functions γ_x and γ_y already incorporate ω, the system matrices of the PML formulation are frequency dependent. For a simulation problem involving multiple frequencies the PML contributions of the system matrices must be assembled separately for each testing frequency.

In order to attain a well-posed problem, boundary conditions on the outer edge of the absorbing layer Γ_{L} have to be imposed. When using the non-integrable absorbing functions (4.46), homogeneous Dirichlet boundary conditions, i.e. $\bar{p}(\boldsymbol{x}) = 0$ when $x \in \Gamma_{\mathrm{L}}$ are applicable.

The above formulation of the PML is not applicable for the time domain simulation of unbounded radiation or scattering problems, as indicated by the frequency dependence of the system matrices. The time domain implementations known to the author rely on the splitted formulation of PML equations, see e.g. [30, 50, 77, 80], which is out of the scope of this chapter. Similarly—also due to the frequency dependence of the system matrices—the modal solution is not an option for the PML formalism presented above.

Unfortunately, even if a PML is perfect in its continuous form, it is not evident that it will also be perfect in its discretized form. By optimizing to the $\mathbb{L}_2$ error of the solution in numerical test cases Bermúdez *et al.* [30] found the simple absorbing function

$$\sigma_j(x_j) = \frac{c}{a_j^* - x_j} \qquad x_j \in \left[a_j, a_j^*\right] \tag{4.49}$$

optimal absorbing function

providing the best performance among the options examined in Reference [30]. The implementation applied in the following chapters also utilizes the non-integrable absorbing function approach by incorporating equation (4.49).

comparing IEM and PML

Compared to infinite elements introduced in Section 4.3, perfectly matched layers have both advantages and disadvantages. While the system matrices of the IEM are frequency independent, the PML gives frequency dependent system matrices; however, ill-conditioned system matrices are not an issue in case of the PML. There is also a remarkable difference of the mesh requirements of the two methods. While the IEM requires that the mesh satisfies the Atkinson – Wilcox criterion, as discussed above, there is no such requirement for the PML, as the latter does not rely on the multipole expansion (4.22). This means that the application of the PML can result in reduced mesh sizes, especially in the case of isolated radiating surfaces, such as discontinuities on oblong acoustic resonators. On the other hand, using the interpolation functions (4.26), far field results can directly be extracted from the IE solutions, that can only be obtained by means of postprocessing techniques in case of the PML. The above properties justify that neither method is superior in all respects compared to the other, and it is reasonable to choose the most suitable formalism depending on the specific problem.

4.5 Summary

This chapter presented the finite element method for acoustics and two of its extensions for the simulation of unbounded problems, the infinite element and the perfectly matched layer techniques. It is emphasized again that the aim of this chapter was not to give an in-depth overview, but to provide a background of the techniques utilized in the following chapters.

postprocessing

The techniques discussed in this chapter are all utilized in the following for solving specific problems. In certain cases, the calculated pressure and velocity fields are not used directly, but the results are incorporated into one-dimensional waveguide models after postprocessing resulting in *hybrid models*. The methods discussed in this chapter are implemented inside an in-house BEM/FEM toolbox, called `NiHu`, introduced later in Appendix D. All acoustic simulations presented in this thesis were performed using the `NiHu` toolbox.

Chapter 5

Sound design of chimney pipes

A specific design problem in organ building practice, namely the scaling of chimney pipes is discussed in this chapter. An optimization method, based on an acoustic waveguide model of a chimney and a resonator, was developed and tested by laboratory measurements of experimental chimney pipes. The dimensions of the chimney pipes are modified by the optimization algorithm until the specified fundamental frequency is achieved, and a predetermined harmonic partial overlaps with an eigenfrequency of the pipe. Experimental pipes were dimensioned by the optimization method for four different scenarios and were built by an organ builder. The applicability of the proposed technique is validated and illustrated by means of laboratory measurements carried out on the experimental pipes and subjective comparison performed by skilled organ builders. This chapter is a revised and extended version of the paper [J2].

5.1 Introduction

A *chimney pipe*, as shown in Figure 5.1, is a special sort of labial organ pipe. It is constructed by inserting a small open tube (chimney) in the cover of a stopped organ pipe. The length and the diameter of the chimney may vary, giving the organ builder a possibility to adjust the timbre of the instrument. "The wider and taller the chimney is, the more the harmony approaches that of an open pipe; the narrower and shorter it is, the more the harmony approaches that of a closed pipe" [22].

According to the tradition of organ building, the chimneys are usually placed outside the main pipe and have a length varying between 1/5 and 2/5 of the length of the pipe and a diameter around 1/4 that of the pipe [16, 22, 33, 117]. In the survey of pipe ranks by Mahrenholz [95] the diameter ratio is varying between 1/3 and 1/4, while the limits of the length ratio are given as 1/4 and 1/5. These rules remain, however, rather general and are not supported by scientific arguments or experimental evidence. Discussions with organ builders during the co-operative research projects supported by the European Commission [1] have indicated that no generally accepted method exists for designing the chimney. Therefore, the SME (small and medium-sized enterprise) partners of the project have initiated scientific investigations on this topic.

traditional chimney scaling

Scientific study on the role of chimneys was performed first by Helmholtz [71]. He assumed that the role of the chimney is to reinforce the fifth harmonic and therefore concluded that the optimal chimney length should be 2/5 that of the pipe. Extensive experimental work on chimney pipes was carried out by Castellengo [38]. Her work confirmed that the main role of the chimney is to influence the relative amplitude of certain harmonics, both during the steady state and the attack transient.

Kokkelmans *et al.* [86] have investigated the behavior of chimney organ pipes using a simple low frequency approximation of the steady sound field. It was found that the input admittance

input admittance

curve can be used for estimating the effect of the chimney geometry on the pipe tone during the steady state. The ratio of measured amplitudes of the different harmonics correlated well with the modulus of the pipe admittance for these harmonics. Following the opinion of Helmholtz [71] it was initially assumed by the authors that the role of the chimney is to enhance the fifth harmonic. Their calculations and experiments, however, have shown that the design rule proposed by Helmholtz appears to be the least favorable one. A good enhancement of the fifth harmonic partial was obtained by the geometry of chimney length/pipe length $^{2}/_{3}$ and chimney diameter/pipe diameter $^{1}/_{4}$. In this case the third eigenfrequency of the pipe has overlapped with the fifth harmonic of the fundamental frequency.

objective

The objective of the research, initiated by the SME partners and reported here, was to develop a method for designing the sound of chimney pipes to a predefined sound character. In the frame of a recently completed European research project [2] a scaling software was developed for labial organ pipes (see Appendix B). Besides the traditional scaling rules of chimney pipes a new kind of scaling, an optimization of the pipe geometry for a predefined sound character, was also incorporated. The method of optimization and the results of test measurements are presented and discussed in this chapter.

5.2 Methodology

Following the results published in [86] the input admittance function of the chimney pipe was chosen for optimization. The acoustic input admittance function of the pipe is defined as the ratio of the frequency dependent volume velocity and sound pressure at the pipe mouth, as introduced in Section 3.2.4. At the maxima of the input admittance function the pipe gives maximal volume velocity at the mouth, thus, these are also the natural resonance frequencies (eigenfrequencies) of the pipe.

prediction of timbre

Characteristics of the steady state spectrum can be predicted from the input admittance function, see e.g. [86]. In most cases (except for overblowing) the fundamental frequency of the pipe is coincident with the first eigenfrequency of the resonator. The amplitudes of harmonic partials are also affected by the input admittance function. If a partial is coincident with a resonance or anti-resonance, it is amplified or suppressed, respectively. By choosing the proper dimensions for the main resonator and the chimney these effects can be fully exploited and the sound spectrum of the pipe can be tuned.

optimization methods

Optimization methods for achieving the desired sound spectrum are discussed in the following. A simple iteration process and a more complex optimization method are demonstrated, both based on the one-dimensional acoustic waveguide model of the pipe. The discussion is limited to pure acoustic phenomena; hence the effects of the flow noise and the edge tone on the spectrum are not addressed herein.

5.2.1 The one-dimensional waveguide model

waveguide model

Under the cut-on frequency of transversal modes, which is clearly the relevant frequency domain of the pipe sound, the resonator can be quite accurately described by a one-dimensional model. This model, as it is shown in Figure 5.1, consists of two waveguides representing the main resonator and the chimney and the radiation impedances at the open end and the mouth.

The radiation impedance at the open end can be calculated using the formula deduced by Levine & Schwinger [93], see equation (3.65). This proves to be a suitable approximation for the radiation from the open end of the chimney. The radiation impedance from the pipe mouth can be determined using the formulas of Ingerslev & Frobenius, see equations (3.66) and (3.69).

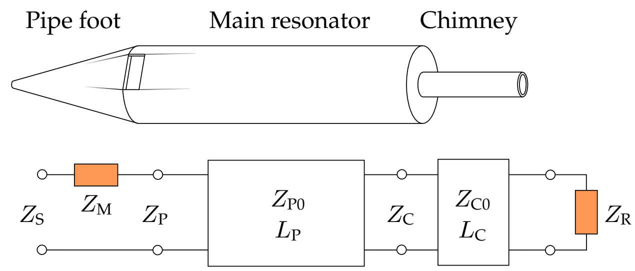

Figure 5.1. Schematic and one-dimensional impedance model of a chimney pipe

The end correction term, ΔL_M is approximated using equation (3.68) as

$$\Delta L_M = \frac{2.3 R_P^2}{\sqrt{W_M H_M}}, \tag{5.1}$$

where R_P represents the inner radius of the main resonator, and W_M and H_M denote the width and the height of the mouth, respectively. Expression (5.1) is valid in the low frequency range for pipes with the usual scaling setting $W_M/H_M \approx 4$.

input impedance

The input impedance of the complete system Z_S can be written using (3.44) twice, with expressing the input impedance of the chimney Z_C first. The chimney is terminated by its radiation impedance Z_R, whereas the main resonator is terminated by the input impedance of the chimney. This gives

$$Z_C = Z_{C0} \frac{Z_R + jZ_{C0} \tan(kL_C)}{Z_{C0} + jZ_R \tan(kL_C)} \qquad \text{and} \tag{5.2}$$

$$Z_S = Z_M + Z_{P0} \frac{Z_C + jZ_{P0} \tan(kL_P)}{Z_{P0} + jZ_C \tan(kL_P)}, \tag{5.3}$$

with L_C and L_P, Z_{C0} and Z_{P0} denoting the physical lengths and acoustic plane wave impedances of the chimney and the main resonator, respectively.

wall losses

To get a more realistic model, viscous and thermal losses can be taken into account. These effects can be non-negligible for the chimney part, where the diameter is relatively small. It is sufficient for our discussion here, that by applying the theory presented in Section 3.2.3, the real valued wave number k and plane wave impedances Z_{P0} and Z_{C0} in equations (5.2) and (5.3) are replaced by the complex valued k', Z'_{P0} and Z'_{C0}, respectively. The latter are dependent on the frequency, viscosity, thermal conductivity and the specific heat of air at constant pressure. Naturally, the latter parameters are dependent on the ambient temperature T_0.

tuning temperature

Since the speed of sound in air has quite strong temperature dependence—as seen in equation (3.16b)—and the acoustic losses are also temperature dependent, the input impedance of a chimney pipe depends not only on the dimensions of the pipe, but also on the temperature. By the optimization, therefore, the temperature has to be fixed (*tuning temperature*).

The input admittance function $Y_S(f) = 1/Z_S(f)$ is dependent on the variables summarized in Table 5.1. In the following this set of parameters is denoted by $\mathcal{P} = \mathcal{P}^* \cup \mathcal{P}_0$, with $\mathcal{P}^*$ representing the unknown variables (optimization targets) and $\mathcal{P}_0$ denoting the known parameters (fixed values). In the next sections a specific and a more general approach is discussed for different $\mathcal{P}^*$ sets.

5.2.2 Optimization by means of an iterative algorithm

In this section one of the simplest cases is discussed, namely when the length of the chimney and the main resonator are unknown, while other variables are kept constant, i.e. $\mathcal{P}^* = \{L_P, L_C\}$.

Notation	Explanation
L_{P}	Length of the main resonator
D_{P}	Inner diameter of the main resonator
L_{C}	Length of the chimney
D_{C}	Inner diameter of the chimney
W_{M}	Mouth width
H_{M}	Mouth height (cutup)
T_0	Tuning temperature

Table 5.1. Variables of the input admittance function in the one-dimensional model

Two parameters are also fixed: the desired fundamental frequency f_1 and the ordinal number n of the harmonic partial that should overlap with an eigenfrequency. The goals of the optimization are (1) to tune the the first eigenfrequency of the pipe to the desired fundamental frequency f_1 and (2) to tune another eigenfrequency to be coincident with the nth partial, $f_n = nf_1$. Since the homogeneous Helmholtz equation (3.28) holds inside the pipe, the inner pressure field can be expressed using the d'Alembert solution (3.29) as

$$\hat{p}(z) = p^{+} \exp(-\mathrm{j}kz) + p^{-} \exp(\mathrm{j}kz). \tag{5.4}$$

reflection coefficients

At the fundamental frequency f_1, a sinusoidal standing waveform develops in the main resonator (see Figure 5.2). The main resonator is terminated by the mouth opening at one side ($z = 0$) and the chimney at the other ($z = L_{\mathrm{P}}$). By expressing the reflection coefficients at both ends ($r|_{z=0}$ and $r|_{z=L_{\mathrm{P}}}$) the following relations are obtained:

$$r|_{z=0} = \frac{p^{+}}{p^{-}} = \frac{Z_{\mathrm{M}} - Z_{\mathrm{P0}}}{Z_{\mathrm{M}} + Z_{\mathrm{P0}}} \qquad \text{and} \tag{5.5}$$

$$r|_{z=L_{\mathrm{P}}} = \frac{p^{-} \exp(\mathrm{j}kL_{\mathrm{P0}})}{p^{+} \exp(-\mathrm{j}kL_{\mathrm{P0}})} = \frac{p^{-}}{p^{+}} \exp(2\mathrm{j}kL_{\mathrm{P}}) = \frac{Z_{\mathrm{C}} - Z_{\mathrm{P0}}}{Z_{\mathrm{C}} + Z_{\mathrm{P0}}}. \tag{5.6}$$

The length of the main resonator (L_{P}) can be determined by combining equations (5.5) and (5.6) and expressing the relation p^{+}/p^{-}:

$$2k_1 L_{\mathrm{P}} = \arg\left\{\frac{p^{+}}{p^{-}}\right\} = \arg\left\{\frac{Z_{\mathrm{M}} - Z_{\mathrm{P0}}}{Z_{\mathrm{M}} + Z_{\mathrm{P0}}} \cdot \frac{Z_{\mathrm{C}} - Z_{\mathrm{P0}}}{Z_{\mathrm{C}} + Z_{\mathrm{P0}}}\right\}, \tag{5.7}$$

with k_1 denoting the wave number corresponding to the fundamental frequency f_1.

At the frequency f_n (i.e. wave number k_n) the sinusoidal standing waveform appears in the chimney part as well, as seen in Figure 5.2. Similarly as above, by expressing the reflection coefficients, the length of the chimney (L_{C}) can be obtained:

$$2k_n L_{\mathrm{C}} = \arg\left\{\frac{Z'_{\mathrm{P}} - Z_{\mathrm{C0}}}{Z'_{\mathrm{P}} + Z_{\mathrm{C0}}} \cdot \frac{Z_{\mathrm{R}} - Z_{\mathrm{C0}}}{Z_{\mathrm{R}} + Z_{\mathrm{C0}}}\right\}, \tag{5.8}$$

where Z'_{P} denotes the input impedance of the main resonator terminated by the mouth impedance Z_{M} at the end. (Note: since the argument function is 2π-periodic it is always possible to find a solution to (5.7) and (5.8) with a valid physical meaning.)

iterative algorithm

Since the length of the chimney must be known to solve the equation for the main resonator length and *vice versa*, a simple iteration can be constructed by making an initial guess on the chimney length ($L_{\mathrm{C}}^{(0)}$), calculating L_{P} from (5.7) and then updating L_{C} and L_{P} by using (5.8) and (5.7) subsequently, in an alternating manner. To find the initial chimney length, the chimney

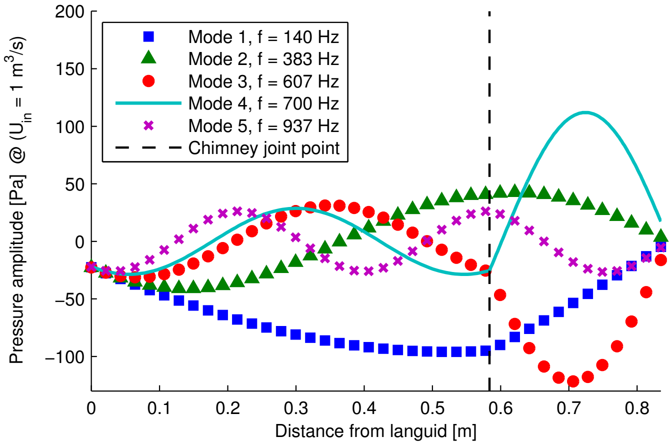

Figure 5.2. Sound pressure waveforms of the first five eigenmodes along the chimney pipe

Iteration	L_C [mm]	$\lvert\Delta L_\mathrm{C}\rvert$ [mm]	L_P [mm]	$\lvert\Delta L_\mathrm{P}\rvert$ [mm]
0	204.49	–	604.18	–
1	244.09	39.60	588.64	15.54
2	249.49	5.40	586.63	1.81
3	250.33	0.84	586.55	0.28
4	250.47	0.14	586.51	0.04
5	250.49	0.02	586.51	< 0.005
6	250.49	< 0.005	586.51	< 0.005

Table 5.2. Results of iterations for the optimization of the main resonator and chimney lengths

can be taken as a half-wavelength resonator with an unflanged and a baffled end, radiating into free space at both sides on the frequency f_n. Using the low frequency length correction term derived from (3.65) for the open end and the low frequency limit of (3.64) for the baffled end, the initial chimney length reads as

$$L_\mathrm{C}^{(0)} = \frac{\lambda_n}{2} - \Delta L_\mathrm{R}^{(\mathrm{uf})} - \Delta L_\mathrm{R}^{(\mathrm{fl})} \approx \frac{\lambda_n}{2} - (0.8216 + 0.6133)R_\mathrm{C} = \frac{\lambda_n}{2} - 1.4349 R_\mathrm{C}, \tag{5.9}$$

with R_C representing the inner radius of the chimney and λ_n denoting the wavelength at the frequency f_n.

This simple iteration proves to be efficient in determining the lengths of the main resonator and the chimney. An example result of the iteration process is displayed in Table 5.2. The fixed parameters were set as $D_\mathrm{P} = 79.00\,\mathrm{mm}$, $D_\mathrm{C} = 28.72\,\mathrm{mm}$, $W_\mathrm{M} = 59.99\,\mathrm{mm}$, $H_\mathrm{M} = 25.66\,\mathrm{mm}$ and $T_0 = 20°\mathrm{C}$. The goal frequency was $f_1 = 140.0\,\mathrm{Hz}$ and n was set to 5, i.e. the fifth harmonic partial at $700\,\mathrm{Hz}$ should overlap with the nearest eigenfrequency of the chimney pipe. The optimization was successful since the fourth eigenfrequency has been tuned in six iteration steps to the exact frequency of $f_5 = 5 \cdot 140\,\mathrm{Hz} = 700\,\mathrm{Hz}$. The resulting eigenfrequencies and sound pressure distributions for unit volume velocity input are shown in Figure 5.2.

5.2.3 Optimization by means of cost functions

In addition to optimizing for the chimney and main resonator lengths, theoretically, optimizing for all geometry parameters listed in Table 5.1 is possible. However, the practically most relevant case is when not only the length but also the diameter of the chimney is to be optimized.

When optimizing for more than two parameters, a simple iterative process cannot be defined straightforwardly and therefore an alternative approach is needed.

Since the dependence of the eigenfrequencies on the pipe dimensions is quite complex, applying a general optimization technique is more feasible than developing a heuristic method. As the optimization goals are well-defined (by the values of the selected fundamental and partial frequencies) a cost function can be constructed that measures the distance of the actual configuration from the ideal one in a special metric. Once the cost function is properly constructed, a global minimization technique needs to be applied to find the optimal values of the variables.

simplex method

A general and widely used method for function minimization is the simplex algorithm first published by Nelder & Mead [89, 109]. The algorithm's advantage is that derivatives are not calculated; only the function is evaluated. The method shows a good convergence for a wide family of functions, as discussed in [89, 109]. The algorithm is implemented inside the `Matlab` function `fminsearch`. It finds the minimum of a scalar function of several variables, starting at an initial estimate. This is generally referred to as *unconstrained nonlinear optimization* [97, 98].

To construct the cost function the deviations of the actual eigenfrequencies from the target frequencies are evaluated. For the fundamental the first resonant frequency is used, while for the nth harmonic, the nearest resonant frequency is taken into account. Therefore a possible formulation of the cost function reads as

the cost function

$$C(\mathcal{P}) = w_1 \cdot [f_1 - f_1^*(\mathcal{P})]^2 + w_n \cdot [nf_1 - f_n^*(\mathcal{P})]^2 \,, \tag{5.10}$$

where $f_1^*(\mathcal{P})$ is the frequency of the first resonance dependent on the parameters, and $f_n^*(\mathcal{P})$ is the eigenfrequency closest to f_n, whereas w_1 and w_n are positive weights.

Since the number of free parameters is three (length of main resonator, length and diameter of the chimney), the optimization by the simplex method could be extended to a third target frequency by adding a third term to the cost function of equation (5.10). In this case simultaneous optimization for the fundamental frequency and two selected harmonic partials is possible.

The value of the cost function (5.10) is zero when both frequency criteria are satisfied. Other cost functions with various parameters can also be constructed; nevertheless, the simple quadratic function has shown good performance and stability in the test process. Therefore this function was chosen to perform the optimization for the setups discussed in the sequel. The best performance with respect to the speed of convergence of the optimization in the test process was achieved using weights with the ratio $w_1/w_n = 10$.

Evaluated cost function values are displayed in Figure 5.3 with the pipe diameter, the width and the height of the mouth kept constant ($D_\mathrm{P} = 79.00\,\mathrm{mm}$, $W_\mathrm{M} = 59.99\,\mathrm{mm}$, $H_\mathrm{M} = 25.66\,\mathrm{mm}$). The lengths of the pipe body and the chimney and the diameter of the chimney are optimized for $f_1 = 140\,\mathrm{Hz}$ fundamental frequency (at $T_0 = 20°\mathrm{C}$ tuning temperature) and perfect overlapping of the fifth harmonic partial ($n = 5$) with an eigenfrequency of the pipe. On the left panel the dependence of the cost function on the chimney and main resonator lengths is shown at fixed chimney diameter ($D_\mathrm{C} = 28.72\,\mathrm{mm}$), while on the right panel the dependence on chimney length and chimney diameter is presented with fixed main resonator length ($L_\mathrm{P} = 586.51\,\mathrm{mm}$).

local minima

As can be seen, the cost function can have more than one local minimum, which means that a simple gradient algorithm could get stuck without finding the global optimum. Compared to the simple iteration process, optimizing by means of the Nelder – Mead (simplex) technique requires considerably more computational effort, since the input admittance function needs to be calculated for the whole frequency domain of interest in each iteration step.

convergence

Depending on the starting point, 50–100 steps were always enough in the tests to find the optimum point, which took 2–4 s computational time on an average desktop computer. However, it is important to choose proper initial values of the variables for the algorithm. It is advisable to carry out the iteration process first with a fixed chimney diameter. The results of the first optimization can be then used as initial values for the optimization process with variable chimney diameter.

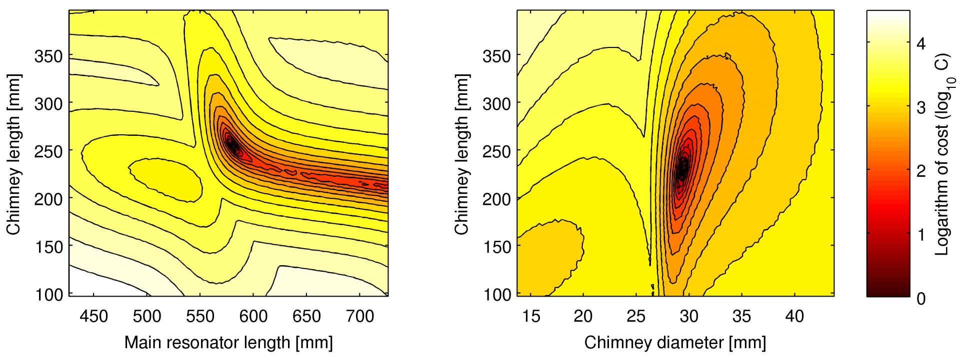

Figure 5.3. Contour plots of the cost function with fixed chimney diameter (left) and fixed main resonator length (right).

Figure 5.4 displays the original and optimized input admittance curves and the normalized modal waveforms of the example pipe. As it is seen, with the original scaling parameters, the 5^{th} partial was near to an input admittance minimum, which would mean the depression of that component. In the optimized case, the fifth harmonic is coincident with a local maximum of the input admittance, and hence its amplification can be expected. The modal waveforms clearly show the role of the chimney at the 3^{rd} and 4^{th} natural resonance frequencies. (In this example case 63 function evaluations were required to perform the optimization; the final residual cost was zero using $\Delta f = 0.5\,\text{Hz}$ frequency resolution and weights $w_1 = 10$ and $w_n = 1$.) effects of optimization

5.2.4 Relation to the perturbation method

An alternative approach for the examination of the effect of the pipe geometry on the eigenfrequencies of the pipe can be developed using *perturbation theory*. This approach has already been used by several authors for the investigation of *vocal tract* shapes. Schroeder [130] developed a perturbation method for vocal tract cross sectional area changes based on the Ehrenfest theorem [54]. Later, Story [134] has applied this technique successfully for "tuning" the area function of vocal tracts. He proposed an algorithm based on so-called *sensitivity functions* to match the natural resonance frequencies of the vocal tract to predefined values by changing the cross sectional area of the tract. This approach was extended by Adachi *et al.* [9] for the perturbation of the length of the tract applied for male–female vocal tract shape conversion. In the following the sensitivity-function-based technique is compared to the optimization algorithms introduced above. sensitivity functions

To establish the sensitivity functions the *Ehrenfest theorem* is used. The theorem states that if an oscillation system is excited in its nth eigenmode with the frequency f_n and energy E_n, then the ratio E_n/f_n remains unchanged as the system is perturbed in an "adiabatic" manner [54]. In case of organ pipes (or vocal tracts) "adiabatic" means that a large number of oscillation periods pass during the perturbation [9]. Thus, the change of the natural frequency δf_n can be calculated from the change of energy δE_n as

$$\frac{\delta f_n}{f_n} = \frac{\delta E_n}{E_n}. \tag{5.11}$$

Ehrenfest theorem

To evaluate the change of energy δE_n the so-called acoustic *radiation force* is used [23]. By means of the radiation force the work done by the adiabatic change is expressed and hence the change of energy in the system δE_n can be determined. The radiation force $P(z)$ for an impermeable wall is given as [130]

$$P_{\text{wall}}(z) = \text{PE}(z) - \text{KE}(z), \tag{5.12}$$

radiation force

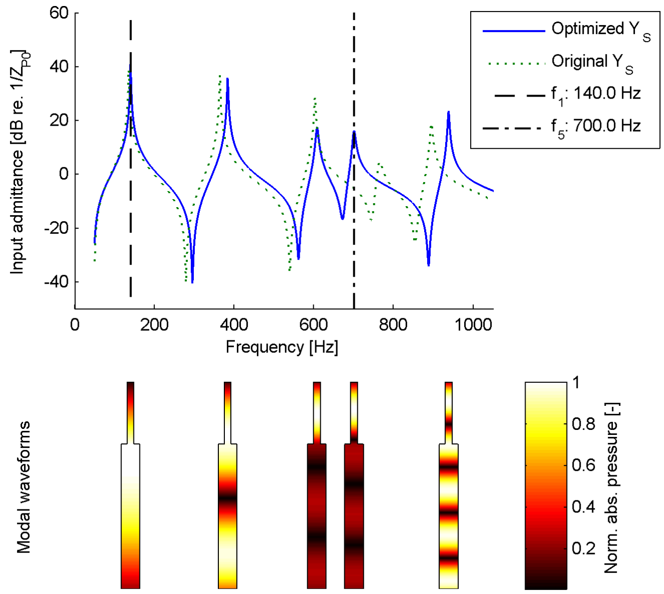

Figure 5.4. Optimization using the cost function. Comparison of the original and optimized input admittances (above). Modal waveforms corresponding to the eigenfrequencies of the optimized pipe (below).

where PE and KE denote the potential and kinetic energy densities, respectively, which are obtained as[1]

$$\mathrm{PE}(z) = \frac{1}{2}\frac{1}{\rho_0 c^2}\left\langle p^2(z,t)\right\rangle \tag{5.13a}$$

$$\mathrm{KE}(z) = \frac{1}{2}\rho_0\left\langle \frac{U^2(z,t)}{S^2(z)}\right\rangle, \tag{5.13b}$$

with $S(z)$ representing the area and $\langle\cdot\rangle$ denoting temporal averaging. For an opening located at the coordinate z_e the radiation force is attained as [9]

$$P_{\text{exit}} = \mathrm{TE}(z_e) = \mathrm{PE}(z_e) + \mathrm{KE}(z_e), \tag{5.14}$$

where TE is the total energy density.

The change of energy can be expressed from the radiation force. Here, we limit ourselves to the case of concatenated cylindrical ducts, such as chimney pipes. A more general discussion is found in [9, 130]. It is assumed that the geometry is composed of N_s cylindrical ducts, with area S_i, length L_i, occupying the regions $z_{i-1} \leq z \leq z_i$. $i = 1, 2 \ldots N_s$. The perturbation consists of changes of two kinds: (1) the change of the cross sectional areas, represented by δS_i, and (2) the change of the lengths of the sections, denoted by δL_i. The changes of energy due to area and length perturbations are found following [9] as

$$\delta E_n^{(S)} = \sum_{i=1}^{N_s} \delta E_{n,i}^{(S)} = -\sum_{i=1}^{N_s} \delta S_i \int_{z_{i-1}}^{z_i} P_n(z)\,\mathrm{d}z, \tag{5.15a}$$

$$\delta E_n^{(L)} = \sum_{i=1}^{N_s} \delta E_{n,i}^{(L)} = -\sum_{i=1}^{N_s} \delta L_i S_i \mathrm{TE}_{n,i}. \tag{5.15b}$$

[1]For the evaluation of the potential and kinetic energies the nonlinear Euler equation (3.9) must be dealt with. The derivation of equations (5.13) is found in [9].

The upper indices (S) and (L) refer to changes due to area and length perturbations, respectively. The notations P_n and TE_n denote that the radiation force and the total energy density are evaluated for the nth natural resonance. Since the total energy density $\mathrm{TE}_{n,i}$ is constant in each cylindrical section of the pipe, the integration boiled down to a multiplcation in (5.15b).

To apply the perturbation method for the optimization of the geometry it is useful to express the sensitivity functions for the area and length changes. The sensitivity functions $G_{n,i}^{(S)}$ and $G_{n,i}^{(L)}$ relate the relative change of the area and the length of the ith section, respectively, to the relative change of the nth natural resonance frequency. Using (5.15) we get

$$\frac{\delta f_{n,i}^{(S)}}{f_n} = \frac{\delta E_{n,i}^{(S)}}{E_n} = G_{n,i}^{(S)} \frac{\delta S_i}{S_i} \quad \Longrightarrow \quad G_{n,i}^{(S)} = -\frac{1}{E_n} S_i \int_{z_{i-1}}^{z_i} P_n(z)\,\mathrm{d}z, \tag{5.16a}$$

$$\frac{\delta f_{n,i}^{(L)}}{f_n} = \frac{\delta E_{n,i}^{(L)}}{E_n} = G_{n,i}^{(L)} \frac{\delta L_i}{L_i} \quad \Longrightarrow \quad G_{n,i}^{(L)} = -\frac{1}{E_n} L_i S_i \mathrm{TE}_{n,i}. \tag{5.16b}$$

length and area sensitivity functions

By means of the d'Alembert solution (5.4) the radiation force and the potential, kinetic, and total energies can be expressed and their integral for each cylindrical section can be evaluated analytically. Thus, the sensitivity functions in (5.16) are also obtained in an analytical manner.

An automatic optimization procedure for modifying the tract area function was introduced by Story [134] and has been extended for length modifications by Adachi *et al.* [9]. Here, the latter iterative algorithm is discussed briefly. Let us denote the normalized difference between the actual resonant frequency and the target frequency by ζ_n, using the same notations as above

$$\zeta_n = \frac{n f_1 - f_n^*}{f_n^*}. \tag{5.17}$$

The iterative update rule introduced by Adachi *et al.* [9] reads as

$$S_i^{(m+1)} = S_i^{(m)} \left(1 + \alpha \sum_{n=1}^{N_f} \zeta_n G_{n,i}^{(S)}\right) \qquad \text{for} \quad i = 1, 2, \dots N_s \tag{5.18}$$

$$L_i^{(m+1)} = L_i^{(m)} \left(1 + \beta \sum_{n=1}^{N_f} \zeta_n G_{n,i}^{(L)}\right) \qquad \text{for} \quad i = 1, 2, \dots N_s. \tag{5.19}$$

iterative algorithm

Here N_f denotes the number of eigenfrequencies to be tuned, the upper indices (m) and $(m+1)$ refer to the original and updated values in the mth iteration, respectively. The parameters α and β control the perturbation amplitudes of the area and the length, respectively, and are determined in an experimental manner to provide convergence. The algorithm of Adachi *et al.* implements constraints for the maximal length and the minimal area, and a limit that prevents the solution from becoming unnaturally discontinuous [9]. These constraints are not considered here.

In order to test the applicability of the sensitivity approach for chimney pipe optimization the iterative algorithm introduced above was implemented. In the following we focus on the simplest case of optimizing the length of the main resonator and the chimney, as already introduced in Section 5.2.2. In this case only (5.19) is used in the iterative algorithm. Starting from the given initial main resonator and chimney lengths, the sensitivity functions (5.16) are evaluated. The normalized differences ζ_n are obtained using (5.17) by evaluating the input admittance function and finding its corresponding peaks. Then, either the chimney or the main resonator length is updated, in an alternating manner, using the update rule given in (5.19). The same steps are repeated until ζ_n are all sufficiently small, or the maximum number of iterations is reached without convergence.

The results of the sensitivity-function-based iterative algorithm are discussed in the following for the pipe introduced above ($D_\mathrm{P} = 79.00\,\mathrm{mm}$, $D_\mathrm{C} = 28.72\,\mathrm{mm}$, $W_\mathrm{M} = 59.99\,\mathrm{mm}$, $H_\mathrm{M} =$

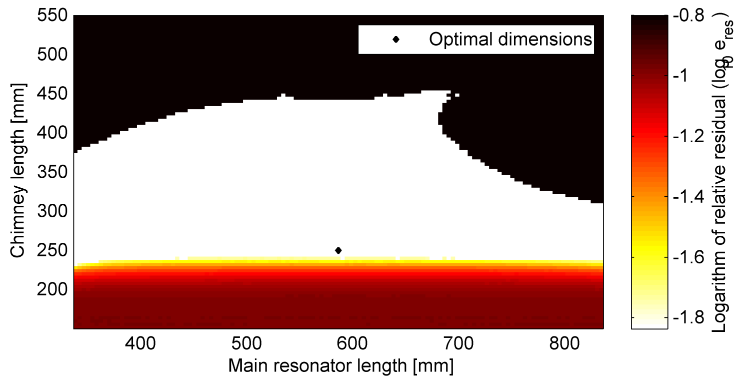

Figure 5.5. Convergence of the sensitivity-function-based approach for chimney pipe optimization

$25.66\,\mathrm{mm}$, and $T_0 = 20°\mathrm{C}$). The goal fundamental frequency was $f_1 = 140.0\,\mathrm{Hz}$ and the fifth harmonic partial was selected for amplification. Unlike in the case of the heuristic iterative algorithm and the cost function method discussed in the previous sections, it should also be determined *a priori* which eigenfrequency will amplify the selected partial to be able to use the sensitivity functions. Here, based on the results shown in Figure 5.4, the fourth eigenfrequency was selected. The critera of convergence were chosen as that both the first and the fourth eigenfrequency must differ lest than 25 cents ($< 1.5\%$) from the target frequencies. The maximal number of iterations was set as 25. Among a few values tried $\beta = 1$ seemed a reasonable choice providing fast convergence in a wide range of initial lengths.

Figure 5.5 shows the results of the optimization based on sensitivity functions for different initial main resonator and chimney lengths. The displayed residual is the maximum of the normalized errors, i.e. $e_{\mathrm{res}} = \max\{\zeta_1, \zeta_4\}$. As shown by the white area in the diagram, the algorithm provides convergence in a wide range of initial resonator and chimney lengths. It was found that convergence is obtained in less than ten iterations in the whole region of convergence. Depending on the starting point of the algorithm, different solutions are reached with resulting main resonator and chimney lengths in between $531.9\,\mathrm{mm} \leq L_{\mathrm{P}} \leq 600.5\,\mathrm{mm}$ and $238.5\,\mathrm{mm} \leq L_{\mathrm{C}} \leq 448.6\,\mathrm{mm}$, respectively; with longer chimneys going with shorter main resonators and *vice versa*.

Interestingly, the optimum point found by the heuristic iterative algorithm (marked by the black diamond marker in Figure 5.5) is not near the center of the region of convergence, as far as the initial length of the chimney is considered. When the initial chimney length is much greater than the optimal, convergence is still reached; however, if the initial chimney length is decreased a little, the iteration no longer converges. In particular, the initial guess for the chimney length given by equation (5.9), which is $L_{\mathrm{C}}^{(0)} = 204.49\,\mathrm{mm}$ in this case, is out of the region of convergence. Apparently, as the initial chimney length is increased, the residual abruptly increases after a certain point; whereas if the initial chimney length is decreased, the residual increases in a gradual manner in a narrow region. When convergence is not reached the algorithm gets stuck around a suboptimal solution and the residual ceases to decrease after a few iterations.

The heuristic iterative method introduced in Section 5.2.2 provides convergence in the whole region shown in Figure 5.5 with a maximum of eight iterations and tends to the same optimal result in the whole region. Since this iterative method does not require the evaluation of sensitivity functions, it is much more efficient computationally. From these results, it can be assessed that the performance of the sensitivity approach in its current form is inferior compared to the heuristic iterative algorithm for chimney pipe length optimization. It can be argued that the sensitivity-based approach can be improved or optimized for the special case of chimney pipe optimization; however, such examinations are out of the scope of the study presented in this chapter.

Parameter	Value	Parameter	Value
Pitch	C3 (131 Hz)	Tuning temperature (T_0)	23 °C
Resonator length* (L_P)	600 mm	Material	75% tin, 25% lead
Inner diameter* (D_P)	79 mm	Wall thickness	0.9 mm
Mouth width* (W_M)	60 mm	Length of foot	200 mm
Mouth height* (H_M)	19 mm	Languid thickness	6 mm
Chimney length* (L_C)	180 mm	Languid angle	70°
Chimney inner diameter* (D_C)	19 mm	Flue width	0.8 mm

*Parameters used for the optimization process

Table 5.3. Design parameters of the reference pipe.

Name (optimized for ...)	A2 (3rd)	A3 (3rd)	B4 (4th)	C5 (5th)
Main resonator length [mm]	564.0	576.7	742.9	852.5
Chimney length [mm]	193.3	118.0	99.1	51.1
Inner diameter of chimney [mm]	10.7	14.3	29.4	29.3

Table 5.4. Optimized dimensions for the four experimental pipes

5.3 Sound design of experimental chimney pipes

5.3.1 Laboratory measurements of optimized pipes

The applicability of the optimization algorithm was tested by designing chimney pipes to conform to the desired sound spectra. As a starting point a design by an organ builder (Werkstätte für Orgelbau Mühleisen, Leonberg, Germany) was selected. The dimensions of a 4′ C3 chimney pipe[2] were applied as initial data for the optimization process. The dimensions of this reference pipe are given in Table 5.3. reference pipe

The parameters marked by * in Table 5.3 can be used for the optimization process. At first, the general properties of chimney pipes were studied by means of the optimization software. It was found that three different sorts of chimneys may be used for optimization: (1) thin and medium long chimneys ($L_C \sim \lambda/15$, $D_C < 2D_P/7$), (2) short and medium wide chimneys ($L_C \sim \lambda/20$, $2D_P/7 < D_C < 2D_P/5$), and (3) long and wide chimneys ($L_C > \lambda/12$, $D_C \sim D_P/2$).

For the comparison measurements three dimensions of the pipes, which cannot be changed easily in practice (i.e. the inner diameter of the pipe, the mouth width and the cutup) were fixed. Optimizations by the remaining three free parameters led to nine different musically meaningful scenarios: the pipe was optimized for the third, fourth, fifth (twice), sixth and seventh partial and three times for two neighboring partials (fourth–fifth, fifth–sixth, sixth–seventh).

In order to test the optimization, one reference pipe and three experimental pipes (pipes A, B and C) were built with different body lengths but the same inner diameter, mouth width and cutup. Adjustable plugs, designed to hold the chimneys and mount them in the corresponding pipe, were fabricated for each chimney diameter given by the optimization. Thus, ten plugs were made, one for the reference pipe and nine for realizing the nine different scenarios. These plugs provide a tight mount of the chimneys in the pipes with the possibility of adjusting the active length of the main resonator. The full lengths of the main resonator of pipes A, B, and C are 723, 812, and 883 mm, respectively. The four optimized set of dimensions given in Table 5.4 are selected from the nine scenarios for presenting the results of the comparison measurements. test pipes

[2]Here and in the sequel pitches are numbered using the *scientific pitch notation*.

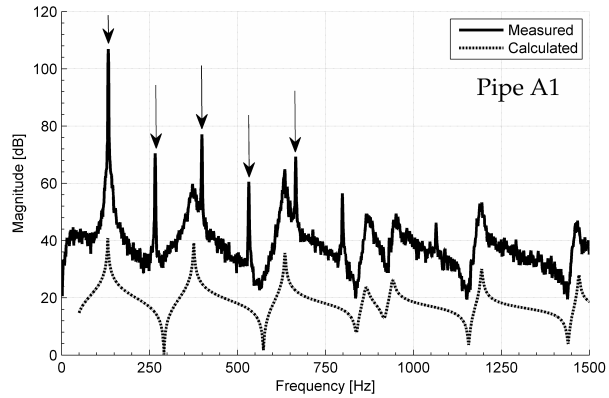

Figure 5.6. Comparison of the measured sound pressure spectrum to the calculated input admittance curve of the reference pipe A1. (The first five harmonic partials are marked by arrows.)

test setup

The experiments were performed in the following way. First, the dimensions of the reference pipe were adjusted to the values given in Table 5.3, and the pipe was tuned and voiced at $700\,\mathrm{Pa}$ wind pressure in the windchest to $131\,\mathrm{Hz}$ frequency and to a proper attack of the sound. Then pipes A, B, and C were adjusted to the same dimensions and were voiced also to the same frequency and sound at $700\,\mathrm{Pa}$. From this point on, the dimensions and the voicing setup of the pipes were kept constant during the experiments.

tuning and voicing

The results of the optimization process were tested by adjusting the dimensions of the experimental pipe to the values calculated by the optimization process. The pipe was placed on the windchest beside the reference pipe, and the resonator length was modified slightly until the same frequency was obtained. This tuning was achieved by minimizing the beating between the pipes. This step was necessary, because the recorded sounds of the nine experimental pipes and of the reference pipe were intended to be used for subsequent subjective evaluation.

sound recordings

The sound of the pipes were measured in the anechoic room of the Fraunhofer Institute for Building Physics (IBP) by two microphones, located close ($50 \pm 5\,\mathrm{mm}$) to the mouth and the open end of the chimney, respectively. A third microphone was placed at a distance of $2\,\mathrm{m}$ from the pipe, in order to record the sound for listening tests. The microphone signals were recorded in a PC using an 8-channel 16-bit sound card (RME Hammerfall DSP).

The recorded signals of the three microphones were analyzed by a `Matlab`-based in-house sound analysis software tool (see Appendix A). The measured sound spectra and the calculated optimized input admittance funtions of the reference pipe and the four selected experimental pipes are shown and discussed in the next section.

5.3.2 Validation of admittance calculations with spectrum measurements

The spectrum of the sound pressure measured near the mouth of the reference pipe (pipe A1) and the input admittance calculated from the dimensions of the pipe are shown in Figure 5.6. For all following figures the vertical scale is given in dB sound pressure level (SPL). The amplitude of the admittance curve is also measured in dB, and is shifted to match the spectrum.

admittance and spectrum

As can be seen in Figure 5.6 the significant curve progression of the measured sound pressure spectrum matches the calculated input admittance curve very well; the frequency positions of the maxima and minima are the same and the profile of the admittance curve follows almost exactly the baseline of the spectrum. The only difference is that the maxima and minima of the admittance curve are sharper than that of the measured spectrum. It means that the real losses in the chimney pipes are larger than the calculated ones. This problem will be discussed in more detail later. Harmonic partials can be found in the sound spectrum as sharp peaks (marked by arrows in Figures 5.6–5.10). These lines are not present in the calculated admittance, because sustained oscillations cannot be treated by the applied acoustic model.

It can be seen in Figure 5.6 that the third and the fifth harmonic partials have higher frequency than the closest eigenfrequencies. Therefore, these partials are not amplified effectively; the sound is dominated by the fundamental component. The second strongest component, which is the third partial, is more than $30\,\mathrm{dB}$ weaker than the fundamental. The total sound pressure level L_p was measured as $108.7\,\mathrm{dB}$ at the pipe mouth. pipe A1

Pipe A2 was optimized for the third partial. The input admittance curve, resulted by the optimization process and the measured sound spectrum are shown in Figure 5.7. The overlapping of the third partial with the second eigenfrequency is perfect, and the third eigenfrequency is shifted closer to the fifth partial. As a result, the third partial becomes about $15\,\mathrm{dB}$ stronger than before. The fifth partial is also stronger now by about $5\,\mathrm{dB}$. The total sound pressure level is also higher, it has increased to $L_p = 111.2\,\mathrm{dB}$. pipe A2

The next pipe (B4), was optimized to the fourth partial. The corresponding spectrum and input admittance curve are shown in Figure 5.8. The optimization process was also entirely successful in this case. The perfect overlapping of the third eigenfrequency with the fourth partial has resulted in a significant enhancement of the fourth partial. Due to the quite large downward shift of the eigenfrequencies, the third and fifth partials are located now in the "valleys" and are very weak therefore. The sound spectrum is very different from the spectra of pipe A1 (Figure 5.6) and pipe A2 (Figure 5.7); while those can be characterized by strong odd partials, the third and fifth partials in the spectrum of pipe B4 (Figure 5.8) are weak. pipe B4

The next example is the optimization of the experimental chimney pipe to the fifth harmonic partial. This goal can be achieved by bringing the third eigenfrequency to overlap with the fifth harmonic partial. This solution was described in [86] and the corresponding spectrum and input admittance curve of our laboratory experiments are shown in Figure 5.9. In this case, even though the pipe is optimized for the fifth partial, the third partial will also be strong, sometimes even stronger than the fifth partial. Therefore, in order to arrive at a strong fifth harmonic partial and a considerably weaker third, another possibility for the optimization was also explored, as discussed in the next paragraph. pipe A3

The calculated input admittance curve and the measured sound spectrum of pipe C5 can be seen in Figure 5.10. In this case the eigenfrequencies are shifted further downwards; the fourth eigenfrequency is brought to overlap with the fifth partial. As a consequence, the fifth partial is enhanced. However, the second partial is also stronger, both partials have increased by about pipe C5

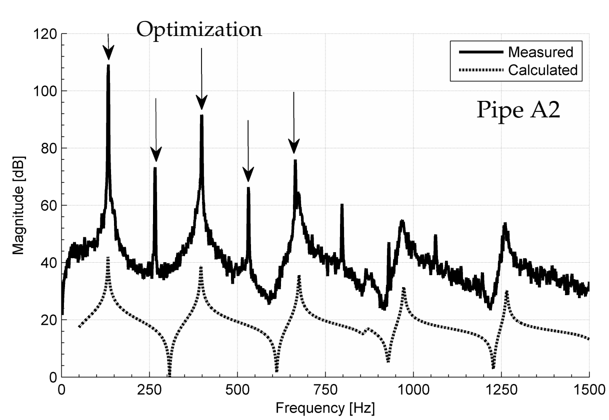

Figure 5.7. Comparison of the measured sound pressure spectrum to the calculated input admittance curve of pipe A2. (Harmonic partials are marked by arrows.)

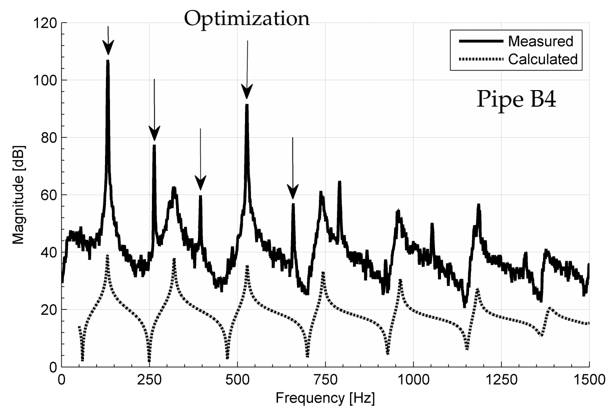

Figure 5.8. Comparison of the measured sound pressure spectrum to the calculated input admittance curve of pipe B4. (Harmonic partials are marked by arrows.)

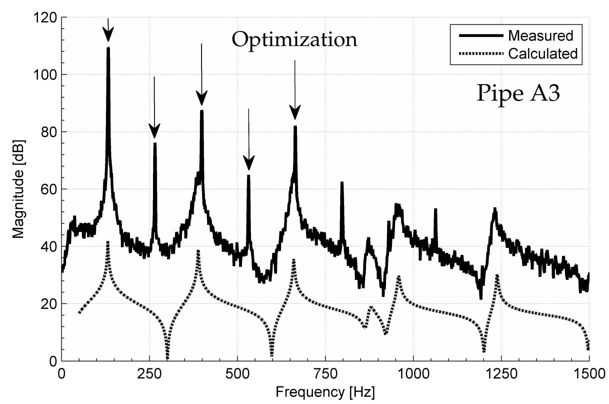

Figure 5.9. Comparison of the measured sound pressure spectrum to the calculated input admittance curve of pipe A3. (Harmonic partials are marked by arrows.)

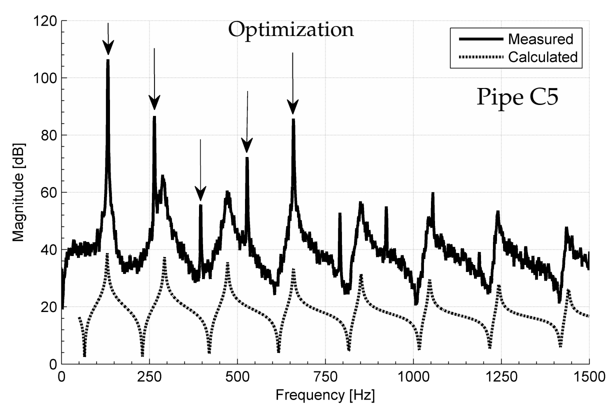

Figure 5.10. Comparison of the measured sound pressure spectrum to the calculated input admittance curve of pipe C5. (Harmonic partials are marked by arrows.)

	A2 – A1	A3 – A1	B4 – A1	C5 – A1
Partial	SPL diff. [dB]	SPL diff. [dB]	SPL diff. [dB]	SPL diff. [dB]
1st	1.6	1.4	2.4	2.1
2nd	2.9	2.2	−19.9	9.5
3rd	15.7	10.5	8.7	−21.3
4th	6.4	4.6	26.2	9.7
5th	5.5	11.8	−12.3	16.8
6th	6.7	6.3	9.4	−3.8

Table 5.5. Sound level differences of the partials of the optimized pipes compared to the reference pipe A1.

15 dB in comparison to the reference pipe. On the other hand, the third partial, which was the second strongest one in the steady state spectrum of the reference pipe and in that of pipe A3, becomes very weak. Therefore, the character of the sound has changed significantly.

5.4 Results of the initial listening experiments

As mentioned earlier, the measurements were carried out in the anechoic chamber of the IBP. Simultaneously with the recordings at the mouth and chimney end, the sound of the chimney pipes were recorded by a third microphone, located at 2 m distance from the pipe. These recordings are intended for listening tests, but they were also analyzed. Sound level differences of the first six partials of the optimized pipes and the reference pipe A1 are summarized in Table 5.5.

sound samples

The enhancement of the targeted partials due the optimization can also be observed in the far field spectra. Such large changes in the levels of partials are probably well audible. Therefore, sound samples of pairs of recordings were prepared. The attack was removed by applying a two-second-long fade-in at the beginning of the recordings so that the listeners could focus solely on the properties of the steady state sound. Samples of pairs were prepared by the faded-in recordings of the reference pipe A1 and the optimized pipes A2, A3, B4, C5, A6, B7, A8, and B9. Since the prepared recordings sound quite strange, the listener should be familiar with the sound of chimney pipes and should be able to distinguish different partials in the pipe sound. Therefore, two experienced voicers were asked to perform the listening test.

pipes A1–A3

The results of a listening test performed by the well known voicers Konrad Mühleisen (KM) and Johannes Kirschmann (JK) are summarized as follows. Both voicers found the two sounds of the pairs very different. The reference sound A1 was described with a very strong fundamental (KM) with the major fifth (third partial) is also audible (JK). Both voicers could hear the significant increase of the major fifth in the sound A2. JK noticed an increase of the major third (fifth partial) as well. The judgment of sound A3 was similar for both listeners; they heard the increase of the major fifth and major third. Both of them described the fifth to be stronger than the third.

pipe B4

The large increase of the level of the fourth partial (second octave) was clearly audible for both voicers in case of pipe B4. JK identified the more enhanced component correctly as the second octave of the fundamental, while KM heard an enhanced major fifth. They also noticed the increase of higher partials; KM heard a weak minor seventh (seventh partial), while JK noticed a weak major third (fifth partial) in the sound. But according to the measurements the levels of the sixth and ninth partials have increased from A1 to B4.

pipe C5

The judgements of the voicers about the A1–C5 pair were contradictory; while JK heard an increase of the major third (fifth partial), KM noticed a strong major fifth (third partial). The voicers' opinions on the listening tests of the other pipe pairs are summarized later in form of a conclusion of the main results.

The voicers can always identify the increase of higher partials in the sound, but in spite of their 30–40 years experience they cannot unambiguously identify which partials have been enhanced. They quite often confuse harmonic partials. On the other hand, they notice the occurrence or enhancement of a partial even when its level is 30–40 dB below of the level of the fundamental.

applicability of the method

Both voicers found the method of chimney pipe optimization as very promising for organ building. Since chimney pipes in the baroque style pipe organs should have a sound rich in major fifth, while romanticism requires more major third in the sound, a method which helps organ builders in the design and dimensioning of their chimney pipes to the desired character of sound, would facilitate their work. Thus, it would be very useful and could clearly find application in the everyday practice of organ building.

5.5 Discussion and concluding remarks

The experimental results presented in the previous section show a very good agreement between the sound pressure spectra, measured in the vicinity of the mouth of the pipe, and the calculated input admittance curve. However, the maxima and minima of the input admittance curve are sharper than the maxima and minima in the baseline of the measured spectrum. The reasons of this discrepancy are that the acoustic losses of the pipe are underestimated and no noise is considered in the admittance calculation. Only wall losses (viscous and thermal) and the radiation loss at the chimney end have been taken into account in the calculations. The radiation loss at the mouth and sound absorption in the air inside the pipe have been neglected.

Because of the quadratic dependence of the neglected losses on frequency, a gradual loss increase, consequently a broadening of the maxima and minima of the admittance curve with increasing frequency may be expected in the calculated input admittance. The presented optimization method can be successfully applied to tune the eigenfrequencies of the pipe; but it is less effective in determining the relative strengths of the eigenmodes. This drawback might be corrected by incorporating all absorption and radiation losses into the optimization algorithms.

The proposed heuristic iterative algorithm was also compared to an alternative optimization approach that is based on the perturbation method and sensitivity functions and has already been applied successfully by other authors for vocal tract shape optimization. It was found that the heuristic technique provides better computational efficiency and a wider region of convergence for the optimization of the length of the main resonator and the chimney than the sensitivity-function-based algorithm.

In the steady state the acoustic excitation and the losses of the pipe are in equilibrium. It means that the acoustic power supplied by the interaction of air flow from the flue with the sound field in the vicinity of the upper lip equals the acoustic loss at each harmonic partial of the pipe. Since the excitation of labial organ pipes can be effectively manipulated in practice by the traditional methods of voicing adjustment, skilled voicers can influence the strengths of the partials to some extents by changing the direction of the air jet at the labium and by modifying the jet velocity at the upper lip as a part of the voicing procedure. In such way, the voicer may enhance the desired harmonic partial by skillful voicing manipulations. When this partial is already enhanced by a natural resonance of the pipe, less voicing effort is needed for achieving the desired sound quality.

The last fine adjustment of the sound character of organ pipes is usually performed *in situ* after completing the building and mounting of the pipe organ in the acoustic space. Voicing is not merely a handicraft, but an artistic activity that provides the unique sound quality of pipe organs. Therefore, its role in pipe organ building has to be maintained, preserved, and facilitated by scientific design methods. The optimization method of chimney pipes presented in this chapter perfectly fulfills the latter purpose.

Chapter 6

Experimental examination of the acoustic behavior of tuning slots

The effect of tuning slots on the sound characteristics of labial organ pipes is investigated in this chapter by means of laboratory experiments. Besides changing the pitch of the pipe, the tuning slot also plays an important role in forming the timbre. The objectives of this contribution are to document the influence of tuning slots built with different geometries on the pipe sound and to validate the observed tendencies by means of reproducible experiments. It is found that the measured steady state sound spectra show unique characteristics, typical only of tuning slot organ pipes. By separately adjusting the geometrical parameters of the tuning slots on experimental pipes, the impact of each scaling parameter on the steady state spectrum is determined. It is shown that the scaling procedures used currently in organ building practice do not provide sufficient control over the sound characteristics, leaving the capabilities provided by the tuning slot unexploited. Subjective comparison made by organ builders of sound recordings of various setups confirms that the observed sound quality of pipes equipped with a tuning slot is strongly dependent on the physical dimensions of the slot. This chapter is a revised and extended version of the paper [J3].

6.1 Introduction

The *tuning slot* (or *Expression* in German) is a tuning device mostly used by narrow scaled open labial pipes (such as *salicionals* or narrow *gambas*); however, sometimes they are applied to wider *diapason* pipes as well. These slots are generally located near the open end of the pipe, as it is shown on the left hand side of Figure 6.1. When the opening is cut into the pipe, organ metal is usually rolled up at the bottom of the slot in order to make the pipe tunable. This tuning device not only affects the pitch of the pipe, it also has a great influence on the character of the sound. The sound of tuning slot pipes is usually identified by their "softer", less "harsh" timbre. Discussions with organ builders during the cooperative research projects supported by the European Commission [2] have indicated that no generally accepted method exists for designing tuning slots. Neither does the current design practice provide control over the timbre of the pipe. Therefore, the partners of the project have initiated scientific investigations on this topic. tuning slots

There are three design parameters of rectangular tuning slots: the width and the height of the slot and the length of the pipe above the slot. These three parameters are denoted in the following by w_S, h_S, and L_S, respectively. There are very few written sources in pipe organ literature containing design rules of tuning slots. The book by Ellerhorst [57, pp. 211–212] briefly mentions tuning slot design and suggests the dimensions $w_S/D_P \approx 1/2$ and $h_S/D_P \approx 1$, with D_P design parameters

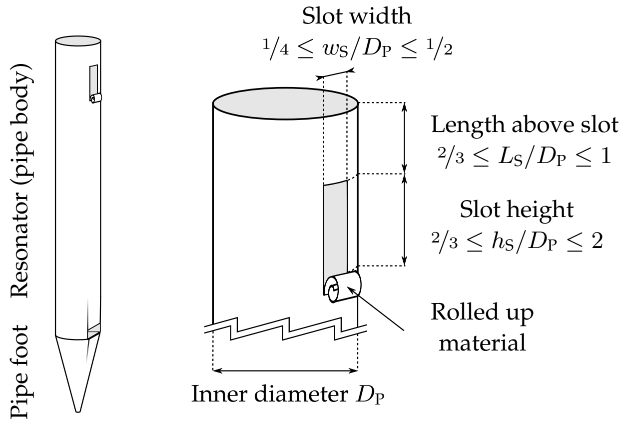

Figure 6.1. Schematic of a labial organ pipe with tuning slot (left) and the general rules of tuning slot design used currently in practice by German organ builders (right).

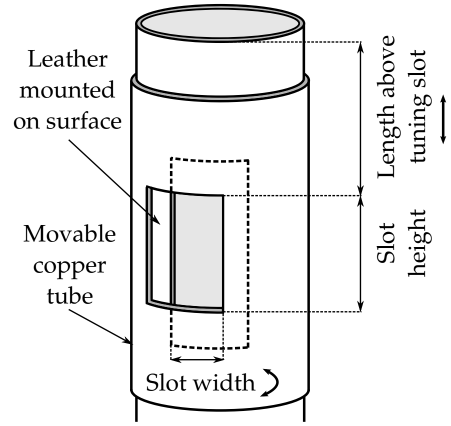

Figure 6.2. Adjustable tuning slot

denoting the inner diameter of the pipe. Two further sets of rules, both of which are currently used by well-known German organ building companies, are also given here as examples.[1] The set of rules of the first company is: $1/3 \leq w_S/D_P \leq 2/5$, $h_S/D_P \approx 2$, and $L_S/D_P \approx 2/3$. The rules of the second company are only slightly different: $1/4 \leq w_S/D_P \leq 1/2$, $2/3 \leq h_S/D_P \leq 1$, and $3/4 \leq L_S/D_P \leq 1$. Both companies use wider slots (relative to the diameter) for stops with wider scaling. The design rules mentioned above are summarized on the right hand side of Figure 6.1.

As will be shown later, the parameters of the slot should vary with the desired timbre and not depend only on the pipe diameter. To the best knowledge of the author the acoustic behavior of objective tuning slots of labial organ pipes has remained undocumented in the scientific literature so far. Therefore the objective here is to investigate the acoustic effects of the tuning slot as well as the influence of its design parameters on the sound.

6.2 Experimental methodology

6.2.1 Experimental pipes

All laboratory measurements were carried out on three different experimental pipes. The reference pipe, a narrow open labial pipe without tuning slot, was used in order to demonstrate the sound spectrum differences between pipes with and without tuning slots. Pipe #1 was built with a fixed tuning slot and the pipe wall rolled up at the lower edge of the slot (as shown in Figure 6.1). The length above the tuning slot L_S could be changed by attaching sleeves with different lengths to the pipe. This pipe was used for investigating the effect of L_S on the sound spectrum. Experimental pipe #2, designed for investigating the effect of slot size and slot position on the adjustable frequency, was mounted with an adjustable tuning slot. An external copper tube with a fixed tuning slot sized slot was pulled over the original pipe, partly covering a rectangular opening cut into the pipe wall, as it is illustrated in Figure 6.2. Under the copper tube the pipe body was covered with a thin layer of leather in order to provide a perfect fit of the two elements and a tight seal between them. The height of the slot was adjustable by partly covering the slot on the copper tube, whereas the width of the slot was tuned by rotating it. The position of the tuning slot was adjusted by sliding the copper tube vertically. The reference pipe and experimental pipe #1 were mounted with beards on the sides of the pipe mouth. The ratio of the inner diameter and the

[1]Since these rules are secrets of each organ building company, the names of the companies are not mentioned.

Parameter	Symbol	Values [mm]		
Pipe	–	Ref.	#1	#2
Resonator length	L_{P}	917	727	858
Tone length	L_{T}	917	644	693–738
Inner diameter	D_{P}	49.6	35.1	35.0
Wall thickness	T_{W}	1.3	0.7	1.0
Mouth widht	W_{M}	41.0	28.4	27.0
Total cutup height	–	9.6	7.0	7.0
Free cutup height	H_{M}	6.5	4.9	5.0
Slot height	h_{S}	N/A	60.6	5–45
Slot width	w_{S}	N/A	7.5	8–18
Fundamental [Hz]	f_1	169.5	234.2	207.0
Effective length [mm]	L_{eff}	1014.7	734.4	834.8
Scaling [–]	$D_{\mathrm{P}}/L_{\mathrm{P}}$	0.0541	0.0545	0.0505

Table 6.1. Dimensions of the experimental pipes

tone length (diameter scaling) of the reference pipe and experimental pipe #1 is almost the same, while the diameter scaling of experimental pipe #2 varies with the variable tone length. The scaling of mouth width and cutup are the same for all pipes: mouth width to circumference $\approx 1/4$, cutup to mouth width $\approx 1/4$. The physical dimensions of the experimental pipes are displayed in Table 6.1.

The parameters given in Table 6.1 are interpreted as follows. The pipe length L_{P} is the length of the pipe body from the languid to the open end of the pipe. The tone length L_{T} is the distance between the languid and the lower edge of the tuning slot. The total cutup height H_{M} is the distance of the lower and upper lips, i.e. the total height of the pipe mouth. Since the bottom part of this area is partly covered by the languid from inside, the free cutup height H_{MF} is used as the effective height of the mouth opening. The fundamental frequencies were determined using the default settings of the pipes.[2] Since the resonator is open at the mouth and at the open end (and at the tuning slot, if applicable), the *effective length* of the pipe is defined as half of the wavelength corresponding to the fundamental frequency. The diameter to tone length ratio $D_{\mathrm{P}}/L_{\mathrm{T}}$ is a key property of the scaling since it influences the most important acoustic characteristics of the resonator, such as stretching of the natural resonance frequencies (eigenfrequencies), quality factors of resonances and the radiated sound power [102]. Therefore, to be able to compare the sound characteristics with each other, it is desirable to have the $D_{\mathrm{P}}/L_{\mathrm{T}}$ ratios as close as possible. As it is seen in the last row of Table 6.1, the reference pipe and experimental pipe #1 fulfill this criterion.

effective pipe length

6.2.2 Measurement and analysis tools

All measurements were carried out in the anechoic room of the Fraunhofer Institute for Building Physics (IBP). Figure 6.3 gives an overview of the experimental setup. The air supply from a blower provided 686 Pa (equivalent to 70 mm water gauge) pressure in the windchest on which the experimental pipes were placed. This pressure was controlled by means of a pressure sensor (type 163PC01D36, Honeywell Sensing and Control) which was connected to the windchest by a tube. The signals were recorded using two 1/2″ B&K 4165 condenser measurement microphones, located at a distance of 50 ± 5 mm from the corresponding openings. In case of the reference pipe, one microphone was located near the mouth and the other one near the open end, while in case of the other two pipes they were placed near the mouth and the tuning slot, respectively.

sensors

[2] In case of experimental pipe #2 the configuration $w_{\mathrm{S}} = 16$ mm, $h_{\mathrm{S}} = 30$ mm, and $L_{\mathrm{S}} = 97$ mm was chosen as a representative setup.

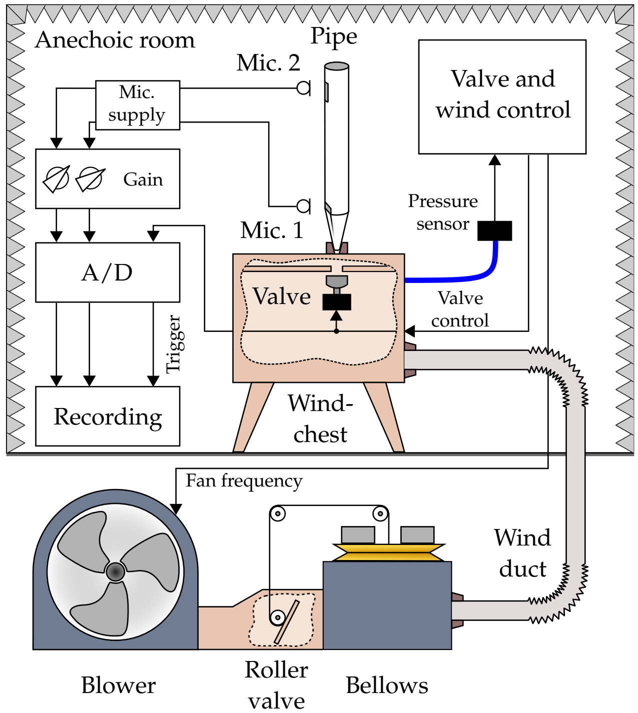

Figure 6.3. Measurement setup

The microphones were calibrated by means of a B&K 4230 sound level calibrator and supplied by a B&K 2804 type microphone power supply. The microphone signals were amplified by an AMSELEC electronic signal conditioning system with a gain adjustable in 10 dB steps. The amplified microphone signals were digitized by a Data Translation Simultaneous A/D card using 50 kHz sampling frequency. Two-channel recordings were saved into standard wave files for subsequent spectral analysis. Each recording took ten seconds and was triggered by the valve control signals, as depicted in Figure 6.3. The analysis of all recordings was performed using the tool `SoundAnalysis` (see Appendix A). Four seconds of the steady state sound were cut out from each recording. The fundamental frequency f_1 was determined from this stationary part with ± 0.02 Hz accuracy. After the detection of the fundamental frequency the signal was resampled using a sampling frequency $f_s = 64 f_1$. This resampling ensured coherent sampling of the harmonic partials. Then, the steady state spectrum was calculated by means of a FFT, using 4096 sample points, a Hanning window function and 85% overlapping of the time windows. The overlapping spectra were averaged, providing $60 \leq N_A \leq 100$ averages depending on the fundamental frequency. This resulted in an excellent noise reduction while avoiding spectral leakage and picket fence effects at the same time.

recordings

analysis

6.3 Experimental results

6.3.1 The effect of the tuning slot on the sound characteristics

To be able to demonstrate the effect of the tuning slot on the sound spectrum of the pipe, the sound spectra of the reference pipe and experimental pipe #1 were compared. Sound samples were recorded at the labium and the open end of both pipes as well as near the tuning slot

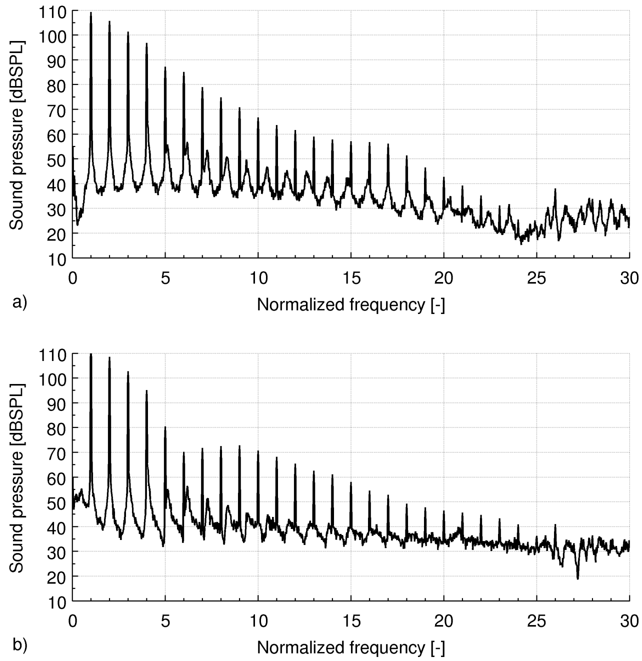

Figure 6.4. Steady state sound spectrum of the reference pipe. a) open end. b) pipe mouth.

of experimental pipe #1. Direct comparison of the measured spectra was difficult, because the fundamental frequencies of the pipes were different (169.5 and $231.6\,\mathrm{Hz}$, respectively). Therefore, the *normalized frequencies* (see p. 12) are shown in Figures 6.4 and 6.5.

reference spectrum

Sound spectrum of the reference pipe are shown in Figure 6.4. In the spectrum measured at the pipe mouth (Figure 6.4b), there is a local minimum located at the 6^{th} partial. This phenomenon is common for open labial organ pipes without tuning slot, as shown by Miklós & Angster [101]. In the spectrum measured at the open end (Figure 6.4a) such a minimum can not be seen, the amplitude of the partials is slowly decaying. Both at the mouth and at the open end more than twenty partials are distinguishable. In both spectra the fundamental is the strongest component. The equivalent sound pressure levels are $114.4\,\mathrm{dBSPL}$ at the open end and $116.9\,\mathrm{dBSPL}$ at the mouth.

spectra of pipe #1

Figure 6.5 shows the measurement results of experimental pipe #1 with $h_{\mathrm{S}} = 30\,\mathrm{mm}$ and $L_{\mathrm{S}} = 48\,\mathrm{mm}$, attained by covering $30\,\mathrm{mm}$ from the top of the slot. For experimental pipe #1 the octave is about $3\,\mathrm{dB}$ stronger than the fundamental in all three recordings. There are much more similarities between the spectra of the open ends of both pipes than between the spectra of the mouth openings. Contrary to the case of the reference pipe, there is no minimum among the first few partials in the spectrum measured at the mouth (see Figure 6.5c). The latter spectrum and the spectrum at the open end (Figure 6.5a) are quite similar. The spectrum measured at the tuning slot (Figure 6.5b) is remarkably different from the spectrum measured at the open end or at the mouth of both pipes. A quasi-periodic structure of the partials is seen with the 10^{th} and 19^{th} partials having local minimal amplitude. The amplitude difference of neighboring partials near these minima is up to $20\,\mathrm{dB}$. The equivalent loudness levels are 114.1, 112.8, and $109.5\,\mathrm{dBSPL}$ for the mouth, tuning slot, and open end recordings, respectively.

tuning slot spectrum

Some of the natural resonance frequencies (eigenfrequencies) of both pipes can also be identified from the spectrum by the broad resonance profiles in the spectral baseline.[3] The observed

[3] The relation of the spectral baseline and natural resonance frequencies were already examined in Section 3.5, see Figure 3.4 and the corresponding discussion. The same approach is utilized here.

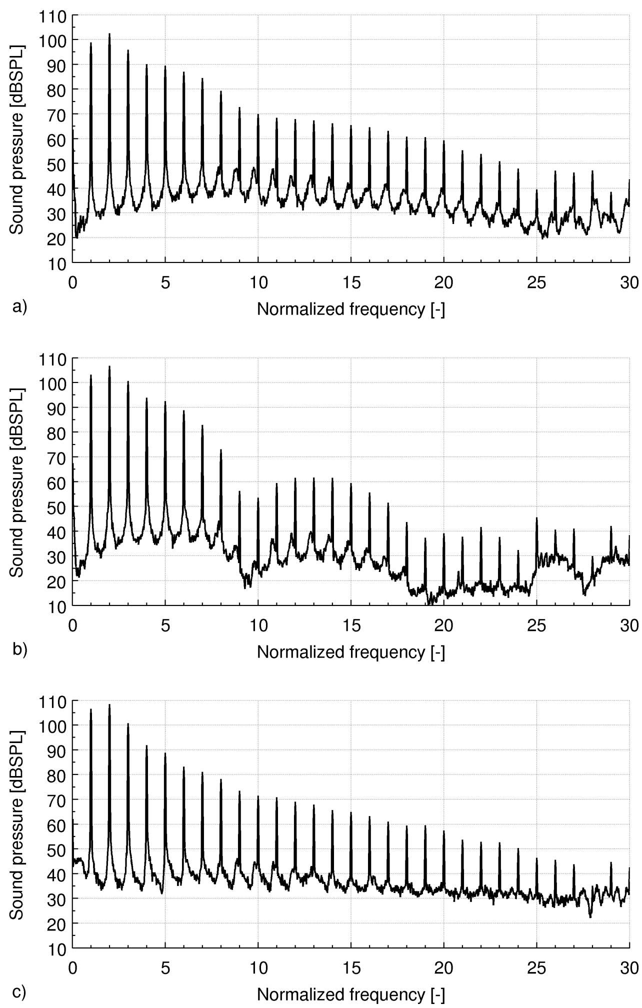

Figure 6.5. Steady state sound spectra of experimental pipe #1 with the setup $h_S = 30\,\mathrm{mm}$, $w_S = 7.5\,\mathrm{mm}$, and $L_S = 48\,\mathrm{mm}$. Measured at a) open end, b) tuning slot, c) pipe mouth.

spectral behavior of tuning slot pipes can also be better understood by examining the natural resonance frequencies of the pipe. Taking the spectra at the open end (Figure 6.4a and Figure 6.5a) it is seen that the first few eigenfrequencies are very near to the harmonic partials in both cases. However, the behavior of higher eigenfrequencies is significantly different. For the reference pipe a slight stretching of the successive eigenfrequencies is observable[4] which means that the inharmonicity of the natural frequencies of the pipe is slowly increasing with the frequency. This phenomenon is characteristic of open labial pipes [102]. Contrariwise, for experimental pipe #1 (and also for all other configurations with tuning slot presented here), the natural resonance frequencies are compressed instead of stretched; and their inharmonicity appears abruptly, as it can be seen in the spectral baseline between the 8^{th} and 11^{th} partial in Figure 6.5. Due to the inharmonicity, the resonator cannot amplify the corresponding partials effectively, and therefore the amplitudes of the partials drop quickly within this narrow region.

eigenfrequency structure

The characteristics described above for experimental pipe #1 are typical only of tuning slot pipes, and all the tuning slot pipes examined have shown a similar spectral behavior. These typical properties are summarized as follows.

[4]See Figure 3.4(b) for a detailed view of the same pipe.

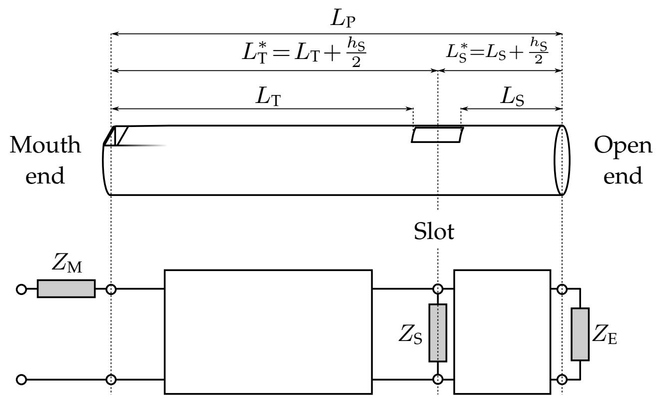

Figure 6.6. Simplified one-dimensional model of the resonator of a labial pipe with tuning slot

1. Tuning slot pipes show a compression of the successive natural frequencies compared to the harmonic partials in the middle harmonic region, instead of the typical stretching in the case of labial pipes without tuning slots.

2. The inharmonicity of the natural resonance frequencies can change more abruptly than in case of pipes without tuning slot. This can result in a quick drop of the amplitudes of harmonic partials in the first inharmonic region. This quick drop is best observable in the spectrum measured near the tuning slot.

3. A quasi-periodic behavior can be observed in the envelope of the partials' amplitudes (the so-called *formant structure*) as well as in the base line (see Figure 6.5b). The background of this phenomenon is addressed in Section 6.3.3.

6.3.2 A simplified one-dimensional model of the tuning slot pipe

For the interpretation of the results presented in the sequel, a simplified one-dimensional acoustic model of the resonator of the tuning slot pipe is constructed first. The acoustic model, based on woodwind tonehole models (see Section 7.2), consists of two waveguide elements, representing the pipe parts below and above the position of the tuning slot. The lengths associated with these elements are $L_T^* = L_T + h_S/2$ (pipe length below the slot position) and $L_S^* = L_S + h_S/2$ (pipe length above the slot position), respectively. The pipe radiates sound from the mouth, from the tuning slot, and from the open end, and the corresponding radiation impedances are denoted by Z_M, Z_S, and Z_E, respectively. The schematic of the resonator and the acoustic circuit of the one-dimensional model are depicted in Figure 6.6. The effective lengths of the waveguide elements are the former lengths (L_T^* and L_S^*) incorporating the end corrections ΔL_M, ΔL_S, and ΔL_E associated with the radiation impedances, respectively. It is assumed furthermore, that the length correction associated with the tuning slot is symmetrical for the main resonator part and the tube part above the slot. The above assumptions are generally accepted for the similar configuration of woodwind toneholes [45, 83, 92].

Since the resonator is open at the tuning slot, the effective length of the resonator—and hence the fundamental frequency—is expected to depend mostly on the length below the slot (tone length L_T) and the size of the slot. The length above the slot (L_S) is expected to have only minor effects on the fundamental frequency.

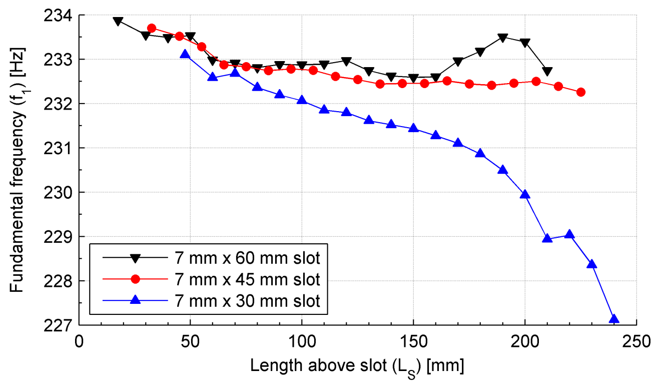

Figure 6.7. Effect of changing the length above the tuning slot (L_S) on the fundamental frequency (f_1) of experimental pipe #1 with different tuning slot sizes.

6.3.3 Effect of the length above the tuning slot

To be able to determine the effect of the length above the tuning slot (L_S) measurements were performed on experimental pipe #1, with an additional paper tube attached to the upper end of the pipe. Three series of measurements were made: in the first series the original tuning slot height of $60\,\mathrm{mm}$ was used, while in the second and third series 15 and $30\,\mathrm{mm}$ were covered from the original slot height at the top of the slot resulting in 45 and $30\,\mathrm{mm}$ heights, respectively. The length of the additional tube was adjusted from 210 to $30\,\mathrm{mm}$ in $10\,\mathrm{mm}$ steps with $\pm 1\,\mathrm{mm}$ accuracy. The tone length was kept constant throughout these measurements.

impact on the fundamental frequency

Figure 6.7 displays the measured fundamental frequencies. As seen, in the case of the largest and the middle slot size, the fundamental frequency is affected by the length above the tuning slot only to a minimal extent. The maximal difference between the fundamentals is $< 1.5\,\mathrm{Hz}$ which corresponds to < 12 cents. In the case of the $30\,\mathrm{mm}$ slot height, L_S has a greater influence on the fundamental frequency, especially for longer tubes. This behavior is in agreement with the one-dimensional model. The main part of the resonator is terminated by the resultant impedance of Z_S and the input impedance of the tube part above the slot Z_T, connected in a parallel manner. Since the radiation impedance Z_S is inversely proportional to the square root of the area of the slot, in case of larger slots (i.e. slot area comparable to the cross section of the pipe) L_S can only have a minor effect on the resultant termination impedance and hence the fundamental frequency.[5]

impact on the envelope

The effect of changing L_S on the mouth-spectrum is remarkable. The strength of the partials is affected by this change to a great extent. This phenomenon is demonstrated in Figure 6.8. As it is seen the envelope is significantly different in all three cases shown in the diagram. In the first case, with $L_S = 40\,\mathrm{mm}$ no local minima are seen among the amplitudes of the first fifteen partials. The amplitudes decay “smoothly” with the frequency, except for the second partial, which is a bit stronger than the fundamental in all three cases. With longer tube above the slot, local minima among the amplitudes are observed. With $L_S = 100\,\mathrm{mm}$ the 7th partial represents such a local minimum possessing a relative amplitude of $-37\,\mathrm{dB}$ and the 5th–7th are 10–$15\,\mathrm{dB}$ weaker than in the $L_S = 40\,\mathrm{mm}$ case. By increasing the length above the slot to $L_S = 190\,\mathrm{mm}$ the local amplitude minimum is shifted to the 3rd partial, which becomes $15\,\mathrm{dB}$ weaker than in the previous two cases. The 8th and 12th partials also have local minimal amplitudes. The amount of these changes is large enough to be clearly audible in the steady state sound, which naturally influences the observed sound quality of the pipes as will be shown in Section 6.5.

impact on the eigenfrequency structure

The effect of L_S on the sound spectrum can be examined in more detail by looking at the

[5]The results displayed in Figure 6.7 will be compared to a more detailed model in Section 7.6.2.

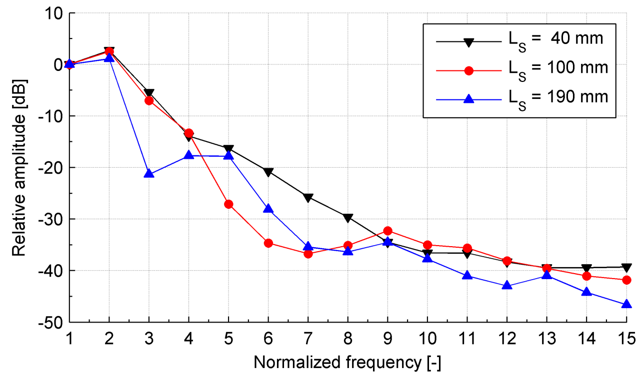

Figure 6.8. Effect of L_S on the amplitudes of the harmonic partials at the pipe mouth (slot size $7.5\,\mathrm{mm} \times 60\,\mathrm{mm}$). Note: the markers are connected with continuous lines only to enhance the visibility; the non-marked values have no physical meaning.

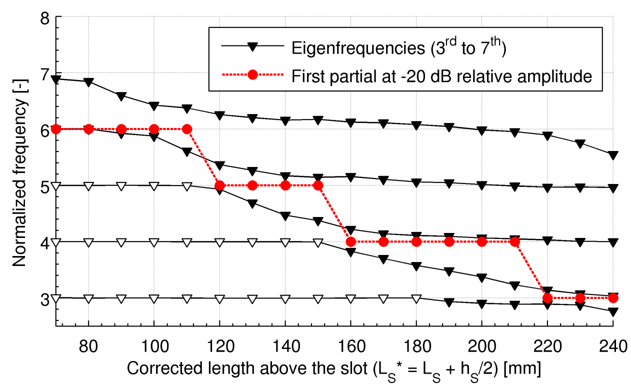

Figure 6.9. Effect of L_S on the eigenfrequencies of pipe #1. Empty markers denote eigenfrequencies undistinguishable from partials (slot size $7.5\,\mathrm{mm} \times 60\,\mathrm{mm}$).

change of natural resonance frequencies, which is depicted in Figure 6.9. In the figure the natural resonances of the pipe were determined from the steady state sound spectra. For the sake of an easier comparison with Figure 6.10 the *waveguide length* $L_S^* = L_S + h_S/2$ (with $h_S = 60$ mm here) is displayed as the independent variable.

When the eigenfrequency was indistinguishable from a harmonic partial in the spectrum, an empty marker was plotted instead of a filled one for this frequency. It can be seen that the first few natural frequencies overlap with the corresponding partials and that the higher eigenfrequencies are slightly compressed, i.e. shifted downwards. The degree of compression grows with an increasing value of L_S^*. The number of the overlapping eigenfrequencies and harmonic partials decreases from 6 (at $L_S = 40\,\mathrm{mm}$) to 2 ($L_S > 150\,\mathrm{mm}$). As long as the eigenfrequency overlaps with the partial, the partial is amplified by the resonator, whereas when the eigenfrequency moves away from the overlapping position the corresponding partial becomes remarkably weaker in the steady state spectrum. The dotted line indicates the serial number of the first partial in the spectrum that has at least $20\,\mathrm{dB}$ smaller amplitude than the fundamental. As it can be seen, the number of strong partials decreases with increasing L_S from 5 partials ($L_S < 90\,\mathrm{mm}$) to 2 partials ($L_S > 180\,\mathrm{mm}$). Thus, the harmonic content of the sound is reduced by increasing L_S.

impact on the harmonic content

The frequencies of the minima of the baseline of the spectrum near the tuning slot have also shown strong dependence on the length above the tuning slot. The normalized frequency of

baseline minima

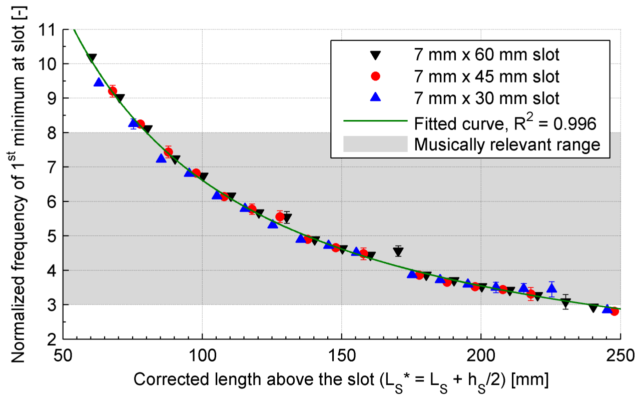

Figure 6.10. Effect of L_S on the first local minimum of the tuning slot spectra of experimental pipe #1 with different slot sizes.

the first minimum is shown in Figure 6.10 as a function of L_S^*. The frequency is normalized by dividing by the fundamental frequency of each configuration.

The fitted curve in Figure 6.10 is $f_\mathrm{min}/f_1 = a/(x+b)$ with f_min representing the frequency of the first minimum in the spectrum, x denoting the waveguide length L_S^* in millimeters. The fit resulted in $x = 764\,\mathrm{mm}$ and $b = 15.5\,\mathrm{mm}$ with a coefficient of determination $R^2 = 0.996$. By substituting $f_1 = c/(2L_\mathrm{eff})$, where L_eff is the effective length of pipe #1 (see Table 6.1), the frequency can be expressed as $f_\mathrm{min} = c/1.92(L_\mathrm{S} + h_\mathrm{S}/2 + b)$. This value is close to the first longitudinal resonance frequency of a tube with an effective length of $L_\mathrm{S} + h_\mathrm{S}/2 + b$. Hence, the fit parameter b can be interpreted as a length correction applied to the tube length above the tuning slot. Therefore, it can be assumed that the quasi-periodic structure of the sound spectrum at the tuning slot is caused by the longitudinal resonances of the pipe section above the tuning slot. This relation is also verified by the one-dimensional model. At the frequencies of longitudinal resonances the input impedance of the tube section above the slot becomes essentially zero, resulting in near zero termination impedance of the main part of the resonator and hence minimal sound pressure measured at the tuning slot.

quasi-periodic behavior explained

The relevant part of the curve in Figure 6.10 is where the location of the minimum is between the 8th and 3rd harmonic partials ($80\,\mathrm{mm} < L_\mathrm{S}^* < 240\,\mathrm{mm}$), shown by the gray area in the diagram, since this range covers the partials with musical relevance. Apparently, the length of the upper waveguide of the original pipe #1 is very small compared to the lengths of the aforementioned range ($L_\mathrm{S}^* = 48\,\mathrm{mm}$), thus the original choice of L_S for pipe #1 seems to be suboptimal.

By comparing Figures 6.9 and 6.10 it can be seen that the frequency of the first partial with $-20\,\mathrm{dB}$ relative amplitude compared to the fundamental in the mouth spectrum is in good correspondence with the frequency of the first minimum of the envelope measured at the slot.

From the results presented in the above paragraphs, it can be assessed that the length above the tuning slot L_S has a great influence on the eigenfrequency-structure and hence the observed sound quality of the pipe. Furthermore, it can also be stated, that to arrive at a desired timbre of the pipe L_S should not depend solely on the diameter D_P, but should be chosen in accordance with the targeted number of strong harmonics in the steady state pipe sound.

6.3.4 Effect of the slot size

In this section the effect of changing the slot width and height is examined. The measurements presented in the following paragraphs were performed on experimental pipe #2, making use of the adjustable tuning slot. The size and the position of the tuning slot were adjusted as described in Section 6.2.1. Three distinct values of L_S were used in three measurement series. First, the

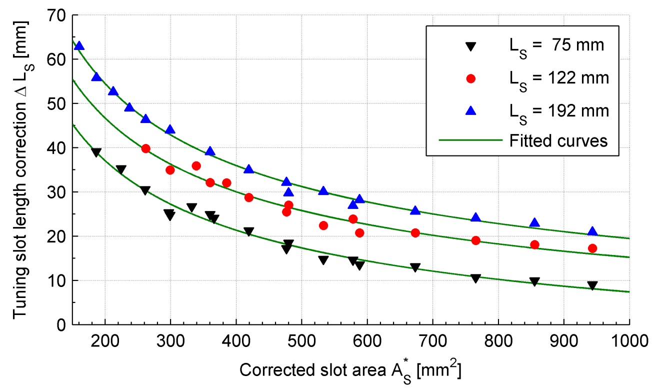

Figure 6.11. Tunings slot length correction ΔL_S as a function of the corrected slot area A^*_S

copper tube was slid to the downmost position, so that the bottom edge of the slot on the copper tube was in line with the lower edge of the larger slot cut into the pipe wall (see Figure 6.2). Furthermore, an additional paper tube was attached to the resonator providing $L_\mathrm{S} = 192\,\mathrm{mm}$. In the second case the paper tube was removed, which resulted in $L_\mathrm{S} = 122\,\mathrm{mm}$. Finally, in the third series, the top edges of the inner and outer slots were aligned, which gave $L_\mathrm{S} = 75\,\mathrm{mm}$. The height of the slot was adjusted in three steps to 45, 30 and $15\,\mathrm{mm}$, whereas its width was varied from 8 to $18\,\mathrm{mm}$ in $2\,\mathrm{mm}$ steps.

Since the tone length of the pipe L_T became remarkably different for the three series, to be able to determine the effect of the slot size on the fundamental frequency, the length correction of the tuning slot ΔL_S was calculated as

$$\Delta L_\mathrm{S} = L_\mathrm{eff} - (L^*_\mathrm{T} + \Delta L_\mathrm{M}), \tag{6.1}$$

with $L^*_\mathrm{T} = L_\mathrm{T} + h_\mathrm{S}/2$ being the waveguide element length of the pipe from the languid to the slot and ΔL_M denoting the length correction at the mouth opening, calculated using the relation (3.68). Because of the geometrical similarity of the mouth and tuning slot openings, a fitting formula similar to (3.68) is chosen for the slot length correction ΔL_S as

$$\Delta L_\mathrm{S} = a + \frac{b}{\sqrt{A^*_\mathrm{S}}}, \tag{6.2}$$

where a and b are fitted constants and A^*_S is defined as

$$A^*_\mathrm{S} = h_\mathrm{S} w_\mathrm{S} \left(\frac{h_\mathrm{S}}{w_\mathrm{S}}\right)^m, \tag{6.3}$$

with m being a custom-fit real factor. The quantity A^*_S is referred to as the *corrected slot area* hereafter. The need for this correction term indicates that the area of the slot in itself is insufficient to predict the change of effective length caused by the slot; yet the shape of the slot must also be taken into account. corrected slot area

Figure 6.11 displays the dependence of the slot length correction ΔL_S on the corrected slot area A^*_S, and the fitted curves for the three different lengths over the slot. The best fit to the plot was achieved by setting $m = 1/6$. These fits resulted in $R^2 = 0.981$, 0.966 and 0.995 for $L_\mathrm{S} = 75$, 122, and $192\,\mathrm{mm}$, respectively. The curves are quite similar with different offsets. The offset, determined by the fit parameter a, depends mostly on L_S. As it is seen, the slot length correction ΔL_S is strongly dependent on the slot area, especially when the slot is relatively small. In the case of larger slots the length correction is rather insensitive to the slot area, but the influence of the length above the slot becomes dominant. impact on slot length correction

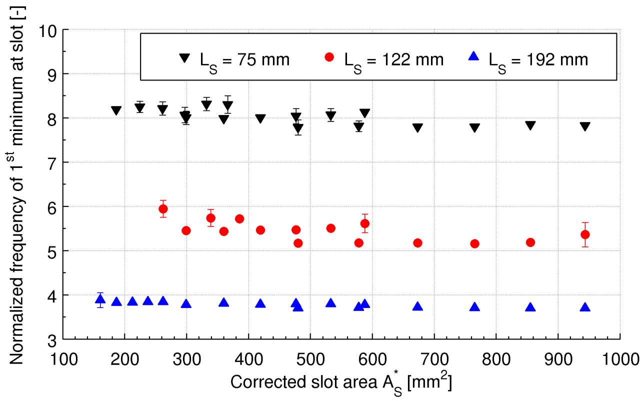

Figure 6.12. Dependence of the first minimum $f_{\min}$ measured in the slot spectrum on the corrected slot area A_S^* with different setups of the length above the slot L_S.

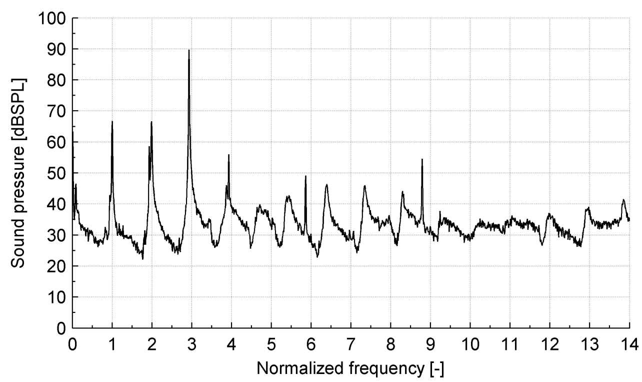

Figure 6.13. Overblowing of pipe #2 with the setup $h_S = 25\,\mathrm{mm}$, $w_S = 10\,\mathrm{mm}$, and $L_S = 122\,\mathrm{mm}$.

impact on baseline minima

Figure 6.12 displays the normalized frequency of the first minima in the spectra measured near the tuning slot ($f_{\min}/f_1$) as a function of the corrected slot area A_S^*. As it can be seen, the slot size has only a small influence on the frequency of the minimum, especially when the length above the slot is greater. Figures 6.10, 6.11, and 6.12 indicate that the formant structure of the sound spectrum can be adjusted by the length L_S^* of the upper waveguide, while the frequency of the pipe can be tuned by the corrected slot area A_S^*. The latter is explained by Figure 6.11 since the pitch is inversely proportional to the effective length of the pipe that incorporates the length correction of the tuning slot. These results can be applied for the development of an improved scaling method of organ pipes with tuning slots, as will be discussed in Section 6.4.

6.3.5 Overblowing

It was observed during the measurements that both of the examined pipes (pipe #1 and #2) have shown a tendency to overblow when the slot area was small and the pipe body was long above the slot. By overblowing the second or the third eigenfrequency has become dominant in the sound. This kind of overblowing occurred without changing the pressure in the windchest. The effect is demonstrated in Figure 6.13, where the steady state spectrum of experimental pipe #2 is shown with the setup $h_S = 25\,\mathrm{mm}$, $w_S = 10\,\mathrm{mm}$, and $L_S = 122\,\mathrm{mm}$.

overblown spectrum

As it is seen, in this case the third eigenfrequency is dominant in the sound, and its frequency is slightly lower than three times the first eigenfrequency. The original fundamental and its first and second octave are also present and still hearable in the sound. However, a strong oscillation has built up at the third natural resonance. Sharp peaks of the 2nd and 3rd partials of this new pitch can be observed slightly below the normalized frequencies of 6 and 9. The overall level of the sound has decreased about $15\,\mathrm{dB}$ compared to the non-overblowing case, whereas the noise level (the baseline of the spectrum) has increased slightly. Although the observed phenomenon is acoustically very interesting, it is undesirable and irrelevant for tuning slot pipes in organ building practice. Therefore, overblown sound recordings have been excluded from the investigations presented in this chapter. Nevertheless, the tendency that a longer tube above the slot and a smaller slot size can result in unwanted overblowing has to be taken into account (by avoiding too small slots, e.g.) in the scaling process of labial organ pipes with tuning slots.

6.3.6 Potentials of the tuning slot

The observed tendencies are as follows.

1. The tuning slot length correction ΔL_{S} and correspondingly the fundamental frequency of the pipe f_1, are influenced both by the area of the tuning slot A_{S} and the length above the slot L_{S}. The effect of the length above the slot L_{S} on the fundamental frequency was found to be smaller in case of larger slots and greater in case of smaller slots.

2. The eigenfrequency-structure is mostly determined by the corrected length above the slot, i.e. $L_{\mathrm{S}}^* = L_{\mathrm{S}} + h_{\mathrm{S}}/2$. Changing the width of the slot w_{S} does not have a significant influence on them.

3. The eigenfrequencies of the pipe also determine the harmonic content of the sound and the quasi-periodic spectral envelope of the steady state sound measured near the tuning slot. Therefore, the parameters affecting the eigenfrequencies also have a strong influence on the timbre of the pipe.

Gaining control over the effects discussed above would be useful in pipe design practice since new knowledge about the effect of the tuning slot may be incorporated into the scaling procedure resulting in more effective sound design of tuning slot pipes. The current design techniques of traditional organ building do not use these capabilities to full capacity. sound design possibility

6.4 Proposal of a novel design approach for tuning slots

Based on the measurement results presented in the previous section, a novel scaling approach is proposed here. Making use of the findings that the eigenfrequency-structure and the resulting timbre of the pipe is dependent mainly on the length above the tuning slot L_{S} and that the width of the slot w_{S} has no significant influence on them, the tuning slot construction depicted in Figure 6.14 is proposed.

The length above the tuning slot L_{S} should be chosen corresponding to the desired number of strong harmonics in the pipe sound, denoted by N_{harm}. Since the number of strong harmonics is inversely proportional to the corrected length $L_{\mathrm{S}}^* = L_{\mathrm{S}} + h_{\mathrm{S}}/2$, as it was shown in Figures 6.9 and 6.10, the following rule can be applied:

$$L_{\mathrm{S}} = \frac{L_{\mathrm{eff}}}{N_{\mathrm{harm}}} - \Delta L_{\mathrm{E}} - \Delta L_{\mathrm{S}}, \tag{6.4}$$

with L_{eff} being the effective length of the pipe (obtained from the fundamental frequency) and ΔL_{E} and ΔL_{S} denoting the length corrections of the open end and the slot, respectively. These latter length corrections should be evaluated by means of a suitable acoustic model, which problem is addressed in the next chapter.

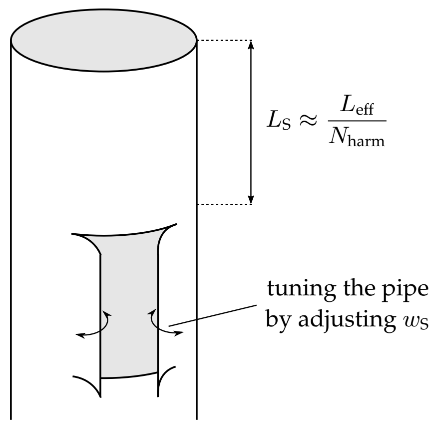

Figure 6.14. The proposed design approach for tuning slots of labial organ pipes

The area of the slot should be selected such that overblowing is avoided. From the measurement results presented in the previous section, the choice $1/4 \leq A_S/S_P \leq 2/3$ seems reasonable, with S_P denoting the cross sectional area of the pipe.

Changing the width of the slot w_S can make the pipe retunable by making use of the dependence of the slot length correction on the area of the slot, shown in Figure 6.11. As the effect of changing w_S on the eigenfrequency-structure of the pipe was found to be small, tuning the pipe by small adjustments of the width of the slot can be expected to leave the timbre of the pipe unchanged.

Since the proposed method provides control over the number of strong harmonics in the pipe sound, it can be applied for the sound design of labial organ pipes mounted with a tuning slot. Nevertheless, this novel approach has to be tested by different experimental pipes before it can be applied in practice. Furthermore, it is also important to justify which values of N_{harm} are relevant from a practical point of view. This question is addressed in the next section by means of a preliminary listening experiment.

6.5 Subjective evaluation of pipe sounds

It was found during the measurements, that with changing the physical dimensions of the tuning slot, not only the objective parameters of the sound spectra changed, but the pipe sounds were also quite different from a subjective point of view. In particular, by increasing the length above the tuning slot L_S the number of strong harmonics in the sound decreased, which resulted in sounds with different characters. In order to justify the perceived quality of pipe sounds with different number of strong harmonics a subjective experiment was prepared.

sound samples

Three times six sound recordings of pipe #1 were selected for a subjective comparison from the measurements presented in Section 6.3.3. As discussed there, three series of measurements were carried out with fixed slot heights ($60\,\mathrm{mm}$, $45\,\mathrm{mm}$, and $30\,\mathrm{mm}$) and twenty different lengths above the tuning slot. The width of the slot was unchanged ($7.5\,\mathrm{mm}$). Seven sound samples were selected for listening from the twenty recordings of each series: The sound of the pipe without an additional paper tube was selected as the reference sample, and six samples were selected with different number (7, 6, 5, 4, 3, and 2) of strong harmonics. The samples were prepared from the sounds recorded by the microphone near (at a distance of $50 \pm 5\,\mathrm{mm}$) the mouth of the pipe in all cases. Six-six pairs (i.e. six times the reference sample plus six selected samples) of samples were prepared from the three measurement series. The first sample was always the reference sample of the given series. The attack was removed by applying a one-second-long fade-in at the beginning of the sound samples.

Since the sound of single organ pipes is unfamiliar for common people, the listener should be familiar with the sound of organ pipes with tuning slots and should be able to distinguish different partials in the pipe sound. Therefore, two experienced voicers were asked to take part in the evaluation. Both voicers have listened to the prepared sample pairs in a random order and their opinions concerning the differences of the timbre and loudness between the reference sample and the second sample were noted and evaluated.[6] The results of the comparison carried out by the well-known voicers Konrad Mühleisen and Johannes Kirschmann are summarized as follows.

Both voicers recognized in all cases that the timbres of the reference sound and the following sound were different. They could also hear that the sound becomes more and more "round" and "hollow" (i.e. more dominant fundamental tone in the recorded pipe sound) with decreasing number of strong harmonic components. The characteristics of the reference sound and the sample with seven strong partials were found a bit too sharp and harsh, while samples with six and five partials were assessed as nice pipe sounds with rich overtone content. Below five strong partials the samples sounded more and more "round" and "hollow", and the loudness gradually decreased. No significant difference was found between the three sample series with different slot heights. The dependency of the timbre on the additional length above the slot was the same. However, sound samples with $30\,\mathrm{mm}$ slot height sounded a bit "forced"; i.e., the octave was enhanced in the sound. These pipes were close to overblowing. The most balanced sounds were found in samples of pipes with $45\,\mathrm{mm}$ slot height.

optimal harmonic content

The voicers were quite surprised when they learned that the best sounds were produced by pipes with 2–3 D_P additional length above the tuning slot since the traditional length above the slot is smaller or equal to the pipe diameter. The sounds of such pipes were assessed as too sharp in the subjective comparison. This result also indicates that in order to achieve a better perceived sound quality the traditional scaling rules should be revised in the case of labial organ pipes with tuning slots.

6.6 Summary

Detailed investigations of two labial organ pipes with adjustable tuning slots, which distinguish the sound of these pipes from the sound of common labial pipes (with *tuning roll*, *tuning ring* or *clear cut end* opening) have revealed properties that had not been known before. The presented results of the experiments may allow the development of improved scaling rules methods for pipes equipped with tuning slots.

improved scaling

By choosing the effective length above the tuning slot appropriately the harmonic partials above a desired frequency limit can be suppressed and hence the timbre of the pipe can be designed. The applicability of this approach was confirmed by the subjective comparison presented in Section 6.5. Thus, the desired sound characteristics of the pipe can be achieved by the proper selection of the length above the slot and of the slot height. These two parameters have to be determined by the scaling procedure and kept constant during the voicing and tuning adjustments. The pitch of the pipe can then be tuned by adjusting the width of the slot.

Contrary to traditional scaling rules, the length of the pipe section above the tuning slot has to be related to the effective length of the pipe and not to its diameter. The results of the experiments and listenings have shown that long slots are ineffective (i.e. when the slot is large, changing its size by rolling the material in and out does not provide enough control over the pitch), while pipes with short slots show a tendency of overblowing. Best results have been obtained by slot heights comparable to the diameter of the pipe.

[6] The voicers' opinions were noted and evaluated by Judit Angster and András Miklós, co-authors of the paper [J3].

need for an improved acoustic model

These findings are also supported by the simple one-dimensional model of the resonator; however, this model is not explicit enough for applying it in the development of a new, improved scaling method for organ pipes with tuning slots. Therefore, an improved version of the acoustic model presented in Section 6.3.2 is needed, which allows a precise calculation of all dimensions of the pipes in the scaling process. This acoustic model also provides the possibility of a direct quantitative comparison of measured and simulated characteristics of tuning slot pipes. The improved acoustic model of labial organ pipes with tuning slots is presented in the next chapter.

Chapter 7

Modeling the tuning slots of labial organ pipes

A suitable acoustic model for the characterization of tuning slots of labial organ pipes is presented in this chapter. Since the tuning slot arrangement is similar—but not identical—to that of toneholes in woodwind instruments, the adaptability of the well-established tonehole model for the specific problem is examined. A numerical model utilizing the finite element (FE) and perfectly matched layer (PML) techniques is set up for the simulation of tuning slots with design parameters varying over a wide range. Analytical tonehole models and the proposed numerical tuning slot model are both combined with analytical one-dimensional waveguide models to predict the acoustic behavior of tuning slot pipes. Comparison to measurements carried out on experimental pipes proves that the hybrid waveguide/finite element model can predict the most important acoustical properties of the tuning slot pipe with good accuracy. The FEM also overcomes the limitations of traditional tonehole models relying on the equivalent T-circuit approximation. By means of the FE model the eigenfrequency-structure and its impact on the character of the sound can be foretold in the design phase, by which a more efficient scaling of tuning slot pipes can be achieved. This chapter is a revised and extended version of the paper [J4].

7.1 Introduction

results of experiments

In the previous chapter experimental examination of tuning slots of labial organ pipes was reported. It was shown that the design parameters of the slot have a great influence on the sound characteristics and the perceived sound quality of the pipe. It was also proven that currently applied design traditions do not provide sufficient control over the timbre. The conclusions of the previous chapter were that the acoustic effects of changing the slot parameters can be qualitatively understood, although, to be able to predict the influence of the slot geometry on the acoustic parameters of the pipe precisely, a reliable acoustic model of a pipe resonator with tuning slot is required. Therefore, this chapter focuses on the acoustic model.

tonehole research

Since the musically relevant frequency range of the pipe sound is under the cut-on frequency of transversal acoustic modes inside the resonator, it is useful and common to represent the resonator by means of a one-dimensional acoustic model. To the best knowledge of the author no established acoustic model exists for the specific problem of treatment of tuning slots. Nevertheless, the rectangular tuning slot is a symmetric discontinuity in the cylindrical pipe body, which is similar to the arrangement of toneholes of woodwind instruments. The latter topic has already been investigated by a number of researchers and various models have been published based on analytical [24, 83] and numerical [53, 91, 92] calculations and experimental results [45, 82,

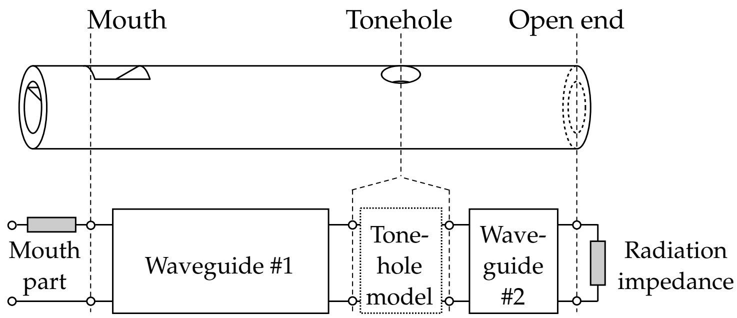

Figure 7.1. Schematic and one-dimensional model a simplified woodwind instrument with one tonehole

108]. These models can be used for the approximate characterization of the tuning slot, however, due to geometrical dissimilarities their applicability is limited and therefore should be examined. This topic is addressed in Section 7.3.

objective The main objective of this chapter is to find a suitable acoustic model for the simulation of the tuning slot. Therefore, woodwind tonehole models and a numerical approach based on the finite element and perfectly matched layer methods are examined and compared to measurement results. The aim of the simulations is to achieve a reliable prediction of the behavior of the tuning slot, by which the timbre of the pipe can be controlled in the design phase.

7.2 The woodwind tonehole model

This and the following sections focus on elaborating an accurate acoustic model of the tuning slot, by which the measured results can be reproduced accurately. To achieve this objective, woodwind tonehole models are examined and a hybrid model of the pipe is set up utilizing one-dimensional transmission line elements and results of simulations carried out by means of the finite element method.

1D model A one-dimensional acoustic model of a woodwind instrument with a single tonehole is shown in Figure 7.1. The model consists of two acoustic waveguide elements, a two-port tonehole model and two lumped two-pole elements representing the radiation impedances at the mouth and open end of the instrument. The first waveguide represents the instrument from the mouth to the position of the tonehole, while the second waveguide stands for the remaining part of the instrument up to the open end. The configuration of a common cylindrical tonehole is shown in Figure 7.2. Using the general notation of the corresponding literature, a denotes the radius of the main bore, b stands for the (effective) radius of the tonehole and t represents the height of the side bore. The ratio b/a is denoted by δ.

This setup has been investigated by a number of researchers. Some of them [24, 45, 53, 82, 83, 91, 92, 108] developed tonehole models which have been applied for the calculation of acoustic properties of woodwind instruments, such as the clarinet, the flute or the recorder. These models are applicable for a relatively large range of parameters δ and t. Tonehole models of several authors are reviewed in the following and their applicability for tuning slot modeling is examined later on.

7.2.1 The T-circuit model

The tonehole can be represented by an equivalent T-circuit in a one-dimensional waveguide model. This model was first introduced by Benade [24] and has been generalized by Keefe [83],

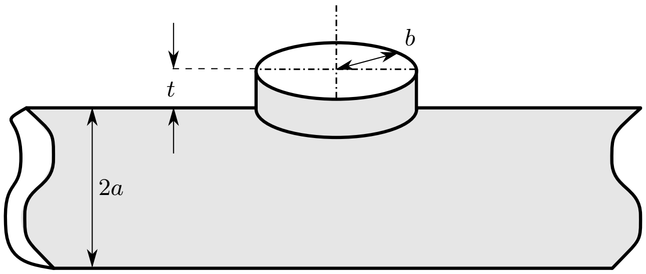

Figure 7.2. Configuration of a typical cylindrical tonehole in the main bore of a woodwind instrument. a – main bore radius, b – tonehole radius, t – tonehole chimney height

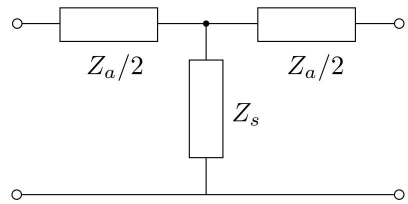

Figure 7.3. Equivalent T-circuit of a tonehole. Z_s – shunt impedance, Z_a – series impedance

who also published measurement data [82] verifying the theoretical results.

T-circuit model

The T-circuit model is depicted in Figure 7.3. It is composed of a shunt impedance Z_s and two series impedances $Z_a/2$. This general model is the basic structure used by most of the authors, however, each of them gives slightly different formulations for the values of the shunt and series impedances based on theoretical deductions, experimental, or computer simulation results. The same model is also used in wave-digital modeling of woodwind instruments, see e.g. [144].

One of the recent works in the topic is by Lefebvre & Scavone [91, 92]. They have developed a novel formula for the length correction parameters of an open tonehole based on data fit approximations to finite element simulation results. Their formulation provides a better fit than the previous models for lower values of δ. They report that "The most important discrepancy between current tonehole theories and our simulation results concerns the frequency dependence of the shunt length correction for toneholes of short height ..." [91]. This specific issue is addressed later in Section 7.5.

In the following the calculation of the parameters of the T-circuit is discussed. The work by Dalmont *et al.* [45] is followed and extended regarding the evaluation of tonehole parameters. The open hole shunt impedance Z_s is defined in [45] as

tonehole shunt impedance

$$Z_s = Z_i + Z_o, \tag{7.1}$$

with Z_i and Z_o denoting the inner and outer correction impedances, respectively. In a low frequency approximation, with neglecting the radiation losses for the time being, equation (7.1) can be expanded as

$$Z_s = Z_i + Z_o = \mathrm{j}kZ_{\mathrm{H0}}(t + t_i + t_m + t_r), \tag{7.2}$$

where k is the wave number and $Z_{\mathrm{H0}} = \rho_0 c/(\pi b^2)$ is the acoustic plane wave impedance of the side bore, with ρ_0 denoting the average density of air, and c representing the speed of sound. The terms t_i, t_m, and t_r denote the inner, the matching volume, and the radiation length corrections and are discussed later.

7.2.2 Radiation impedance

To take the real part of the radiation impedance into account as well, the outer impedance Z_o is calculated as a tube of length $t + t_m$ terminated by the radiation impedance Z_r, which gives [45]

outer impedance

$$Z_o = Z_{\mathrm{H0}} \frac{Z_r + \mathrm{j}Z_{\mathrm{H0}} \tan k(t + t_m)}{Z_{\mathrm{H0}} + \mathrm{j}Z_r \tan k(t + t_m)}. \tag{7.3}$$

Using equation (7.1) with the equivalent length approximation of Z_i leads to

$$Z_s = \mathrm{j}kZ_{\mathrm{H0}}t_i + Z_o. \tag{7.4}$$

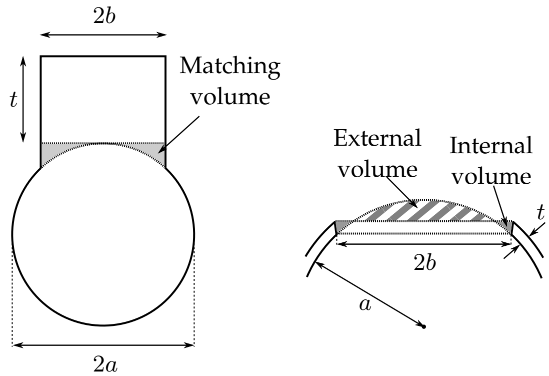

Figure 7.4. The matching volume. Left: Definition using the tonehole model. Right: problem of interpretation in case of small wall thickess

radiation impedance

To evaluate the value of Z_r the geometry of the flange must be known. Two cases can be calculated analytically, (1) when the flange is infinite, or (2) when there is no flange at all, as discussed in Section 3.4. The formulas (3.64) and (3.65) can be utilized to obtain the reflection coefficient R_r and the corresponding length correction t_r. When the opening is considered elliptical, the length correction is scaled by a corresponding factor $K(\varepsilon)$, as defined in eq. (3.66). Finally, the radiation impedance Z_r is obtained by using eq. (3.63).

In reality, the geometry of the flange is somewhere in between the infinite flange and unflanged limits. It can be considered as a rectangular opening with a cylindrical flange, similar—but not identical—to setup (f) of the paper by Dalmont *et al.* [46].[1]

7.2.3 Matching volume correction

The matching volume is depicted in Figure 7.4, where the area corresponding to the matching volume is marked by gray. The equivalent length correction value of $t_m = V_m/S_{\mathrm{H}}$, with V_m denoting the matching volume, is approximated by Nederveen *et al.* [108] as

mathcing volume correction

$$t_m = \frac{b\delta}{8}\left(1 + 0.207\,\delta^3\right). \tag{7.5}$$

As it can be seen, the matching volume is an external correction to toneholes. If the wall thickness is very small, the matching volume correction can turn out to be negative, as illustrated in the right hand side of Figure 7.4. This issue is addressed in Section 7.3.

7.2.4 Inner length correction

Different formulas for the inner length correction term t_i can be found in [53, 83, 92, 108]. Dalmont *et al.* [45] use the relation obtained by Nederveen *et al.* [108] for the calculation of various toneholes. The formula reads as

inner length correction

$$t_i = \left(0.82 - 1.4\,\delta^2 + 0.75\,\delta^{2.7}\right)\,b. \tag{7.6}$$

It is emphasized [83, 91] that t_i is difficult to calculate analytically, and for small values of t the coupling between the inner and outer acoustic fields prevents the separate analysis of outer and inner length corrections.

[1] Reference [46] is a numerical study that investigates the radiation impedances of tubes with different flanges.

7.2.5 Shunt length correction

The total equivalent shunt length correction t_s is derived from the shunt impedance Z_s as

$$t_s = \mathfrak{Re}\left\{\frac{Z_s}{\mathrm{j}kZ_{\mathrm{H0}}}\right\}. \tag{7.7}$$

total shunt corerction

7.2.6 Series impedance

The series length correction t_a of an open tonehole is determined by Nederveen *et al.* [108] as

$$t_a = -0.28\, b\delta^4. \tag{7.8}$$

series length correction

Dalmont *et al.* [45] also use the above formula.[2] The open hole series length correction can also be calculated from the series impedance Z_a as

$$t_a = \mathfrak{Re}\left\{\frac{Z_a}{\mathrm{j}kZ_{\mathrm{H0}}}\right\}. \tag{7.9}$$

7.3 One-dimensional waveguide model of a tuning slot pipe

As mentioned in the Introduction, a one-dimensional acoustic model of the organ pipe with tuning slot could describe the acoustic properties of the pipe in the musically relevant frequency range. Using the one-dimensional model, the input admittance function and the natural resonance frequencies of the resonator can be predicted, which have a great effect on the sound characteristics, as shown by the experiments reported in Chapter 6.

The waveguide model of woodwind instruments presented in Figure 7.1 can also be applied for labial organ pipes with tuning slots. However, the following issues should be taken into consideration:

1. The tuning slot of an organ pipe is generally not cylindrical, which means that an equivalent tonehole with the same effective radius is only an approximation of the real configuration. In spite of the fact that δ is varying in the same range as for woodwind instruments in most cases, the shape of the opening can have a remarkable effect on the sound characteristics, especially in the high frequency range. rectangular geometry

2. In a tuning slot configuration, the ratio t/b is much smaller than for a usual woodwind bore. Therefore it is more difficult to separate internal and external impedances and the derived length corrections. All analytical models known to the authors derive the parameters of the equivalent T-circuit under the assumption $t > b$, which does not hold for the tuning slots of organ pipes. small wall thickness

3. Toneholes can be open, closed, or partly covered by keys, which modify the radiation impedance of the side bores. For the tuning slot, nevertheless, only the open case is relevant.

Rectangular tuning slots may be treated similarly as the mouths of labial organ pipes. Based on the approximation of the mouth length correction proposed by Ingerslev & Frobenius [78] (see equations 3.66 and 3.67), the rectangular tuning slot with height h_S and width w_S can be approximated by an equivalent ellipse with the same area and axis length ratio. This gives:

$$e_{\mathrm{h}} = \frac{h_{\mathrm{S}}}{\sqrt{\pi}} \qquad \text{and} \qquad e_{\mathrm{w}} = \frac{w_{\mathrm{S}}}{\sqrt{\pi}}, \tag{7.10}$$

equivalent ellipse

[2] Eq. (2) of [45] uses a scaling of δ^2, but [91] suggests the scaling of δ^4, which gives a better fit to measurements.

where e_{h} and e_{w} are the two semiaxes of the ellipse.

Radiation and inner corrections of the tuning slot may also be approximated similarly as the corresponding length corrections of woodwind tuning holes. In this case the radius b of the tonehole has to be substituted by the equvivalent radius of the tuning slot. However, it is not straightforward to interpret the matching volume correction, since the wall width is small compared to the radius of the pipe and there is no extra tube attached to provide a wall around the tuning slot. Nevertheless, in case of oblong rectangular tuning slots, the resulting matching volume correction is very small ($|t_m| \ll t + t_r$) and can be neglected.

matching volume interpretation

Based on the above considerations it would be possible to extend the application of the woodwind tonehole model to the tuning slots of labial organ pipes. However, some of the assumptions and approximations (see points 1 and 2 in the numbered list above) of the tonehole model do not apply for tuning slots. Therefore, an other way is chosen; the quantification of the serial and shunt impedances Z_a and Z_s of the equivalent T-circuit of the tuning slot by numerical simulation. Shunt and series length corrections can then be determined by equations (7.7) and (7.9), for the sake of comparison with the corresponding length corrections of the tonhole model.

7.4 Simulation method

In this section a finite element simulation method is described, adapting the technique proposed by Lefebvre & Scavone [91, 92]. The main difference of the current simulation setup and the one presented in [91] is that here rectangular tuning slots are used instead of cylindrical bores. The technique to emulate free field conditions of the open tonehole is also different from the one applied in [91] and [92].

Following [91], the tuning slot is represented as a two-port, characterized by its frequency dependent transmission matrix (TM, see Section 3.3.2). With p_{in}, v_{in} and p_{out}, v_{out} denoting input and output pressure and particle velocity, respectively, the transmission matrix $\mathbf{T}$ is written similar to (3.52) as

transfer matrix

$$\begin{bmatrix} p_{\mathrm{in}} \\ Z_0 v_{\mathrm{in}} \end{bmatrix} = \begin{bmatrix} T_{11} & T_{12} \\ T_{21} & T_{22} \end{bmatrix} \begin{bmatrix} p_{\mathrm{out}} \\ Z_0 v_{\mathrm{out}} \end{bmatrix}, \tag{7.11}$$

where $Z_0 = \rho_0 c$.[3]

Using (7.11) the TM of a cylindrical tube with length L reads as (see also eq. 3.57)

$$\mathbf{T}_{\mathrm{cyl}}(kL) = \begin{bmatrix} \cos kL & \mathrm{j} \sin kL \\ \mathrm{j} \sin kL & \cos kL \end{bmatrix}. \tag{7.12}$$

Using the T-circuit equivalence, and introducing the notations $\bar{Z}_s = Z_s / Z_{\mathrm{P0}}$ and $\bar{Z}_a = Z_a / Z_{\mathrm{P0}}$, with $Z_{\mathrm{P0}} = \rho_0 c / (\pi a^2)$ denoting the acoustic plane wave impedance of the tube, the transimssion matrix of the slot $\mathbf{T}_{\mathrm{slot}}$ can be written as

TM of the tuning slot

$$\mathbf{T}_{\mathrm{slot}} = \begin{bmatrix} 1 & \bar{Z}_a/2 \\ 0 & 1 \end{bmatrix} \begin{bmatrix} 1 & 0 \\ 1/\bar{Z}_s & 1 \end{bmatrix} \begin{bmatrix} 1 & \bar{Z}_a/2 \\ 0 & 1 \end{bmatrix} = \begin{bmatrix} 1 + \dfrac{\bar{Z}_a}{2\bar{Z}_s} & \bar{Z}_a \left(1 + \dfrac{\bar{Z}_a}{4\bar{Z}_s}\right) \\ \dfrac{1}{\bar{Z}_s} & 1 + \dfrac{\bar{Z}_a}{2\bar{Z}_s} \end{bmatrix}. \tag{7.13}$$

simulation arrangement

Since the tuning slot can only be examined as a part of a tube section, in order to get its TM, the slot is placed into a symmetrical tube of length $2L_{\mathrm{cyl}}$, similar to the methodology of [91] and [92]. The simulation arrangement is shown in Figure 7.5. To be able to emulate free field radiation conditions near the tuning slot opening, the finite element model is extended with an exterior part, which is indicated by the transparent green box in the figure. This extension is

[3]There is a mistake in [91] as they give the acoustic plane wave impedance, however they use the specific impedance in the deduction. Therefore the specific impedances are used herein.

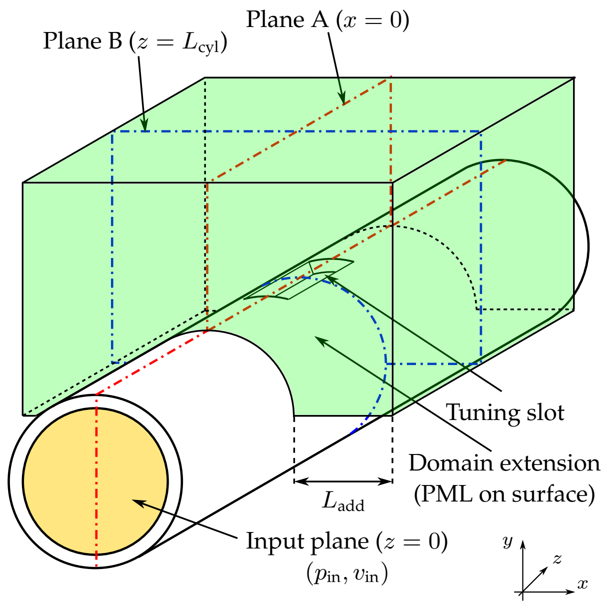

Figure 7.5. Arrangement for numerical characterization of tuning slots

needed to provide a transition into the absorbing layer and for visualizing the radiated field near the slot. There are no explicit requirements on the size of this extension L_{add} [30]. This exterior simulation domain is bounded by absorbing elements, provided by the Perfectly Matched Layer (PML) technique. The PML formulation was implemented using unbounded absorbing functions following [30] (see also Section 4.4.2 and eq. 4.49).

Since the arrangement is symmetric, only one quarter of the whole domain needs to be simulated, which allows better resolution (more degrees of freedom) of the geometry discretization. The separated quarters are illustrated by plane A and B in Figure 7.5. We define the two symmetry planes as follows. Plane A is the $y - z$ plane located at $x = 0$ and plane B is the $x - y$ plane located at $z = L_{\text{cyl}}$. Because of the symmetry, zero particle velocity can be assumed on plane A in case of plane wave excitation at the input plane ($z = 0$). symmetry

The transmission matrix of the whole simulated object $\mathbf{T}_{\text{obj}}$ can be written as

$$\mathbf{T}_{\text{obj}} = \mathbf{T}_{\text{cyl}}\mathbf{T}_{\text{slot}}\mathbf{T}_{\text{cyl}}, \tag{7.14}$$

thus, the TM of the tuning slot is expressed as

$$\mathbf{T}_{\text{slot}} = \mathbf{T}_{\text{cyl}}^{-1}\mathbf{T}_{\text{obj}}\mathbf{T}_{\text{cyl}}^{-1}. \tag{7.15}$$

To be able to extract the TM of the whole object $\mathbf{T}_{\text{obj}}$ from the FE calculations, the simulation is performed using two different sets of boundary conditions. On the input plane the pressure is always defined as constant. A symmetric and an antisymmetric case is set up, by defining zero particle velocity (Neumann) and zero pressure (Dirichlet) condition on symmetry plane B, respectively. On the output plane, the pressure and particle velocity values can be given as boundary conditions

$$\begin{aligned} p_{\text{out}}^{(\text{s})} &= p_{\text{in}}^{(\text{s})} \qquad & v_{\text{out}}^{(\text{s})} &= -v_{\text{in}}^{(\text{s})}, \\ p_{\text{out}}^{(\text{a})} &= -p_{\text{in}}^{(\text{a})} \qquad & v_{\text{out}}^{(\text{a})} &= v_{\text{in}}^{(\text{a})}. \end{aligned} \tag{7.16a}$$

The upper indices $\cdot^{(\text{s})}$ and $\cdot^{(\text{a})}$ denote the symmetric and antisymmetric cases, respectively. It should be noted that in the simulation arrangement the cylindrical sections and the domain extension are only needed to be able to attain the matrix $\mathbf{T}_{\text{slot}}$. The results are not influenced by the

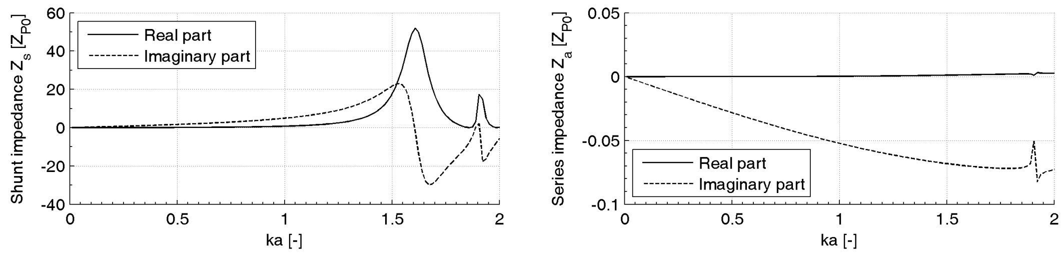

Figure 7.6. Typical shunt (left plot) and series (right plot) impedances Z_s and Z_a for a tuning slot. ($a = 17.5\,\mathrm{mm}$, $h_\mathrm{S} = 20\,\mathrm{mm}$, $w_\mathrm{S} = 12\,\mathrm{mm}$ and $t = 1.5\,\mathrm{mm}$)

sizes L_cyl and L_add if the latter are chosen properly. To obtain the values in the TM, the following relation is used:

$$\begin{bmatrix} p_\mathrm{in}^\mathrm{(s)} \\ Z_0 v_\mathrm{in}^\mathrm{(s)} \\ p_\mathrm{in}^\mathrm{(a)} \\ Z_0 v_\mathrm{in}^\mathrm{(a)} \end{bmatrix} = \begin{bmatrix} p_\mathrm{out}^\mathrm{(s)} & Z_0 v_\mathrm{out}^\mathrm{(s)} & 0 & 0 \\ 0 & 0 & p_\mathrm{out}^\mathrm{(s)} & Z_0 v_\mathrm{out}^\mathrm{(s)} \\ p_\mathrm{out}^\mathrm{(a)} & Z_0 v_\mathrm{out}^\mathrm{(a)} & 0 & 0 \\ 0 & 0 & p_\mathrm{out}^\mathrm{(a)} & Z_0 v_\mathrm{out}^\mathrm{(a)} \end{bmatrix} \begin{bmatrix} T_{11} \\ T_{12} \\ T_{21} \\ T_{22} \end{bmatrix}. \tag{7.17}$$

After equation (7.17) is solved, the parameters $\bar{Z}_a$ and $\bar{Z}_s$ can be calculated as

$$\begin{aligned} \bar{Z}_a &= 2(T_{11} - 1)/T_{21} \qquad \text{and} \\ \bar{Z}_s &= 1/T_{21}. \end{aligned} \tag{7.18}$$

choice of tube length

It is worth discussing the choice of the parameter L_cyl. Theoretically, for an arbitrary value of L_cyl, $\mathbf{T}_\mathrm{cyl}$ can be evaluated analytically using (7.12). If the propagation is assumed to be lossless—as this is the case in the present FE simulations—the resulting $\mathbf{T}_\mathrm{cyl}$ is always invertible and well-conditioned, and (7.15) can be applied to calculate $\mathbf{T}_\mathrm{slot}$ from $\mathbf{T}_\mathrm{obj}$ and $\mathbf{T}_\mathrm{cyl}$. However, from a numerical viewpoint, choosing a too high value for L_cyl is not recommended. This is explained by the inevitable appearance of the numerical dispersion error.

A lower limit on L_cyl can be imposed by the requirement that the transfer matrix description of the object and the boundary conditions (7.16) are only valid when the wavefront at the input and output planes can be regarded as planar. Since at the tuning slot this assumption does not hold, L_cyl has to be large enough that the perturbations caused by the slot vanish. It was found by trying a few different setups that choosing L_cyl as 3–4 times the inner diameter of the tube is sufficient.[4]

typical behavior

Figure 7.6 displays the typical behavior of the shunt and series impedances Z_s and Z_a evaluated from the finite element model by means of equation (7.18). In the low frequency regime ($ka < 1$) the equivalent length approximations are suitable for both impedances, since a linear fit provides good match in this region. At low frequencies, the real part of the impedances is negligible compared to the imaginary part. At higher frequencies, however, the shunt impedance Z_s shows a resonant behavior with a remarkably strong peak at $ka \approx 1.65$. Another peak at $ka \approx 1.9$ is also observable in both impedance curves. This resonant peak has been observed at approximately the same frequency with different slot sizes in the same tube. By looking at the simulated pressure field inside the tube, it is found that this second resonant peak is due to the inevitable excitation of the first transversal mode of the tube. This phenomenon is illustrated in Figure 7.7. As it can be seen in the left panel, there is a strong transversal component in the simulated pressure field already at $ka = 1.53$. At higher frequencies, as shown in the right panel for $ka = 1.91$, longitudinal and transversal oscillations are both present in the whole tube.

[4] There is no information given on the value of L_cyl in Refs. [91, 92] by Lefebvre & Scavone.

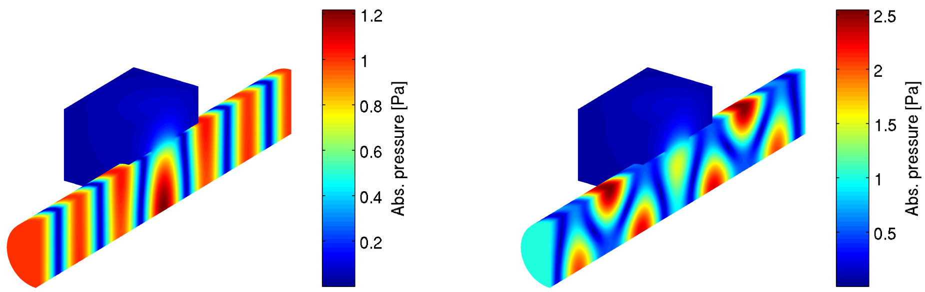

Figure 7.7. Resonant behavior observed in FE simulations of tuning slots ($a = 17.5\,\text{mm}$, $h_\text{S} = 20\,\text{mm}$, $w_\text{S} = 12\,\text{mm}$ and $t = 1.5\,\text{mm}$). Symmetric boundary conditions. Left: $ka = 1.53$. Right: $ka = 1.91$.

Case	#1 a)	#1 b)	#1 c)	#2 a)	#2 b)
a		10 mm		10 mm	
δ		0.70		1.00	
t/b		1.30		1.01	
h_S/w_S	1.0	2.0	3.0	2.0	4.0
L_cyl			80 mm		
L_add			15 mm		
L_PML			5 mm		
N_PML			6		
DOF		$\approx 74\,000$		$\approx 83\,000$	
$(ka)_\text{max}$		6.37		6.32	

Table 7.1. Physical and model parameters of validation cases

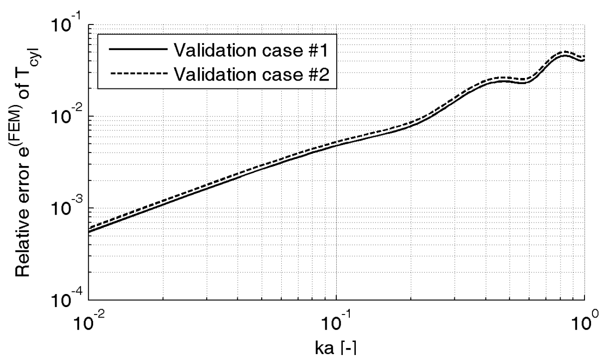

Figure 7.8. Effect of numerical dispersion in validation cases

7.5 Comparison of tonehole and tuning slot models

7.5.1 Validation

In order to validate the method and the numerical model, two test cases of references [45] and [91] have been examined. In the original test cases cylindrical toneholes were used, which were replaced by rectangular ones, keeping the effective radii $b = \sqrt{h_\text{S} w_\text{S}/\pi}$ of the holes unchanged. In order to examine the effect of the oblongness of the slot, models with different h_S/w_S ratios were created. The parameters of the validation models are listed in Table 7.1. validation cases

Parameters L_cyl, L_add and L_PML refer to the length of the cylindrical section, the additional length of the domain extension, and the thickness of the PML, respectively. N_PML denotes the number of elements in the PML along the layer thickness. The maximal frequency $(ka)_\text{max}$ has been calculated from the generated mesh as a maximal frequency, where the element edge length is smaller than $\lambda/12$ with λ denoting the wavelength. The reason for using such a low tolerance (12 elements per wavelength instead of the usual 6 to 8) is to minimize the effect of numerical dispersion errors.

To be able to identify the magnitude of numerical errors, the error of the TM of the cylindrical

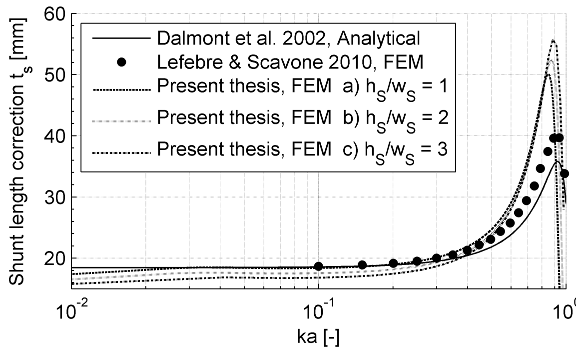

Figure 7.9. Open tonehole shunt length correction – validation case #1

numerical error

tube section is evaluated as

$$e^{(\mathrm{FEM})} = \frac{\|\mathbf{T}_{\mathrm{cyl}}^{(\mathrm{ana})} - \mathbf{T}_{\mathrm{cyl}}^{(\mathrm{FEM})}\|}{\|\mathbf{T}_{\mathrm{cyl}}^{(\mathrm{ana})}\|}, \tag{7.19}$$

with the upper indices (ana) and (FEM) denoting matrices calculated from the analytical and FE models, respectively. The notation $\|\cdot\|$ denotes the 2-norm.

The numerical error is displayed in Figure 7.8. As it can be seen, the numerical error scales approximately linearly with the frequency with some small oscillations. To be able to obtain the TM of the tuning slot the inverse of $\mathbf{T}_{\mathrm{cyl}}$ is needed, therefore these errors should be kept as small as possible. Using the parameters given in Table 7.1 the numerical error remained $< 5\%$ in the whole frequency range of interest ($ka < 1$) for the two validation cases. Furthermore, the effect of numerical dispersion errors on the resulting $\mathbf{T}_{\mathrm{slot}}$ can remarkably be reduced by using $\mathbf{T}_{\mathrm{cyl}}^{(\mathrm{FEM})}$ in (7.15). This approach was followed in the evaluation.

To be able to compare the results of different models, the length correction parameters are derived after the impedances are obtained from eq. (7.18) as

$$t_a = \mathfrak{Re}\left\{\bar{Z}_a \frac{\delta^2}{\mathrm{j}k}\right\} \qquad \text{and} \qquad t_s = \mathfrak{Re}\left\{\bar{Z}_s \frac{\delta^2}{\mathrm{j}k}\right\}. \tag{7.20}$$

The factor δ^2 arises from the ratio of the tube and hole plane wave impedances $Z_{\mathrm{P0}}/Z_{\mathrm{H0}} = \delta^2$.

The results for the open tonehole shunt length correction t_s are displayed in Figure 7.9. Beside the analytical results, the data points of Figure 2 of Ref. [91] are also shown in the diagram.

validation case #1

For case #1 with $h_{\mathrm{S}}/w_{\mathrm{S}} = 1$ the data shows good match in the low and middle frequency range. As the ratio $h_{\mathrm{S}}/w_{\mathrm{S}}$ is increased, the low frequency shunt length correction decreases. At higher frequencies ($ka > 0.5$) some deviations are observed between the simulation results and the analytical model. Our FE simulation provides higher maximal t_s values than the analytical model and the other FE model. At the same time the location of the maximum position is shifted a bit downwards ($ka \approx 0.85$ instead of $ka \approx 0.90$). The maximal deviation from the FE model of Lefebvre & Scavone is around 20% with $h_{\mathrm{S}}/w_{\mathrm{S}} = 1$. By increasing $h_{\mathrm{S}}/w_{\mathrm{S}}$, the maximal value of the shunt length correction increases and the frequency of the maximum is slightly shifted upwards, as it can be seen in the figure.

effect of oblongness

The results for the series length corrections are displayed in Table 7.2.[5] Data of numerical simulations and the analytical model show a good match, for test case #1 with $h_{\mathrm{S}}/w_{\mathrm{S}} = 1$, however, when the slot is more oblong, the resulting values of t_a become larger. This effect leads to more significant deviations for test case #2 because of the larger value of δ.

[5] The series length correction t_a has a negative value (see eq. 7.8), therefore the positive values reported in Table 3 of Ref. [91] have been corrected. Also the results of Dalmont *et al.* [45] have been rescaled with the correct δ^4 factor.

Case	δ	t/b	h_S/w_S	Model	t_a [mm]
Case #1	0.7	1.30	N/A	Dalmont *et al.*[45]	-0.47
			N/A	Lefebvre & Scavone[91]	-0.50
			1.0	Present thesis, FEM	-0.50
			2.0	Present thesis, FEM	-0.75
			3.0	Present thesis, FEM	-0.97
Case #2	1.0	1.01	N/A	Dalmont *et al.*[45]	-2.90
			N/A	Lefebvre & Scavone[91]	-2.80
			2.0	Present thesis, FEM	-4.20
			4.0	Present thesis, FEM	-6.60

Table 7.2. Comparison of series length corrections t_a in the two validation cases using different models

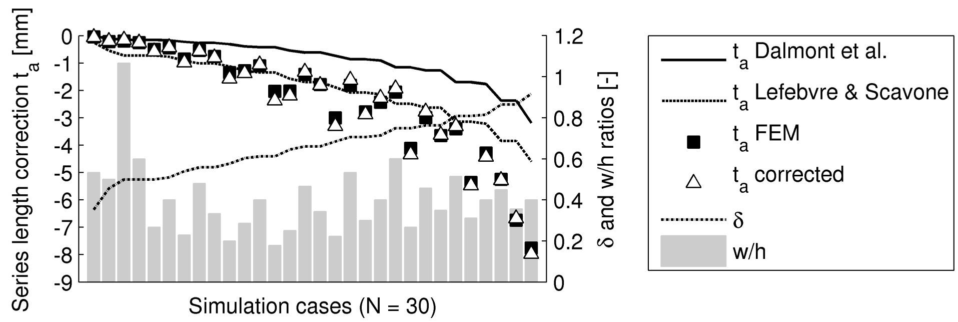

Figure 7.10. Comparison of results from different formulations of the series length correction t_a to numerical simulations of tuning slot setups with δ and h_S/w_S varying over a great range. "t_a corrected" is calculated using eq. (7.22).

In the following the background of the discrepancies observed between the numerical and the analytical slot models is briefly reviewed. The examination is performed by comparing the predictions of length correction coefficients of both models.

7.5.2 Evaluation of the series length correction

Figure 7.10 displays the comparison of different approximations for the series length correction t_a. The diagram also displays the results obtained by Lefebvre & Scavone [92], given as

$$t_a = b\delta^2 \left[-0.35 + 0.06 \tanh(2.7\, t/b)\right]. \tag{7.21}$$

As it is seen, the discrepancy between the numerical tuning slot simulation and tonehole models from Dalmont *et al.* [45] and Lefebvre & Scavone [92] are higher in case of larger values of δ and h_S/w_S. In these cases both tonehole models fail to foretell the series length correction provided by the FEM. This observation is in good correspondence with the results to be presented in Section 7.6, as the underestimation of the series length correction leads to the underestimation of the fundamental frequency.

Nevertheless, with a small modification of the formula of Dalmont *et al.* for the series length correction a good fit to the simulation results can be achieved. The proposed correction takes the oblongness of the slot into account simply as multiplying the original length correction value in equation (7.8) by the ratio of h_S/w_S as

$$t_a = -0.28\, \delta^4 b \frac{h_S}{w_S}. \tag{7.22}$$

modified series length correction

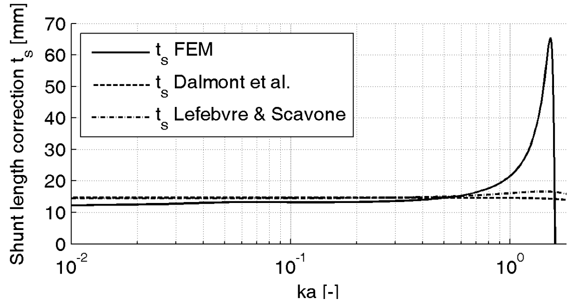

Figure 7.11. Frequency dependent behavior of the shunt length corrections given by different models. Experimental pipe #2, $h_\text{S} = 20\,\text{mm}$, $w_\text{S} = 12\,\text{mm}$.

This simple correction form provides very good agreement for the series length correction t_a in the whole range of the simulated parameters, as it can be seen in Figure 7.10 indicated by the triangular markers.

7.5.3 Evaluation of the shunt length correction

From Figure 7.6 it can immediately be seen, that the equivalent length approximation of Z_s only works in the low frequency regime since the impedance curve becomes non-linear at higher frequencies. In the models of Dalmont *et al.* [45] and Lefebvre & Scavone [92] this behavior is treated by regarding the shunt length correction t_s as dependent on the frequency as it was indicated e.g. in Figure 7.9.

discrepancies

Figure 7.11 displays the evaluated shunt length correction for the tuning slot of pipe #2 with $h_\text{S} = 20\,\text{mm}$ and $w_\text{S} = 12\,\text{mm}$ provided by different models as a function of ka. A significant dissimilarity is observed between the FEM and the other two models. In the very low frequency range ($ka < 0.1$) similar values for t_s are provided by all three models, however, strong dependence on the frequency is only given by the FE model. The dissimilarities are significant where $ka > 0.6$.

Dalmont *et al.* [45] treat the inner length correction t_i—which is already incorporated into the shunt length correction—as independent of frequency, and hence, the frequency dependence of t_s is a result of that of the radiation impedance Z_r and the finite wall thickness t. The latter is too small in case of tuning slots to show frequency dependent behavior in this frequency range. Lefebvre & Scavone gave a formula for the approximation of the frequency dependence of t_i used for toneholes of shorter heights (see equation (32) of reference [92]). However, this formulation only means a slight deviation from the model of Dalmont *et al.* in this case.

acoustic coupling

Due to the thin walls ($t/b \ll 1$), the coupling between the inner and outer acoustic fields is remarkably stronger in case of tuning slots than for woodwind toneholes, which prevents the separation of inner and outer length corrections [83, 91]. It can be stated that the limitations of traditional tonehole models relying on the equivalent T-circuit low frequency length corrections are exceeded at such low tonehole heights.

From the validation results presented above, it can be assessed that the proposed numerical treatment is capable of predicting the equivalent parameters of toneholes and tuning slots with sufficient accuracy. Furthermore, it can also be assessed that the rectangular geometry can have a remarkable effect on the corresponding length correction parameters, especially in case of oblong slots. In the following sections the equivalent length correction parameters of real tuning slots are calculated and the results are compared to measurement data.

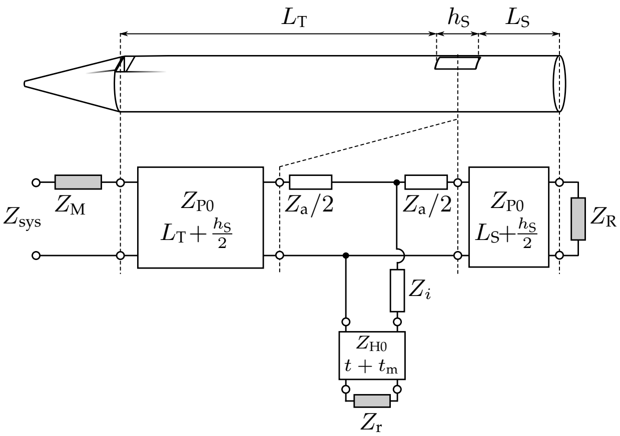

Figure 7.12. The one-dimensional waveguide model of a tuning slot pipe

7.6 Comparison of simulations and measurements

This section presents direct comparisons of measurement results with simulations using the one-dimensional waveguide model of the pipe. The comparison is carried out applying both the analytical model of Dalmont *et al.* [45] and the FEM model introduced above. Lefebvre & Scavone [91, 92] have already performed the numerical simulation of a great number of toneholes with various geometries and compared the results to different tonehole models. However, the simulation of a complete resonator using the numerical tonehole (or tuning slot) model and its comparison to measurement results has not been published yet to the best knowledge of the author. The measurements presented in the sequel were performed on the experimental pipes introduced previously in Section 6.2.1.

7.6.1 The complete model

Figure 7.12 depicts the complete acoustic waveguide model of the tuning slot pipe. This model is used for the comparison to measurement results both with the analytical and the FE formulation of the slot parameters. The calculation procedure of the elements inside the model is summarized briefly in the following.

The parameters of the waveguide elements are determined as follows. The model length of the tube section above the slot is $L_S^* = L_S + h_S/2$. The length of the main resonator element is $L_T^* = L_T + h_S/2$, as introduced in Section 6.3.2. The radiation impedance at the open end Z_R is obtained using the formulas (3.63) and (3.65). The radiation impedance at the mouth opening Z_M is calculated using equation (3.68). calculation method

In case of the model of Dalmont *et al.*, the slot impedances, Z_s and Z_a were evaluated using equations (7.3), (7.4), and (7.9). The incorporated equivalent lengths, t_m, t_i, and t_a were calculated using equations (7.5), (7.6), and (7.8), respectively. The radiation impedance at the tuning slot Z_r was attained by means of equations (3.66), (3.67), and (7.10).

When the slot model was evaluated from the finite element simulations, the parameters Z_a and Z_s were directly calculated from the postprocessed acoustic fields, using equations (7.17) and (7.18). All other elements were evaluated analytically, as described above.

For both models two frequency dependent functions were calculated: (1) the input admittance $Y_{sys}(f)$ of the complete pipe and (2) the radiated sound pressure from the tuning slot $p_{slot}(f)$, assuming unit input particle velocity at the pipe mouth. The input admittance function can be compared to the baseline of the spectrum measured at the pipe mouth, whereas the calculated calculated quantities

Pipe	h_S [mm]	w_S [mm]	δ [–]	h_S/w_S [–]	L_S [mm]	Meas. [Hz]	Ana. [Hz]	Error [cent]	FEM [Hz]	Error [cent]
#1	60.6	7.5	0.682	8.08	17.6	233.9	228.3	−42	231.5	−18
					90.0	232.8	226.8	−46	230.5	−17
					150.0	232.6	225.8	−51	230.2	−18
					210.0	232.7	225.5	−55	230.0	−21
#2	10.0	16.0	0.408	0.63	130.0	205.7	205.9	2	207.8	17
	20.0	12.0	0.500	1.67	117.0	206.6	206.2	−3	207.2	5
	30.0	14.0	0.660	2.14	99.0	207.0	205.9	−9	207.8	6
	45.0	8.0	0.612	5.63	93.0	206.7	206.1	−5	208.3	14
	45.0	18.0	0.918	2.50	77.0	207.2	205.3	−16	207.4	1

Table 7.3. Comparison of the Dalmont and FEM models for the prediction of the fundamental frequency with different tuning slot sizes. ("Ana.": Model of Dalmont *et al.*)

sound pressure spectrum at the tuning slot can be compared to the baseline of the spectrum measured at the slot.

Altogether more than fifty finite element models were created, with different slot heights and widths. Each slot simulation was performed in the nondimensionsal frequency range of $0.01 \leq ka \leq 2$ in 128 equal steps, which corresponds approximately to $30\,\mathrm{Hz} \leq f \leq 6.2\,\mathrm{kHz}$ for the experimental pipes. The calculation of the functions Y_{sys} and p_{slot} were performed using the same frequency range with 32 768 points, leading to $\Delta f \approx 0.2\,\mathrm{Hz}$ frequency resolution. For the increased resolution, the values of Z_a and Z_s were determined by linear interpolation from the calculated values of the FE simulation of the corresponding geometry.

7.6.2 Prediction of the fundamental

To be able to assess the quality of the results provided by the models, one of the most important properties is the fundamental frequency. The first eigenfrequency of the resonator of the pipe, which can be predicted by the acoustic model, and the fundamental frequency of the pipe sound, which can be measured in a sound recording, are not identical generally, as the latter is influenced by the blowing pressure to a small extent. However, the two frequencies are usually very close and therefore it is worth comparing them in the lack of precise input admittance measurements. It should be noted that in the following discussion these different quantities are compared to each other.

For this comparitive examination, external paper tubes of different lengths were attached to the open end of pipe #1, providing different values for the pipe length above the slot L_S, as explained in Section 6.3.3. Changing L_S only affected the fundamental frequency to a minimal extent as shown in Figure 6.7. The size of the slot was not modified for pipe #1. However, different slot sizes were set up for pipe #2, while the pipe was always retuned to $\approx 207\,\mathrm{Hz}$ by comparing its pitch to a reference pipe. This way all three parameters h_S, w_S, and L_S were changed at the same time for pipe #2 without changing the fundamental frequency.

evaluation The measured and predicted fundamental frequencies are presented in Table 7.3. As it can be seen, in case of pipe #1, the fundamental is underestimated with approximately 40–50 cents of error using the tonehole model of Dalmont *et al.* The FE slot model reduces this error to around 20 cents. This discrepancy can be due to the series length correction coefficient t_a in the analytical model, since the oblongness of the slot is not taken into account in eq. (7.8). This issue was addressed above in Section 7.5. It is also observed that increasing L_S slightly increases the error of the estimation for both models.

In case of pipe #2 both models give a prediction of the first eigenfrequency that is close to

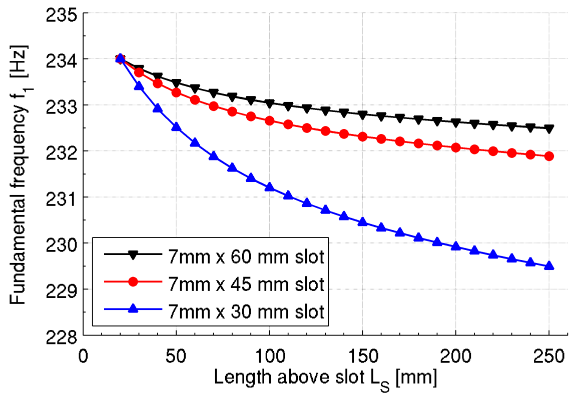

Figure 7.13. Fundamental frequencies predicted by the tuning slot model for different values of h_S and L_S

the measured fundamental frequency, the greatest absolute error being $\approx 2\,\mathrm{Hz}$, corresponding to $17\,\mathrm{cents}$. The parameters h_S/w_S and δ vary in a relatively wide range for the cases presented in Table 7.3; however, the ratio h_S/w_S is always significantly lower than that of pipe #1. It can be assessed that both models give a suitable prediction of the first natural resonance frequency when the slot is not too oblong.

It is worth comparing the results for the measured fundamental frequencies presented in Figure 6.7 with the first eigenfrequencies given by the tuning slot model. To this end, the prediction for the fundamental frequency was evaluated by means of the analytical tuning slot model, making use of the correction for the series length correction introduced in eq. (7.22). The results are presented in Figure 7.13. To facilitate the comparison the curves are shifted so that $f_1 = 234\,\mathrm{Hz}$ is shown for $L_S = 20\,\mathrm{mm}$ in all cases. This corresponds to shifting the curves by 0.55, -0.79, and $-1.63\,\mathrm{Hz}$ for $h_S = 60$, 45, and $30\,\mathrm{mm}$, respectively. As far as the magnitude of the effect of changing L_S on the fundamental frequency is concerned, a good match with Figure 7.13 is found, as the predicted fundamental frequency is affected to a larger extent by changing L_S in case of smaller slots. However, the resulting curves are somewhat different from the measured data. This difference is best observable in case of the $7\,\mathrm{mm} \times 30\,\mathrm{mm}$ slot, where in case of the measurements the greatest change of the fundamental occurs around $L_S \approx 200\,\mathrm{mm}$, while the acoustic model gives the greatest change where L_S is the smallest. The reason of this discrepancy may be sought in the coupling of the excitation and the resonator, which is not incorporated into the acoustic model; however, this issue has not been examined yet in detail.

7.6.3 Prediction of the eigenfrequency-structure

Figure 7.14 displays the comparison of the third to sixth eigenfrequencies of experimental pipe #1 obtained from spectrum measurements (see also Figure 6.9) and the two simulation models as a function of the pipe length above the slot L_S. As it can be seen, both models capture the compressing behavior of eigenfrequencies and follow the tendency correctly when L_S is increased. However, the analytical tonehole model significantly underestimates the eigenfrequencies, and the resulting compression ratios differ remarkably from the measurement results. On the other hand, the numerical tuning slot model predicts the eigenfrequencies with very good accuracy, only minor deviations are observable in case of the fifth and sixth modes.

An example of the observed discrepancies of the eigenfrequency-structure given by the two models is depicted in Figure 7.15. The diagram displays the comparison of the input admittance of pipe #2 with the slot setup $w_S = 18\,\mathrm{mm}$, $h_S = 45\,\mathrm{mm}$, and $L_S = 77\,\mathrm{mm}$ in the middle frequency range. A remarkable dissimilarity between the two models is seen, especially around $1\,350\,\mathrm{Hz}$,

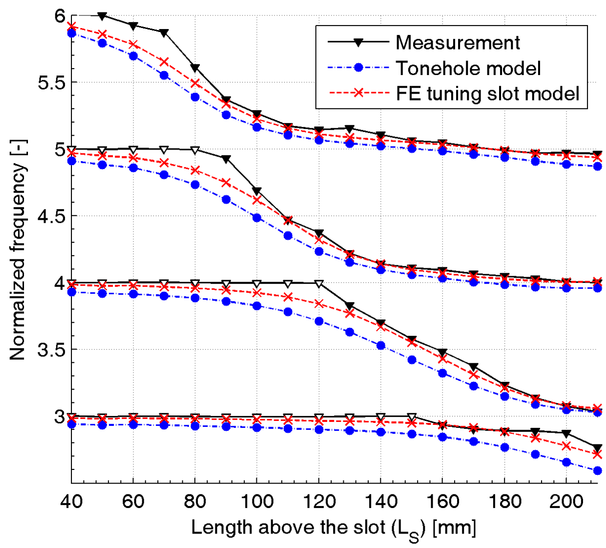

Figure 7.14. Comparison of the measured and simulated eigenfrequency-structure of pipe #1 with changing the length above the slot. The third to sixth eigenfrequencies are displayed (from bottom to top).

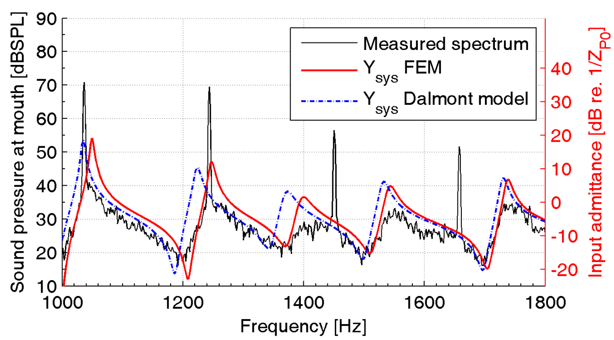

Figure 7.15. Example of the observed dissimilarities of the FEM and analytical model in the mid-frequency range. Pipe #2, $h_S = 20\,\mathrm{mm}$, $w_S = 12\,\mathrm{mm}$, and $L_S = 117\,\mathrm{mm}$.

where the analytical model predicts a local admittance maximum and the FEM model gives an admittance minimum. Apparently, these differences are only present in the middle frequency range. In the lower and higher ranges the input admittance functions show a good match. Similar discrepancies were observable in case of larger ($\delta > 0.7$) and oblong ($h_S/w_S > 2$) slots.

From the results presented above it can be assessed, that the accuracy of the prediction of the eigenfrequency-structure is improved to a great extent by applying the FE tuning slot model.

7.6.4 Direct comparison to measured spectra

Figure 7.16 presents the direct comparison of the measured spectra and simulated quantities. The diagrams show the results for experimental pipe #2 with the setup $h_S = 20\,\mathrm{mm}$, $w_S = 12\,\mathrm{mm}$, and $L_S = 117\,\mathrm{mm}$ (same as Fig. 7.15).[6] Since the cutoff frequency of the pipe is approximately $5\,700\,\mathrm{Hz}$, the theoretical range of validity of the one-dimensional waveguide model covers the displayed frequency range.

[6] As $p_{\mathrm{slot}}(f)$ is calculated assuming unit input particle velocity, the absolute amplitudes of the curves are not expected to match.

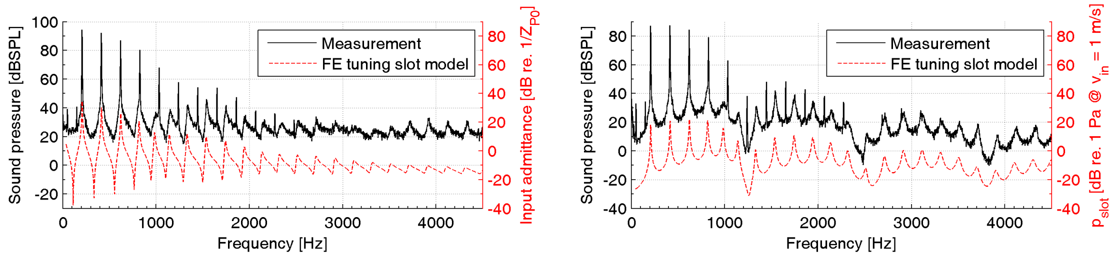

Figure 7.16. Comparison of measured spectra and simulated quantities. Experimental pipe #2, $h_\mathrm{S} = 20\,\mathrm{mm}$, $w_\mathrm{S} = 12\,\mathrm{mm}$, and $L_\mathrm{S} = 117\,\mathrm{mm}$. Left: Measurement at the mouth opening and the simulated input admittance. Right: Spectrum measured and simulated at the slot.

As it can be seen, a very good match of the spectral baselines and simulated functions is achieved in the whole frequency range. The calculated input admittance closely follows the baseline of the spectrum measured at the mouth opening. Higher eigenfrequencies (from the sixth mode) are also clearly followable in the measured spectrum. The abrupt inharmonicity appearing near the 5$^\mathrm{th}$–6$^\mathrm{th}$ mode can clearly be observed both in the measured spectrum and in the simulated input admittance function.

As far as the spectrum at the slot is concerned, it can be seen that the baseline is predicted with good accuracy using the numerical tuning slot model. The quasi-periodic envelope structure is attained with good precision. Similarly good match of the calculated functions and measured spectra has been found using different slot geometries on both pipes.

7.7 Conclusions

The design parameters of tuning slots were shown to have a great effect on the eigenfrequency-structure and the resulting sound quality in the previous chapter. The purpose of this chapter was to find a suitable acoustic model of the tuning slot, by which the effects observed in the measurements can be foretold.

Therefore, woodwind tonehole models were reviewed, with attention paid on the geometrical dissimilarities and the limitations of the common T-circuit model. By adapting the simulation technique proposed by Lefebvre & Scavone [91, 92], a numerical tuning slot model was set up utilizing the finite element and perfectly matched layer methods. The analytical tonehole and numerical tuning slot models were applied in the one-dimensional waveguide model of various pipes. Results from different models were directly compared to measurement data, examining the fundamental and the eigenfrequency-structure. The presented measurements and comparisons cover a wide range of slot parameters, regarding the effective radius and the oblongness of the slot.

The observed discrepancies between the models were explained by the examination of the equivalent lengths. It was shown that there is a remarkable deviation in the prediction of the series length correction t_a for large ($\delta \approx 1$) and oblong ($h_\mathrm{S}/w_\mathrm{S} \geq 2$) slots. Also the frequency dependence of the shunt length correction differs greatly in the numerical and analytical models. The latter difference is explained by the very low ratio of wall thickness to effective slot radius (t/b), where limitations of traditional analytical tonehole models are already exceeded.

It was found that both models can predict the fundamental frequency with good accuracy, except for the case of highly oblong slots ($h_\mathrm{S}/w_\mathrm{S} \approx 8$), where the analytical tonehole model underestimates the fundamental to a significant extent. The eigenfrequency-structure of the pipe is also predicted reliably by means of the finite element slot model, whereas significant dissimilarities of the two models were observed especially in the middle frequency range.

Finally, it can be stated that the proposed hybrid (waveguide/finite element) model can successfully be applied for the simulation of labial organ pipes with tuning slots. The model is capable of foretelling the most important acoustic properties of the resonator with good accuracy. Using the database created from the more than fifty finite element models, simulation of further tuning slot pipes can readily be performed. With the reliable prediction of the fundamental frequency and the eigenfrequency-structure, better control over the sound characteristics of tuning slot pipes could be attained in the future, exceeding the limitations of slot design rules currently applied in organ building practice. The latter goals could be achieved by incorporating the results of the acoustic model presented in this chapter into the design approach proposed in the previous chapter.

Chapter 8

Modeling the resonators of reed organ pipes

This chapter presents a hybrid technique for the acoustical modeling of resonators and shallots of lingual organ pipes. The proposed approach combines the one-dimensional model of an axisymmetric resonator and the three-dimensional finite element method extended by infinite elements for the simulation of the radiation impedance. From the FE/IE simulations a scalable database is created which facilitates the incorporation of the numerical results into the one-dimensional model. A simple low frequency approximation is applied to model the acoustic radiation from the shallot into the pipe boot. The introduced technique is validated by means of comparisons to transfer function measurements performed on resonators of different forms. The results indicate that the incorporation of the finite element results into the model leads to a remarkable improvement in the prediction of the natural resonance frequencies of the resonator. This chapter is a revised and extended version of the conference paper [C11].

8.1 Introduction

Unlike labial organ pipes discussed in Chapters 5–7, the pitch of lingual organ pipes is determined by the frequency of the vibrating tongue, rather than the acoustic modes of the resonator. Nevertheless, the resonator has an essential role in forming the timbre of pipe. Furthermore, due to the acoustic feedback mechanism, the resonator can also affect the frequency of the tongue vibration in a smaller or greater extent, depending on the strength of their coupling. Although the resonators of lingual pipes can have various forms, a great number of stops (such as *Crumhorns*, *Trumpets*, *Oboes* etc.) consist of axisymmetric pipes having conical and cylindrical parts. To be able to characterize such resonators acoustically, the one-dimensional transmission line model of cylindrical ducts—introduced in Section 3.3.2—is extended in this chapter to conical and composite waveguides.

symmetric resonators

Discussions with organ builder partners in the framework of a European project [3] have revealed that there are no common rules for designing the resonators of reed pipes. Measurements also prove that the design traditions applied currently in practice do not exploit the capabilities of the resonator to a full capacity. To arrive at a better efficiency of resonator design—i.e., to be able to scale the resonator based on the desired timbre—a first step is the establishment of an acoustical model capable of foretelling the acoustic behavior of the pipe accurately.

objective

This chapter introduces a novel hybrid technique for the prediction of the input admittance and input impedance functions of the shallot–resonator acoustic system. First, the theory of the propagation of acoustic waves in axisymmetric ducts is reviewed in Section 8.2. A simulation

structure

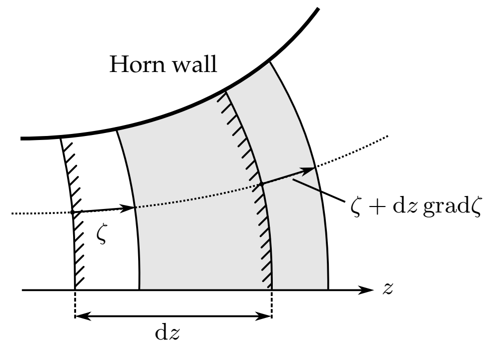

Figure 8.1. Motion of a curved shell of gas in a flaring horn, after [26]

technique for the radiation impedance from a conical pipe end is presented next in Section 8.3. Section 8.4 discusses a simple low frequency acoustic model of the shallot. Finally, the proposed method is validated by comparing the predicted frequencies of natural resonance to that of the same obtained by measurements in Section 8.5. An application based on the modeling approach presented in this chapter is introduced in Appendix C.

8.2 Wave propagation in axisymmetric ducts

8.2.1 Webster's horn equation

Propagation of acoustic waves in horns with axial symmetry have already been studied for long. In a low frequency approximation, where only waves propagating in the longitudinal direction are considered, the motion can be described by means of a one-dimensional wave equation, similar to the Helmholtz equation (3.28).

The wave equation can be derived following Benade & Jansson [26]. Let us consider the equation of motion for a curved shell of gas between two surfaces of equal phase, $S(z)$ and $S(z + \mathrm{d}z)$, as depicted in Figure 8.1. The volume of the gas is approximated by $S\mathrm{d}z$. When a sound wave propagates along the horn, the surface of the shell that was at z moves a distance of ζ, whereas the other surface moves the amount $\zeta + \mathrm{d}z\,\mathrm{grad}\zeta$. It should be noted that ζ must be defined to connotate the motion averaged over the surface of the shell [26].

The change of the shell volume can then be expressed as

$$\frac{\mathrm{d}V}{V} = \frac{1}{S}\frac{\mathrm{d}}{\mathrm{d}z}\left(S\zeta\right). \tag{8.1}$$

The instantaneous pressure produced by the change of volume $\mathrm{d}V$ is found as

$$p(z) = -B\frac{\mathrm{d}V}{V} = -\frac{B}{S}\frac{\mathrm{d}}{\mathrm{d}z}\left(S\zeta\right), \tag{8.2}$$

with $B = \rho_0 c^2$ denoting the bulk modulus of the fluid. Using Newton's second law, the accelaration of the mass of air contained in the shell can be written as

$$S\rho_0\mathrm{d}z\frac{\partial^2\zeta}{\partial t^2} = -\mathrm{d}z\frac{\partial p}{\partial z}S. \tag{8.3}$$

Finally, the wave equation is attained by eliminating ζ from equations (8.2) and (8.3). This is achieved by taking the second time derivative of (8.2), the derivative with respect to z of (8.3), and then substituting the former into the latter. With assuming that ρ_0 and c are constant in the domain of insterest, the result is *Webster's horn equation*, i.e.

Webster's horn equation

$$\frac{1}{c^2}\frac{\partial^2 p(z,t)}{\partial t^2} = \frac{\partial^2 p(z,t)}{\partial z^2} + \frac{1}{S}\frac{\partial p(z,t)}{\partial z}\frac{\mathrm{d}S}{\mathrm{d}z}. \tag{8.4}$$

Assuming time harmonic changes and defining the wave variable $\Psi(z) = \hat{p}(z)r(z)$, with $r(z)$ denoting the inner radius of the horn, the Webster equation can be rearranged in order to attain a form similar to the Helmholtz equation (3.21) as

$$\frac{\partial^2 \Psi(z)}{\partial z^2} + \left(k^2 - \frac{1}{r(z)} \frac{\partial^2 r(z)}{\partial z^2} \right) \Psi(z) = 0. \tag{8.5}$$

The function appearing in the second term on the right hand side

$$H(z) = \frac{1}{r(z)} \frac{\partial^2 r(z)}{\partial z^2} \tag{8.6}$$

horn function

is usually referred to as the *horn function*. It can be seen that equation (8.5) reduces to the one-dimensional Helmholtz equation (3.28) in case of a cylindrical duct, i.e. $r = \mathrm{const}$. Furthermore, if a conical duct is considered, i.e. $\mathrm{d}r/\mathrm{d}z = \mathrm{const}$, the horn function vanishes and equation (8.5) becomes identical to the Helmholtz equation (3.28) for the variable $\Psi(z)$.

Webster's horn equation (8.4) and its frequency domain form (8.5) have already been studied by a number of researchers. A complete review with more than two hundred references is found in [55]. Despite that the horn equation is already known for a hundred years, wave propagation in axisymmetric ducts is still being a subject of examinations, see e.g. references [69, 88].

It is useful to express the acoustic quantities, i.e. the volume velocity $U(z)$ and impedance $Z(z)$ from the wave variable $\Psi(z)$. The volume velocity is found by making use of the linearized version of Euler's equation (3.12) as

$$U(z) = \frac{S(z)}{\mathrm{j}\omega\rho_0} \frac{\Psi r' - \Psi' r}{r^2}. \tag{8.7}$$

volume velocity

The impedance $Z(z)$ is the ratio of the pressure $p(z)$ and the volume velocity $U(z)$:

$$Z(z) = \frac{p(z)}{U(z)} = \frac{\mathrm{j}\omega\rho_0}{S(z)} \frac{\Psi r}{\Psi r' - \Psi' r}. \tag{8.8}$$

acoustic impedance

8.2.2 Transmission line model of conical ducts

The transfer matrix relating the input and output sound pressure and acoustic volume velocity of a conical horn is defined in the same manner as in the case of cylindrical ducts. Making use of relations (8.7) and (8.8) the elements of the transfer matrix are attained by assuming zero volume velocity (to get T_{11} and T_{21}), or assuming zero pressure (to get T_{12} and T_{22}) at the output, respectively. The final expression for a cone of length L at the wave number k is obtained after some tedious steps (see e.g. [116, p. 106]) as

$$\mathbf{T}_{\text{cone}}(kL) = \begin{bmatrix} -m\dfrac{\sin(kL - \theta_{\text{out}})}{\sin\theta_{\text{out}}} & \mathrm{j}m\dfrac{1}{Z_{0,\text{out}}}\sin kL \\[2ex] \mathrm{j}mZ_{0,\text{in}}\dfrac{\sin(kL + \theta_{\text{in}} - \theta_{\text{out}})}{\sin\theta_{\text{in}}\sin\theta_{\text{out}}} & \dfrac{1}{m}\dfrac{\sin(kL + \theta_{\text{in}})}{\sin\theta_{\text{in}}} \end{bmatrix}, \tag{8.9}$$

transfer matrix of a conical duct

where m denotes the ratio of output and input radii $m = r_L/r_0$, the plane wave impedances are defined as $Z_{0,\text{in}} = \rho_0 c/(r_0^2\pi)$ and $Z_{0,\text{out}} = \rho_0 c/(r_L^2\pi)$, and the angles are $\theta_{\text{in}} = \tan^{-1}(kz_{\text{in}})$ and $\theta_{\text{out}} = \tan^{-1}(kz_{\text{out}})$, with z_{in} and z_{out} representing the distance of the cone's input and output planes from the apex, respectively. It is seen that by taking $r_L = r_0$ the expression gives the same result as (3.57).

For a composite duct consisting of straight, flaring, or tapering axisymmetrical sections, the resulting transfer matrix is calculated as the product of the sections' transfer matrices. Naturally, by expressing the input impedance from the transimmsion matrix—see equation (3.58)—the input impedance of a composite resonator can be found, as it is shown in Figure 8.2.

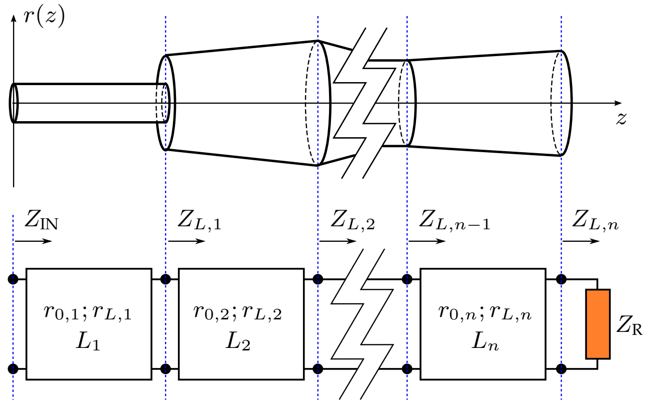

Figure 8.2. Geometry and equivalent distributed parameter circuit of an arbitrary composite resonator consisting of n sections and radiating into free field

8.2.3 Viscothermal losses

In case of a flaring or tapering section it is not straightforward to evaluate the effect of viscothermal losses. As proven in [88], the resulting lossy wavenumber k' and the corresponding wall absorption coefficient α_{w} can not be expressed in a simple analytical manner. Therefore, in order to incorporate viscothermal losses, an approximative approach is applied. The conical section is divided into n smaller sections, each having the length of L/n. Then, equation (3.40) is evaluated for each small section with substuting the effective radius r_{eff} in place of a. Since the wall absorption coefficient is inversely proportional to the radius, the effective radius of the ith small section $r_{\mathrm{eff}}^{(i)}$ is obtained as the harmonic mean of the input and output diameters:

effective radii

$$r_{\mathrm{eff}}^{(i)} = 2\left(\frac{n}{(n-i+1)r_0 + (i-1)r_L} + \frac{n}{(n-i)r_0 + ir_L}\right)^{-1}. \tag{8.10}$$

8.3 Simulation of the radiation impedance

An other problem occuring in case of open conical pipe ends is the calculation of the radation impedance. There are no analytical formulations known to the author that could explicitly evaluate the radiation impedance from a flaring or tapering pipe end. In the corresponding literature different approximations are applied for the characterization of the radiation and wave propagation properties of conical pipe ends and junctions, see e.g. references [39, 40, 59, 70]. In order to overcome the limitations of analytical approximations of the radiation impedance, finite element (FE) modeling is applied in this study. These simulations are discussed in the sequel.

finite element model

In the finite element simulation, the air column enclosed by a conical resonator section was meshed using hexahedral elements. Models of conical air columns with different opening angles α were constructed. Free field radiation conditions were taken into account by means of *infinite elements* (see Section 4.3). To be able to apply the infinite element method, the simulation domain had to be extended by a circumscribing cylinder, onto which infinite elements were attached. Since the model had two planes of symmetry in the cartesian coordinate system, only $1/4$ of the whole geometry had to be built allowing better spatial resolution at the same computational cost. The simulation arrangement is depicted in Figure 8.3.

The opening angle α of the cone models was varied from $-60°$ to $+60°$ in $2°$ steps resulting in a total of 61 different models. All meshes were created automatically utilizing the mesh creation and manipulation tools of `NiHu` (see Appendix D). The parameters of the generated finite

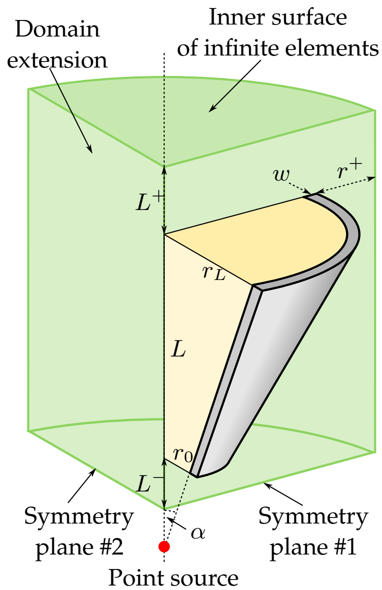

Figure 8.3. Arrangement of the finite/infinite element simulation of the radiation impedance from a conical pipe end

Parameter	Symbol	Value [mm]
Radius at open end	r_{L}	25.0
Maximal cone length	L_{max}	75.0
Minimal cone length	L_{min}	12.0
Wall width	w	2.00
Maximal radius	$r_{0,\mathrm{max}}$	75.0
Minimal radius	$r_{0,\mathrm{min}}$	5.0
Extension radius	r^+	25.0
Extension above	L^+	50.0
Extension below	L^-	6.25
Infinite element order	P	6
Elements / λ [–]	—	12
Degrees of freedom [–]	DOF	165–276 k

Table 8.1. Geometry and model parameters of the finite / infinite element models applied in radiation impedance simulations

element models are summarized in Table 8.1. In order to keep the number of elements and nodes at a computationally affordable quantity, the conditions $r_{0,\mathrm{min}} \leq r_0 \leq r_{0,\mathrm{max}}$ and $L_{\mathrm{min}} \leq L \leq L_{\mathrm{max}}$ were always enforced. Infinite elements of polynomial order $P = 6$ were applied, with the polynomials defined in accordance with equations (4.26) and (4.27). The latter choice resulted in very small reflection from the inner surface of the infinite elements and a reasonable computational effort at the same time. The element size was chosen to provide at least 12 elements per wavelength at the largest test frequency, which resulted in 165 000 to 276 000 degrees of freedom.

The excitation was given as a point source located at the apex of the cone, except the case of the cylindrical pipe (i.e. $\alpha = 0°$), when a plane wave source was assumed. The amplitude of the source was always normalized to give unit pressure at the center point of the bottom (input) plane of the conical section. The excitation was incorporated into the simulation by imposing Dirichlet boundary conditions on the input plane of the conical section. excitation

The simulations were run using the FE/IE model assembler tools of the `NiHu` toolbox and the built-in BiCGSTAB iterative solver of Matlab. The test frequencies covered the range of nondimensional frequencies kr_{L} from 0.001 to 3.82, divided into 256 equal steps. The simulation was run in six parallel threads on one node of a computational grid with Intel Xeon X5680 cores running at 3.33 GHz and took approximately a total of 120 hours to finish for all 61 models.

From the FE/IE simulation the pressure field $\hat{p}(\boldsymbol{x}, k)$ was obtained for the whole simulation domain, given by the finite element interpolation functions and the corresponding nodal weights. The radiation impedance was calculated using the formula postprocessing

$$Z_{\mathrm{R}}(k) = \frac{1}{|S|} \frac{\int_S p(\boldsymbol{x}, k)\,\mathrm{d}\boldsymbol{x}}{\int_S v_n(\boldsymbol{x}, k)\,\mathrm{d}\boldsymbol{x}}, \tag{8.11}$$

radiation impedance

with S denoting the cross section surface at the open end of the cone and $v_n(\boldsymbol{x}, k)$ being the normal component of the particle velocity. The latter was obtained making use of the linearized Euler equation (3.12). The integral in equation (8.11) was calculated as the weighted sum of the nodal values with the weighting factors being proportional to the size of the corresponding elements. By means of equation (8.11) the finite element results of the 61 models are transformed

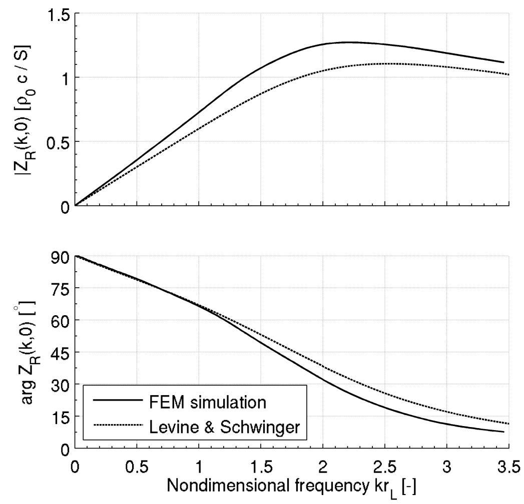

Figure 8.4. Comparison of the radiation impedance from an unflanged circular pipe end obtained by finite element simulations and the formulation of Levine & Schwinger [93]

into a single equivalent concentrated parameter, represented by the bivariate function $Z_\mathrm{R}(k, \alpha)$, which can readily be inserted into the one-dimensional acoustic model shown in Figure 8.2.

comparison with Levine & Schwinger

Simulation results were compared to the theoretical values calculated for a cylindrical tube by Levine & Schwinger [93], see also equation (3.65). The comparison of the resulting radiation impedance for the unflanged cylindrical ($\alpha = 0°$) tube is shown in Figure 8.4. The magnitude of the impedance $|Z_\mathrm{R}(k, 0)|$ is shown in units normalized by the acoustic plane wave impedance $Z_0 = \rho_0 c/S$. The finite element method gives a greater magnitude for the radiation impedance, with a maximal difference of $\approx 20\%$ from the analytical approximation, observed around $kr_\mathrm{L} \approx 2.0$. The phase of the impedance $\arg Z_\mathrm{R}(k, 0)$ is very similar for the two models, only small deviations of 7–8° are observed. One reason of the deviation between the two models can be the finite thickness of the walls, which is inherently taken into account in the FEM, but disregarded by the analytical approximation.

Figure 8.5 presents the results of the finite element model for the full range of simulated opening angles ($-60° \leq \alpha \leq +60°$). The amplitude and the phase of the complex quantity $Z_\mathrm{R}^{(\mathrm{sim})}/Z_\mathrm{R}^{(\mathrm{L\&S})}$ are displayed, with $Z_\mathrm{R}^{(\mathrm{sim})}$ and $Z_\mathrm{R}^{(\mathrm{L\&S})}$ denoting the simulated and analytically calculated values, respectively. In the frequency range above the cutoff frequency, no results are displayed. (Note: the cutoff frequency is smaller than $kr_\mathrm{L} = 3.82$ in case of tapering sections, since the input diameter is greater in these cases.) The results shown in Figure 8.4 are the same profiles as the ones found at $\alpha = 0°$ in Figure 8.5.

From the top plot of Figure 8.5 it can be seen that the difference in the magnitudes is significant in case of highly flaring or tapering cones. For example, in case of a flaring tube with $\alpha = -30°$ angle of opening, the estimation for the absolute value of the radiation impedance differs as much as 30% even in the low frequency range. The phase difference shown in the bottom plot of Figure 8.5 has a typical range of $-10°$ to $+10°$. Greater differences up to $-25°$ are only observed in case of quickly tapering cones at high frequencies. With the phase differences being relatively small, the deviations in the magnitude of the radiation impedance can readily be interpreted as discrepancies of the corresponding length corrections. Since the length correction affects the effective length of the resonator, better prediction of the radiation impedance can result in the more accurate approximation of the input admittance function and frequencies of natural resonance of the whole resonator. These expectations are tested later in Section 8.5.

expectations

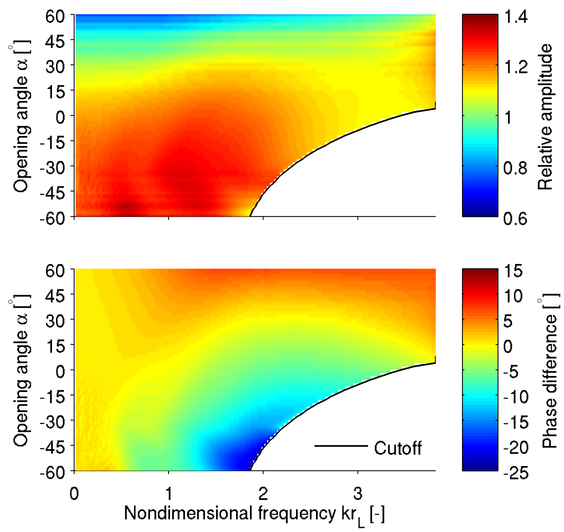

Figure 8.5. Results of radiation impedance simulation for conical pipe ends compared to the analytical approach for a straight open end of Levine & Schwinger [93]

8.4 A low frequency shallot model

Since the shallot is also a part of the acoustic resonator of a reed pipe, it also has to be incorporated into the one-dimensional model for the proper approximation of the input admittance and natural resonance frequencies. The tongue side of the shallot can have various forms, which can have a significant effect on the sound characteristics of the pipes, see e.g. publications [O2] or [C16]. Because of the movement of the tongue during sound generation, the radiation impedance of the tongue side of the shallot depends on the amplitude of the tongue vibration and can not be calculated or simulated in a straightforward manner. Furthermore, in the thin opening viscous and thermal losses can have a great influence on the acoustic behavior of the shallot. Thus, the exact quantification of this impedance is not an objective of this chapter, yet a much simpler, low frequency approximation is sought, which can easily be applied in the one-dimensional framework and in the design practice of resonators.

In the low frequency approximation the radiation from the tongue side of the shallot is represented by a single length correction parameter ΔL_{sha}, which is determined in the sequel. Since the boot end of the shallot is open, its acoustic length should be calculated from the opening point taking into account the length correction effect, as shown in Figure 8.6(b). The opening point is located at the beginning of the free tongue part, at the position of the tuning wire, as indicated in Figure 8.6.[1] The length correction is proportional to the change of acoustic impedance at the opening. Since the acoustic impedance is inversely proportional to the cross sectional area, the magnitude of the length correction is dependent mainly on the change of the area at the opening. The surface of the wave fronts inside the shallot equals the cross sectional area of the shallot S_{sha}, while the surface of the opening S_{open} is the free surface of the small wedge appearing under the tongue, as depicted in Figure 8.6(a). The open surface is marked by transparent green in the figure. Similar to the length correction of the mouth in case of labial organ pipes, see eq. (3.68), the relation for the length correction of the shallot can be defined as

$$\Delta L_{\text{sha}} = C\frac{S_{\text{sha}}}{\sqrt{S_{\text{open}}}}, \tag{8.12}$$

shallot length correction

[1]Due to the reed curvature and friction effects in the small opening the effective free length may be shorter a few millimeters; however, this effect is not taken into account here.

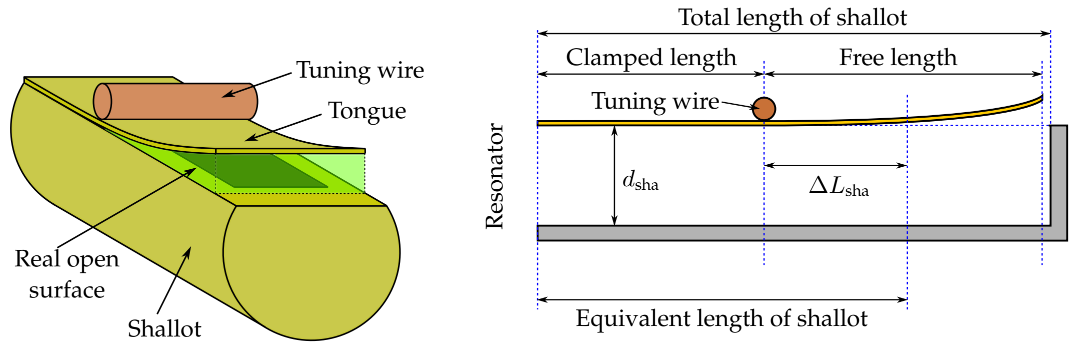

(a) Open surface under the tongue

(b) Shallot length correction and effective length

Figure 8.6. Calculation of the effective length of the shallot

where ΔL_{sha} is the length correction, $S_{\text{sha}} = \pi r_{\text{sha}}^2$ is the cross sectional area of the shallot, S_{open} is the surface of the opening with the tongue being in its equilibrium position, r_{sha} is the inner radius of the shallot, and C is a dimensionless constant that is to be determined such that the best fit to measurement results is attained.

The value of C depends on the geometry of the opening. As it was discussed earlier in Section 3.4.2, in case of the pipe mouth of a labial pipe $C = 0.732$ is appropriate. The exact value can not be determined in a straightforward manner; however, comparison to measurement results indicate that $C \approx 2.2$ is a reasonable choice here, which leads to good agreement with measured data. The area of the opening S_{open} is also cumbersome to calculate explicitily, but can be approximated well by regarding the two sides of the opening as triangles. In this case the opening area is obtained as

equivalent opening surface

$$S_{\text{open}} \approx h_{\text{open}} \left(l_{\text{free}} + w_{\text{tongue}} \right) , \tag{8.13}$$

with h_{open} denoting the height of the opening, l_{free} the free length of the tongue, and w_{tongue} the tongue width. The typical values of surface ratios were in between 1.0 and 5.0 for the shallots examined, which means that the length correction is roughly between twice and four times the inner diameter of the shallot.

Finally, the effective length of the shallot can be calculated as displayed in Figure 8.6, by summing the clamped length of the tongue L_{clamped} and the length correction:

effective length of shallot

$$L_{\text{sha,eff}} = L_{\text{clamped}} + \Delta L_{\text{sha}}. \tag{8.14}$$

Despite the simplicity of the above approximations, they can lead to accurate results in the low frequency range, as will be shown in the following. Nevertheless, since the length correction and the radiation impedance are frequency dependent in reality, the error of the approximation is expected to increase with the frequency. To follow the tendencies of impacts of changing the geometry of the resonator and the shallot—and to validate the acoustic model—the above approximation is sufficient, as the first few eigenfrequencies that influence the sound characteristics to the greatest extent are always located in the low frequency range.

8.5 Validation

In this section the proposed one-dimensional acoustic model of axisymmetric resonators and shallots is validated by means of comparison to measurement results. First, a measurement tech-

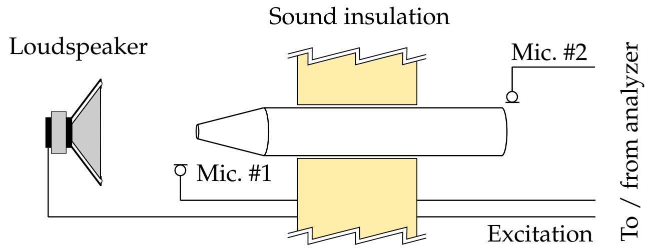

Figure 8.7. Arrangement of transfer function measurements

nique is introduced for the determination of the transfer function and the natural resonance frequencies of the resonator. Then, results from measurements and the one-dimensional model are compared for different resonator types. This section aims at presenting the capabilities of the proposed acoustic model without discussing all results in detail; hence, not all measurements and results are presented here. For a detailed description of all measurement results the reader is referred to the technical report [T4].

8.5.1 Transfer function measurements

To attain the eigenfrequencies of a resonator experimentally, either its input impedance function or its transfer function must be measured. When the complete input impedance function is not needed explicitly, or when the special equipment to measure the input impedance function is not available at hand, it is easier to measure the transfer function as it requires less effort and can be carried out using general equipment. The transfer function relates the sound pressure at the open end of the resonator with that at the resonator input. The maxima of the transfer function are coincident with the maxima of the input admittance function; however, the minima of the input admittance (i.e. maxima of the input impedance) can not be obtained from the transfer function measurement. In case of reed pipes it would be more appropriate to find the maxima of the input impedance, as far as the coupling to the excitation mechanism or sound synthesis is concerned. However, for the separate examination of the acoustic resonator and the shallot the examination of the input admittance is also suitable. In the following paragraphs the term eigenfrequency refers to a maximum of the input admittance.

measurement setup

To determine the transfer function of the resonator a function generator, a loudspeaker, and two calibrated microphones are required as depicted in Figure 8.7. The transfer function measurement is performed in an anechoic room, where minimal disturbance from the acoustic environment can be ensured. The loudspeaker is located near the input end of the resonator, at a distance so that the resonator input is already in the far field of the speaker. The first micrhophone is placed near (at a distance of $\approx 10\,\mathrm{cm}$) the resonator input and is used in order to measure the input and compensate for the frequency characteristics of the loudspeaker. The second microphone is located at a distance of $\approx 5\,\mathrm{cm}$ from the output end of the resonator. In order to attenuate the direct propagation from the loudspeaker to the second microphone and thus increase the signal to noise ratio, the two ends of the resonator should be insulated from each other by means of sound absorbing materials, as much as possible.

excitation and evaluation

The measurement can be carried out using a broadband excitation signal, such as a swept sine, white noise, or MLS. The transfer function can be calculated by postprocessing the recorded microphone signals, or it can readily be attained using a two-channel FFT analyzer. The measurements presented in the sequel were carried out in the anechoic chamber of the Fraunhofer Institute for Building Physics. The excitation was emitted by an ordinary loudspeaker built into a box and the signals were recorded by two BK 4165 type 1/2" condenser microphones. The excitation was a swept sine from 0 to $8\,000\,\mathrm{Hz}$ frequency, provided by a two-channel FFT analyzer (HP-35670A) that also evaluated the measured transfer functions with $1\,\mathrm{Hz}$ resolution.

Parameter	Values [mm] Normal length	Double length
Wall width	0.75	0.75
Outer Ø open end	28.70	28.70
Outer Ø foot end	11.35	11.90
Lateral length of foot	89.0	86.0
Length of straight part	265.5	918.0

Table 8.2. Geometry of *Crumhorn* resonators

Parameter	Value
Wall width	1.0 mm
Inner length	57.5 mm
Outer diameter	7.35 mm
Tounge free length	15.0 mm
Tounge width	7.1 mm
Tongue opening height	0.7 mm
Equivalent opening area	15.5 mm^2
Shallot effective length	55.1 mm

Table 8.3. Parameters of the *Crumhorn* shallot

	Normal length						Double length					
	Without shallot			With shallot			Without shallot			With shallot		
M.	Meas	Calc	Err	Meas	Calc	Err	Meas	Calc	Err	Meas	Calc	Err
1^{st}	378	379	4.6	292	292	0.0	148	149	11.7	106	106	0.0
2^{nd}	880	881	2.0	809	814	10.7	307	309	11.2	273	275	12.6
3^{rd}	1 399	1 402	3.7	1 281	1 304	30.8	476	478	7.3	448	450	7.7
4^{th}	1 894	1 896	1.8	1 671	1 735	65.1	649	651	5.3	624	626	5.5
5^{th}	2 354	2 358	2.9	2 095	2 166	57.7	824	826	4.2	797	802	10.8

Table 8.4. Comparison of measured and calculated mode frequencies of normal and double length *Crumhorn* resonators without shallot. Measured and calculated values are in Hz units, errors are given in cents.

8.5.2 *Crumhorn* pipes

*Crumhorn*s are beating reed pipes, whose resonators consist of a long cylindrical section with open end and a short conical part that connects the cylindrical part and the shallot (see the resonator shown in Figure 8.7). Two *Crumhorn* resonators are examined here, a normal length and a "double length" version, both operating with the same shallot. The pipes were scaled and tuned to 2′ C pitch, i.e. 262 Hz, with the dimensions listed in Tables 8.2 and 8.3. Interestingly, the total length of the double length pipe is nearly three times that of the normal length pipe.

The measured and calculated eigenfrequencies for the normal and double length Crumhorn pipes with and without shallot are shown in Table 8.4. When the resonators were examined without the shallot, a very good match of measured and calculated eigenfrequencies is observed, with the maximal discrepancy being smaller than 12 cents. A similarly good fit is found for the higher modes, which are not shown in the table. When the shallot is also considered, good match is only found in the low frequency regime. The increasing discrepancy of the results is better observable in case of the normal length pipe, where the error of the prediction goes up to 65 cents at the fourth mode. Such tendencies are expected as the acoustic model of the shallot presented in Section 8.4 relies on a low frequency approximation.

8.5.3 The *Vox humana* resonator

The design of the *Vox humana* ("human voice") resonator differs a lot from the *Crumhorn* resonator regarding both its geometry and its purpose. The *Vox humana* resonator consists of three sections: (1) the shallot continues in a thin straight neck, which has a length of 2/5 of that of the complete resonator, (2) a flaring section, nearly as long as the neck, where the diameter increases greatly, and (3) a tapering section, which is open at the top. The resonator is cut to tune and can be tuned

Parameter	Value [mm]	Parameter	Value [mm]
Wall width at pipe foot	1.0	Outer Ø at open end	19.0
Wall width at open end	1.4	Lateral length of neck	56.5
Outer Ø at foot end	11.9	Lateral length of mid part	64.7
Outer Ø at middle	52.0	Lateral length of top part	35.5

Table 8.5. Geometry of the *Vox humana* resonator

Mode	Meas	$Z_\mathrm{R}^{(\mathrm{L\&S})}$	Err	$Z_\mathrm{R}^{(\mathrm{sim})}$	Err
1st	**735**	**788**	**120.5**	**748**	**25.7**
2nd	2 319	2 339	14.9	2 317	−1.5
3rd	3 192	3 239	25.3	3 212	10.8
4th	4 605	4 695	33.5	4 650	16.8
5th	5 425	5 566	44.4	5 502	24.4
6th	6 469	6 695	59.4	6 619	39.7

Table 8.6. Measured and calculated eigenfrequencies of the *Vox humana* resonator. $Z_\mathrm{R}^{(\mathrm{L\&S})}$: Z_R calculated by formulas of Levine & Schwinger, $Z_\mathrm{R}^{(\mathrm{sim})}$: Z_R obtained from FE / IE models. Eigenfrequencies displayed in Hz units, errors are in cents.

only in one direction by cutting from the top. While the *Crumhorn* resonator (with shallot) is tuned near the fundamental frequency, the *Vox humana* is usually tuned to the third harmonic of the fundamental (196 Hz for this pipe) in order to amplify the fifth above the octave in the steady state pipe sound. This resonator is only examined without its shallot here, for the sake of brevity. The geometrical parameters of the resonator are listed in Table 8.5.

radiation impedance models

Table 8.6 displays the measurement and calculation results for the eigenfrequencies of the *Vox humana* resonator. The calculation was performed with two different settings. First, the theory of Levine & Schwinger [93] was used for the calculation of the radiation impedance Z_R, see eq. (3.65). The corresponding results are shown in the column $Z_\mathrm{R}^{(\mathrm{L\&S})}$. Second, radiation impedance results from the finite element simulations presented in Section 8.3 were substituted into the one-dimensional model. The respective results are shown in the column $Z_\mathrm{R}^{(\mathrm{sim})}$. As can be seen, applying the FEM results to determine the radiation impedance has a remarkable effect on the accuracy of the results, especially in the case of the first eigenfrequency. While the analytical formula leads to an error of 120 cents in this case, the FEM impedance model significantly reduces this error to 26 cents. Apparently, the impact of the radiation impedance is smaller on the frequencies of higher modes and the errors given by the two approaches have the same order of magnitude here with the FEM errors being slightly smaller.

FEM / PML simualation

In order to get a picture of the sound pressure field in the resonator at the frequencies of natural resonance, a finite element model of the resonator was assembled. The simulation arrangement imitated that of the transfer function measurements, as shown in Figure 8.8(a). Free field wave propagation conditions were ensured by applying the perfectly matched layer (PML) technique, as introduced in Section 4.4. The excitation was a point source located in the axis of the resonator, below the neck. The simulation was performed using the toolbox `NiHu`, see Appendix D.

The pressure fields inside the resonator are shown in Figure 8.8(b) for the first four modes. The planar and spherical wavefronts are clearly observable in the cylindrical and conical parts of the resonator, respectively. Except for the first mode, the strongest pressure oscillations develop in the straight neck part of the resonator. The resulting eigenfrequencies show a good match with the measured ones with a slight underprediction of their frequencies, except for the first mode.

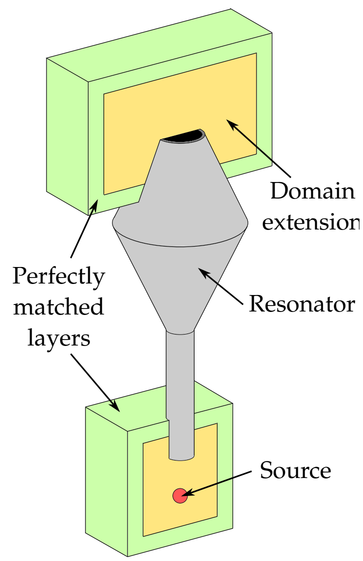

(a) Simulation arrangement

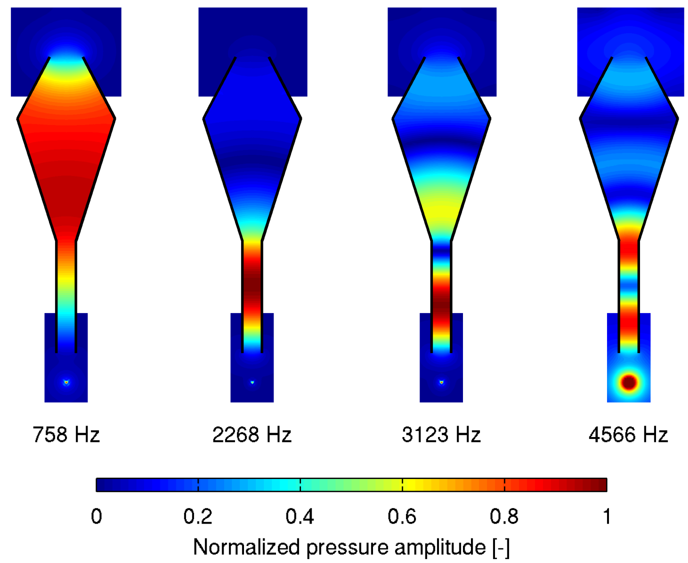

(b) First four acoustic modes of the resonator

Figure 8.8. Simulation of the *Vox humana* resonator

evaluation

Based on the results presented in this section, it can be assessed, that the two proposed supplements for the one-dimensional resonator model—i.e. calculation of the radiation impedance by means of the FEM and the low frequency shallot model—can both be successfully applied for the prediction of the natural resonance frequencies of axisymmetric resonators. Both the radiation impedance and the shallot models could be extended by taking other effects (such as viscothermal losses) into account; however, these improvements are out of the scope of this chapter.

8.6 Concluding remarks

In this chapter a one-dimensional modeling approach for composite resonators having axial symmetry was introduced. Such resonators are used in a great number of reed pipe stops in the organ, such as the *Crumhorn*, the *Trumpet*, the *Oboe*, the *Clarinet*, and the *Vox humana* among others. The general transmission line model was supplemented by two novel components: (1) the finite element simulation of the radiation impedance, and (2) a low frequency shallot model. By means of comparison to measurement results it was shown, that the one-dimensional model with the proposed extensions is capable of the more accurate prediction of the natural resonance frequencies of axisymmetric resonators and shallots of reed organ pipes. The results presented in this section have been incorporated into the software tool `ReedResonatorSim`, introduced later in Appendix C.

application

Chapter 9

Air jet and edge tone simulation in an organ pipe foot model

Different computational fluid dynamic (CFD) models for the simulations of the air jet emerging in the windway of a labial organ pipe are reported and evaluated in this chapter. The numerical examination is carried out using 2D and 3D geometries with a laminar and a Large Eddy Simulation (LES) model. Two different configurations of the air jet are investigated here. First, the free jet is examined, without the interacion with the upper lip. The quality of the simulation results for this model is assessed by means of comparison to reproducible hot wire anemometer measurements carried out on a high precision pipe foot model. In the second arrangement, the upper lip is included in the model and the jet shows oscillations around this edge. The modal frequencies of the resulting edge tone are compared to sound recordings of the edge tone on the same pipe foot model. It is shown, that the extension of the simulation model into three dimensions has a remarkable impact on the quality of the simulation results in both configurations. This chapter is a revised and extended version of the conference paper [C13].

9.1 Introduction

Examination of the air jet and edge tone generation in flue organ pipes by means of computational fluid dynamics aims at gaining knowledge about the effect of the geometry of the pipe mouth and the parameters adjusted in various voicing steps on the sound generation of the pipe, especially in the attack phase. While these effects can also be investigated by means of experiments [12, 119], the numerical framework provides more flexibility and is cheaper than measuerements on prototypes requiring special equipment. motivation

In particular, the aim of the study presented here is to extend two-dimensional air jet and edge tone simulations published recently by Vaik & Paál [140] into three dimensions. The reason for this extension is twofold. On the one hand, the effect of the 3D extension on the simulation results—which was claimed to be negligible by the aforementioned authors—can be examined. On the other hand, 3D simulations are necessary to model geometries that are inherently three-dimensional. One specific example is the simulation of *nicking*, a voicing step often applied in labial organ pipes, which can be an interesting target of future examinations.

Beside playing an important role in the sound generation of air reed wind instruments, the edge tone phenomenon is also present in other industrial applications, such as the wind noise generated by pantographs of high-speed electric trains, for example. It was found earlier (see e.g. [44, 73]) that the edge tone has tonal components with clearly distinguishable frequencies, also called modes or stages [121]. In case of labial organ pipes the resulting characteristics of the the edge tone phenomenon

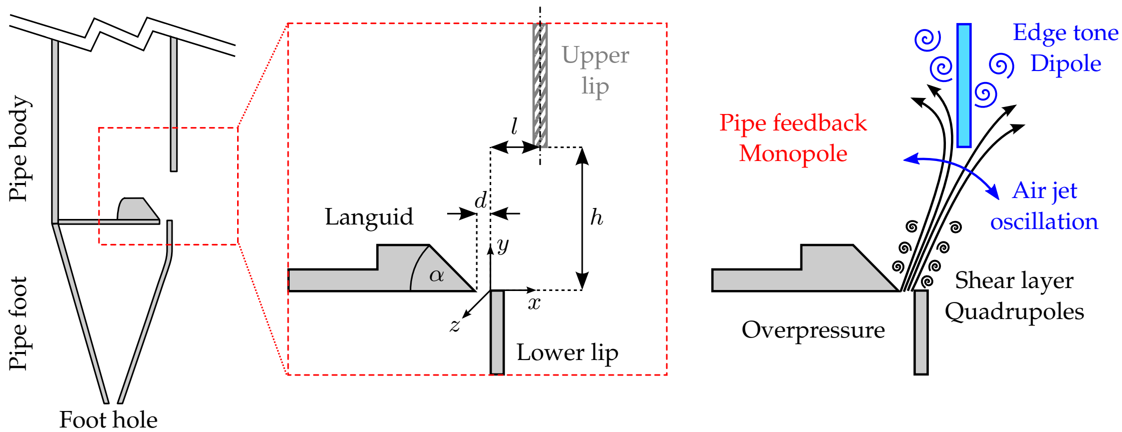

Figure 9.1. Außerlechner's pipe foot model [18, 19]. Left: geometry and adjustable parameters. Right: Air jet and edge tone generation in the foot model and the corresponding aeroacoustic source types.

pipe sound are attained by the coupling of the excitation mechanism and the acoustic resonator, as it was discussed in Chapter 2. In the process of voicing the organ builders tune the excitation (i.e. the air jet and the edge tone) to arrive at the desired speech of the pipe. This is traditionally done by modifying the flow geometry in fine steps during the voicing phase, see Section 2.1.4. The edge tone is also an important component of the pipe sound in the attack transient, it can often be heard in the initial phase of the sound. In the steady state pipe sound, the edge tone can also appear in some special cases, resulting in a "rough" sound. The latter phenomenon was studied recently by Trommer *et al.* [139].

recent results

The edge tone and its effect on the sound generation of flue organ pipes have already been investigated by a number of researchers, as it was discussed in Chapter 2. In a recent paper by Vaik & Paál [140] flow simulation results in an organ pipe foot model using different turbulence models have been published. Good agreement with the measurements of Außerlechner *et al.* [19] has been found. However, the investigations were limited to two-dimensional models and thus three-dimensional effects inside the flow field were not considered.

objectives

The objectives of this contribution are to extend the flow simulation model into three dimensions and to assess the quality of the results obtained using 2D and 3D models by means of comparison with previous CFD results and measurements. Two main flow configurations are examined. In the first case a free jet without upper lip is discussed and the resulting flow profiles are evaluated. The second case focuses on the edge tone with the analysis of its tonal components.

9.2 The pipe foot model

The pipe foot model of Außerlechner [18, 19] is displayed in Figure 9.1. The purpose of this model is to provide a chance for carrying out precise reproducible measurements and to offer the possibility to tune various parameters of the geometry by means of precision micrometer screws. The left hand side of Figure 9.1 shows the adjustable parameters. The position of the model parts are defined in a cartesian coordinate system with the origin being at the inner edge of the lower lip. The width of the windway is denoted by d, the angle of the languid is α. The upper lip is a removable component in the model, its x and y coordinates are denoted by l and h, respectively.

The model works the same way as the foot of a real labial organ pipe. It is set up on a windchest, which is connected to a ventilation system, providing the required air flow. When the valve in the windchest is opened, air flows inside the pipe foot and an overpressure is created. Due to this overpressure air starts to flow from the pipe foot through the windway forming a thin jet.

If the upper lip is removed, the jet is considered free. In this case *shear layers* are present on both sides of the jet as depicted in the right hand side of Figure 9.1. The vortices inside the shear layer form a *Kármán vortex street*. From the aeroacoustic point of view the pressure fluctuations of the free jet flow inside the shear layer are quadrupole sources with a broadband noise spectrum. the free jet

When the upper lip is present in the model, the air jet hits it and starts a quasi-periodic motion around the edge. The pressure fluctuations on the sides of the lip have opposite phases in operation, and hence the lip acts as a dipole sound source. Due to the oscillation of the air jet, vortices are generated near the edge of the upper lip as depicted in the right hand side of Figure 9.1. edge tone generation

In a complete pipe model, the acoustic feedback from the resonator has a very strong effect on the flow in the steady state and the oscillation frequency of the jet are synchornized with the acoustic oscillations in the resonator in this configuration. From an aeroacoustic viewpoint, the presence of the resonator also means the appearance of a monopole sound source. Nevertheless, our discussion here is limited to the free jet and edge tone generartion cases. Thus, the resonator is not a part of the computational model and the acoustic feedback effect is not considered here.

9.3 The numerical framework

The numerical model was implemented inside the `OpenFOAM 2.1` framework [118] based on the three-dimensional *finite volume method*. The governing equations of the model are the conservation of mass (3.2) and the conservation of momentum (3.5). By assuming constant density and taking both pressure and shear forces into account in the momentum conservation equation, the incompressible set of *Navier – Stokes equations* are obtained. For a *newtonian fluid* the set of equations to be solved over the numerical grid is:

$$\frac{\partial \overline{u}_i}{\partial x_i} = 0 \tag{9.1a}$$

$$\frac{\partial \overline{u}_i}{\partial t} + \frac{\partial \left(\overline{u_i u_j}\right)}{\partial x_j} = -\frac{1}{\rho_0}\frac{\partial \overline{p}}{\partial x_i} + 2\nu \frac{\partial S_{ij}}{\partial x_j}, \tag{9.1b}$$

Navier – Stokes equations

with u denoting the velocity, p the pressure, ρ_0 the density, and ν the kinematic viscosity of the fluid. The notation $\bar{\cdot}$ symbolizes grid-filtered variables. The rate of strain tensor S is defined as $S_{ij} = \frac{1}{2}(\partial \overline{u}_i/\partial x_j + \partial \overline{u}_j/\partial x_i)$. Einstein notation is applied here and subsequently. The grid-filtered advection term $\overline{u_i u_j}$ can be expressed as

$$\overline{u_i u_j} = \tau^r_{ij} + \overline{u}_i \overline{u}_j, \tag{9.2}$$

with the *residual stress tensor* τ^r_{ij} containing all unclosed terms. When no turbulence model is used (i.e. in the laminar approximation), the residual stress tensor τ^r_{ij} is simply omitted.

9.3.1 Dynamic Smagorinsky LES turbulence model

In order to arrive at a more sophisticated approximation of the grid-filtered advection term $\overline{u_i u_j}$ compared to the simple laminar model, different turbulence models can be applied. Applying turbulence models can enhance the reliability of the CFD simulations without the need of increasing the spatial resolution of the computational domain and hence keeping the computational costs affordable. One of the popular choices of turbulence models is the Smagorinsky model thanks to its simplicity. In the Smagorinsky turbulence model [132] the residual stress tensor τ^r_{ij} is approximated by introducing the artificial kinematic viscosity (also known as eddy viscosity) denoted by ν_T as follows:

$$\tau^r_{ij} - \frac{1}{3}\delta_{ij}\tau^r_{kk} = -2\nu_T \overline{S}_{ij} = -2C\Delta^2 \left|\overline{S}\right| \overline{S}_{ij}, \tag{9.3}$$

artificial kinematic viscosity

where δ_{ij} is the Kronecker symbol, Δ is the grid size and C is the Smagorinsky constant. The shorthand notation $\left|\overline{S}\right| = (2\overline{S}_{kl}\overline{S}_{kl})^{1/2}$ is applied.

In the LES framework filtering by a so-called test filter, denoted by $\widehat{\cdot}$ is introduced. By applying the test filter to the Navier – Stokes equations (9.1), an approximation of the subtest-scale stress tensor T_{ij} can be attained similar to (9.3)

$$T_{ij} - \frac{1}{3}\delta_{ij}T_{kk} = -2C\widehat{\Delta}^2\left|\widehat{\overline{S}}\right|\widehat{\overline{S}}_{ij}, \tag{9.4}$$

where $\widehat{\Delta}$ is the test filter width. By expressing the resovled turbulent stress tensor L_{ij} the Germano identity is obtained:

$$L_{ij} = T_{ij} - \widehat{\tau}^r_{ij} = \widehat{\overline{u}_i\overline{u}_j} - \widehat{\overline{u}}_i\widehat{\overline{u}}_j. \tag{9.5}$$

The dynamic Smagorinsky LES model proposed by Lilly [94] finds the locally dependent value of C by substituting (9.4) into (9.5) and using a least-squares error method to satisfy the resulting overdetermined tensor equation. The optimal solution is found as

dynamic Smagorinsky model

$$C = \frac{1}{2}\frac{L_{ij}M_{ij}}{M_{ij}^2}, \qquad \text{with} \qquad M_{ij} = \Delta^2\widehat{\left|\overline{S}\right|\overline{S}_{ij}} - \widehat{\Delta}^2\left|\widehat{\overline{S}}\right|\widehat{\overline{S}}_{ij}. \tag{9.6}$$

The model described by equations (9.3) and (9.6) was incorporated into the simulations with the choice $\widehat{\Delta}/\Delta = 2$ and using a simple top-hat filter as the test filter. The grid-size Δ was approximated as $\Delta = V_{\text{cell}}^{1/3}$ with V_{cell} denoting the cell volume.

9.3.2 Mesh generation

Because of the complexity of the geometry setting up a structured mesh is not straightforward. Hence, unstructured triangular meshes were built based on the geometry data of Außerlechner's pipe foot model, presented in Section 9.2.

The unstructured meshes were created using Delaunay triangularization with a goal function over the geometry on the element size l_e. The smallest elements with $l_e \approx 0.04\,\mathrm{mm}$ were located in the windway and around the lower edge of the upper lip, where the smallest coherent flow structures are expected. It was ensured that the edge length of neighboring elements do not differ from each other more than 5%, which results in a smooth transition of the size of the elements over the whole mesh. Contrary to the model of Vaik & Paál [140], the complete pipe foot was not a part of the mesh, only a smaller pressure tank was incorporated to imitate the pipe foot. The latter reduces the number of elements in the mesh, while at the same time it can also be expected not to influence the simulation results outside of the pipe foot.

mesh geometry

Two different mesh configurations were created. In the "Jet" configuration the upper lip was not a part of the model, whereas in case of the "Edge" configuration the upper lip was also included. The meshes were generated using one of the settings also reported in Refs. [18, 19, 140] with $d = 1.3\,\mathrm{mm}$, $\alpha = 45°$, $h = 10\,\mathrm{mm}$ and $l = 4.05\,\mathrm{mm}$. The width of the walls was set as $1\,\mathrm{mm}$, the width of the languid was $4\,\mathrm{mm}$ at the jet side and $2\,\mathrm{mm}$ on the other side. The pressure tank representing the pipe foot had a size of $7\,\mathrm{mm} \times 7\,\mathrm{mm}$. The size of the computational domain was chosen as $-40\,\mathrm{mm} \leq x \leq 60\,\mathrm{mm}$ and $-20\,\mathrm{mm} \leq y \leq 90\,\mathrm{mm}$ in the "Jet" case and $-30\,\mathrm{mm} \leq x \leq 45\,\mathrm{mm}$ and $-20\,\mathrm{mm} \leq y \leq 70\,\mathrm{mm}$ in the "Edge" case. Close-up views of the two generated meshes with the element edge size l_e are displayed in Figure 9.2.

2D and 3D meshes

Both for the "Jet" and "Edge" configurations two- and three-dimensional meshes were created. Since two-dimensional meshes are not explicitly handled in `OpenFOAM 2.1`, the 2D meshes were also three-dimensional, with only one element along the z-axis. The 3D meshes were created by extruding the 2D mesh in the z direction to a distance of d using 16 elements along the z-axis. The key properties of the resulting meshes are summarized in Table 9.1.

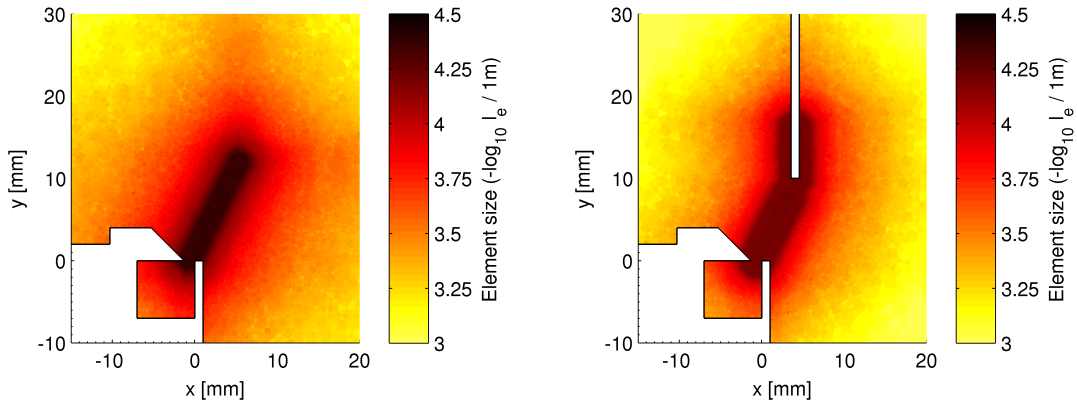

(a) "Jet" mesh (b) "Edge" mesh

Figure 9.2. Close-up view of the generated triangular meshes

Mesh name	Jet2D	Edge2D	Jet3D	Edge3D
Cells	27 625	38 111	442 000	609 766
All faces	96 864	133 801	1 135 449	1 569 151
Internal faces	41 261	56 754	1 074 551	1 479 729
Processor cores	4	4	32	48
Average # cells / core	6 906	9 528	13 813	12 704
Average # shared faces / core	156	126	1 169	1 044

Table 9.1. Mesh statistics and decomposition properties

Due to the large number of cells and faces ($> 10^6$ faces in case of 3D meshes) parallelization was an essential part of handling the problem. The 2D problems were run using 4 processor cores, whereas 32 and 48 cores were used in 3D simulations in the "Jet" and "Edge" cases, respectively. The parallelization was performed using the Scotch decomposition method [123], which minimizes the communication (i.e. the number of shared faces) between the cores. The results of the decomposition are also shown in Table 9.1.

9.3.3 Boundary conditions

Inlet At the left and bottom boundaries of the pressure tank a fixed total pressure of p_{foot} was set.

Free flow Free flow boundary conditions were provided by prescribing a dynamic inlet/outlet condition depending on the current pressure. In case of overpressure this boundary condition acts as an outlet condition with u_j evaluated from the flux. In case of underpressure the boundary functions as an inlet with zero pressure gradient.

Walls No-slip boundary condition with $u_j = 0$ and $\partial p/\partial n = 0$.

Front & back In case of 2D models an *empty* boundary condition was imposed on the front and back walls, prescribing no flow through these surfaces. Whereas, for 3D models *cyclic* boundary conditions were set up providing continuity of the front and back surfaces of the mesh.

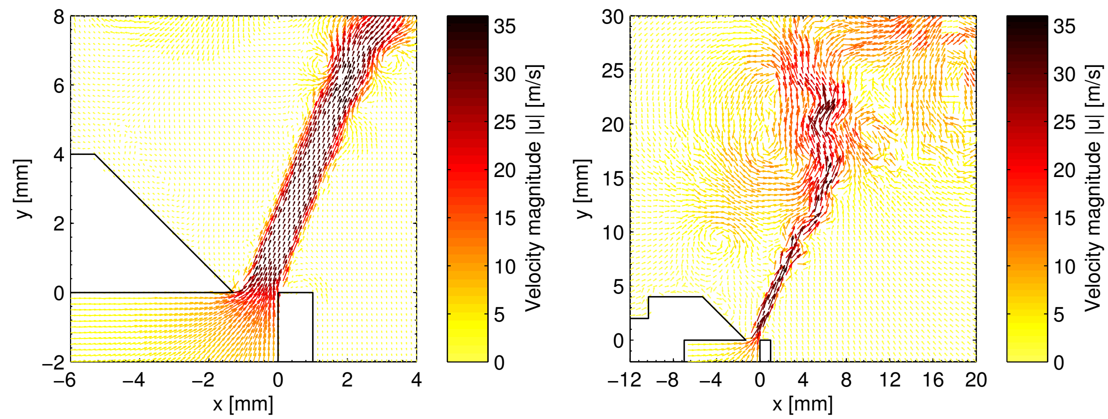

(a) Close-up on the windway

(b) Larger structures of the flow field

Figure 9.3. Visualization of the flow in the "Jet" case (2D laminar model, $t = 5.0\,\mathrm{ms}$)

9.3.4 Time stepping

The simulations were performed using $\Delta t = 5 \cdot 10^{-7}\,\mathrm{s}$ time steps, which ensured a Courant number always less than 1. The 2D simulations were run up to $T_{\mathrm{max}} = 0.2\,\mathrm{s}$, whereas the 3D configurations were run setting $T_{\mathrm{max}} = 0.1\,\mathrm{s}$. This resulted in $4 \cdot 10^5$ and $2 \cdot 10^5$ time steps in the 2D and 3D cases, respectively. The complete flow field was saved every 100$^{\text{th}}$ time step for subsequent visualization.

9.4 Results and discussion

All simulations presented in the sequel were run using the setting $p_{\mathrm{foot}} = 700\,\mathrm{Pa}$. This setup was chosen since it is used by both Außerlechner *et al.* [18, 19] and Vaik & Paál [140]. Using *Bernoulli's law* with an average density of $\rho_0 = 1.2\,\mathrm{kg/m^3}$ the maximum jet velocity u_{jet} is obtained as

Bernoulli equation

$$u_{\mathrm{jet}} = \sqrt{\frac{2p_{\mathrm{foot}}}{\rho_0}} \approx 34\ \mathrm{m/s}, \tag{9.7}$$

which justifies the use of the incompressible model, since the Mach number $\mathrm{Ma} = u_{\mathrm{jet}}/c \ll 1$ with c denoting the speed of sound ($c \approx 343\ \mathrm{m/s}$ in this case).

The corresponding *Reynolds number* can be evaluated from the flue width d. With the kinematic viscosity $\nu = 1.5 \cdot 10^{-5}\,\mathrm{m^2/s}$

Reynolds number

$$\mathrm{Re} = \frac{u_{\mathrm{jet}} d}{\nu} \approx 2\,950, \tag{9.8}$$

which means that the jet operates near the transition Reynolds number ($\mathrm{Re}_{\mathrm{tr}} = 2\,300$), thus the flow cannot be assessed purely laminar, neither purely turbulent.

9.4.1 Simulation of the free air jet

free jet properties

To examine the quality of different numerical models, the free air jet without the upper lip was modeled first. Four different models were tested, 2D and 3D configurations using the laminar and LES model. The visualization of the flow is shown in Figure 9.3. As it can be seen in Figure 9.3(a), the jet is not filling out the whole windway, yet it is separated from the sharp edges. This phenomenon is known as the *vena contracta* effect. This observation is in agreement with the

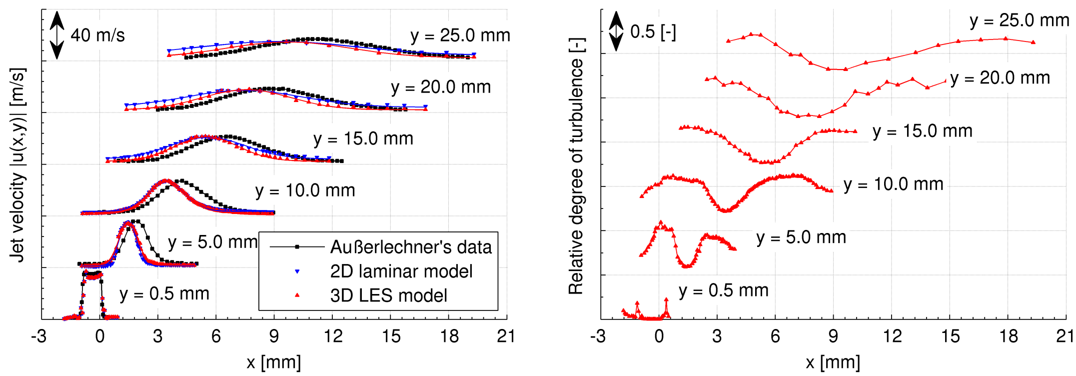

(a) Comparison of jet velocity profiles

(b) Turbulence degree profiles (3D LES model)

Figure 9.4. Simulated velocity and turbulence profiles

Parameter	Measured	Vaik & Paál	2D laminar	2D LES	3D laminar	3D LES
w [mm] ($y = 5\,\text{mm}$)	1.16	N/A	0.85	0.86	0.97	0.95
w [mm] ($y = 10\,\text{mm}$)	2.34	1.11	1.90	1.91	1.93	1.96
w [mm] ($y = 15\,\text{mm}$)	3.55	1.82	3.91	3.83	3.16	3.27
w [mm] ($y = 20\,\text{mm}$)	4.75	3.85	6.02	5.98	4.40	4.52
w [mm] ($y = 25\,\text{mm}$)	5.92	5.34	8.07	8.41	6.53	6.36
θ_{jet} [°] (Averaged)	26.1	23.2	22.3	22.8	22.2	22.5

Table 9.2. Parameters of fitted Gaussian profiles to simulated air jets using different models compared against measurements [19] and previous CFD simulations [140].

measurements [19] and previous CFD analysis [140]. The Kármán vortex street on the two sides of the jet can also be distinguished. Figure 9.3(b) displays the larger structures of the flow field at the same time instance.

Außerlechner *et al.* [19] have measured the flow profiles along the x-axis using a hot wire anemometer at different heights on the y-axis. Profiles corresponding to these measurement positions were extracted from the simulated flow field in the following manner. In case of 3D simulations the flow field was first averaged along the z direction. The profiles were evaluated using the time average of the magnitude of the velocity field sampled in the finite volume cells corresponding to the measurement lines of Außerlechner at $y = 0.5; 5; 10; 15; 20$ and $25\,\text{mm}$, respectively. A comparison of simulated and measured velocity profiles is shown in Figure 9.4(a). The computed profiles are in good agreement with the measured ones, however, the center point of the profiles are slightly shifted to the left.

velocity profiles

In [18] the corresponding turbulence profiles are also reported. The relative degree of turbulence $\text{Tu}(x, y)$ is evaluated as the standard deviation of the velocity magnitude divided by its time average. The resulting turbulence profiles are plotted for the 3D LES model in Figure 9.4(b). The shape of the profiles are in good agreement with the ones shown in Figure 3.13. of Ref. [18]; however, the magnitudes are somewhat higher compared to the measurements.

turbulence profiles

Außerlechner *et al.* [19] have fitted Gaussian functions to the measured velocity profiles as

$$\langle |u(x,y)| \rangle \approx u_0(y) + \sqrt{\frac{2}{\pi}} \frac{A(y)}{w(y)} \exp\left(-2 \left(\frac{x - x_c(y)}{w(y)} \right)^2 \right), \qquad (9.9)$$

Gaussian profile fit

with $|u(x, y)|$ representing the magnitude of the velocity, $\langle \cdot \rangle$ symbolizing time averaging, u_0 de-

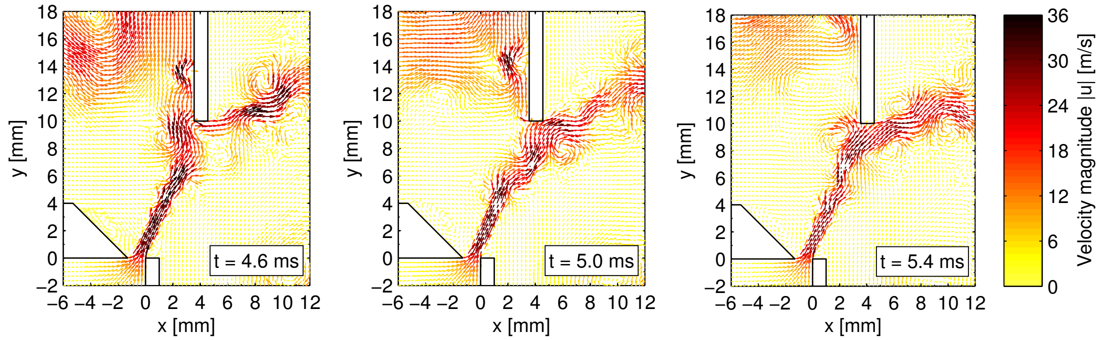

Figure 9.5. Visualization of the air jet oscillation around the upper lip (2D laminar model)

noting the offset velocity, A the maximal amplitude, w the half width of the jet, and x_c the x-position of the centerline with all the parameters on the right hand side depending on the y-position of the jet profile. The same fit was performed on the profiles obtained from the simulations.

comparison of velocity profiles

The fitted values are presented in Table 9.2. The fit values for Vaik & Paál were created by fitting (9.9) to the re-digitalized data of Fig. 8 of [140].[1] The fit provided very good results with coefficients of determination of $R^2 \geq 0.98$ for all four models. As it can be seen, both the laminar and LES 3D models provide a much better match to the measured values than 2D models. The width of the profiles at $y = 5\,\mathrm{mm}$ and $y = 10\,\mathrm{mm}$ are slightly underestimated by all models. The width of the other ($y > 10\,\mathrm{mm}$) profiles are greatly overestimated by 2D models, but are predicted with good accuracy by means of the 3D models. Contrary to the results presented here, the 2D laminar model of Vaik & Paál—which is the only model reported for free jet simulations in [140]—underestimates the profile width in all cases and gives higher maximal velocity of the profiles at the same time. These dissimilarities may arise from issues such as insufficient mesh resolution; however, such deviations are not addressed in [140].

jet exit angle

The jet exit angle θ_{jet} is slightly underestimated by all models, as it is also seen in Figure 9.4(a). This small discrepancy can be explained by the fact that the complete pipe foot was replaced by a small pressure tank in our numerical model. However, Vaik & Paál have also obtained slightly smaller values for θ_{jet} than the measured ones with the complete pipe foot included in their simulations.

9.4.2 Simulation of edge tone generation

The edge tone generation was also simulated using the four different models introduced above. Figure 9.5 depicts the movement of the air jet oscillating around the edge of the upper lip. On the left hand side of the figure, at $t = 4.6\,\mathrm{ms}$ the jet is moving from the left to the right. In the middle picture, at $t = 5.0\,\mathrm{ms}$ the jet has nearly reached its rightmost position, whereas in the right hand side, at $t = 5.4\,\mathrm{ms}$ its already moving back, from right to left, hitting the edge with its centerline. The typical vortex generation process in this flow configuration is also clearly followable in Figure 9.5.

Since the edge tone acts as a dipole sound source the spectra of pressure forces acting on the upper lip contain the same tonal components as the edge tone. The amplitudes of pressure force components are not directly comparable to microphone edge tone measurements reported by Außerlechner *et al.* [19], as the propagation from the edge to the microphone position is supposedly strongly dependent on the frequency. Also the pressure force spectra are expected to have higher noise baseline since they contain the forces of vortices shedding from the upper lip

[1] The fit was unsuccessful in the $y = 5\,\mathrm{mm}$ case for the data of Vaik & Paál.

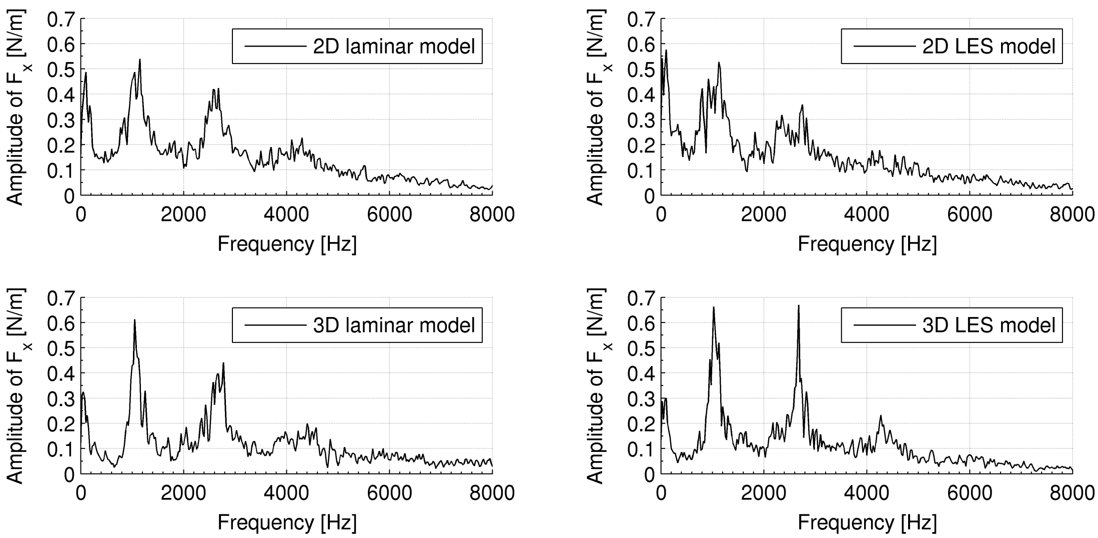

Figure 9.6. Spectra of pressure forces acting on the upper lip.

Mode	Measured	Vaik & Paál	2D laminar	2D LES	3D laminar	3D LES
	Mode frequencies [Hz]					
I.	$1\,060$	$1\,100$	$1\,150$	$1\,125$	$1\,050$	$1\,025$
II.	$2\,610$	$2\,940$	$2\,675$	$2\,750$	$2\,675$	$2\,675$
III.	$4\,465$	$4\,600$	N/A	$4\,575$	N/A	$4\,300$

Table 9.3. Comparison of measured and simulated frequencies of edge tone modes

and other unsteady pressure fluctuations, which are attenuated by the acoustic propagation to a great extent. Nevertheless, the frequencies of the tonal components observed in the pressure force spectra should be comparable and in good agreement with the tonal components of the radiated sound of the edge tone.

pressure force spectra

The pressure force spectra were calculated as follows. The forces acting on the upper lip were evaluated every 10th time step leading to $f_s = 200\,\mathrm{kHz}$ sampling rate. Since the Reynolds number is of order 10^3, the pressure forces are dominant over viscous forces. Only the x component of the forces were taken into account. The forces were normalized by dividing them by the z-size of the model, therefore the resulting normalized forces are interpreted as $\mathrm{N/m}$. An FFT window size of $8\,000$ points were chosen, which corresponds to a time window of $T_{\mathrm{win}} = 0.04$ s and a frequency resolution of $\Delta f = 25$ Hz. Spectra of successive time windows were evaluated using Hann window function and 85% overlapping between the time windows. Finally, the amplitudes of the spectra were averaged with 27 and 11 averages—resulting from the above method—in the 2D and 3D cases, respectively. The resulting spectra are displayed in Figure 9.6.

spectrum comparison

As it is seen in Figure 9.6, the predicted edge tone components are close in frequency in all cases. The exact values of the calculated frequencies are listed in Table 9.3. In case of 2D models, there is an artifact in the spectra in the low frequency range, around $125\,\mathrm{Hz}$. These components are also found in the spectra reported by Vaik & Paál [140]. The artifact components are not present in the 3D model and the low frequency fluctuations have remarkably smaller amplitudes in the 3D cases. Also the baseline of the spectra is much lower in the 3D cases despite the lower number of spectral averages. This is due to the fact that the evaluation of pressure forces is done by integration over the surface of the upper lip, hence it inherently contains averaging in the

z direction. It can also be seen that in case of the 3D LES model, the second and third modes become remarkably stronger than in other cases.

tonal components

The third edge tone mode could not be clearly detected in the laminar simulations. The frequencies of the modes attained from the simulations are in good agreement with the measurements reported in [19]. As it is seen, the 2D models slightly overestimate the mode frequencies, whereas the 3D models provide a better match with the measurements. The prediction of mode frequencies using the 3D models are also better than the ones obtained by Vaik & Paál [140], especially for the second mode, where the deviation between the measured and the simulated mode frequency is reduced from 13% to less than 3%.

9.5 Concluding remarks

Simulations of the air jet and edge tone generation in the foot model of a labial organ pipe were reported in this chapter. Two- and three-dimensional models were created, extending the scope of recent simulations by Vaik & Paál [140]. The quality of the computational models were assessed by means of comparison against measurement results of Außerlecher *et al.* [18, 19]. Good agreement of measurements and simulations was found both in the "Jet" and "Edge" cases.

findings

It has been shown that 3D models give better fit to the measured jet velocity profiles, whereas 2D models overestimate the width of the air jet to a significant extent. The models successfully capture other characteristic properties of the flow field, such as the *vena contracta* effect at the jet exit. In case of edge tone simulations very good agreement of the measured and simulated tonal components have been found. The 3D models give excellent agreement with measured mode frequencies, yet 2D models give a slight overestimation. From the results presented here, it can be assessed that by taking 3D effects of the flow field into account the quality of air jet and edge tone CFD simulations can be significantly increased, and better match to measurement results can be attained at a cost of increased computational effort.

possible improvements

As it was seen, the pressure forces obtained from CFD simulations can only be compared to edge tone sound measurements in an indirect manner. This difficulty could be overcome by applying an aeroacoustic propagation model to simulate the acoustic pressure field near the pipe mouth. This would enable a more detailed evaluation of edge tone simulations. In order to get a realistic sound generation model of an organ pipe, the "Edge" model presented here has to be extended by acoustic feedback from the pipe resonator. Incorporating the latter extensions into the model are among the future plans of the author.

Chapter 10

Conclusions and outlook

This final chapter briefly summarizes the results of the research presented in the thesis. Novel results contributing to pipe organ research are listed briefly in Section 10.1. Thesis statements are given in Section 10.2. Possibilities of further research on the topics addressed in this thesis are discussed finally in Section 10.3.

10.1 Contributions

The dissertation presented the following new results.

- A novel scaling method for chimney pipes was introduced in Chapter 5. The proposed technique relies on the one-dimensional acoustic model of the pipe and incorporates an iterative and a global optimization routine for determining the geometry of the resonator. The process offers sound design by the amplification / suppression of the targeted harmonic partials in the steady state sound. The applicability of the proposed technique was validated by means of measurements and listening tests performed on chimney pipes built with optimized resonators.

- A measurement campaign performed on labial organ pipes with tuning slots revealed previously unknown properties of the pipe sound. Reproducible measurements on experimental pipes were reported in Chapter 6, and the impact of each scaling parameter of the tuning slot on the character of the pipe sound was documented. It was proven by measurements and listening experiments that current design rules of tuning slots are suboptimal and do not lead to the best achievable sound characteristics. It was also shown that in order to fully exploit the capabilities of the tuning slot, the length above the slot should be proportional to the length of the pipe length instead of the diameter.

- For the accurate characterization of the acoustic behavior of labial pipes with a tuning slot, Chapter 7 introduced a hybrid technique incorporating 1D waveguide elements and 3D finite element simulation results. It was shown that the proposed approach gives reliable prediction of the eigenfrequency-structure of the pipe and overcomes the limitations of previous analytical models.

- The numerical characterization of the radiation impedance of an open conical pipe end was given in Chapter 8. By post-processing the computational results, the resulting bivariate impedance function was incorporated into the one-dimensional acoustic model. It was proven that the resulting hybrid model improves the accuracy of the prediction of the eigenfrequencies in case of tapering pipe ends.

- A low frequency acoustic model of the shallot was introduced in Chapter 8. The model was validated by means of comparison with results of transfer function measurements.
- Three-dimensional flow simulations of the edge tone configuration in an organ pipe foot model were presented in Chapter 9. It was shown that by extending the simulation into three dimensions a remarkable improvement on the predicted properties of the flow field is attained. This statement was validated by comparison to measurements and 2D simulation results found in the corresponding literature.

10.2 Theses

Thesis group I (Optimization of chimney pipe resonators)
I have introduced a novel methodology for the sound design of chimney pipes. Based on the one-dimensional acoustic model of the pipe, I have derived an optimization strategy for scaling the resonator. Contrary to traditional methods, the proposed technique provides control over the timbre of the pipe in the scaling phase. I have validated the applicability of the method by means of objective and subjective comparisons.

Thesis I.1
I have shown by means of theoretical and experimental examination that the current design rules of chimney pipe resonators are suboptimal, since they do not allow sound design in the scaling phase and leave certain capabilities of the resonator unexploited. [C3, C2, J2]

Thesis I.2
I have proposed a new methodology for the optimal design of chimney pipe resonators. I have suggested two optimization procedures for different sets of target parameters. The amplification of the chosen partials is achieved by tuning the eigenfrequencies of the resonator through the geometry parameters. I have verified the applicability of the proposed technique by means of laboratory measurements and subjective evaluation of the sound quality of experimental pipes built using the optimization procedure. [C8, C6, C5, J2]

Thesis group II (Tuning slot characterization and modeling)
I have performed a measurement campaign in order to accurately assess the impact of the tuning slot on the acoustic behavior of labial organ pipes. I have proven that current design rules for tuning slot pipes do not provide sufficient control over the character of the sound. I have developed a novel model for the characterization of tuning slots using finite element simulation. I have shown, that by using the proposed model, an optimal scaling method can be developed, overcoming the limitations of current design rules.

Thesis II.1
I have found that the steady state spectrum of labial organ pipes mounted with a tuning slot has a unique behavior. I have determined and documented the impact of scaling parameters on the sound characteristics by means of reproducible measurements. I have proven that the observed tendencies are explained by the tuning slot's effect on the eigenfrequency-structure of the pipe. [C4, C7, J3]

Thesis II.2
I have shown by spectral analysis and subjective evaluation of recorded pipe sounds, that current design rules of thumb do not provide sufficient control over the timbre. I have recommended an alternative scaling approach, which revises the relation between the parameters of the slot and that of the pipe and can be utilized for the sound design of tuning slot pipes. [J3]

Thesis II.3
I have proposed a new formulation for the equivalent acoustic parameters of tuning slots based on the results of finite element simulations. I have verified that the novel technique gives a more accurate prediction of the eigenfrequencies than traditional woodwind tonehole models applied to tuning slots of labial organ pipes. [C6, C7, C5, J4]

Thesis group III (Development of modeling methodology)
I have achieved novel results regarding the simulation of acoustic and fluid flow phenomena in labial and lingual organ pipes by the combined usage of the one-dimensional waveguide, the three-dimensional finite and infinite element, and finite volume techniques.

Thesis III.1 (Modeling resonators of reed organ pipes)
I have introduced a methodology that combines a one-dimensional acoustical model with three-dimensional finite – infinite element simulation of the radiation impedance. I have shown that by means of post-processing the simulation results, the method can adaptively be applied in the acoustical waveguide type simulation of axisymmetric resonators. I have also proven that the proposed technique gives better prediction of the eigenfrequencies than traditional methods, without additional computational effort. [C11, C15]

Thesis III.2 (3D simulation of edge tone generation)
I have extended previous two-dimensional CFD models of the air jet and edge tone generation into three dimensions. I have shown that this extension, which is claimed to be indifferent by other authors, has a significant impact on the simulation results. I have also shown that the proposed three-dimensional model provides a better fit to measured data regarding both free jet and edge tone simulations. [C13]

10.3 Outlook on further research possibilities

This section gives a brief outlook on some of the possibilities for the continuation of the research presented in this dissertation. Only a few aspects are mentioned here, which I think are the most relevant ones.

sound synthesis

In my opinion, the most important step of further research would be the application of the results for the physical-model-based *sound synthesis* of organ pipes. In case of labial pipes this could be carried out making use of the excitation models given in the cited literature. An interesting part of these applications would be the sound synthesis of pipes with optimized geometry. By this step, the acoustic and flow simulation models could be joined. With an enhanced sound synthesis model, the attack transient of the pipe sound could also be synthesized, which would mean a great advance for predicting the percieved sound quality of the pipes. In case of lingual pipes, implementation of the sound synthesis would first require a more detailed investigation of the flow–acoustic coupling in the shallot.

losses and energy balance

Together with the model-based sound synthesis, the linear and nonlinear losses and the energy balance of the sound generation should be investigated in more detail. By this examination the accuracy of optimization methods based on the acoustic model of the pipe could be enhanced and the resulting sound spectrum could be foretold with better reliability, especially regarding the amplitudes of the partials in the pipe sound.

shallot forms

As far as lingual pipes are concerned different shallot constructions could be examined in more detail. As preliminary results indicate (see e.g. [O2, C16]), the shallot construction has a remarkable effect on the character of the pipe sound. A better understanding of the phenomena taking place in the shallot would also be advantageous for the establishment of an improved acoustic model of reed pipes.

numerical simulations

Regarding numerical simulations, there are various improvements possible. In case of acoustical finite element models the incorporation of viscothermal losses would enhance the accuracy of simulation results. Further three-dimensional simulations could also be carried out: one of the interesting problems would be the examination of the radiation impedance of sloped pipe terminations. For three-dimensional flow simulations of the edge tone, and the sound generation mechanism of labial organ pipes, one of the interesting topics would be the CFD characterization of certain voicing steps. For example, by means of 3D models the effect of *nicking* could be examined.

coupled model

The establishment of a strongly coupled mechanical–fluid flow–acoustical model of reed pipes would mean a great advance in the examination of the sound generation of lingual organ pipes. However, due to the complexity and the computational costs involved, it can be expected that the formulation of such a model would require a few more years of research.

10.4 Final remarks

This thesis was typeset using LaTeX 2_ε.[1] The bibligropaphy and the list of publications were created using the `biblatex`[2] package and `biber`.[3] All drawings were created by the author using the `PGF` and `TikZ` packages[4] and `Inkscape`.[5] All diagrams were created using the plotting tools of `Matlab`.[6] The source files of the dissertation were kept under version control using `git`.[7]

[1] http://www.latex-project.org/
[2] http://www.ctan.org/pkg/biblatex
[3] http://biblatex-biber.sourceforge.net/
[4] http://www.ctan.org/pkg/pgf
[5] http://www.inkscape.org/en/
[6] http://www.mathworks.com
[7] http://git-scm.com

Appendices

Appendix A

SoundAnalysis

A.1 Introduction

`SoundAnalysis`[1] is a software tool developed in the framework of the European projects INNOSOUND and REEDDESIGN. The application is suited to the needs of organ builder partners of the projects as well as it fits the requirement of being able to evaluate and compare sound recordings carried out in great numbers. The tool has also been used for the evaluation of the measurements presented in Chapters 5–6 of this thesis. This appendix briefly introduces the main functionalities of the software tool.

A.2 Signal processing functions

The tool provides a user friendly GUI (Graphical User Interface) for the signal processing tasks required for the objective analysis of organ sounds. The signal processing algorithms have been selected to work on organ pipe sounds (i.e. one note is played in each recording with a few-second-long steady state part); however, the sound of other woodwind or brass instruments, such as that of recorders, clarinets, or trumpets can also be analyzed using the program. In its present form the software tool is not capable of analyzing quickly decaying sounds like that of classical guitars or drums. The typical signal processing tasks needed for the analysis of organ pipe sounds are as follows.

Sound sample preparation The tool works as a simple wave editor, in which single- and multi-channel recordings can be imported, edited, and exported. The channels from different recordings can be combined into new single- or multi-channel wave files with arbitrary time shifts.

Calibration In order to get the absolute sound pressure level of the recording, a calibration signal is needed, which is usually provided by a pistonphone calibrator. When a calibration recording is available, the program detects the amplitude of the calibration signal and calculates the amplitudes of the recordings relative to this signal. Multi-channel calibration recordings using microphones of different sensitivities are also supported.

Segmentation It is a common requirement to perform different types of analyses on different segments of a recording, such as the separate analysis of attack and steady state sound. The software tool supports the automated detection of attack, decay and steady state parts in

[1] © A. Miklós, S. Pitsch, P. Rucz, and T. Trommer, 2010–2013.

a recording. Alternatively, the user can manually pick an arbitrary segment from a sound sample to analyze.

Frequency detection Proper detection of the fundamental frequency is an important yet not straightforward step in the analysis. The tool offers two automated algorithms for the detection of the fundamental frequency, which are also able to estimate the fluctuation of the detected frequency. Alternatively, the user can specify an approximate fundamental frequency, which is refined by the program. Once the fundamental frequency is detected properly, the signal can be resampled, by which coherent sampling can be ensured, leading to excellent signal to noise ratio and avoiding spectral leakage and the picket fence effect at the same time.

Steady state analysis In the steady state the analysis is usually performed by evaluating a number of subsequent FFT-windows and averaging the resulting amplitudes. `SoundAnalysis` provides extensive control over the parameters of the analysis, such as the FFT-window function, the window size, overlapping, and averaging settings. Global attributes, such as the equivalent loudness level of the recording are evaluated automatically once the analysis is completed.

Transient analysis In the transient state, the results of FFT-windows are not averaged, yet their results are stored and displayed together providing a time-frequency-amplitude visualization of the pipe sound. In organ sound, the attack transients are of special importance, since they play a key role in the subjective assessment of the sound quality.

Viewing the results The tool also provides different ways of displaying the analysis results. Steady state results can be viewed as amplitude spectra, spectra with envelopes or envelope only. Transient results can be viewed in a two-dimensional plot displaying the amplitude history of the selected harmonics, or in a two- or three-dimensional spectrogram.

A.3 An example analysis

In this section an example analysis presented on one sound recording of experimental tuning slot pipe #2, introduced in Chapter 6. The setting with slot width $w_\mathrm{s} = 12\,\mathrm{mm}$ and slot height $h_\mathrm{s} = 35\,\mathrm{mm}$ is chosen here. The recording was performed using two calibrated condenser microphones, as it was described in Section 6.2.2. As a preprocessing step, the single-channel recordings of the calibration signal and the pipe sounds are merged into two-channel files using the *Cut editor* tool of `SoundAnalysis`, with Channels #1 and #2 representing the microphones located near the mouth and the tuning slot, respectively.

Figure A.1 displays the main window of the software tool. In the top part of the window, in the *Wave files* and *Wave cuts* panels, recordings can be imported and cut into segments. When a calibration signal is loaded, the amplitudes can be detected in the *Calibration* panel. Once the calibration was successful, the green *Calibrated* signal indicates that subsequent analyses are automatically performed in calibrated mode. In the panel called *Frequency detection*, the algorithm for fundamental frequency detection can be customized. The parameters of the analysis are adjustable in the *Analysis setup* panel. Different settings are stored for stationary, attack and decay analyses. When the analysis is completed, the graphs are shown in a new window, where the user can adjust the properties of the display and store the results. Finally, in the *Analysis results* panel, old results can be reopened and compared using various types of plots.

The steady state analysis results are shown in Figure A.2. By plotting the two spectra on top of each other the differences of the levels and the envelopes can immediately be observed. Following local baseline maxima in the spectra, the frequencies of natural resonanace of the resonator can also be detected. In the frequency axis, normalized units are chosen, which can easily be set

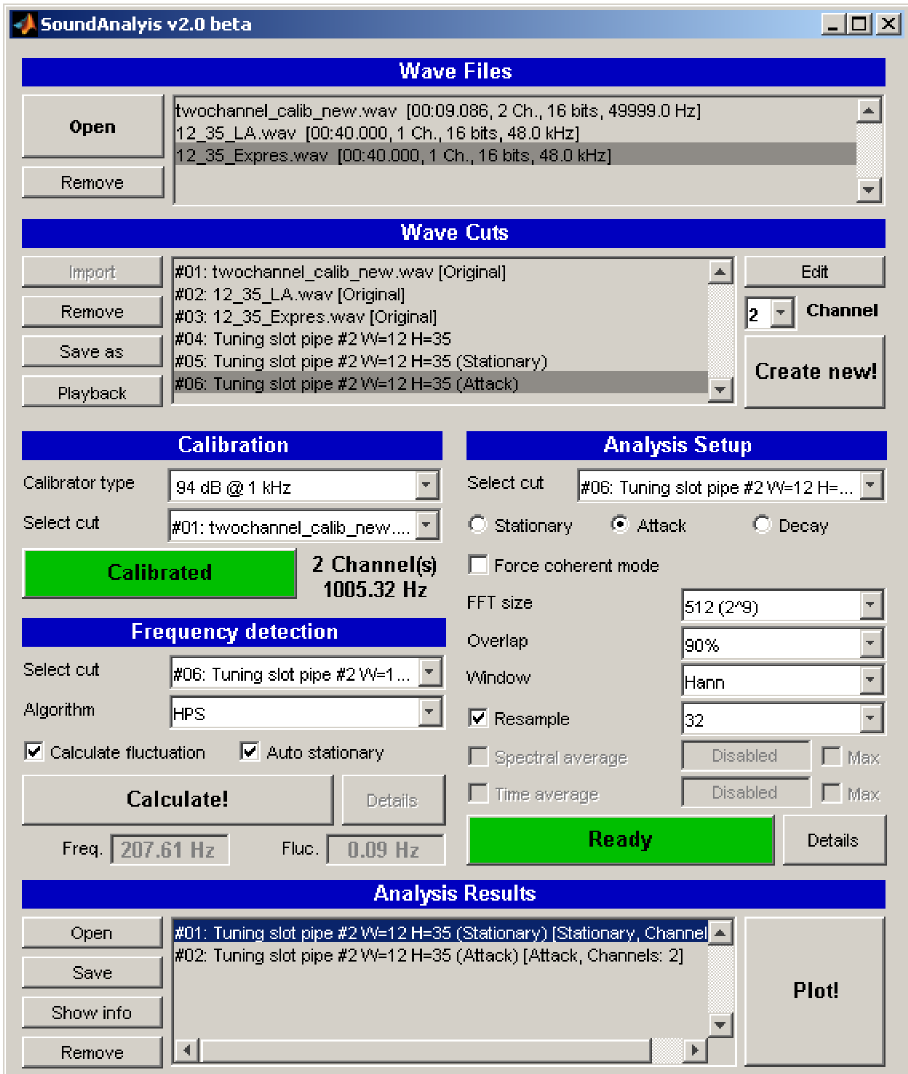

Figure A.1. The main window of `SoundAnalysis v2.0`

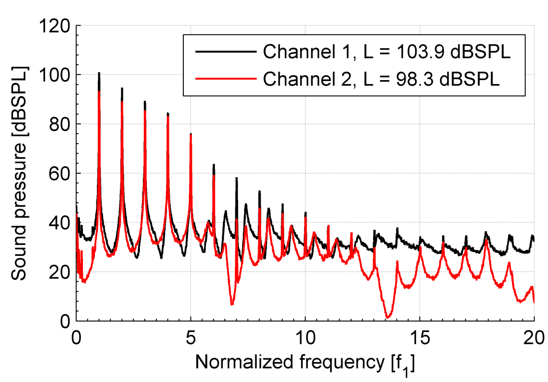

Figure A.2. Stationary analysis results

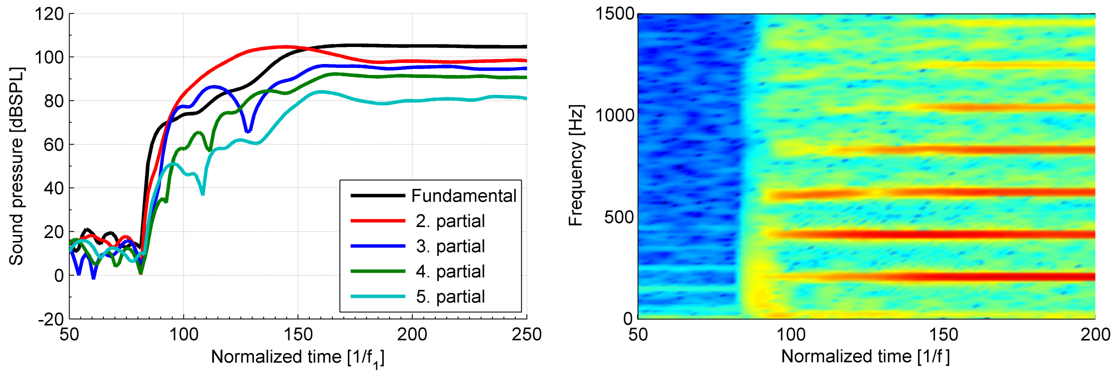

(a) Partials view (b) Spectrogram view

Figure A.3. Attack analysis results

in the tool, facilitating the comparison of spectra with different fundamental frequencies. The effective loudness values are also automatically calculated, and it can be seen that the measured loudness is about $5\,\mathrm{dB}$ greater at the mouth of the pipe than at the tuning slot.

Analysis results of the attack transient are shown in Figure A.3. Data from the mouth microphone (Channel #1) are displayed only; however, the characteristics of the transient are quite similar for both channels. Thanks to the coherent analysis achieved by resampling the signal, the number of FFT window points can be reduced without losing the accuracy of the computed amplitudes. Thus, the time resolution of the analysis can be increased and a detailed picture on the attack can be obtained. The time scale in both plots of Figure A.3 is given in a non-dimensional scale, the unit being the duration of one period of the steady state sound.

In Figure A.3(a) the time history of the amplitudes of the first five partials is depicted. As it was observed in Figure A.2, the fundamental is the strongest component in the steady state in both channels. Nevertheless, as it is seen in Figure A.3(a), in the attack phase the second and third partials are both stronger than the fundamental at times $100 < t < 150$. The steady state sound builds up after a hundred periods and from that point the amplitudes of the partials do not change with time.

Figure A.3(b) displays the same attack but in a spectrogram view. By a detailed examination of the spectrogram interesting effects can be found that are unseen in the amplitude history plot of the partials. Such interesting effect is observed near the third partial around the hundredth period in the transient. As it can be seen, the red "line" corresponding to the third partial breaks around $t = 130$. Taking a closer look at the spectrogram, it is also found that the first part of the line ($t < 130$) has a slightly lower frequency than the second part ($t > 130$). This indicates that the third eigenfrequency (that is slightly lower than three times the fundamental) is also excited in the attack transient; however, in the steady state the first eigenfrequency becomes dominant.

The possibility of the detailed analysis of the attack transients of labial pipes is a useful tool for the organ building community, since the properties of the attack greatly affect the percieved sound quality of the pipes. By using `SoundAnalysis` organ builders can assess the effect of various scaling, voicing, and tuning adjustments in an objective manner, supplementing their subjective observations.

Appendix B

INNOScale scaling software

In this appendix the software tool called `INNOScale`[1] is introduced, which was developed during the INNOSOUND project. The program supports the computer aided design of flue pipe ranks using traditional and novel scaling methods. More details about the software code are found in the technical report [T3] and the conference paper [C10].

B.1 Introduction

In the last two decades, the traditional method of organ pipe scaling has been supplemented by computer aided methods that facilitate the calculation of the main parameters of the pipes. One example known to the author is the tool called `M!` by Laukhuff Orgelbau.[2] `INNOScale` aims at providing a user friendly interface for performing the tasks of the traditional scaling procedure, as well as making innovative methods accessible to the organ building community. The main features of the tool are the following.

- Support of customisable scale definition points and graphical editing of scaling lines: The user can choose the density of the scaling points and manipulate the lines while the software automatically interpolates the scale for middle points.
- Support of various types of stops: The most often used pipe forms are handled by the tool together with several special configurations, such as *aliquots*, *transitions* or *mixture* registers.
- Support of innovative scaling functions: Beside the traditional methodology, `INNOScale` incorporates novel scaling procedures developed in the frame of the INNOSOUND project.
- Compatibility with `Microsoft Excel`: All scaling tables and other data can be exported to Excel format for further editing, printing etc.

B.2 The traditional scaling method

The reference scale Besides the pipe's fundamental frequency that is basically determined by the length of the resonator, the most important parameter is the diameter (or effective diameter in case of rectangular or conical pipe ranks) of the pipe. Due to the length correction effect, the diameter has a great influence on the eigenfrequency-structure of the pipe; furthermore, it also determines the sound power radiated by the pipe. In the traditional design

[1] © J. Kirschmann, A. Miklós, S. Pitsch, and P. Rucz, 2010–2012.

[2] http://www.en.laukhuff.de/about-us.html (The software code `M!` is currently unavailable from the website.)

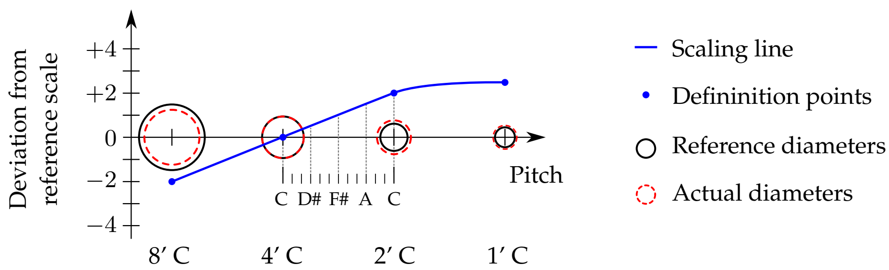

Figure B.1. Scaling lines and the calculation of pipe diameters

method of flue pipe ranks, the diameters are defined by a so called *reference scale*. The most well-known standard scale is that of Töpfer [138], which assigns a diameter of $155.0\,\mathrm{mm}$ to an 8′ C pipe and uses a ratio of $\sqrt[4]{8} : 1$ for the diameters of pipes having one octave difference in pitch. In `INNOScale` the user can choose from various predefined reference scales, and custom reference scales can also be created.

Pipe ranks In a pipe organ different pipe ranks occupy different ranges of pitch. Furthermore, in case of some stops (e.g. *aliquots*) the musical note of the pipes is different from the keyboard note. Therefore, the keyboard and musical range for each stop has to be defined separately. `INNOScale` supports the definition of an arbitrary number of stops for each *division* of an organ. The musical and keyboard range for each stop can be configured separately along with further settings.

Scaling lines Once the reference scale is set up and the pitch range of each pipe rank is determined, the *scaling lines* are set up. Scaling lines are interpreted as deviations from the reference scale, by which the organ builder can define wider and narrower scales for different pipe ranks and can also adapt the scaling to the acoustics of the hall where the organ is installed. How scaling lines work is demonstrated by Figure B.1. The deviations from the reference scale are given in units of semitones: for example a $+2$ semitone deviation for a C_2 pipe means that the pipe becomes wider and gets the reference diameter of the $B\flat_1$ pipe; whereas in case of a -2 semitone deviation the pipe becomes narrower and gets the reference diameter of the D_2 pipe.

Calculation Once the diameters of the pipes are known from the reference scale and the scaling lines, further parameters, such as the width of the mouth or the height of the cutup can be determined. For example a common rule used is to set mouth width to inner circumference to $1 : 4$ and cutup height to mouth width also to $1 : 4$. In `INNOScale`, these factors are adjustable in a flexible manner: the user can easily define constants, simple arithmetic or geometrical progressions, and custom functions to set up these factors.

The calculation procedure is controlled in the main window of `INNOScale`, as shown in Figure B.2, and is performed in four steps for each stop.

1. Definition of the stop, the corresponding scaling line, and other input parameters, such as the mouth width to circumference factor.

2. Calculation of pipe dimensions. From the input parameters, all dimensions are calculated automatically at once.

3. Manual modifications. After the automatized calculation each computed parameter can be edited manually.

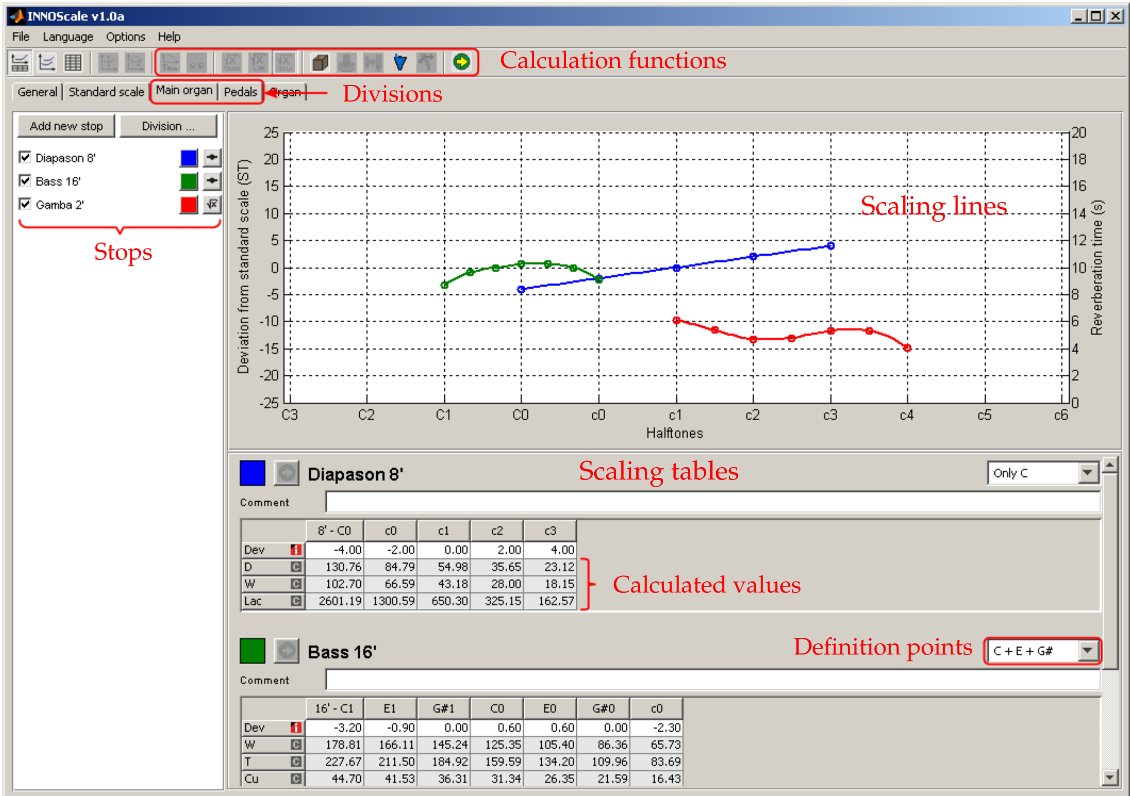

Figure B.2. The main window of `INNOScale`

4. Locking. Once all the values are set up correctly, the scaling tables can be locked, which means that no changes can be made and automatic calculations do not affect the parameters calculated for the specific stop.

B.3 Innovative calculation functions

Apart from the traditional scaling functionality, the software code aims to be extendible by novel calculation methods that can help achieving optimal sound design of various pipe ranks. Currently, the tool supports the following novel design methods.

Reverberation time data Organ builders usually judge the acoustics of a room by clapping and listening to the reverberation. Then, they scale the pipes according to this subjective judgement. An alternative, more objective approach is to measure the frequency dependent reverberation time in the hall by means of room acoustic measurement equipment. Once such data is available, it can be imported into `INNOScale` and displayed as a reverberation time line in the scaling diagram. Then the user can adjust the sound power of the pipes—by modifying the scaling lines and thus the diameters—according to the exact measured data in each frequency band.

Pipe foot data function Sound power is also dependent on the air volume flux into the resonator. Organ builders influence this parameter by changing the windsystem pressure and the ratio of flue (windway area) and foot hole cross sections. Based on experimental pressure loss data [124] three parameters of the pipe foot can be calculated and displayed in the scaling table: the flue width, the diameter of the foot hole, and the ratio of pressures inside

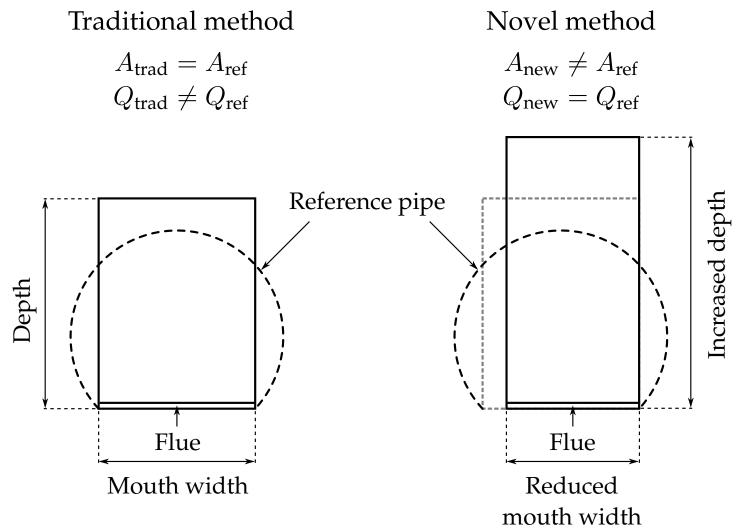

Figure B.3. The traditional and the novel method for scaling wooden pipe ranks

the groove (tone channel) and pipe foot. Any two of these parameters have to be given by the user and the third one is calculated by the program.

Edge tone frequency function The frequency of the air jet oscillating around the upper lip of a labial organ pipe without resonator is called edge tone frequency (see Chapter 9). Its ratio to the fundamental frequency and acoustic eigenfrequencies of the pipe influences the sound to a great extent, especially in the attack transient phase. In practice, the frequency of the edge tone is usually changed by increasing the height of the cutup. The purpose of this new function in `INNOScale` is to help the user finding the cutup height necessary to achieve the required ratio of edge tone and fundamental frequencies. The calculations are based on empirically determined relations [18] and pre-defined parameters, such as the frequency ratio, the flue width, the wind pressure, and pressure loss coefficients.

Scaling function for wooden pipe ranks Wooden pipes always have a rectangular cross section and in the traditional scaling practice their mouth widths are equal to those of the reference pipes. Their depths are traditionally calculated so that the rectangular cross section equals the circular cross section of the reference pipes, as shown in Figure B.3. This process sometimes leads to too wide pipes, so that the total width of the rank does not fit into the space available inside the organ. In order to overcome this difficulty a new scaling technique was developed, where the organ builder can define smaller widths for the pipes, given as a percentage relative to the traditional widths. Then, to avoid an essential change of the timbre, the depths of the pipes are calculated so that the amount of viscothermal wall losses becomes identical to that of the reference pipes [58], see the right hand side of Figure B.3.

Chimney pipe scaling The sound design method for chimney pipe resonators introduced in Chapter 5 has also been incorporated into `INNOScale`. The user can select the harmonic to be emphasized in the sound and the program runs the optimization routine to obtain the dimensions of the pipe. The set of parameters which are optimized by the process can also be chosen by the user from a number of possible configurations.

Appendix C

ReedResonatorSim

This appendix briefly introduces a software tool called `ReedResonatorSim`[1] that supports the computer aided design of resonators and shallots of reed organ pipes. The methodology implemented in the tool was presented already in Chapter 8. This appendix discusses some details of the implementation and demonstrates the capabilities of the tool by an example design problem. Further information about the software code can be found in the technical report [T5].

C.1 Introduction

As it was discussed in Chapter 8 there are no common rules in organ building practice for the design of resonators and shallots of lingual organ pipes. `ReedResonatorSim` aims at providing a simple modeling tool for the organ building community to be able to test the impact of changing the geometry of the resonator or the shallot on the resulting sound characteristics. The program implements two main functions:

1. Calculation of the input admittance function and the eigenfrequencies. Foretelling the frequencies of natural resonance is beneficial in resonator design, since the steady state sound spectrum of the pipe can be formed by tuning the eigenfrequencies of the resonator–shallot system. Furthermore, the strength of the coupling between the tongue vibration and the acoustic feedback can also be predicted from the input admittance function.

2. Synthesis of the sound radiated from the open resonator end. By providing a suitable excitation to the acoustic model, the steady state spectrum of the radiated sound can be simulated and sound samples can be synthesized. Although the exact reproduction of the sound of a reed pipe is a far too complex task to implement in such a simple tool, comparison of the generated sound samples facilitates the subjective assessment of the expected sound quality of different resonator designs.

C.2 Implementation

Acoustic model `ReedResonatorSim` is based on the one-dimensional acoustic model of axisymmetric resonators introduced in Chapter 8. The calculation of the input admittance is performed with making use of the transmission matrix equation (8.9). The user can choose from different radiation impedance models, such as that of Norris & Scheng (3.64), Levine & Schwinger (3.65), or the finite element results, presented in Section 8.3. The shallot model is implemented as introduced in Section 8.4.

Excitation The excitation signal can be incorporated into the simulation in two different ways. First, results of laser vibrometer recordings can directly be imported from wave files. The fundamental frequency of the recording is automatically detected and the user can transpose the signal to the desired frequency. Alternatively, simulated excitation signals can be used, which are created based on the observed properties of laser vibrometer measurements carried out in the framework of the project REEDDESIGN. The user can control the fundamental frequency, the filtering parameters and the signal to noise ratio of the simulated excitation signal. The artificial excitation signal proves to be useful as the noise inherently contained in measured signals can easily be removed. In both cases the excitation is interpreted as a volume velocity source acting at the input end of the shallot, defined in the frequency domain by the function $\hat{U}_{\text{in}}(\omega)$.

Sound synthesis The sound pressure radiated from the open end of the resonator is synthesized from the acoustic model and the excitation signal $\hat{U}_{\text{in}}(\omega)$ in the following manner. By rearranging the equations of the transmission matrix model (8.9), the relation between the input volume velocity $\hat{U}_{\text{in}}(\omega)$ and the output sound pressure $\hat{p}_{\text{out}}(\omega)$ is found as

$$\hat{p}_{\text{out}}(\omega) = H(\omega) \cdot \hat{U}_{\text{in}}(\omega) = \left(T_{21}(\omega) + \frac{T_{22}(\omega)}{Z_{\text{R}}(\omega)} \right)^{-1} \hat{U}_{\text{in}}(\omega). \tag{C.1}$$

The above can be evaluated once the radiation impedance $Z_{\text{R}}(\omega)$ is known. The time domain signal $p_{\text{out}}(t)$ is obtained by the inverse Fourier-transform (implemented using IFFT) of the output pressure $\hat{p}_{\text{out}}(\omega)$

$$p_{\text{out}}(t) = \mathcal{F}^{-1} \left\{ \hat{p}_{\text{out}(\omega)} \right\} = \mathcal{F}^{-1} \left\{ H(\omega) \cdot \hat{U}_{\text{in}}(\omega) \right\}. \tag{C.2}$$

The tool implements a very simple synthesizer that produces an ADSR[2] envelope which modulates the amplitude of the signal, so that the sound sample $p_{\text{sample}}(t)$ is obtained as

$$p_{\text{sample}}(t) = A_{\text{ADSR}}(t) \cdot p_{\text{out}}(t), \tag{C.3}$$

with $A_{\text{ADSR}}(t)$ denoting the ADSR function.

Since the simulation of a realistic attack transient would require much more effort (see e.g. references [128] or [C15]), the ADSR is chosen for the sake of simplicity. By the simple fade-in the attack is masked and the listener can concentrate on the steady state characteristics of the sound.

C.3 A *Vox humana* example

As an example, the *Vox humana* resonator presented in Section 8.5.3 is modeled here. Figure C.1 shows the user interface of `ReedResonatorSim` with the *Vox humana* project file loaded. In the topmost region of the window, the geometry of the resonator is displayed; the values can be edited, conical sections can be added or removed. Next, the parameters of the shallot and the tongue can be configured. These values are needed to calculate the effective length of the shallot, as discussed in Section 8.4. In the *Calculation and simulation* panel, the eigenfrequencies can be computed and the radiated sound can be simulated. Finally, in the bottom part of the window, stored results can be quickly compared to each other.

The calculated input admittance function of the *Vox humana* resonator is shown in Figure C.2. In the left hand side (Figure C.2(a)) the input admittance without the shallot is shown, whereas the right hand side (Figure C.2(b)) displays the calculated input admittance of the complete

[2] Attack – Decay – Sustain – Release

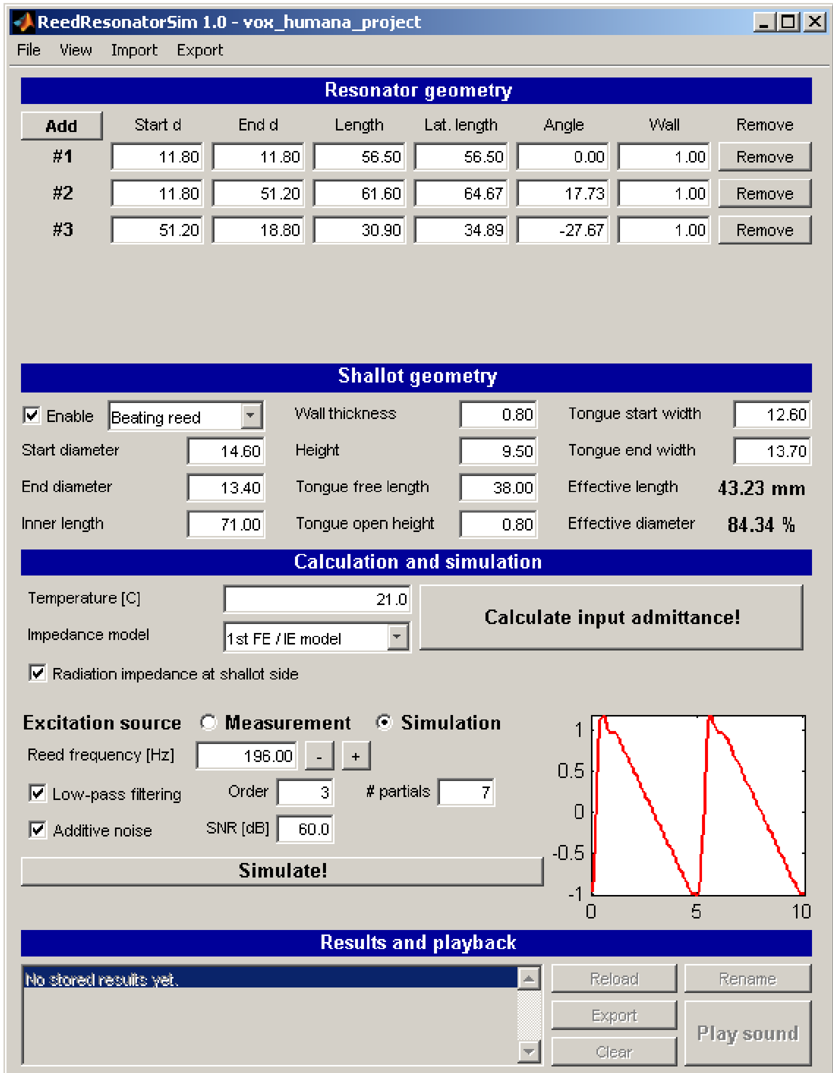

Figure C.1. The main window of the tool `ReedResonatorSim` with the *Vox humana* project loaded

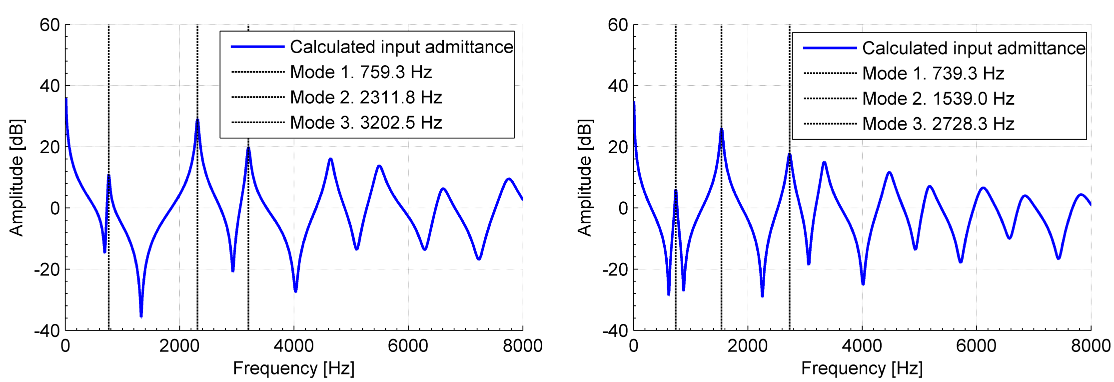

(a) Input admittance without shallot

(b) Input admittance with shallot

Figure C.2. Calculated input admittance of the *Vox humana* resonator

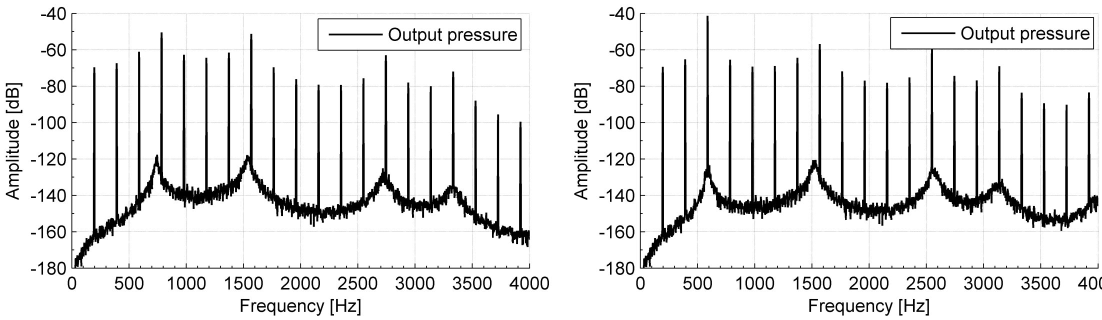

(a) Original sound spectrum

(b) Sound spectrum with modified geometry

Figure C.3. Sound spectra of a *Vox humana* pipe, simulated by `ReedResonatorSim`

shallot–resonator system. As it can be seen, the frequencies of natural resonanance are affected by the shallot to a great extent: while the frequency of the first mode remains nearly the same, upper modal frequencies are shifted downwards significantly.

Figure C.3(a) shows the steady state sound spectrum resulting from the simulated excitation signal. The harmonic partials are identified by the regular, periodic sharp peaks, while maxima of the input impedance are found by observing the broad peaks in the baseline of the spectrum. An impedance maximum is present between the third and fourth partials, in correspondence with the first acoustic mode of the resonator–shallot system. As it can be seen, the first acoustic mode amplifies the fourth partial (second octave) in the sound to a great extent, while the third and the fifth harmonics are also enhanced. Since the *Vox humana* should amplify the third harmonic, it can be assessed that the original resonator design is suboptimal.

To achieve a better amplification of the third harmonic, the geometry of the resonator must be changed. However, it is not straightforward to tell how different parameters would affect the input impedance function. The objective of `ReedResonatorSim` is to provide a user friendly interface for modeling the effect of such changes. By modifying the values in the *Resonator geometry* panel and evaluating the input impedance function and the modal frequencies, the impact of each parameter can be assessed and different configurations can be compared with each other.

For example, by changing the length of the third section from $30.90\,\mathrm{mm}$ to $50.35\,\mathrm{mm}$, the frequency of the first acoustic mode of the resonator–shallot system can be tuned to $588\,\mathrm{Hz}$ which is exactly three times the fundamental frequency. The resulting steady state sound spectrum is shown in Figure C.3(b). By comparing the two spectra of Figure C.3, the remarkable difference is conspicuous. It can also be observed that the frequencies of higher modes are also shifted down, except for the second mode, whose frequency remained nearly the same. The steady state characteristics of the two sounds can also be compared in a subjective manner by playing the corresponding sound samples.

Appendix D

`NiHu`: A BEM/FEM toolbox for acoustics

This appendix briefly introduces `NiHu`[1], a `C++`- and `Matlab`-based toolbox for boundary and finite elements. This toolbox was utilized in the thesis for all acoustical finite element simulations. Therefore, this appendix demonstrates only the finite element parts of `NiHu`. The capabilities of the tool are illustrated by means of solving a two-dimensional academic problem.

D.1 The example problem

In this example an acoustical scattering problem of a plane wave reflected from an acoustically rigid cylinder is solved. It is assumed that the plane wave travels in the positive x direction and has a frequency of $f = 400\,\mathrm{Hz}$. The cylinder is located at the origin and its radius is chosen as $R_{\mathrm{cyl}} = 0.5\,\mathrm{m}$. We define the boundary Γ as the surface of the cylinder, i.e. $\Gamma = \{(x,y) \mid x^2+y^2 = R_{\mathrm{cyl}}^2\}$. The material properties of the fluid are chosen as average density $\rho_0 = 1.2\,\mathrm{kg/m^3}$ and speed of sound $c = 343\,\mathrm{m/s}$. We are looking for the sound pressure $p(\boldsymbol{x},\omega)$, with $\omega = 2\pi f$, in the domain of interest $\boldsymbol{x} \in \Omega$, which is defined explicitly in the sequel.

The problem at hand involves scattering, hence the solution $p(\boldsymbol{x})$ is found as the superposition of the incident $p_{\mathrm{inc}}(\boldsymbol{x})$ and the scattered $p_{\mathrm{scat}}(\boldsymbol{x})$ pressure fields, as it was discussed in Section 4.1.5. The same holds for the particle velocity $\boldsymbol{v}(\boldsymbol{x})$. As the cylinder is acoustically rigid, the normal particle velocity v_n vanishes on its surface, and thus $v_{n,\mathrm{scat}}(\boldsymbol{x}) = -v_{n,\mathrm{inc}}(\boldsymbol{x})$ if $\boldsymbol{x} \in \Gamma$. Since the incident pressure field and its normal derivative on Γ are known analytically, only the reflected pressure field is sought. The latter is found by imposing a Neumann boundary condition on Γ as $\bar{v}_n(\boldsymbol{x}) = -v_{n,\mathrm{inc}}(\boldsymbol{x})$, and solving the resulting boundary value problem.

The solution can be found analytically following [106, p. 401]. Assuming that the incident wave has unit amplitude, the solution in polar coordinates (r,ϕ) reads as

$$p_{\mathrm{refl}} = \sum_{m=0}^{\infty} A_m \cos(m\phi) H_m^{(2)}(kr), \tag{D.1}$$

with

$$A_m = -\epsilon_m(-\mathrm{j})^{m+1}\mathrm{e}^{\mathrm{j}\gamma_m}\sin\gamma_m \qquad \epsilon_m = \begin{cases} 1 & \text{if} \quad m = 0 \\ 2 & \text{if} \quad m \geq 1 \end{cases} \tag{D.2}$$

and

$$\tan\gamma_0 = -\frac{J_1(kR_{\mathrm{cyl}})}{N_1(kR_{\mathrm{cyl}})} \qquad \tan\gamma_m = -\frac{J_{m-1}(kR_{\mathrm{cyl}}) - J_{m+1}(kR_{\mathrm{cyl}})}{N_{m+1}(kR_{\mathrm{cyl}}) - N_{m-1}(kR_{\mathrm{cyl}})}. \tag{D.3}$$

[1] © Péter Fiala and Péter Rucz, 2009–2014. Some functions supporting PML are by Bence Olteán.

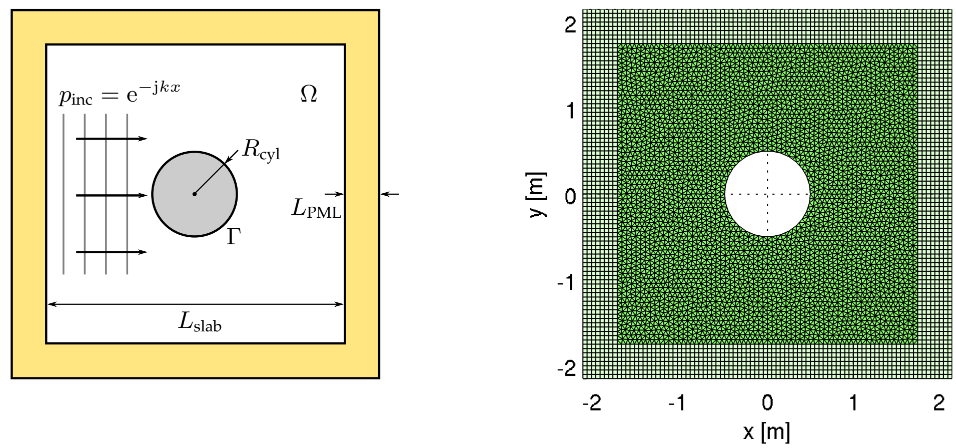

(a) Arrangement of the example problem

(b) The generated FE/PML mesh

Figure D.1. The arrangement and the discretized model of the example problem

The result of the finite element simulation will be compared to the above solution. The simulation arrangement is depicted in Figure D.1(a). In the finite element model the simulation domain Ω is defined as $\Omega = \{(x, y) \mid -L_{\mathrm{slab}}/2 \le x, y \le L_{\mathrm{slab}}/2 \,\wedge\, x^2 + y^2 \ge R_{\mathrm{cyl}}^2\}$, with the choice of $L_{\mathrm{slab}} = 3.5\,\mathrm{m}$. Since the problem has open boundaries, the perfectly matched layer method is applied for emulating free field conditions on the outer boundary of the mesh. The thickness of the layer is chosen as $L_{\mathrm{PML}} = 0.4\,\mathrm{m}$.

D.2 Finite element solution code

In this section the finite element solution of the example problem is followed step-by-step together with the corresponding `Matlab` codes.

D.2.1 Parametrization

First, the global parameters are set, i.e. the properties of the material and the source frequency.

```
% Material and excitation properties
rho = 1.2;                   % Average density of air [kg/m^3]
c = 343;                     % Speed of sound [m/s]
f = 400;                     % Frequency of excitation [Hz]
om = 2*pi*f;                 % Angular frequency [rad/s]
```

Next, the parameters of the geometry and the discretized model are configured. The element size is chosen as $L_e = 0.05\,\mathrm{m}$, which roughly corresponds to 16 elements per wavelength. Using this configuration we have $N_{\mathrm{PML}} = 8$ elements along the thickness of the PML.

```
% Geometry
R_cyl = 0.5;                 % Radius of the cylinder [m]
N_cyl = 60;                  % Number of elements on cylinder
L_slab = 3.5;                % Side length of computational domain [m]
Le = 0.05;                   % Length of elements [m]
N_slab = ceil(L_slab / Le); % Number of elements along the edge
```

```
12 tol = 1e-3;                % Relative tolerance
13 % PML parameters
14 N_PML = 8;                 % Number of PML elements in the layer
15 L_PML = 0.4;               % Thickness of PML layer [m]
16 L_sum = L_slab + 2*L_PML;  % Total side length [m]
```

D.2.2 Mesh generation

Our mesh consists of two parts, i.e. the pure FE mesh, and the attached PML. The inner mesh is generated first, by creating its contour and using automatic triangular mesh generation. The latter is provided by the `mesh2d` function of the `MESH2D`[2] toolbox.

```
17 % Create contour
18 cylinder = create_circle_boundary(R_cyl, N_cyl/2);
19 slab_in  = translate_mesh( ...
20     create_slab_boundary(L_slab, N_slab/2), -1/2*L_slab*[1, 1, 0]);
21 contour = join_meshes(cylinder, slab_in);
22 % Create triangle mesh
23 [p,t] = mesh2d(contour.Nodes(:,2:3), contour.Elements(:,5:6), ...
24     struct('hmax', Le), struct('output', false));
25 mesh = pt2nihumesh(p, t);    % NiHu mesh from points and triangles
```

The function `pt2nihumesh` converts the generated nodes and triangles into the mesh format of `NiHu`. Note: The `mesh2d` function halves all the edges on the boundary, thus, in lines 18 and 20 the parameters N_{cyl} and N_{slab} are halved.

The PML mesh is generated by creating a square with a side length of $L_{\mathrm{slab}} + 2L_{\mathrm{PML}}$, and cutting out its middle part. The latter is performed in lines 29–30 using the `mesh_section` function. After the middle elements are cut out, the corresponding nodes are eliminated by calling the function `drop_unused_nodes`.

```
26 % Create the PML mesh
27 pml_mesh = translate_mesh( ...
28     create_slab(L_sum, N_slab+2*N_PML), -1/2*(L_sum)*[1, 1, 0]);
29 pml_mesh = mesh_section(pml_mesh, ...
30     1/2*L_slab*[-1+tol, -1+tol, -inf; 1-tol, 1-tol, inf], 'none');
31 pml_mesh = drop_unused_nodes(pml_mesh);
32 % Assign PML properties
33 pml_mesh.Elements(:,2) = 224;        % PML elem identifier
34 pml_mesh.Properties = [1, 3, 1, L_PML, 0, 0];
```

The PML properties are assigned to the mesh in lines 33–34.

When both parts of the mesh are constructed, they are joined together and their coincident nodes are merged. The material properties are configured in line 38. Finally, the absorbing function of the PML is configured in lines 39–40. The function `pml_sigma_glob` implements the unbounded absorbing function as defined by equation (4.49).

```
35 % Join the meshes
36 model = merge_coincident_nodes(join_meshes(mesh, pml_mesh), 1e-3);
37 model = drop_mesh_IDs(model);
38 model.Materials(1, 3:4) = [rho, c];
39 model.PMLData = {1, @pml_sigma_glob, @pml_sigma_glob, [], ...
40     [-L_slab/2 L_slab/2], [-L_slab/2 L_slab/2], []};
```

[2] © Darren Engwirda, 2009. See: http://www.mathworks.com/matlabcentral/fileexchange/25555-mesh2d

The generated mesh is displayed in Figure D.1(b), with the PML part shown in transparent green for clarity. The numerical model has 6 541 nodes and 10 182 elements comprising 7 686 triangles in the inner part and 2 496 quadrangles in the absorbing layer.

D.2.3 System matrix assembly

In the next step, the system matrices of the FE–PML model are assembled. The matrices $\mathbf{K}$ and $\mathbf{M}$ from equation (4.13) are constructed by calling the `model_mk` function. The matrices $\mathbf{K}^{(\mathrm{PML})}$ and $\mathbf{M}^{(\mathrm{PML})}$ are assembled separately by calling `pml_mk`. Then, the two subsystems are joined by the function `model_system`.

```
41 % System matrix assembly
42 [I, J, M, K, DOF] = model_mk(model, 'ind');          % Pure FEM
43 [Ip, Jp, Mp, Kp, DOFp] = pml_mk(model, om, 'ind');   % Pure PML
44 % Join subsystems
45 [M, K, DOF] = model_system({I J M K DOF}, {Ip Jp Mp Kp DOFp});
46 A = model_a(get_boundary(model));    % Excitation matrix
```

The reason for assembling the pure FE and the PML system matrices in two subsequent steps is that the former are independent of the frequency, while the latter are not. If we would solve the same problem with a number of different testing frequencies, the pure FE matrices would need to be assembled only once. Finally, the matrix $\mathbf{A}$ from equation (4.13) is assembled. The structure of the sparse system matrices $\mathbf{K}$ and $\mathbf{M}$ is displayed in Figure D.2(a). The size of the matrices and hence the number of DOFs of the system correspond the number of nodes in the mesh.

D.2.4 Excitation and boundary conditions

Before the definition of the excitatation the nodes on the boundary are selected in line 48 by the `mesh_select` function.

```
47 % Find excitation indices
48 i_exc = mesh_select(model, sprintf('r < %f', R_cyl*(1+tol)), 'ind');
```

The incident field generated by a plane wave is obtained by calling the function `incident` with the parameter `'plane'`. The function calculates the incident pressure and its normal derivative. For the latter, we make use of the fact that the normal vector on $\boldsymbol{x} \in \Gamma$ is given as $\boldsymbol{n}(\boldsymbol{x}) = -\boldsymbol{x}/R_{\mathrm{cyl}}$. The normal particle velocity is attained using relation (4.3).

```
49 % Calculate incident field
50 [p_inc, q_inc] = incident('plane', [1 0 0], model.Nodes(: ,2:4), ...
51     -model.Nodes(:, 2:4) / R_cyl, om/c);
52 % Calculate the reflected normal velocity
53 v_refl = zeros(size(model.Nodes, 1), 1);
54 v_refl(i_exc) = -1./(1i*om*rho)*q_inc(i_exc);
```

D.2.5 Solution

The numerical solution is performed using `Matlab`'s direct solver. In line 56 equation (4.12) is solved. After executing lines 56–57 the vector $\mathbf{p}_{\mathrm{sol}}$ contains the complex sound pressure values in the nodal coordinates of the mesh.

```
55 % Numerical solution
56 p_refl = (K - om^2*M)\(1i*om*A*v_refl);
57 p_sol = p_inc + p_refl;
```

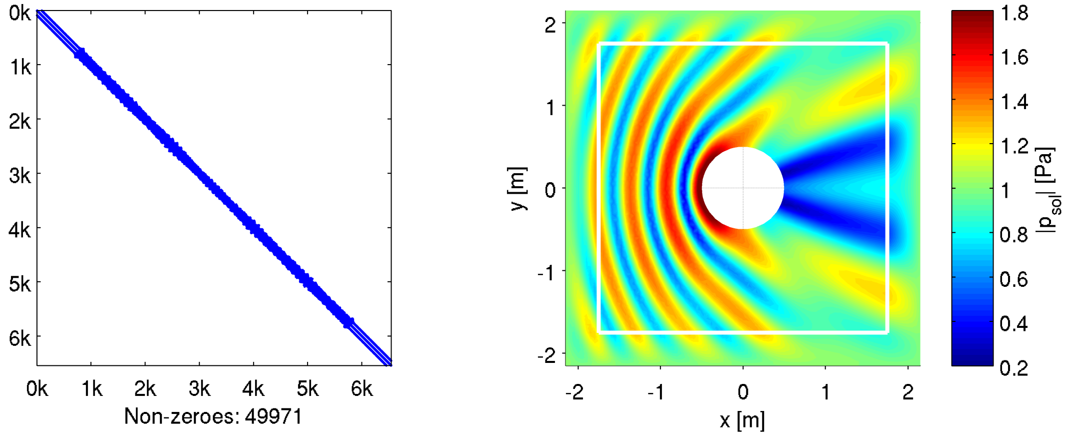

(a) Structure of the system matrices

(b) The numerical solution

Figure D.2. System matrix structure and the resulting acoustic field

The analytical solution is attained by evaluating equations (D.1)–(D.3). The infinite sum in (D.1) is truncated to $m_{\max} = 100$ and evaluated by the function `planewave_cyl2d` in line 59.

```
58 % Analytical solution
59 p_ana_refl = planewave_cyl2d(model.Nodes(:,2:3), R_cyl, om/c, 100);
60 p_ana = p_inc + p_ana_refl;
```

The numerical result is depicted in Figure D.2(b). As it is seen, the reflection from the cylindrical obstacle perturbs the incident planar wavefield to a great extent. The thin white rectangle indicates the transition interface of standard finite elements and the perfectly matched layer. Going outwards in the absorbing layer, the amplitude converges to the amplitude of the incident wave, as expected.

D.2.6 Validation

Finally, the error of the solution is computed by comparing the numerical and analytical results. This is done by evaluating

$$\varepsilon = \frac{\|\mathbf{p}_{\mathrm{sol}} - \mathbf{p}_{\mathrm{ana}}\|}{\|\mathbf{p}_{\mathrm{ana}}\|}, \tag{D.4}$$

with $\|\cdot\|$ denoting the 2-norm. Since the amplitude of the reflected field decays exponentially inside the PML, the DOFs corresponding to the nodes inside the PML are excluded from the evaluation of (D.4). The nodes of the pure FE region are selected in lines 62–63.

```
61 % Find fem indices
62 i_fem = mesh_select(model, ...
63     sprintf('abs(x) < %f & abs(y) < %f', L_slab/2,L_slab/2), 'ind');
64 % Calculate error
65 err = norm(p_ana(i_fem) - p_sol(i_fem))/norm(p_ana(i_fem));
66 fprintf('Log10 L2 error of solution: %f\n', log10(err));
```

The output reads as:

```
Log10 L2 error of solution: -1.704463
```

This corresponds to a relative error of $\varepsilon \approx 1.97\%$, which proves that our numerical solution is correct. The execution time of the whole example code is less than $3\,\mathrm{s}$ on an average desktop computer.

The above example demonstrated that a relatively complex acoustical problem involving finite elements and perfectly matched layers can be modeled and solved from scratch in about 60 lines of code using the `Matlab` routines of the `NiHu` toolbox. Besides the simplicity of the code, it was also seen that the toolbox also provides a considerable amount of insight into the internals of the finite element method, that are hidden by commercial FE software. The latter feature is especially useful in education, where understanding how the solution process works is as important as the actual solution of the specific problem.

D.3 `NiHu`-related publications

To this date, only the boundary element and pre- and postprocessing utilities of the toolbox are published, see references [C9, C12, C14, J5]. Besides these papers, eight bachelor's and master's theses from the Laboratory of Acoustics and Studio Technologies have utilized and contributed to the `NiHu` toolbox in the last four years. The toolbox is open source, distributed under the GNU public license and can be downloaded from http://last.hit.bme.hu/nihu.

Appendix E

Industrial project partners

Carrying out the research presented in the dissertation would not have been possible without the research projects INNOUSOUND and REEDDESIGN and the support of the organ building firms participating in them. The support of the organ builder partners listed in Table E.1 is acknowledged and greatly appreciated.

Partner	Country	Projects
Blancafort Orgueners de Montserrat SL	Spain	I, R
Boogard Ide – Orgelmakerij Boogaardboog	Netherlands	I
Famiglia Artigiana Fratelli Ruffatti s.n.c.	Italy	I, R
Flentrop Orgelbouw B.V.	Netherlands	I, R
Johannes Klais Orgelbau GmbH & Co. KG	Germany	I, R
Manufacture d'Orgues Mühleisen G. Walther & Associés	France	I, R
Oficina e Escola de Organaria Limitada	Portugal	I, R
Orgelbau Schumacher GmbH	Belgium	I, R
Pécsi Orgonaépítő Manufaktúra Kft.	Hungary	I, R
Werkstätte für Orgelbau Mühleisen GmbH	Germany	I, R

Legend: I – participated in INNOUSOUND, R – participated in REEDDESIGN

Table E.1. Organ builder partners participating in the European projects INNOUSOUND and REEDDESIGN

Bibliography

[1] "INNOPIPEORG" (Project Reference: #17712), in the Sixth Framework Program of the European Union (Framework Program on Research, Technological Development and Demonstration CRAFT – European Commission), COOP-CT-2005-017712 (2005).

[2] "INNOSOUND" (Project Reference: #222104), in the Seventh Framework Program of the European Union (Framework Program on Research, Technological Development and Demonstration Research for SME – European Commission), FP7-SME-2008-1 (2008).

[3] "REEDDESIGN" (Project Reference: #286539), in the Seventh Framework Program of the European Union (Framework Program on Research, Technological Development and Demonstration Research for SME – European Commission), FP7-SME-2011-1 (2011).

[4] M. Abel, S. Bergweiler, R. Gerhard-Multhaupt. "Synchronization of organ pipes: experimental observations and modeling." In: *Journal of the Acoustical Society of America* 119.4 (2006), pp. 2467–2475. DOI: 10.1121/1.2170441.

[5] S. Adachi. "CFD analysis of air jet deflection – Comparison with Nolle's measurments." In: *Proceedings of the Stockholm Music Acoustics Conference*. Stockholm, Sweden, Aug. 2003, pp. 313–316.

[6] S. Adachi. "Principles of sound production in wind instruments." In: *Acoustical Science and Technology* 25.6 (2004), pp. 400–405. DOI: 10.1250/ast.25.400.

[7] S. Adachi, M. Sato. "Time-domain simulation of sound production in the brass instrument." In: *Journal of the Acoustical Society of America* 97.6 (1995), pp. 3850–3861. DOI: 10.1121/1.412398.

[8] S. Adachi, M. Sato. "Trumpet sound simulation using a two-dimensional lip vibration model." In: *Journal of the Acoustical Society of America* 99.2 (1996), pp. 1200–1209. DOI: 10.1121/1.414601.

[9] S. Adachi, H. Takemoto, T. Kitamura, P. Mokhtari, K. Honda. "Vocal tract length perturbation and its application to male-female vocal tract shape conversion." In: *Journal of the Acoustical Society of America* 121.6 (2007), pp. 3874–3885. DOI: 10.1121/1.2730743.

[10] T. Akamura, Y. Nagao, T. Iwasaki, K. Nakano, K. Takahashi, T. Kobayashi, T. Takami, A. Nishida, M. Aoyagi. "Numerical analysis of the interaction between fluid flow and acoustic field at the mouth-opening of a flue instrument." In: *Proceedings of the Meetings on Acoustics – ICA 2013*. Vol. 19. Paper 2aMU5. Montreal, Canada, 2013, *–8. DOI: 10.1121/1.4799957.

[11] Y. Ando. "On the sound radiation of semi-infinite circular pipe of certain wall thickness." In: *Acustica-Acta Acustica* 22 (1969), pp. 219–225.

[12] J. Angster, G. Paál, W. Garen, A. Miklós. "Effect of voicing steps on the stationary spectrum and attack transient of a flue organ pipe." In: *Proceedings of the International Symposium on Musical Acoustics*. Vol. 19, Part 5, Book 2. Edinburgh: Institute of Acoustics, 1997, pp. 285–294.

[13] R. J. Astley. “Infinite elements.” In: *Computational Acoustics of Noise Propagation in Fluids – Finite and Boundary element methods*. Ed. by S. Marburg and B. Nolte. Springer, 2008, pp. 199–230.

[14] R. J. Astley, J. Hamilton. “The stablilty of infinite element schemes for transient wave problems.” In: *Computer Methods in Applied Mechanics and Engineering* 195 (2006), pp. 3553–3571. DOI: 10.1016/j.cma.2005.01.026.

[15] R. J. Astley, G. J. Macaulay, J.-P. Coyette, L. Cremers. “Three-dimensional wave-envelope elements of variable order for acoustic radiation and scattering: Part I. Formulation in the frequency domain.” In: *Journal of the Acoustical Society of America* 103 (1998), pp. 49–63. DOI: 10.1121/1.421106.

[16] G. A. Audsley. In: *Organ-stops and their artistic registration*. Republication of the original edition by The H. W. Gray Co., New York, 1921. Dover Publications, Inc., New York, 2002, pp. 226–229.

[17] G. A. Audsley. *The art of organ-building, Volume I*. Republication of the original edition by Dodd, Mead, and Co., New York, 1905. Dover Publications, Inc., New York, 2011.

[18] H. Außerlechner. “Strömungsakustische Untersuchungen des Schneidentons und Visualisierungen der Freistrahls mithilfe eines Orgelpfeifenfußmodells (Aeroacoutic examination of the edge tone and visualization of the free jet by means of an organ pipe foot model.” In German. PhD thesis. University of Stuttgart, Faculty of Civil and Environmental Engineering, 2010.

[19] H. Außerlechner, T. Trommer, J. Angster, A. Miklós. “Experimental jet velocity and edge tone investigations on a foot model of an organ pipe.” In: *Journal of the Acoustical Society of America* 126.2 (2009), pp. 878–886. DOI: 10.1121/1.3158935.

[20] J. Backus, T. C. Hundley. “Wall vibrations in flue organ pipes and their effect on tone.” In: *Journal of the Acoustical Society of America* 39.5 (1966), pp. 936–945. DOI: 10.1121/1.1909975.

[21] G. K. Batchelor. *An introduction to Fluid Dynamics*. Cambridge University Press, 1967.

[22] F. Bedos de Celles. In: *L'Art du Factuer d'Orgue (The art of organ building)*. In French. Bärenreiter Verlag, Kassel, 1958, p. 1766.

[23] K. Beissner. “The acoustic radiation force in lossless fluids in Eulerian and Lagrangian coordinates.” In: *Journal of the Acoustical Society of America* 103.5 (1998), pp. 2321–2332. DOI: 10.1121/1.422751.

[24] A. H. Benade. “On the mathematical theory of woodwind finger holes.” In: *Journal of the Acoustical Society of America* 30.12 (1960), pp. 1591–1608. DOI: 10.1121/1.1907968.

[25] A. H. Benade. “On the propagation of sound waves in a cylindrical conduit.” In: *Journal of the Acoustical Society of America* 44.2 (1968), pp. 616–623. DOI: 10.1121/1.1911130.

[26] A. H. Benade, E. V. Jansson. “On plane and spherical waves in horns with nonuniform flare I. Theory of radiation, resonance frequencies, and mode conversion.” In: *Acustica-Acta Acustica* 31.2 (1974), pp. 79–98.

[27] L. L. Beranek. *Acoustics*. Acoustical Society of America, New York, 1993.

[28] J.-P. Berenger. “A perfectly matched layer for the absorption of electromagnetic waves.” In: *Journal of Computational Physics* 114 (1994), pp. 185–200. DOI: 10.1006/jcph.1994.1159.

[29] A. Bermúdez, L. Hervella-Nieto, A. Prieto, R. Rodrígez. “Perfectly matched layers.” In: *Computational Acoustics of Noise Propagation in Fluids – Finite and Boundary element methods*. Ed. by S. Marburg and B. Nolte. Springer, 2008, pp. 167–196.

[30] A. Bermúdez, L. Hervella-Nieto, A. Prieto, R. Rodríguez. "An optimal perfectly matched layer with unbounded absorbing function for time-harmonic acoustic scattering problems." In: *Journal of Computational Physics* 223 (2007), pp. 469–488. DOI: 10.1016/j.jcp.2006.09.018.

[31] J. Biermann, O. v. Estorff, S. Petersen, C. Wenterodt. "Higher order finite and infinite elements for the solution of Helmholtz problems." In: *Computer Methods in Applied Mechanics and Engineering* 198 (13–14 2009), pp. 1171–1188. DOI: 10.1016/j.cma.2008.11.009.

[32] C. P. Boner. "Acoustic spectra of organ pipes." In: *Journal of the Acoustical Society of America* 10 (1938), pp. 32–40. DOI: 10.1121/1.1915953.

[33] H. Bouasse. *Instruments á Vent (Wind instruments)*. In French. Librarie Delagrave, Paris, 1930.

[34] R. N. Bracewell. *The Fourier transform and its applications*. Third edition. McGraw-Hill, 2000.

[35] J. M. Buick, M. Atig, D. J. Skulina, D. M. Campbell, J. P. Dalmont, J. Gilbert. "Investigation of non-linear acoustic losses at the open end of a tube." In: *Journal of the Acoustical Society of America* 129.3 (2011), pp. 1261–1272. DOI: 10.1121/1.3543987.

[36] D. S. Burnett. "A three-dimensional acoustic infinite element based on a prolate spheroidal multipole expansion." In: *Journal of the Acoustical Society of America* 96.5 (1994), pp. 2798–2816. DOI: 10.1121/1.411286.

[37] B. C. Carlson. "Elliptic integrals." In: *NIST handbook of mathematical functions*. Ed. by F. W. J. Olver, D. W. Lozier, R. F. Boisvert, and C. W. Clark. National Institute of Standards and Technology – Cambridge University Press, 2010. Chap. 19.

[38] M. Castellengo. "Contribution á l'etude de experimentale des tuyaux á bouche (Contribution to the experimental study of tube terminations)." In French. PhD thesis. Université de Paris VI, Paris, France, 1976.

[39] R. Caussé, J. Kergomard, X. Lurton. "Input impedance of brass instruments – Comparison between experiment and numerical models." In: *Journal of the Acoustical Society of America* 75.1 (1984), pp. 241–254. DOI: 10.1121/1.390402.

[40] W. Chester. "The acoustic impedance of a semi-infinite tube fitted with a conical flange: Part II." In: *Journal of Sound and Vibration* 116.2 (1987), pp. 371–377. DOI: 10.1016/S0022-460X(87)81308-1.

[41] J. W. Coltman. "Sounding mechanism of the flute and organ pipe." In: *Journal of the Acoustical Society of America* 44.4 (1968), pp. 983–992. DOI: 10.1121/1.1911240.

[42] J. W. Coltman. "Jet drive mechanisms in edge tones and organ pipes." In: *Journal of the Acoustical Society of America* 60 (1976), pp. 724–733. DOI: 10.1121/1.381120.

[43] L. Cremer, H. Ising. "Die selbsterregten Schwingungen von Orgelpfeifen." In: *Acustica* 19 (1967–1968), pp. 143–153.

[44] D. G. Crighton. "The jet edge-tone feedback cycle; linear theory for the operating stages." In: *Journal of Fluid Mechanics* 234 (1992), pp. 361–391. DOI: 10.1017/S002211209200082X.

[45] J.-P. Dalmont, C. J. Nederveen, S. Dubos, V. Méserette, E. Sligte. "Experimental determination of the equivalent circuit of an open side hole: linear and non linear behaviour." In: *Acustica-Acta Acustica* 88.4 (2002), pp. 567–575.

[46] J.-P. Dalmont, C. J. Nederveen, N. Joly. "Radiation impedance of tubes with different flanges: numerical and experimental investigations." In: *Journal of Sound and Vibration* 244.3 (2001), pp. 505–534. DOI: 10.1006/jsvi.2000.3487.

[47] H. Dänzer, W. Kollmann. "Über die Strömungsverhältnisse an der Lippenöffnung von Orgelpfeifen." In: *Zeitschrift für Physik* 144 (1956), pp. 237–243. DOI: 10.1007/BF01327084.

[48] J. W. Demmel. *Applied numerical linear algebra*. Society for Industrial and Applied Mathematics, Philadelpha, 1997.

[49] S. Dequand, J. F. H. Willems, M. Leroux, R. Vullings, M. Weert, C. Thielout, A. Hirschberg. "Simplified models of flue instruments: Influence of mouth geometry on the sound source." In: *Journal of the Acoustical Society of America* 113.3 (2003), pp. 1724–1735. DOI: 10.1121/1.1543929.

[50] J. Diaz, P. Joly. "A time domain analysis of PML models in acoustics." In: *Computer Methods in Applied Mechanics and Engineering* 195 (2006), pp. 3820–3853. DOI: 10.1016/j.cma.2005.02.031.

[51] D. Dreyer, S. Petersen, O. Estorff. "Effectiveness and robustness of improved infinite elements for exterior acoustics." In: *Computer Methods in Applied Mechanics and Engineering* 195 (2006), pp. 3591–3607. DOI: 10.1016/j.cma.2005.01.019.

[52] D. Dreyer, S. Petersen, O. Estorff. "Efficient infinite elements based on Jacobi polynomials." In: *Computational Acoustics of Noise Propagation in Fluids – Finite and Boundary element methods*. Ed. by S. Marburg and B. Nolte. Springer, 2008, pp. 231–250.

[53] V. Dubos, J. Kergomard, A. Khettabi, J.-P. Dalmont, D. H. Keefe, C. J. Nederveen. "Theory of sound propagation in a duct with a branched tube using modal decomposition." In: *Acustica-Acta Acustica* 85.2 (1999), pp. 153–169.

[54] P. Ehrenfest. "On adiabatic changes of a system in connection with the quantum theory." In: *KNAW Proceedings* 19 I (1917), pp. 576–597. URL: http://www.dwc.knaw.nl/DL/publications/PU00012386.pdf.

[55] E. Eisner. "Complete solutions of the "Webster" horn equation." In: *Journal of the Acoustical Society of America* 41.4 (1967), pp. 1126–1146. DOI: 10.1121/1.1910444.

[56] S. A. Elder. "On the mechanism of sound production in organ pipes." In: *Journal of the Acoustical Society of America* 54.6 (1973), pp. 1554–1564. DOI: 10.1121/1.1914453.

[57] W. Ellerhorst. *Handbuch der Orgelkunde (Handbook of organ science)*. In German. Verlagsanstalt Benziger & Co. A.G., 1936.

[58] E. Esteve Fontestad. "Innovative method for the development of optimal scaling of the depth and width of wooden organ pipes." MA thesis. Universidad Politécnica de Valencia, 2008.

[59] P. Eveno. "Wave propagation and radiation in a horn: Comparison between models and measurements." In: *Acustica-Acta Acustica* 98 (2012), pp. 158–165.

[60] B. Fabre, A. Hirschberg. "Physical modeling of flue instruments: A review of lumped models." In: *Acustica-Acta Acustica* 86.4 (2000), pp. 599–610.

[61] F. J. Fahy. *Foundations of engineering acoustics*. Elsevier Academic Press, 2001.

[62] J. Fischer, M. Abel. "Synchronization of nonlinear, acoustical oscillators." In: *DAGA2012 38. Jahrestagung für Akustik*. Ed. by H. Hanselka. Deutsche Gesellschaft für Akustik e.V. (DEGA). Darmstadt, Germany, 2012, pp. 197–198.

[63] N. H. Fletcher. "Nonlinear interactions in organ flue pipes." In: *Journal of the Acoustical Society of America* 56.2 (1974), pp. 645–652. DOI: 10.1121/1.1903303.

[64] N. H. Fletcher. "Sound production by organ flue pipes." In: *Journal of the Acoustical Society of America* 60 (1976), pp. 1119–1132. DOI: 10.1121/1.381174.

[65] N. H. Fletcher. "Autonomous vibration of simple pressure-controlled valves in gas flows." In: *Journal of the Acoustical Society of America* 93.4 (1993), pp. 2172–2180. DOI: 10.1121/1.406857.

[66] N. H. Fletcher, L. M. Douglas. "Harmonic generation in organ pipes, recorders, and flutes." In: *Journal of the Acoustical Society of America* 68.3 (1980), pp. 767–771. DOI: 10.1121/1.384815.

[67] N. H. Fletcher, T. D. Rossing. *The physics of musical instruments*. Springer, 1991.

[68] D. Givoli. "Computational absorbing boundaries." In: *Computational Acoustics of Noise Propagation in Fluids – Finite and Boundary element methods*. Ed. by S. Marburg and B. Nolte. Springer, 2008, pp. 145–166.

[69] T. Hélie. "Unidimensional models of acoustic propagation in axisymmetric waveguides." In: *Journal of the Acoustical Society of America* 114.5 (2003), pp. 2633–2647. DOI: 10.1121/1.1608962.

[70] T. Hélie, X. Rodet. "Radiation of a pulsating sphere: Application to horn radiation." In: *Acustica-Acta Acustica* 89 (2003), pp. 565–577.

[71] H. Helmholtz. *On the sensation of tone*. Dover, New York, 1954.

[72] A. Hirschberg, R. W. A. Laar, J. P. Marrou-Maurières, A. P. J. Wijnands, H. J. Dane, S. G. Kruijswijk, A. J. M. Houtsma. "A quasi-stationary model of air flow in the reed channel of single-reed woodwind instruments." In: *Acustica-Acta Acustica* 70.2 (1990), pp. 146–154.

[73] D. K. Holger, T. A. Wilson, G. S. Beavers. "Fluid mechanics of the edge tone." In: *Journal of the Acoustical Society of America* 62.5 (1977), pp. 1116–1128. DOI: 10.1121/1.381645.

[74] A. Houmat. "Mapped infinite p-element for two-dimensional problems of unbounded domains." In: *Computers and Geotechnics* 35 (2008), pp. 608–615. DOI: 10.1016/j.compgeo.2007.09.007.

[75] M. S. Howe. *Theory of Vortex Sound*. Cambridge University Press, 2003.

[76] T. M. Huber, M. Fatemi, R. Kinnick, J. Greenleaf. "Noncontact modal analysis of a pipe organ reed using airborne ultrasound stimulated vibormetry." In: *Journal of the Acoustical Society of America* 119.4 (2006), pp. 2476–2482. DOI: 10.1121/1.2171516.

[77] A. Hüppe, M. Kaltenbacher. "Advanced spectral finite element method for computational acoustics in the mid-frequency range." In: *Proceedings of ISMA2010: International Conference on Noise and Vibration Engineering including USD2010*. Ed. by P. Sas and B. Bergen. Katholieke Universiteit Leuven. Leuven, Belgium, 2010, pp. 2351–2360.

[78] F. Ingerslev, W. Frobenius. "Some measurements of the end-corrections and acoustic spectra of cylindrical open flue organ pipes." In: *Transactions of the Danish Academy of Technical Sciences* 1.3 (1947), pp. 1–42.

[79] A. T. Jones. "End corrections of organ pipes." In: *Journal of the Acoustical Society of America* 12 (1941), pp. 387–394. DOI: 10.1121/1.1916116.

[80] B. Kaltenbacher, M. Kaltenbacher, I. Sim. "A modified and stable version of a perfectly matched layer technique for the 3-d second order wave equation in time domain with an application to aeroacoustics." In: *Journal of Computational Physics* 235 (2013), pp. 407–422. DOI: 10.1016/j.jcp.2012.10.016.

[81] F. C. Karal. "The analogous acoustical impedance for discontinuities and constrictions of circular cross section." In: *Journal of the Acoustical Society of America* 25.2 (1953), pp. 327–334. DOI: 10.1121/1.1907041.

[82] D. H. Keefe. "Experiments on the single woodwind tone hole." In: *Journal of the Acoustical Society of America* 72.3 (1982), pp. 688–699. DOI: 10.1121/1.388249.

[83] D. H. Keefe. "Theory of the single woodwind tone hole." In: *Journal of the Acoustical Society of America* 72.3 (1982), pp. 676–687. DOI: 10.1121/1.388248.

[84] E. L. Kinsler, A. R. Frey, A. B. Coppens, J. V. Sanders. *Fundamentals of Acoustics*. Fourth edition. John Wiley & Sons, Inc., 2000.

[85] M. Kob. "Influence of wall vibrations of the transient sound of a flue organ pipe." In: *Acustica-Acta Acustica* 86.4 (2000), pp. 642–648.

[86] S. J. J. M. F. Kokkelmans, M.-P. Verge, A. Hirschberg, A. P. J. Wijnands, R. L. M. Schoffelen. "Acoustic Behavior of Chimney Pipes." In: *Journal of the Acoustical Society of America* 105 (1999), pp. 546–551. DOI: 10.1121/1.424590.

[87] H. Kühnelt. "Simulating the sound genereation in flutes and flue pipes with the Lattice-Boltzmann-Method." In: *Proceedings of the International Symposium on Musical Acoustics*. Nara, Japan, Mar. 2004, pp. 251–254.

[88] Y. Kulik. "Transfer matrix of conical waveguides with any geometric parameters for increased precision in computer modeling." In: *Journal of the Acoustical Society of America* 122 (2007), EL179–EL184. DOI: 10.1121/1.2794865.

[89] J. C. Lagarias, J. A. Reed, M. H. Wright, P. E. Wright. "Convergence properties of the Nelder-Mead simplex method in low dimensions." In: *SIAM Journal of Optimization* 9.1 (1998), pp. 112–147. DOI: 10.1137/S1052623496303470.

[90] L. N. Leet. "Organ pipes." In: *Journal of the Acoustical Society of America* 3 (1931), pp. 242–262. DOI: 10.1121/1.1915558.

[91] A. Lefebvre, G. P. Scavone. "Refinements to the model of a single woodwind instrument tonehole." In: *Proceedings of 20th International Symposium on Music Acoustics (Associated Meeting of the International Congress on Acoustics)*. Sydney and Katoomba, Australia, Aug. 2010. URL: http://isma2010.phys.unsw.edu.au/proceedings/papers/p35.pdf.

[92] A. Lefebvre, G. P. Scavone. "Characterization of woodwind instrument toneholes with the finite element method." In: *Journal of the Acoustical Society of America* 131.4 (2012), pp. 3153–3163. DOI: 10.1121/1.3685481.

[93] H. Levine, J. Schwinger. "On the radiation of sound from an unflanged circular pipe." In: *Physical Review* 73.4 (1948), pp. 383–406. DOI: 10.1103/PhysRev.73.383.

[94] D. K. Lilly. "A proposed modification of the Germano subgrid-scale closure method." In: *Physics of Fluids A* 4.3 (1992), pp. 633–635. DOI: 10.1063/1.858280.

[95] C. Mahrenholz. In: *Die Orgelregister (The organ stops)*. In German. Orgelbau-Fachverlag Rensch, Lauffen am Neckar, Germany, 1987, pp. 114–116.

[96] S. Marburg, B. Nolte. "A unified approach to finite and boundary element discretization in linear time-harmonic acoustics." In: *Computational Acoustics of Noise Propagation in Fluids – Finite and Boundary element methods*. Ed. by S. Marburg and B. Nolte. Springer, 2008, pp. 1–34.

[97] Mathworks. *Description of the function "fminsearch"*. URL: http://www.mathworks.de/help/toolbox/optim/ug/fminsearch.html.

[98] Mathworks. *Description of the simplex algorithm*. URL: http://www.mathworks.de/help/toolbox/optim/ug/brnoxr7-1.html#brnoxyk.

[99] M. E. McIntyre, R. T. Schumacher, J. Woodhouse. "On the oscillations of musical instruments." In: *Journal of the Acoustical Society of America* 74.5 (1983), pp. 1325–1345. DOI: 10.1121/1.390157.

[100] D. M. A. Mercer. "The voicing of organ flue pipes." In: *Journal of the Acoustical Society of America* 23.1 (1951), pp. 45–54. DOI: 10.1121/1.1906727.

[101] A. Miklós, J. Angster. "Sound radiation of open labial organ pipes; the effect of the size of the openeings on the formant structure." In: *Proceedings of the International Symposium on Musical Acoustics*. Washington, 1998, pp. 267–272.

[102] A. Miklós, J. Angster. "Properties of the sound of flue organ pipes." In: *Acustica-Acta Acustica* 86.4 (2000), pp. 611–622.

[103] A. Miklós, J. Angster, S. Pitsch, T. D. Rossing. "Reed vibration in lingual organ pipes without the resonators." In: *Journal of the Acoustical Society of America* 113.2 (2003), pp. 1081–1091. DOI: 10.1121/1.153410.

[104] A. Miklós, J. Angster, S. Pitsch, T. D. Rossing. "Interaction of reed and resonator by sound generation in a reed organ pipe." In: *Journal of the Acoustical Society of America* 119.5 (2006), pp. 3121–3129. DOI: 10.1121/1.2188372.

[105] P. M. Morse. *Vibration and sound*. Second edition. McGraw-Hill, 1948.

[106] P. M. Morse, K. U. Ingard. *Theoretical acoustics*. McGraw-Hill, 1968.

[107] C. J. Nederveen, J.-P. Dalmont. "Pitch and level changes in organ pipes due to wall resonances." In: *Journal of Sound and Vibration* 271 (2004), pp. 227–239. DOI: 10.1016/S0022-460X(03)00643-6.

[108] C. J. Nederveen, J. K. M. Jansen, R. R. Hassel. "Corrections for woodwind tone-hole calculations." In: *Acustica-Acta Acustica* 84.5 (1998), pp. 957–966.

[109] J. A. Nelder, R. Mead. "A simplex method for function minimalization." In: *The Computer Journal* 7 (1965), pp. 308–313. DOI: 10.1093/comjnl/7.4.308.

[110] A. W. Nolle. "Some voicing adjustments of flue organ pipes." In: *Journal of the Acoustical Society of America* 66.6 (1979), pp. 1612–1626. DOI: 10.1121/1.383658.

[111] A. W. Nolle. "Sinous instability of a planar air jet: Propagation parameters and acoustic excitation." In: *Journal of the Acoustical Society of America* 103 (1998), pp. 3690–3705. DOI: 10.1121/1.423089.

[112] A. W. Nolle, C. P. Boner. "Harmonic relations in the partials of organ pipes and of vibrating strings." In: *Journal of the Acoustical Society of America* 13 (1941), pp. 145–148. DOI: 10.1121/1.1916156.

[113] A. W. Nolle, C. P. Boner. "The initial transients of organ pipes." In: *Journal of the Acoustical Society of America* 13 (1941), pp. 149–155. DOI: 10.1121/1.1916157.

[114] Y. Nomura, I. Yamamura, S. Inawashiro. "Acoustic radiation from a flanged circular pipe." In: *Journal of the Physical Society of Japan* 15.3 (1960), pp. 510–517. DOI: 10.1143/JPSJ.15.510.

[115] A. Norris, I. C. Sheng. "Acoustic radiation from a circular pipe with an infinite flange." In: *Journal of Sound and Vibration* 135.1 (1989), pp. 85–93. DOI: 10.1016/0022-460X(89)90756-6.

[116] H. F. Olson. *Elements of acoustical engineering*. Second edition. D. van Nostrand Company, Inc., 1960.

[117] P. Oosterhof, A. Bouman. *Orgelbouwkunde (The art of organ building)*. In Dutch. Spruyt van Mantgenand de Does, Lieden, The Netherlands, 1956.

[118] *OpenFOAM software.* (last visited: January 30, 2014). URL: http://www.openfoam.org/.

[119] G. Paál, J. Angster, W. Garen, A. Miklós. "Sound and flow in the mouth of flue organ pipes. Part II: Transient state." In: *Proceedings of the International Symposium on Musical Acoustics*. Vol. 19, Part 5, Book 2. Edinburgh: Institute of Acoustics, 1997, pp. 333–338.

[120] G. Paál, J. Angster, W. Garen, A. Miklós. "A combined LDA and flow-visualization study on flue organ pipes." In: *Experiments in Fluids* 40 (2006), pp. 825–835. DOI: 10.1107/s00348-006-0114-0.

[121] G. Paál, I. Vaik. “Unsteady phenomena in the edge tone.” In: *International Journal of Heat and Fluid Flow* 28 (2007), pp. 575–586. DOI: 10.1016/j.ijheatfluidflow.2007.04.011.

[122] R. B. Paris. “Struve and related functions.” In: *NIST handbook of mathematical functions*. Ed. by F. W. J. Olver, D. W. Lozier, R. F. Boisvert, and C. W. Clark. National Institute of Standards and Technology – Cambridge University Press, 2010. Chap. 11.

[123] F. Pellegrini. *Scotch and libScotch user's guide*. Last visited: 25/08/2015. URL: https://gforge.inria.fr/docman/view.php/248/7104/scotch_user5.1.pdf.

[124] S. Pitsch. “Entwicklung von neuartigen offenen Windsystemen fr Kirchenorgeln (Development of novel open wind systems for church organs).” In German. PhD thesis. University of Siegen, 2005.

[125] G. R. Plitnik. “Vibration characteristics of pipe organ reed tongues and the effect of the shallot, resonator, and reed curvature.” In: *Journal of the Acoustical Society of America* 107.6 (2000), pp. 3460–3473. DOI: 10.1121/1.429416.

[126] G. R. Plitnik, J. Angster. “The influence of pipe organ reed curvature on tone quality.” In: *Journal of the Acoustical Society of America* 132.5 (), pp. 3502–3511. DOI: 10.1121/1.4756952.

[127] T. Preukschat. “Untersuchung der Klangentstehung bei Zungenorgelpfeifen (Investigation of the sound formation in lingual organ pipes).” In German. MA thesis. Universität Stuttgart, 1. Physikalisches Institut, 2012.

[128] T. Preukschat, J. Angster, A. Miklós. “Simulation of reed vibration in lingual organ pipes.” In: *Proceedings of the International Conference on Acoustics AIA-DAGA 2013*. Ed. by G. Brambilla and W. Kropp. Deutsche Gesellschaft für Akustik e.V. (DEGA). Merano, Italy, 2013, pp. 287–290.

[129] V. S. Ryaben'kii, S. V. Tsynkov. *A theoretical introduction to numerical analysis*. Chapman & Hall/CRC, Boca Raton, 2007.

[130] M. R. Schroeder. “Determination of the geometry of the human vocal tract by acoustic measurements.” In: *Journal of the Acoustical Society of America* 41.4 (1967), pp. 1002–1010. DOI: 10.1121/1.1910429.

[131] J. J. Shirron, I. Babuška. “A comparison of approximate boundary conditions and infinite element methods for exterior Helmholtz problems.” In: *Computer Methods in Applied Mechanics and Engineering* 164.1–2 (1998), pp. 121–139. DOI: 10.1016/S0045-7825(98)00050-4.

[132] J. Smagorinsky. “General circulation experiments with the primitive equations. I. The basic experiment.” In: *Monthly Weather Review* 91 (1963), pp. 99–164.

[133] A. Sommerfeld. “Die Greensche Funktion der Schwingungsgleichung.” In: *Jahresbericht der Deutschen Mathematiker-Vereinigung* 21 (1912), pp. 309–352.

[134] B. H. Story. “Technique for “tuning” vocal tract area functions based on acoustic sensitivity functions.” In: *Journal of the Acoustical Society of America* 119.2 (2006), pp. 715–718. DOI: 10.1121/1.2151802.

[135] G. Szoliva. “Effect of tuning devices on the sound generation for open labial organ pipes.” In Hungarian. MA thesis. Budapest University of Technology and Economics, 2005.

[136] K. Takahashi, T. Iwasaki, T. Akamura, Y. Nagao, K. Nakano, T. Kobayashi, T. Takami, A. Nishida, M. Aoyagi. “Effective techniques and crucial problems of numerical study on flue instruments.” In: *Proceedings of the Meetings on Acoustics – ICA 2013*. Vol. 19. Paper 2aMU3. Montreal, Canada, 2013, *–8. DOI: 10.1121/1.4799959.

[137] S. Thwaites, N. H. Fletcher. “Acoustic admittance of organ pipe jets.” In: *Journal of the Acoustical Society of America* 74.2 (1983), pp. 400–408. DOI: 10.1121/1.389833.

[138] G. D. Töpfer. *Die Theorie und Praxis des Orgelbaus (The theory and practice of organ building)*. In German. Bernhard Friedrich Voigt, Weimar, 1888.

[139] T. Trommer, J. Angster, A. Miklós. "Roughness of organ pipe sound due to frequency comb." In: *Journal of the Acoustical Society of America* 131.1 (2012), pp. 739–748. DOI: 10.1121/1.3651242.

[140] I. Vaik, G. Paál. "Flow simulations in an organ pipe foot model." In: *Journal of the Acoustical Society of America* 133.2 (2013), pp. 1102–1110. DOI: 10.1121/1.4773861.

[141] M. P. Verge, B. Fabre, A. Hirschberg, A. P. J. Wijnands. "Sound production in recorderlike instruments. I. Dimensionless amplitude of the internal acoustic field." In: *Journal of the Acoustical Society of America* 101.5 (1997), pp. 2914–2924. DOI: 10.1121/1.418521.

[142] M. P. Verge, B. Fabre, W. E. A. Mahu, A. Hirschberg, R. R. Hassel, A. P. J. Wijnands, J. J. Vries, C. J. Hogendoorn. "Jet formation and jet velocity fluctuations in a flue organ pipe." In: *Journal of the Acoustical Society of America* 95.2 (1994), pp. 1119–1132. DOI: 10.1121/1.408460.

[143] M. P. Verge, A. Hirschberg, R. Caussé. "Sound production in recorderlike instruments. II. A simulation model." In: *Journal of the Acoustical Society of America* 101.5 (1997), pp. 2925–2939. DOI: 10.1121/1.419481.

[144] M. Walstijn, M. Campbell. "Discrete-time modeling of woodwind instrument bores using wave variables." In: *Journal of the Acoustical Society of America* 113.1 (2003), pp. 575–585. DOI: 10.1121/1.1515776.

[145] C. H. Wilcox. "A generalisation of theorems of Rellich and Atkinson." In: *Proceedings of the American Mathematical Society* 7 (1956), pp. 271–276. DOI: 10.2307/2033184.

[146] C. F. A. Williams. *The story of the organ*. The Walter Scott Publishing Co., Ltd., 1903.

[147] S. Yoshikawa. "Jet-wave amplification in organ pipes." In: *Journal of the Acoustical Society of America* 103.5 (1998), pp. 2706–2717. DOI: 10.1121/1.423113.

[148] S. Yoshikawa. "A pictoral analysis of jet and vortex behaviours during attack transients in organ pipe models." In: *Acustica-Acta Acustica* 86.4 (2000), pp. 623–633.

[149] S. Yoshikawa, H. Tashiro, Y. Sakamoto. "Experimental examination of vortex-sound generation in an organ pipe: A proposal of jet vortex-layer formation model." In: *Journal of Sound and Vibration* 331 (2012), pp. 2558–2577. DOI: 10.1016/j.jsv.2012.01.026.

[150] T. Zászkaliczky. *Az orgona képes krónikája (Illustrated chronicle of the organ)*. In Hungarian. Rózsavölgyi és Társa, 2008.

[151] O. C. Zienkiewicz, R. L. Taylor, J. Z. Zhu. *The finite element method: Its basis and fundamentals*. Sixth. Elsevier Butterworth–Heinemann, Oxford, 2005.

[152] J. Zon, A. Hirschberg, J. Gilbert, A. P. J. Wijnands. "Flow through the reed channel of a single reed music instrument." In: *1er Congrès Français d'Acoustique*. Vol. C2. 1990, pp. 821–824.

[153] W. E. Zorumski. "Generalized radiation impedances and reflection coefficients of circular and annular ducts." In: *Journal of the Acoustical Society of America* 54.6 (1973), pp. 1667–1673. DOI: 10.1121/1.1914466.

[154] C. Zwikker, C. W. Kosten. *Sound Abosrbing Materials*. Elsevier, 1949.

Publications

Journal papers

[J1] P. Rucz. “Determination of organ pipes’ acoustic parameters by means of numerical techniques.” In: *Akusztikai Szemle, Acoustic Review* 10.3–4 (2010), pp. 39–47.

[J2] P. Rucz, T. Trommer, J. Angster, A. Miklós, F. Augusztinovicz. “Sound design of chimney pipes by optimization of their resonators.” In: *Journal of the Acoustical Society of America* 133.1 (2013). IF: 1.56, C: 1, pp. 529–537. DOI: 10.1121/1.4770236.

[J3] P. Rucz, F. Augusztinovicz, J. Angster, T. Preukschat, A. Miklós. “Acoustic behavior of tuning slots of labial organ pipes.” In: *Journal of the Acoustical Society of America* 135.5 (2014). IF: 1.56, pp. 3056–3065. DOI: 10.1121/1.4869679.

[J4] P. Rucz, F. Augusztinovicz, J. Angster, T. Preukschat, A. Miklós. “A finite element model of the tuning slot of labial organ pipes.” In: *Journal of the Acoustical Society of America* 137.3 (2015). IF: 1.56*, pp. 1226–1237. DOI: 10.1121/1.4913460.

[J5] P. Fiala, P. Rucz. “NiHu: an open source C++ BEM library.” In: *Advances in Engineering Software* 75 (2014). IF: 1.40, C: 1, pp. 101–112. DOI: 10.1016/j.advengsoft.2014.05.011.

Conference papers

[C1] P. Rucz, F. Augusztinovicz, P. Fiala. “Simulation of organ pipes’ acoustic behavior by means of various numerical techniques.” In: *Proceedings of the 16th International Congress on Sound and Vibration*. Ed. by D. Bismor. Vol. 3. International Institute of Acoustics and Vibration. Kraków, Poland, July 2009, pp. 1742–1749.

[C2] P. Rucz, J. Angster, F. Augusztinovicz, P. Fiala, A. Miklós, N. Manrique Ortiz. “Simulation of organ pipe transfer function by means of various numerical techniques.” In: *Proceedings of ISMA2010: International Conference on Noise and Vibration Engineering including USD2010*. Ed. by P. Sas and B. Bergen. Paper ID. 335. Katholieke Universiteit Leuven. Leuven, Belgium, 2010, pp. 4673–4684.

[C3] J. Angster, T. Preukschat, T. Trommer, P. Rucz, A. Miklós. “Experimentelle Untersuchung der Wirkung des Rohrs auf den Klang der Rohrflöte.” In: *DAGA2012 38. Jahrestagung für Akustik*. Ed. by H. Hanselka. Paper ID. 447. D. Darmstadt, Germany, 2012, pp. 201–202.

[C4] T. Preukschat, J. Angster, A. Miklós, P. Rucz. “Der Einfluss von Expressionen auf den Orgelpfeifenklang.” In: *DAGA2012 38. Jahrestagung für Akustik*. Ed. by H. Hanselka. Paper ID. 448. D. Darmstadt, Germany, 2012, pp. 203–204.

[C5] P. Rucz, F. Augusztinovicz, J. Angster, P. Fiala, T. Trommer, A. Miklós. “Optimization algorithms for the sound design of chimney and tuning slot organ pipes.” In: *DAGA2012 38. Jahrestagung für Akustik*. Ed. by H. Hanselka. Paper ID. 457. D. Darmstadt, Germany, 2012, pp. 205–206.

[C6] P. Rucz, J. Angster, F. Augusztinovicz, P. Fiala, A. Miklós, T. Trommer. "Optimization and simulation algorithms for the sound design of labial organ pipes." In: *ICSV19 19th International Congress on Sound and Vibration*. Ed. by D. Čiplys. Paper ID. 236. International Institute of Acoustics and Vibration. Vilnius, Lithuania, 2012, *–8.

[C7] P. Rucz, J. Angster, P. Fiala, A. Miklós, B. Olteán, T. Preukschat. "Numerical simulation and optimization algorithms for the sound design of organ pipes with tuning slots." In: *Proceedings of the ISMA2012–USD2012 International Conference on Noise and Vibration Engineering*. Ed. by P. Sas, D. Moens, and S. Jonckheere. Paper ID. 487. Katholieke Universiteit Leuven. Leuven, Belgium, 2012, pp. 4215–4228.

[C8] J. Angster, A. Miklós, P. Rucz, F. Augusztinovicz. "The physics and sound design of flue organ pipes." In: *Journal of the Acoustical Society of America* 132.3 (2012). Abstract of Paper 4pMU3., p. 2069. DOI: 10.1121/1.4755627.

[C9] P. Fiala, P. Rucz. "FMBEM simulation of scattered wave fields excited by multiple moving sources." In: *Proceedings of the International Conference on Acoustics AIA-DAGA 2013*. Ed. by G. Brambilla and W. Kropp. Paper ID. 618. Deutsche Gesellschaft für Akustik e.V. (DEGA). Merano, Italy, 2013, pp. 1209–1212.

[C10] S. Pitsch, P. Rucz, J. Angster, A. Miklós, J. Kirschmann. "Scaling software for labial organ pipes." In: *Proceedings of the International Conference on Acoustics AIA-DAGA 2013*. Ed. by G. Brambilla and W. Kropp. Paper ID. 722. Deutsche Gesellschaft für Akustik e.V. (DEGA). Merano, Italy, 2013, pp. 299–302.

[C11] P. Rucz, J. Angster, F. Augusztinovicz, A. Miklós, T. Preukschat. "Modeling resonators of reed organ pipes." In: *Proceedings of the International Conference on Acoustics AIA-DAGA 2013*. Ed. by G. Brambilla and W. Kropp. Paper ID. 416. Deutsche Gesellschaft für Akustik e.V. (DEGA). Merano, Italy, 2013, pp. 283–286.

[C12] P. Fiala, P. Rucz. "NiHu: A BEM-FMBEM Matlab toolbox." In: *Proceedings of the Inter-Noise 2013 Congress on Noise Control Engineering*. Ed. by W. Talasch. Paper ID. 684. International Institute of Noise Control Engineering. Innsbruck, Austria, 2013, *–10.

[C13] P. Rucz, J. Angster, F. Augusztinovicz, M. M. Lohász, A. Miklós. "Air jet and edge tone simulation in an organ pipe foot model." In: *Proceedings of the Inter-Noise 2013 Congress on Noise Control Engineering*. Ed. by W. Talasch. Paper ID. 748. International Institute of Noise Control Engineering. Innsbruck, Austria, 2013, *–10.

[C14] P. Fiala, P. Rucz. "Formulating various BEM problems with a generic C++ library." In: *DAGA2014 40. Deutsche Jahrestagung für Akustik*. Ed. by B. Kollmeier. Paper ID. 368. Deutsche Gesellschaft für Akustik e.V. (DEGA). Oldenburg, Germany, 2014, pp. 373–374.

[C15] P. Rucz, T. Preukschat, J. Angster, F. Augusztinovicz, A. Miklós. "Simulation of the sound generation of lingual organ pipes." In: *DAGA2014 40. Deutsche Jahrestagung für Akustik*. Ed. by B. Kollmeier. Paper ID. 308. Deutsche Gesellschaft für Akustik e.V. (DEGA). Oldenburg, Germany, 2014, pp. 46–47.

[C16] J. Angster, K. Dolde, P. Rucz, A. Miklós. "The influence of the shallot shape on the sound of Trompete reed pipes." In: *Journal of the Acoustical Society of America* 135 (2014). Abstract of ASA meeting paper, p. 2244. DOI: 10.1121/1.4877348.

Other publications

[O1] P. Rucz, F. Augusztinovicz, P. Fiala. "Orgonasípok akusztikai paramétereinek meghatározása numerikus technikákkal." In: *2009. évi Végzős Konferencia*. Ed. by Z. Heszberger. In Hungarian. Budapesti Műszaki és Gazdaságtudományi Egyetem. Budapest, Magyarország, May 2009, *–4.

[O2] J. Angster, K. Dolde, P. Rucz, A. Miklós. *Einfluss der Kehlenform auf den Klang der Trompeten-Zungenorgelpfeifen*. Oral presentation at the DAGA2014 conference, Oldenburg, Germany, March 11th, 2014.

Internal technical reports

[T1] F. Augusztinovicz, P. Rucz. *INNOSOUND – Computer simulation of pipes with tuning slots (Deliverable 1.2)*. Tech. rep. Budapest University of Technology and Economics, 2009.

[T2] P. Rucz, F. Augusztinovicz. *INNOSOUND – Report on the results of simulation (Deliverable 3.2)*. Tech. rep. Budapest University of Technology and Economics, 2010.

[T3] J. Angster, S. Pitsch, A. Miklós, F. Augusztinovicz, P. Rucz. *INNOSOUND – Internal report: Software code (Deliverable 3.3)*. Tech. rep. Fraunhofer Institute for Building Physics, Steinbeis Transfer Centre, Budapest University of Technology and Economics, 2010.

[T4] P. Rucz, F. Augusztinovicz. *REEDDESIGN – Internal report about the results of computer simulations of the shallot-resonator system (Deliverable 1.2)*. Tech. rep. Budapest University of Technology and Economics, 2012.

[T5] P. Rucz, F. Augusztinovicz. *REEDDESIGN – Design software code for dimensioning reed pipes and reed ranks (Deliverable 4.2)*. Tech. rep. Budapest University of Technology and Economics, 2013.